JAERI-Research
2003-014

STUDY ON SHIELDING DESIGN METHOD OF RADIATION STREAMING IN A TOKAMAK-TYPE DT FUSION REACTOR BASED ON MONTE CARLO CALCULATION

September 2003

Satoshi SATO

日本原子力研究所
Japan Atomic Energy Research Institute

本レポートは，日本原子力研究所が不定期に公刊している研究報告書です。
入手の問合わせは，日本原子力研究所研究情報部研究情報課（〒319-1195　茨城県那珂郡東海村）あて，お申し越しください。なお，このほかに財団法人原子力弘済会資料センター（〒319-1195　茨城県那珂郡東海村日本原子力研究所内）で複写による実費頒布をおこなっております。

This report is issued irregularly.
Inquiries about availability of the reports should be addressed to Research Information Division, Department of Intellectual Resources, Japan Atomic Energy Research Institute, Tokai-mura, Naka-gun, Ibaraki-ken, 319-1195, Japan.

編集兼発行　　日本原子力研究所

Study on Shielding Design Method of Radiation Streaming in a Tokamak-type DT Fusion Reactor based on Monte Carlo Calculation

Satoshi SATO

Department of Fusion Engineering Research
(Tokai-site)
Naka Fusion Research Establishment
Japan Atomic Energy Research Institute
Tokai-mura, Naka-gun, Ibaraki-ken

(Received June 13, 2003)

In tokamak-type DT nuclear fusion reactor, there are various type slits and ducts in the blanket and the vacuum vessel. The helium production in the rewelding location of the blanket and the vacuum vessel, the nuclear properties in the super-conductive TF coil, e.g. the nuclear heating rate in the coil winding pack, are enhanced by the radiation streaming through the slits and ducts, and they are critical concern in the shielding design. The decay gamma ray dose rate around the duct penetrating the blanket and the vacuum vessel is also enhanced by the radiation streaming through the duct, and they are also critical concern from the view point of the human access to the cryostat during maintenance. In order to evaluate these nuclear properties with good accuracy, three dimensional Monte Carlo calculation is required but requires long calculation time. Therefore, the development of the effective simple design evaluation method for radiation streaming is substantially important. This study aims to establish the systematic evaluation method for the nuclear properties of the blanket, the vacuum vessel and the Toroidal Field (TF) coil taking into account the radiation streaming through various types of slits and ducts, based on three dimensional Monte Carlo calculation using the MCNP code, and for the decay gamma ray dose rates penetrated around the ducts.

The present thesis describes three topics in five chapters as follows;

1) In Chapter 2, the results calculated by the Monte Carlo code, MCNP, are compared with those by the Sn code, DOT3.5, for the radiation streaming in the tokamak-type nuclear fusion reactor, for validating the results of the Sn calculation. From this comparison, the uncertainties of the Sn calculation results coming from the ray-effect and the effect due to approximation of the geometry are investigated whether the two dimensional Sn calculation can be applied instead of the Monte Carlo calculation. Through the study, it can be concluded that the three dimensional Monte Carlo calculation is required for the shielding calculation in the tokamak-type DT nuclear fusion rector with many penetrations.

2) In Chapter 3, radiation streaming through the slit between the blanket modules is described, in Chapter 4, that through the small circular duct in the blanket modules is described, in Chapter 5, and that through the large opening duct in the vacuum vessel is described. The nuclear properties of the blanket, the vacuum vessel and the TF coil are systematically calculated for the various configurations. Based on the obtained results, the analytical formulas of these nuclear properties are deduced, and the guideline is proposed for the shielding design.

3) In Chapter 6, in order to evaluate the decay gamma ray dose rate around the duct due to radiation streaming through the large opening duct in the vacuum vessel, the evaluation method is proposed using the decay gamma ray Monte Carlo calculation. By replacing the prompt gamma-ray spectrum to the decay one in the Monte Carlo code, the decay gamma ray Monte Carlo transport calculation is conducted. The effective variance reduction method is developed for the decay gamma ray Monte Carlo calculation in the over-all tokamak region with drastically reducing the calculation time. Using this method, the shielding calculation is conducted for the ITER duct penetration, and the effectiveness of this method is demonstrated.

Keywords: Fusion Reactor, Streaming, Slit, Duct, Monte Carlo Calculation, Sn Calculation, Analytical Formula, Variance Reduction Method

モンテカルロ計算に基づくトカマク型ＤＴ核融合炉の放射線ストリーミングに対する遮蔽設計法の研究

日本原子力研究所那珂研究所核融合工学部
佐藤　聡

(2003年6月13日　受理)

トカマク型ＤＴ核融合炉では、ブランケットや真空容器に様々な形状のスリットやダクトが存在するため、それらからの放射線ストリーミングによるブランケットや真空容器再溶接部のヘリウム生成量、超伝導トロイダルコイルの核発熱や照射損傷等の核的応答を許容値以下にすることは遮蔽設計上の重要課題である。またダクトからの放射線ストリーミングによってブランケットや真空容器を貫通するダクト周囲の崩壊γ線線量率も増大し、メンテナンス時のクライオスタットへのアクセスの観点から、それらもまた重要課題である。これらの核的応答を精度良く評価するためには、３次元モンテカルロ計算が必要であるが、多大な計算時間を必要とする。そこで、放射線ストリーミングに対する有用で簡便な計算手法の開発が非常に重要である。本研究では、ＭＣＮＰコードを用いた３次元モンテカルロ計算に基づいて、様々な形状のスリットやダクトからの放射線ストリーミングを考慮したブランケットや真空容器、トロイダル（ＴＦ）コイルの核的応答に対する系統的な評価手法の構築、及びダクト貫通部周囲の崩壊γ線線量率に対する計算手法の開発を目的としている。

本研究は、３つの課題及び５つの章から構成されている。

１）第２章ではＳｎ計算の結果を検証するために、モンテカルロコードＭＣＮＰによる計算結果とＳｎコードＤＯＴ３．５による計算結果を比較する。レイエフェクトや計算形状の近似によるＳｎ計算結果の不確定性を評価し、２次元Ｓｎ計算の適用性を検討した結果、多数の貫通部を有するトカマク型ＤＴ核融合炉の遮蔽計算に対しては、３次元モンテカルロ計算が必要であると結論できる。

２）第３章では隣り合うブランケットモジュール間のスリット、第４章ではブランケットモジュールを貫通する小口径円管ダクト、第５章では真空容器を貫通する大口径ダクトからの放射線ストリーミングによるブランケットや真空容器、ＴＦコイルの核的応答を、様々な形状に対して系統的な計算を行った。各種ストリーミングに対して、スリットやダクト形状、遮蔽体形状、遮蔽体組成、ホウ素濃度等に対するヘリウム生成量や核発熱率等のパラメータ依存性を３次元モンテカルロ法により系統的に評価し、これらのパラメータの関数として評価近似式を開発した。その結果、簡便で精度良い遮蔽評価により、迅速で汎用的な核融合炉遮蔽設計を実現した。

那珂研究所（東海駐在）〒319-1195　茨城県那珂郡東海村白方白根2-4

3）第６章では真空容器を貫通する大口径ダクトからの放射線ストリーミングによるダクト周囲の崩壊γ線線量率を評価するため、崩壊γ線モンテカルロ計算を用いた評価手法を提案した。計算時間を大幅に短縮させるために、有効な分散低減手法を開発している。本手法をＩＴＥＲダクト貫通部に対する遮蔽計算に適用し、その有効性を実証した。

Contents

目　次

Table Captions

Figure Captions

1. Introduction

1.1 Nuclear Fusion Reactor

The progress in human life, especially in science and technology, has been made by the production of the energy. The modern society has been supported by a variety of energy sources. The energy sources at present are oil, coal, natural gas and nuclear fission. We have now a critical concern that the energy sources from the fossil fuel such as oil, coal, natural gas are dried up in the near future and also they release extensive CO_2 gas which causes the greenhouse effect. The energy production by the nuclear fission reaction has a great advantage from the view point of rich fuel and little CO_2 release. As a result, the energy production by the nuclear fission reaction has already occupied about 40 % of the total electricity in Japan, and the importance of the nuclear fission reactor increases as a fundamental energy source. On the other hand, development of the next generation energy source is an emergency task. Nuclear fusion energy is one of the prominent new energy sources. The nuclear fusion energy has the following advantages,

1) CO_2 gas release is much little,
2) The fuel is infinite for some kinds of fusion reaction,
3) There is no runaway about the nuclear reaction, and the passive safety can be assured during the operation,
4) No fission products can't be produced in the nuclear reaction.

The nuclear fusion reactor is also not influenced by the natural condition, while the wind energy and the solar energy are much influenced by the natural condition. As the realistic solution, the nuclear fusion reactor is the most prominent as the next energy source.

The fusion reactions which can be utilized for energy production are as follows;

$$D + T \rightarrow {}^4He\ (3.52) + n\ (14.06) \quad (1.1)$$

$$D + {}^3He \rightarrow {}^4He\ (3.67) + n\ (14.67) \quad (1.2)$$

$$D + D \rightarrow {}^3He\ (0.82) + n\ (2.45) \quad (1.3)$$
$$\rightarrow T\ (1.01) + p\ (3.03)$$

$$p + {}^6Li \rightarrow {}^4He\ (1.7) + {}^3He\ (2.3) \quad (1.4)$$

$$p + {}^6Li \rightarrow {}^4He + D + p - 1.5\ MeV \quad (1.5)$$

$$n + {}^6Li \rightarrow {}^4He + D + n - 1.5\ MeV \quad (1.6)$$

$$D + {}^6Li \rightarrow {}^7Li\ (0.6) + p\ (4.4) \quad (1.7)$$
$$\rightarrow {}^4He + T + p + 2.6MeV$$
$$\rightarrow 2{}^4He\ (1.12)$$

$$D + {}^6Li \rightarrow {}^7Be\ (0.43) + n\ (2.97) \quad (1.8)$$
$$\rightarrow {}^4He + {}^3He + n + 1.8MeV$$

$$^3He + {}^6Li \rightarrow 2{}^4He + p + 16.9MeV \quad (1.9)$$

$$p + t \rightarrow {}^3He + n - 0.8MeV \quad (1.10)$$

$$p + {}^{11}B \rightarrow 3{}^4He + 8.68MeV \quad (1.11),$$

where the values in parentheses mean the energy of the reaction product in MeV.

Nuclear fusion reaction in Eq (1.1) is the most prominent due to large reaction cross-

section. As the reactor to induce the nuclear fusion reaction shown in Eq. (1.1), there are two main concepts; 1) magnetic confinement, and 2) inertial confinement. The magnetic confinement is the most prominent type, and the tokamak type is the most prominent among of various magnetic confinement types.

The large scale tokamak type machines such as TFTR in Princeton University, JET in EU and JT-60 in JAERI were established in the middle of 1980. The achievement of the plasma confinement is a main objective in these machines. A large number of experiments on the DD reaction expressed by Eq. (1.3) have been conducted in these machines, and the feasibility of the nuclear fusion reaction by the plasma confinement has been demonstrated. Some experiments using the DT reaction have also been conducted in JET and TFTR. The thermal energy of 1.5 – 2 MW was generated by the JET on 9th Nov., 1991 [1.1]. This is the first experimental result that a significant amount of power has been obtained from controlled nuclear fusion reactions.

As the tokamak machine of the next generation, the full-scale DT experimental reactor has been planned by the international collaboration between EU, Russia, Japan and USA. This experimental reactor is called as ITER (International Thermo-nuclear Experimental Reactor). A large number of experiments on the DT reaction with the high fusion power of more than 500 MW and the long duration time of more than 1000 seconds are to be conducted in this machine, though experiments with the low fusion power of about 20 MW and the very short burning duration time have already been conducted in the previous machines. To achieve the self ignition is one of the object in ITER. The conceptual design activity of the ITER had been conducted in 1988 – 1990, and the engineering design activity had been conducted in 1992 – 2001.

The neutron intensity generated with the energy of 14 MeV was about 10^{19} neutrons / second, in the previous fusion machine. It is to be about 10^{21} neutrons / second in ITER, which is two orders of magnitude larger than in the previous fusion machine, and the integrated neutron intensity generated with the energy of 14 MeV is to be about 10^{28} neutrons in ITER. The enormous neutrons are generated in the future fusion reactor such as ITER, the demonstration reactor, the commercial reactor, and the shielding design is critical concern.

1.2 Nuclear Design in Fusion Reactor

A conceptual bird's-eye view of the tokamak-type DT fusion reactor of the next generation such as ITER is shown in Fig. 1.1, in which the blankets, divertors, a vacuum vessel, super conductive (SC) magnets, plasma heating equipment, cryostat and biological shield are the main component of the DT tokamak machine. The hydrogen isotopes as fuels of the nuclear fusion reaction are confined in plasma condition by the SC magnets, for inducing the nuclear fusion reaction. The SC magnets are used to make the magnetic fields in toroidal (circular) and poloidal (height) directions, which are called as TF (Toroidal Field) and PF (Poloidal Field) coils, respectively. Plasma can be confined by the both magnetic fields. Blankets are installed inside the vacuum vessel surrounding the plasma, and they have three objects, 1) to protect the vacuum vessel and the TF coil against the radiation from the plasma, 2) to covert the nuclear heating to the thermal energy, and 3) to produce the tritium as the fuel

via nuclear reaction. In the ITER, the shielding blankets composed of stainless steel (SS) and water are to be installed to protect the vacuum vessel and the TF coil against the radiation. The blanket system for a fusion experimental reactor such as ITER is composed of a number of modules for easy assembly and maintenance, which has a few centimeter wide slits between the adjacent modules [1.2 – 1.4]. The small circular ducts with a few centimeter diameter are bored through the face of the blanket in order to insert the welding and cutting equipments for replacement of the blanket module [1.5]. The divertors are also installed at the lower or upper regions inside the vacuum vessel to remove the impurities and the excessive thermal power due to the heat radiation from the plasma. The large opening ducts are located in the confined space between adjacent TF coils, and they penetrate the blankets and the vacuum vessel. These ducts are used for the beam injection, exhausting the impurity, diagnostics, maintenance for the blanket and divertor, and so on.

Enormous neutrons with energy of 14 MeV are produced by the DT reaction in the plasma region, so the shielding design is critical concern in the DT nuclear fusion reactor. Radiation shielding of the fusion reactor can be divided into two main areas; 1) Biological shielding against radiation, and 2) Shielding for the critical components of the machine. For the former, the shielding concept of the fusion reactor is almost the same as that of the fission reactor. For the latter, in the case of the magnetic confinement fusion reactor, the shielding design is required especially to the SC magnet. The SC magnet is composed of four main materials; 1) the magnet case made of SS (stainless steel), 2) the SC magnet winding pack composed of Nb_3Sn, SS and copper, 3) the stabilizer copper, and 4) the insulator made of epoxy. The influence of radiation on the SC magnet components leads to; 1) the nuclear heating, 2) reduction of the critical current density for the winding pack, 3) the neutron damage of the stabilizer copper, and 4) the neutron and gamma ray damages of the insulator. The restriction of the nuclear heating is connected to the demand of cryostability of the superconductor. The temperature of the superconductor increases with the nuclear heating. When the temperature is higher than the design limit, the super conductive state can not be kept. The critical current density of the winding pack generally increases, reaching a maximum, and then decreases as the neutron fluence increases. The stabilizer copper carries the current in the case that the superconductor temporarily becomes resistive. The resistance of the stabilizer copper is the most important for considering this process. The properties of interest for the insulator design are electrical resistivity, dielectric strength, mechanical strength, and thermal insulation. When the insulator is damaged by the excessive radiation, the unexpected current flow and magnetic force are occurred and the soundness of the SC magnet can not be kept. In order to keep the soundness of the SC magnet, the shielding design must be conducted to satisfy the design limit of the nuclear heating, the neutron fluence of the winding pack, the neutron damage of the stabilizer copper, and the radiation damage of the insulator. As an example, the design limit of the ITER is shown in Table 1.1 for these nuclear properties of the SC magnet.

In addition to the soundness of the SC magnet, the soundness must be kept for the welding part of the structure material. The blanket module is to be replaced by cutting some parts during its life, and the structural material of the residual parts is to be welded to the brand-new blanket module. The helium is produced in SS through the (n, α) reaction by the

neutron irradiation, and it affects weldability. The helium is concentrated at the grain boundary by the heat during welding. When the helium production of the welding part exceed the allowable value, the soundness of the welding part can't be kept. When the TF coils are replaced, the vacuum vessel is also replaced. Therefore the helium production of the rewelding part of the blanket and the vacuum vessel is required to satisfy the allowable value for rewelding. As an example, the design limit of the ITER is also shown in Table 1.1 for the helium production. It is assumed here that rewelding of stainless-steel can be accomplished if the helium production is less than 1 appm [1.6]

For the biological shielding in the ITER, the human access inside the cryostat is not considered during the operation of the fusion reactor. The biological shielding design has been conducted for the only public protection at the site boundary. Personnel access outside the cryostat is, however, required for hands-on maintenance several days after shutdown, and even inside the cryostat for rescue maintenance which might be conducted longer time (~ a month) after shutdown. It is important to minimize the decay gamma-ray dose rates around the large opening ducts in order to make those works possible. In the case of ITER, the design target of 100 μSv/hour in the cryostat is tentatively assumed 10^6 seconds after reactor shut down.

As mentioned above, the slits and ducts with the various configurations exist in the tokamak-type DT nuclear fusion reactor as shown in Fig. 1.1. The nuclear properties of the fusion reactor component and the decay gamma ray dose rates are enhanced by the radiation streaming through these slits and ducts, which brings the large effect on the shielding design.

1.3 Background, Objective and Outline of the Present Study

In general, the shielding design considering the radiation streaming effect is conducted by using the two dimensional Sn method in the preliminary design stage due to an easiness and efficiency of the method. The results by the Sn method, however, are expected to have poor accuracy in the streaming calculation due to the ray-effect and the approximation in the configuration. Finally the shielding design calculation is carried out by three dimensional Monte Carlo method for possible simulation of the actual geometry in order to give more accurate results. The three dimensional Monte Carlo method requires, however, much longer CPU time.

A lot of design studies about the fusion reactor shielding had been performed for last about 25 years. Most of the studies were done based on one or two dimensional Sn methods to evaluate the bulk shielding, in the course of the conceptual overall reactor design including the plasma design, structure design and safety analysis.

Most of them have been conducted for a fixed design taking into account the radiation streaming[1.7 – 1.13]. On the other hand, Shin et al. [1.14, 1.15] and Iida et al. [1.15] proposed the simplified evaluation method of the neutron flux for the radiation streaming with the simple configuration. They are very useful for the rapid evaluation of the neutron flux including the radiation streaming. Zimin et al. proposed the peaking factor of the streaming for the very limited configuration based on the results by two dimensional Sn calculation

[1.11]. Although the results are useful for the limited configuration, a large uncertainty is expected due to the ray-effect.

On the other hand, the systematic evaluation for the configuration with various types of slits and ducts including decay gamma ray dose rates has not been performed for the tokamak type DT nuclear fusion reactor based on three dimensional Monte Carlo calculation. The spatial distribution of induced activity emitting the decay gamma ray is needed in the decay gamma-ray transport calculation. The distribution can be obtained through conventional method by multiplying the neutron flux with the neutron activation cross sections using the activation codes such as ACT-4 [1.17], CINAC [1.18] and FISPACT [1.19]. It requires, however, a very fine (small) cell definition and huge calculation time to obtain the detailed neutron flux distribution in the overall region of the tokamak, which is not realistic for actual design calculation. There has been no simple rapid analytical evaluation method, either which is directly applicable to the shielding design of the tokamak-type fusion reactor, for estimating the helium production and the nuclear properties of the SC magnet.

Therefore, the development of the effective simple design evaluation method for radiation streaming is substantially important. This study aims to establish the systematic evaluation method for the nuclear properties of the blanket, the vacuum vessel and the TF coil taking into account the radiation streaming through various types of slits and ducts, based on three dimensional Monte Carlo calculation using the MCNP code [1.20], and for the decay gamma ray dose rates penetrated around the ducts.

The present thesis describes three topics in five chapters as follows;

1) In Chapter 2, the results calculated by the Monte Carlo code, MCNP, are compared with those by the Sn code, DOT3.5 [1.20], for the radiation streaming in the tokamak-type nuclear fusion reactor, for validating the results of the Sn calculation.

2) In Chapter 3, radiation streaming through the slit between the blanket modules is described, in Chapter 4, that through the small circular duct in the blanket modules is described, and in Chapter 5, that through the large opening duct in the vacuum vessel is described. In these sections, the nuclear properties of the blanket, the vacuum vessel and the TF coil are systematically calculated for the various configurations. Based on these results, the analytical formulas of these nuclear properties are deduced, and the guideline is proposed for the shielding design.

3) In Chapter 6, in order to evaluate the decay gamma ray dose rate around the duct due to radiation streaming through the large opening duct in the vacuum vessel, the evaluation method is proposed using the decay gamma ray Monte Carlo transport calculation. By replacing the prompt gamma-ray spectrum to the decay one in the Monte Carlo code, the decay gamma ray Monte Carlo transport calculation is conducted. The effective variance reduction method is proposed for the decay gamma ray Monte Carlo transport calculation in the over-all tokamak region with drastically reducing the calculation time. Using this method, the shielding calculation is conducted for the ITER duct penetration, and the effectiveness of this method is demonstrated.

Finally, the results obtained in this study are summarized in Chapter 7. The relationship of each chapter is illustrated in Fig. 1.2.

References

[1.1] JET Team, Fusion energy production from a deuterium-tritium plasma in the JET tokamak, Nucl. Fusion 32, 187-203 (1992).

[1.2] P.-H. Rebut, ITER: the first experimental fusion reactor, Fusion Eng. Design, 27, 3-16 (1995).

[1.3] K. Ioki, et al., FW/Blanket and vacuum vessel for RTO/RC ITER, Fusion Eng. Design, 49-50, 467-475 (2001).

[1.4] F. Elio et al., Progress in the ITER Blanket Design, Proc. 17th Symp. on Fusion Eng., San Diego, Oct., (1997).

[1.5] S. Sato, H. Takatsu, T. Kurasawa, et al., Conceptual Design of ITER Shielding Blanket, JAERI-Tech 95-019, (1995).

[1.6] K. Ioki, et al., FW/Blanket and vacuum vessel for RTO/RC ITER, Fusion Eng. Design, 49-50, 467-475 (2001).

[1.7] W. T. Urban et al., Engineering test facility vacuum pumping duct shield analysis, Nucl. Technol. /Fusion 2, 261-271(1982).

[1.8] Y. Seki et al., Radiation streaming calculations for INTOR-J, Nucl. Technol. /Fusion 2, 272-285 (1982).

[1.9] Y. Seki et al., Radiation shielding considerations for the repair and maintenance of a swimming pool-type tokamak reactor, Nucl. Engrg. Des./ Fusion 1, 243-253 (1984).

[1.10] K. Ueki et al., Analysis of 14 MeV neutron streaming through a narrow hole-duct using the Monte Carlo technique, Fusion Technol. 7, 90 (1985).

[1.11] S.A. Zimin, An analysis of radiation streaming through inhomogeneities in the fusion reactor blanket and shield, Fusion Technol. 17, 371 (1990).

[1.12] K. Maki et al., Radiation shielding for superconductive toroidal field coils around the neutral beam injector duct in the ITER design, Fusion Eng. Design. 22, 427-434 (1993).

[1.13] S. Sato et al., Evaluation of radiation streaming through the annular gaps around divertor cooling pipes in fusion experimental reactors, Proceedings of 8th International Conference on Radiation Shielding, Arlington, Texas USA, April 24-28, 1039-1046 (1994).

[1.14] K. Shin et al., Semiempirical formula for energy-space distributions of streamed neutrons and gamma-rays in cylindrical ducts, J. Nucl. Sci. Technol. 25, 8 (1988).

[1.15] K. Shin et al., A simple calculation method for 14 MeV neutron gap streaming, Fusion Eng. Design. 10, 115 (1989).

[1.16] H. Iida et al., A handy method for estimating radiation streaming through holes in shield assemblies, Fusion Eng. Design, 43, 1-14 (1998).

[1.17] Y. Seki, H. Iida, H. Kawasaki, et al., THIDA-2: An Advanced Code System for Transmutation, Activation, Decay Heat and Dose Rate, JAERI 1301, Japan Atomic Energy Research Institute, (1986).

[1.18] H. Fukumoto, "New Approach to Neutron-Induced Transmutation, Radioactivity and Afterheat Calculations and Its Application to Fusion Reactors," J. Ncul. Sci. Technol., 23, 97 (1986).

[1.19] S. W. Cierjacks, et al., Fusion Technol., 24, 277-287 (1993).

[1.20] J. F. Briesmeister, MCNP 4A Monte Carlo N-Particle Transport Code System, Oak Ridge National Laboratory, RSICC Computer Code Collection, (1995).

[1.21] W. A. Rhoades and F. R. Mynatt, The DOT-III two dimensional discrete ordinates transport code, ORNL-TM-4280 (1973).

This is a blank page.

Table 1.1 Shielding design limit of the ITER

Nuclear properties in the superconductive magnet	Design Limit
Nuclaer heating rate in the magnet case	2×10^{-3} w/cm^3
Nuclaer heating rate in the winding pack	1×10^{-3} w/cm^3
Absorbed dose rate in the insulator	10^9 rad
Neutron damage (DPA) in the stbilizer copper	1×10^{-3} dpa
Fast (> 0.1 MeV) neutron fluence in the winding pack	1×10^{19}/cm^2
Helium production in the SS for rewelding	
Cooling water pipe	3 appm
Vacuum vessel	1 appm

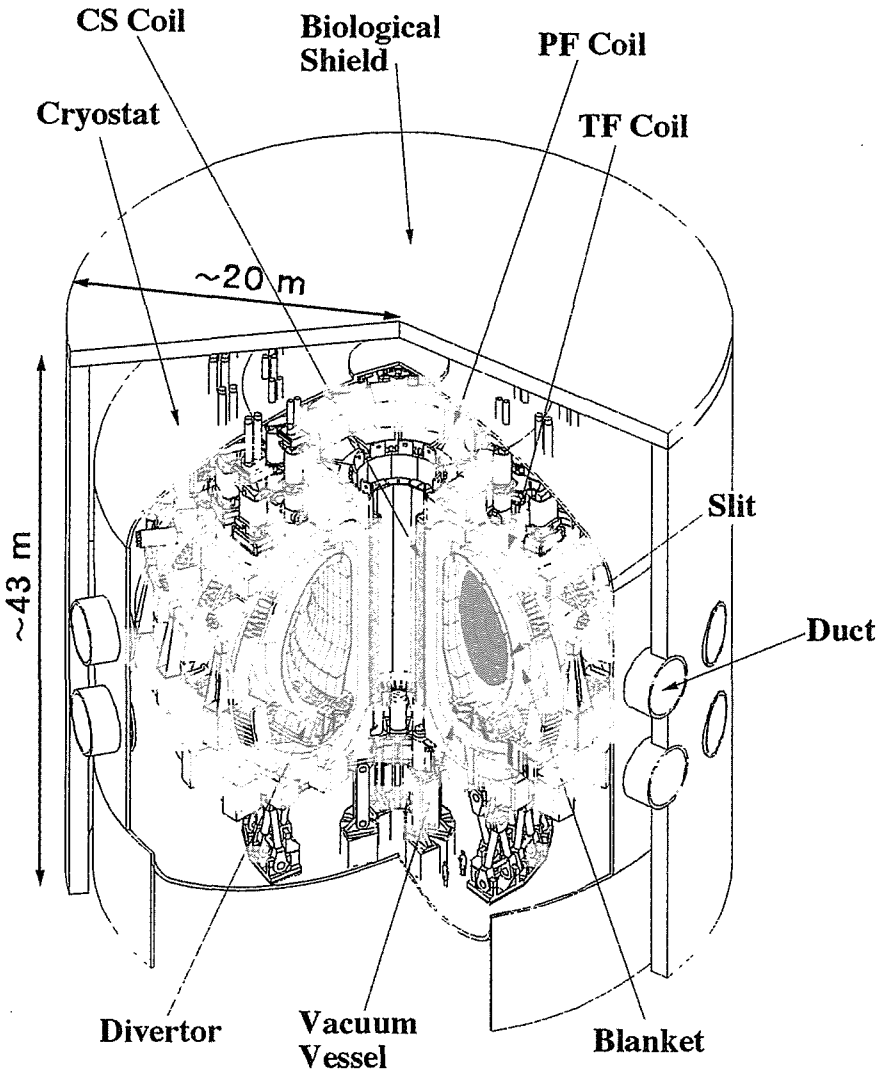

Fig. 1.1 A conceptual bird's-eye view of the tokamak-type DT fusion reactor.

This is a blank page.

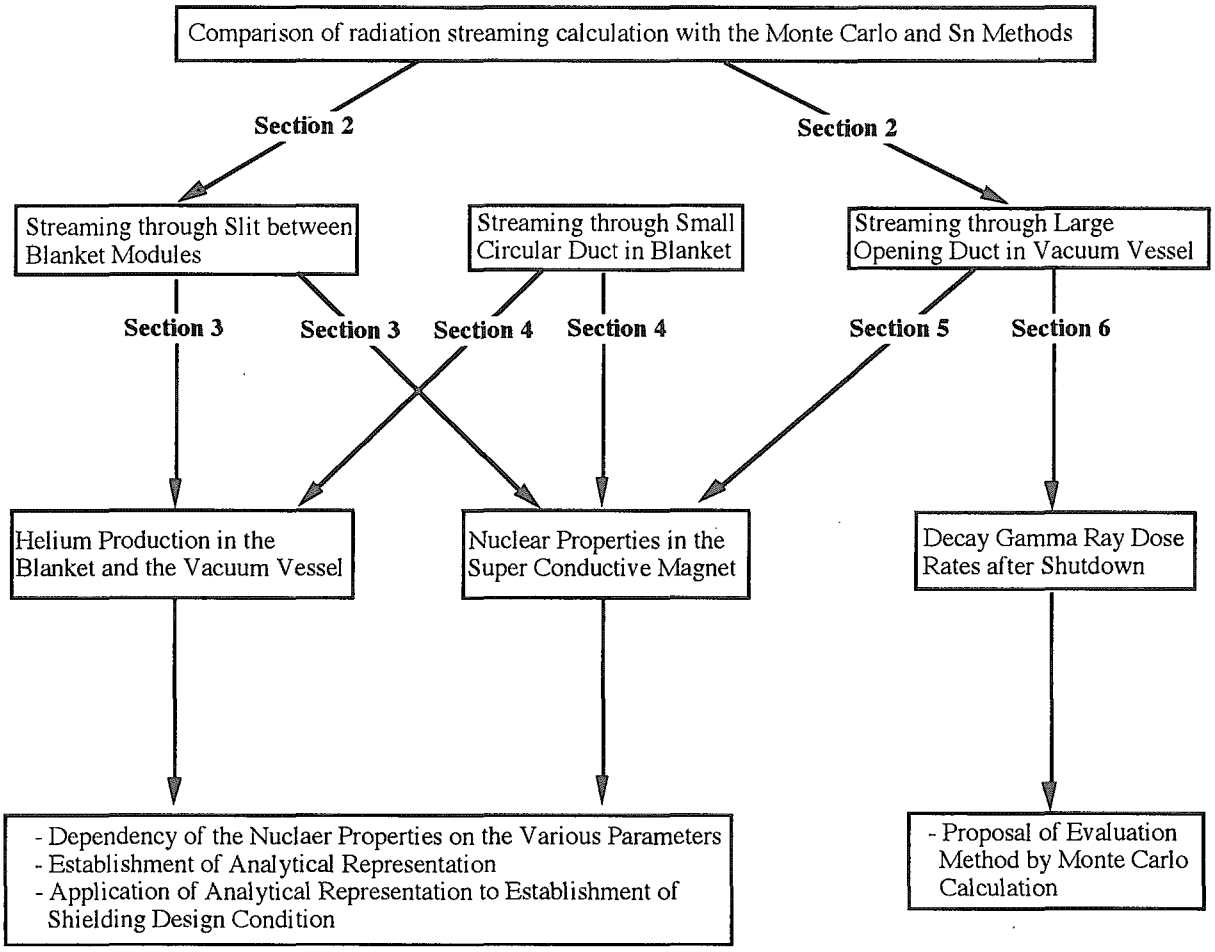

Fig. 1.2 Relationship of each chapter in the present study.

2. Comparison of Monte Carlo Method with Sn Method in Radiation Streaming Calculation

2.1 Introduction

The shielding design calculation has usually been conducted by one, two and three dimensional Sn codes or three dimensional Monte Carlo code in the tokamak-type DT fusion reactor. In the radiation streaming calculation for the shielding design, one dimensional Sn code is not applicable. The deterministic Sn method can give the flux distribution over a whole region of interest at once without any statistical errors. The results given by two or three dimensional Sn codes, however, may give under-estimation due to ray-effect and poor accuracy due to approximation in the geometry. It is also generally expected that the two dimensional Sn calculation is faster than the Monte Carlo calculation, while the three dimensional Sn calculation is not faster than the Monte Carlo calculation.

In order to evaluate the applicapability of the calculation method to the radiation streaming in the tokamak-type nuclear fusion design, the comparison between three dimensional Monte Carlo and two dimensional Sn calculations is perfprmed for the radiation streaming through the slit between the blanket modules and that through the duct with the large opening in the vacuum vessel. In this Chapter, the Monte Carlo calculation results are assumed to be the reference data, and the streaming calculations are performed by the two dimensional Sn (discrete ordinates transport) code DOT3.5. From this comparison, the uncertainties of the Sn calculation results coming from the ray-effect and the effect due to approximation of the geometry are investigated whether the two dimensional Sn calculation can be applied instead of the Monte Carlo calculation.

In this Chapter, the nuclear properties of the blanket and the vacuum vessel, e.g. helium production in stainless steel (SS) for rewelding, are calculated with the radiation streaming through the slit, by Monte Carlo and Sn calculations. The neutron flux distributions are also calculated along the duct with the large opening in the vacuum vessel.

2.2 Streaming through Slit between Blanket Modules [2.1]

The blanket system for a fusion experimental reactor such as ITER is composed of a number of shielding modules for easy assembly and maintenance, which has a few centimeter wide slits between the adjacent modules as mentioned above [2.2]. The examples of the bird's-eye and cross-sectional views of the blanket configuration are shown in Figs. 2.1 and 2.2, respectively. In this design example, shielding blanket modules are welded to the back plates to form a rigid structure through two connection "legs" located at the back of the module as shown in Figs. 2.1 and 2.2. Branch coolant pipes are also connected to the common manifolds as shown in Figs. 2.1 and 2.2. The 2 cm wide slits are installed between the adjacent blanket modules. The legs and the branch pipes will be cut and rewelded in case of replacement of damaged modules.

2.2.1 Calculation method

2.2.1.1 Monte Carlo calculation

Radiation transport calculation is performed using the three dimensional Monte Carlo code MCNP4.2. The continuous energy cross section library FSXLIB-J3 [2.3] based on the evaluated nuclear data library JENDL-3.1 [2.4] is used for the transport calculation, and the helium production cross section library [2.5] based on JENDL-3.1 is used as the nuclear response functions.

The calculational geometry used in the calculation is shown in Fig. 2.3. In this geometry, two SS regions are incorporated behind the plasma and also behind the back plate to take the effect of the back scattering of neutron and gamma ray into account. Volumetric source neutrons in the plasma region shown in Fig. 2.3 are sampled from an isotropic neutron of the energy of 14.06 MeV. For the neutron wall loading of 1 MW/m^2 and the integrated neutron wall loading (neutron fluence) of 1 MWa/m^2, which are the typical conditions for the fusion experimental reactor, helium production in SS are evaluated at the locations D1 and D2 shown in Fig. 2.3 using the point detector estimator. Since the contribution of neutrons of the energy below 0.1 MeV to the helium production is negligibly small except for the helium production in boron, helium productions are evaluated using the neutron flux of the energy above 0.1 MeV in order to reduce the computing time in this Chapter.

2.2.1.2 Sn calculation

Radiation transport calculation is performed using the two dimensional Sn code DOT3.5. The group constant library FUSION-40 [2.6] based on JENDL-3.1 is used for the transport calculation, and the KERMA library [2.7] based on JENDL-3.1 is used as the nuclear response functions. The group structure is shown in Table 2.1.

The calculational geometry in XY coordinates used in the calculation is shown in Fig. 2.4. The Legendre polynomial order in the anisotropical scattering cross section is applied as P5. The number of angles are 160 of isotropic division, which corresponds to S16.

2.2.2 Results and discussions

A contour of the neutron flux with the energy of 14 MeV is shown in Fig. 2.5. The 14 MeV neutron flux through the slit is enhanced due to slit streaming effect, however, it is found that the 14 MeV neutron flux in the slit center has a hollow distribution due to a ray-effect. As an example at the location D2 which is the location at the vacuum vessel surface along the slit, the neutron fluxes, the nuclear heating rate and the helium production obtained by MCNP and DOT3.5 are summarized in Table 2.2. The ratios of these nuclear properties at the location along the slit obtained by MCNP to those by DOT3.5 are shown in Fig. 2.6 as a function of the distance from the front surface of the back plate. It is found that DOT3.5 calculations underestimate the nuclear properties by factors of 2 - 4, possibly due to the ray-effect. From this comparison, it can be concluded that in the shielding calculation of the blanket the three

dimensional Monte Carlo calculation is required to evaluate the radiation streaming through the slit between the adjacent blanket modules with good accuracy.

2.3 Streaming through Duct in Vacuum Vessel [2.8, 2.9]

The large opening ducts, e. g. Neutral Beam Injection (NBI) duct, penetrating the blanket and the vacuum vessel are located in the confined space between the adjacent TF coils in the tokamak-type nuclear fusion reactor as mentioned above. Plasma heating is accomplished with the NBI ducts that enter the plasma region tangentally to the plasma axis [2.10, 2.11]. The NBI ducts are completely open, e. g. 91.5 cm high by 58 cm wide at the plasma facing region, to allow a direct injection of deuterons into the plasma. In the previous studies, the shielding calculations for the ITER NBI ducts are performed using two dimensional Sn calculations [2.12, 2.13]. It is expected that the calculated results enormously overestimate because the infinite continuous opening of the NBI duct is assumed in the Z direction, i. e. poloidal direction, in two dimensional geometry. In addition to the calculational geometry with the 91.5 cm high duct opening which is a reference design, the three dimensional Monte Calro calculations are also done for the geometries with 15 - 158 cm high duct openings for evaluating the calculated errors of the two dimensional Sn calculation. By changing the duct opening height, dependency of the calculated error on the duct opening height for the two dimensional Sn calculation is evaluated here.

2.3.1 Evaluation method and model

2.3.1.1 Monte Carlo calculation

Neutron transport calculations are performed using the three dimensional Monte Carlo code MCNP-4A with the Fusion Evaluated Nuclear Data Library FENDL-1 [2.14]. The vertical cross sectional view used in the calculation is shown in Fig. 2.7, and the horizontal cross sectional view is shown in Fig. 2.8. The calculational geometry represents a quarter of (90°) tokamak device, and it includes all of the main tokamak components such as the blanket modules, vacuum vessel, divertor cassettes, cryostat, biological shield, TF coils, PF coils, three NBI and two standard equatorial ducts, and five divertor and upper ducts. The14 MeV neutron source in the plasma region shown in Figs. 2.7 and 2.8 is sampled according to the fusion reaction distribution.

Spatial distributions are calculated for the neutron flux with the energy of 14 MeV and that with the energy above 0.1 MeV along the NBI duct. The calculations are performed for the duct openings with 15, 30, 60, 91.5, 120 and 158 cm heights. The point detector estimators are fixed at 3 and 6 cm in radius for the geometries with these duct openings, and the neutron fluxes can be estimated with the value of FSD, which represents the statistical error, less than 5 %.

2.3.1.2 Sn calculation

Neutron transport calculation is performed using the DOT3.5 code with nuclear group constant set based on the FENDL-1. The calculational geometry in XY coordinates used in the calculation is shown in Fig. 2.9. The Legendre polynomial order in the anisotropical scattering cross section is applied as P5. The number of angles are 160 of isotropic division.

2.3.2 Results and discussions

Figures 2.10 and 2.11 show the 14 MeV neutron flux distributions along the center axis in the NBI duct, and above 0.1 MeV, respectively. The numerical results by DOT3.5 largely overestimate the neutron flux, which is caused by the assumption of the infinite continuous opening for the NBI duct in the poloidal direction in the calculational geometry. The error, E, in the two dimensional Sn calculation is defined by the following formula;

$$E = C_{2D}(x) / C_{2D}(0) / (C_{3D}(x) / C_{3D}(0)) \quad (2.1),$$

where $C_{2D}(x)$ is the Sn calculated result at x cm distance from the inlet of the duct opening at the plasma facing region, and $C_{3D}(x)$ is the Monte Carlo calculated results. The errors in two dimensional Sn calculation are shown in Fig. 2.12 and 2.13 for the 14 MeV neutron flux and the neutron flux of energy above 0.1 MeV, respectively. By expanding the duct opening height from 15 to 158 cm, the errors become smaller though some fluctuation can be seen due to the complex configuration and statistical error of Monte Carlo calculation. From the small distances of 30 to 100 cm away from the inlet of the duct opening, the Sn calculations give rather good agreement with the Monte Carlo results within factors of 1.3 and 1.2 for the 14 MeV neutron flux and the neutron flux of energy above 0.1 MeV, respectively, for large duct opening heights of 91.5, 120 and 158 cm. But with increasing this distance from 100 to 1000 cm, the Sn results are factors of 1.3 to 4.9 and 1.2 to 7.3 higher than the Monte Carlo results for the 14 MeV neutron flux and the neutron flux of energy above 0.1 MeV, respectively, for these large duct opening heights, even much higher a factor of 5.0 to 37 and 4.7 to 84 with decreasing the duct opening height. In the case of ITER condition with 91.5 cm high duct opening assumed in this Chapter, it is found that the two dimensional Sn calculation overestimate the 14 MeV neutron fluxes by a factor of about five and the neutron flux of energy above 0.1 MeV by a factor of about eight at the cryostat. It can be therefore concluded that the three dimensional Monte Carlo calculation are also required for the shielding calculation around the duct with the large opening in the vacuum vessel in order to evaluate the neutron flux with good accuracy.

2.4 Conclusion

The radiation transport calculations are performed taking into account the radiation streaming through the slit between the adjacent blanket modules and the NBI duct by the three dimensional Monte Carlo code MCNP and the two dimensional Sn code DOT3.5 for comparison, and the following results are obtained.

(1) The nuclear properties in the vacuum vessel surface along the 2 cm wide slit between the

adjacent blanket modules by Sn code are under-estimated by factors of 2 – 4 compared with those by Monte Carlo code due to the ray-effect in about 34 cm thick blanket.

(2) The neutron fluxes along the NBI duct by two dimensional Sn code are over-estimated compared with those by three dimensional Monte Carlo code due to approximation of calculational geometry, i.e. assumption of the infinite continuous opening of the NBI duct in the poloidal direction.

(3) The errors in the two dimensional Sn code are clarified for the NBI duct opening with 15 - 158 cm heights.

(4) In the ITER condition with 91.5 cm high duct opening, the error in the two dimensional Sn code is a factor of about eight at the cryostat for the neutron flux of the energy above 0.1 MeV.

(5) Through the study shown in this Chapter, it can be concluded that the three dimensional Monte Carlo calculation is required for the shielding calculation in the tokamak-type DT nuclear fusion rector with many penetrations.

REFERENCES

[2.1] S. Sato, H. Takatsu, Y. Seki, T. Utsumi, STREAMING ANALYSIS OF GAP BETWEEN BLANKET MODULES FOR FUSION EXPERIMENTAL REACTOR, Fusion Technol., 30, 1129-1033 (1996).

[2.2] S. Sato, et al., "Conceptual Design of ITER Shielding Blanket," JAERI-Tech 95-019, (1995).

[2.3] K. Kosako, et al., "FSXLIB-J3: MCNP Continuous Energy Cross Section Library Based on JENDL-3," JAERI-M 91-187, (1991).

[2.4] K. Shibata, et al., JAERI-1319, (1990)

[2.5] S. Mori, et al., Muti-group Helium and Hydrogen Production Cross Section Libraries for Fusion Neutronics Design, JAERI-M 93-175, (1993).

[2.6] K. Maki. et al., "Nuclear Group Constant Set Fusion-J3 for Fusion Reactor Nuclear Calculations Based on JENDL-3," JAERI-M 91-072, (1991).

[2.7] K. Maki, et al., "Nuclear Heating Constant KERMA Library," JAERI-M 91-073, (1991).

[2.8] S. Sato, R. Plenteda, D. Valenza, et. al., SHIELDING ANALYSES OF THE ITER NBI PORTS, Fusion Technol., 34, 1002-1007 (1998)

[2.9] S. Sato and H. Iida, Monte Carlo Analyses for ITER NBI Duct by 1/4 Tokamak Model, J. Nucl. Sci. Technol, Supplement 1, 258-262 (2000)

[2.10] T. Inoue, et al.: "Design and R&D of high power negative ion source/accelerator for ITER NBI," Proc. 19th Symp. on Fusion Technol., Lisbon, Portugal, Sep. 16-20, 1996, p. 701, Portugal (1996).

[2.11] A. Krylov, et al.: "General design of the neutral beam injection system and integration with ITER," Proc. 19th Symp. on Fusion Technol., Lisbon, Portugal, Sep. 16-20, 1996, p. 697, Portugal (1996).

[2.12] K. Maki, H. Takatsu, Y. Seki, S. Sato, T. Kuroda, Radiation shielding for superconductive toroidal field coils around the neutral beam injector duct in the ITER design, Fusion Eng. Design, 22, 427-434 (1993).

[2.13] K. Maki, H. Takatsu, S. Sato, Y. Seki, Biological shield around the neutral beam injector ducts in the ITER conceptual design, Fusion Eng. Design, 24, 315-325 (1994).

[2.14] S. Ganesan and P. K. McLaughlin, "FENDL/E, Evaluated Nuclear Data Library of Neutron Interaction Cross Sections, Photon Production Cross Sections and Photon-Atom Interaction Cross Sections for Fusion Applications, Version 1.1 of November 1994," IAEA(NDS)-128, Rev. 3, International Atomic Energy Agency, (1996).

Table 2.1 Group structure of FUSION-40

Group	Lower Energy (MeV)	Upper Energy (MeV)	Group	Lower Energy (MeV)	Upper Energy (MeV)
1	1.00E-09	2.15E-07	22	2.83E-01	4.00E-01
2	2.15E-07	4.65E-07	23	4.00E-01	5.66E-01
3	4.65E-07	1.00E-06	24	5.66E-01	8.00E-01
4	1.00E-06	2.15E-06	25	8.00E-01	1.058
5	2.15E-06	4.65E-06	26	1.058	1.4
6	4.65E-06	1.00E-05	27	1.4	1.871
7	1.00E-05	2.15E-05	28	1.871	2.5
8	2.15E-05	4.65E-05	29	2.5	3.162
9	4.65E-05	1.00E-04	30	3.162	4
10	1.00E-04	2.15E-04	31	4	4.516
11	2.15E-04	4.65E-04	32	4.516	5.099
12	4.65E-04	1.00E-03	33	5.099	5.757
13	1.00E-03	2.15E-03	34	5.757	6.5
14	2.15E-03	4.65E-03	35	6.5	7.328
15	4.65E-03	1.00E-02	36	7.328	8.261
16	1.00E-02	2.15E-02	37	8.261	9.314
17	2.15E-02	4.65E-02	38	9.314	10.5
18	4.65E-02	1.00E-01	39	10.5	11.478
19	1.00E-01	1.41E-01	40	11.478	12.549
20	1.41E-01	2.00E-01	41	12.549	13.72
21	2.00E-01	2.83E-01	42	13.72	15

Table 2.2 The neutron flux, the nuclear heating rate and the helium production at the location D2 obtained by MCNP and those by DOT3.5

	MCNP4.2	DOT3.5
14 MeV neutron flux (n/cm^2/s.)	2.5 x 10^{11}	6.9 x 10^{10}
Total neutron flux (n/cm^2/s.)	6.9 x 10^{12}	3.7 x 10^{12}
Neuton heating rate (mW/cm^3)	1.5 x 10^{-2}	5.8 x 10^{-3}
Helium production (appm)	0.66	0.25

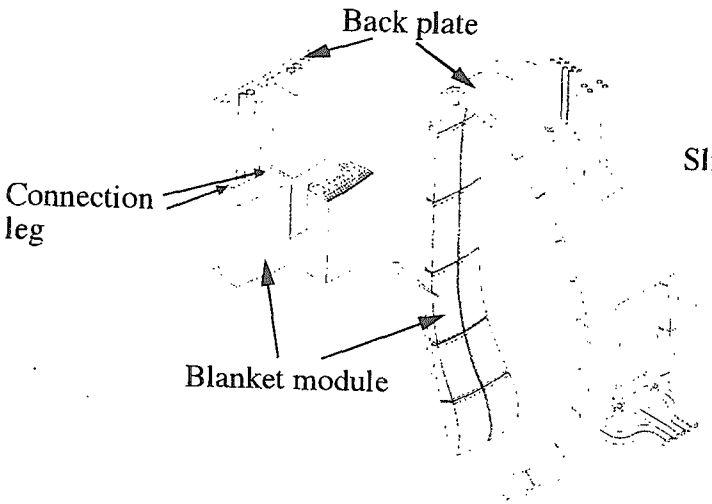

Fig. 2.1 Bird's-eye view of the blanket configuration.

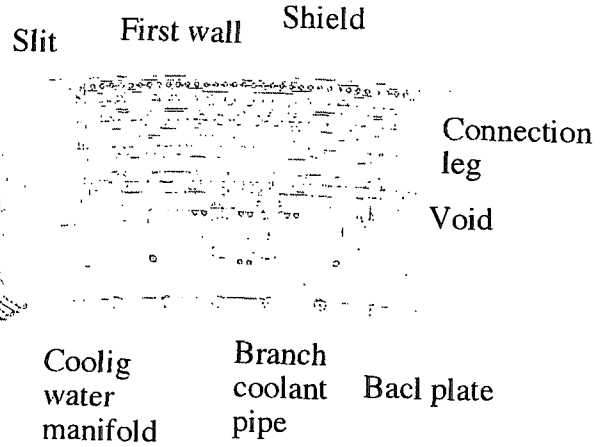

Fig. 2.2 Cross-sectional view of the blanket configuration.

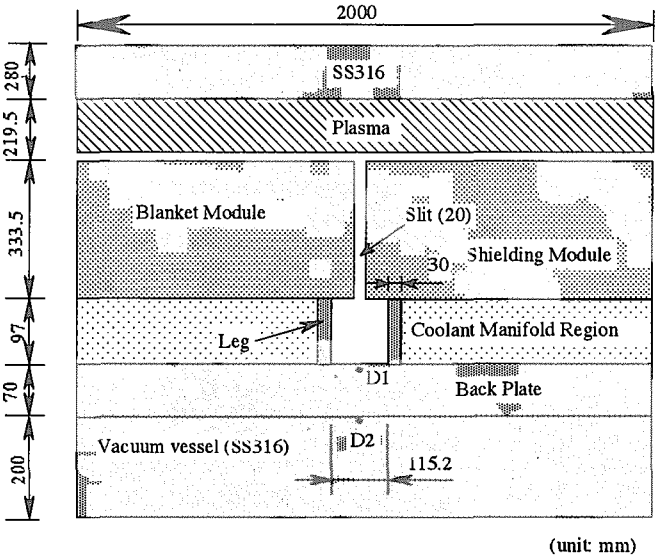

Fig. 2.3 MCNP calculational geometry.

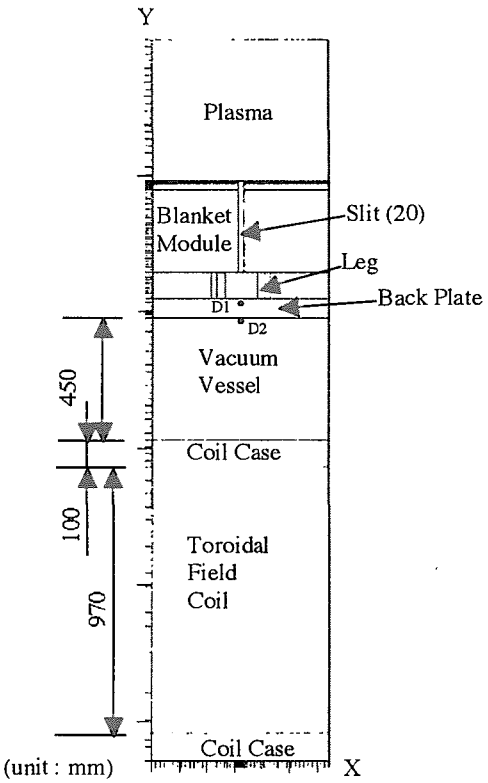

Fig. 2.4 DOT calculational geometry (XY coordinate).

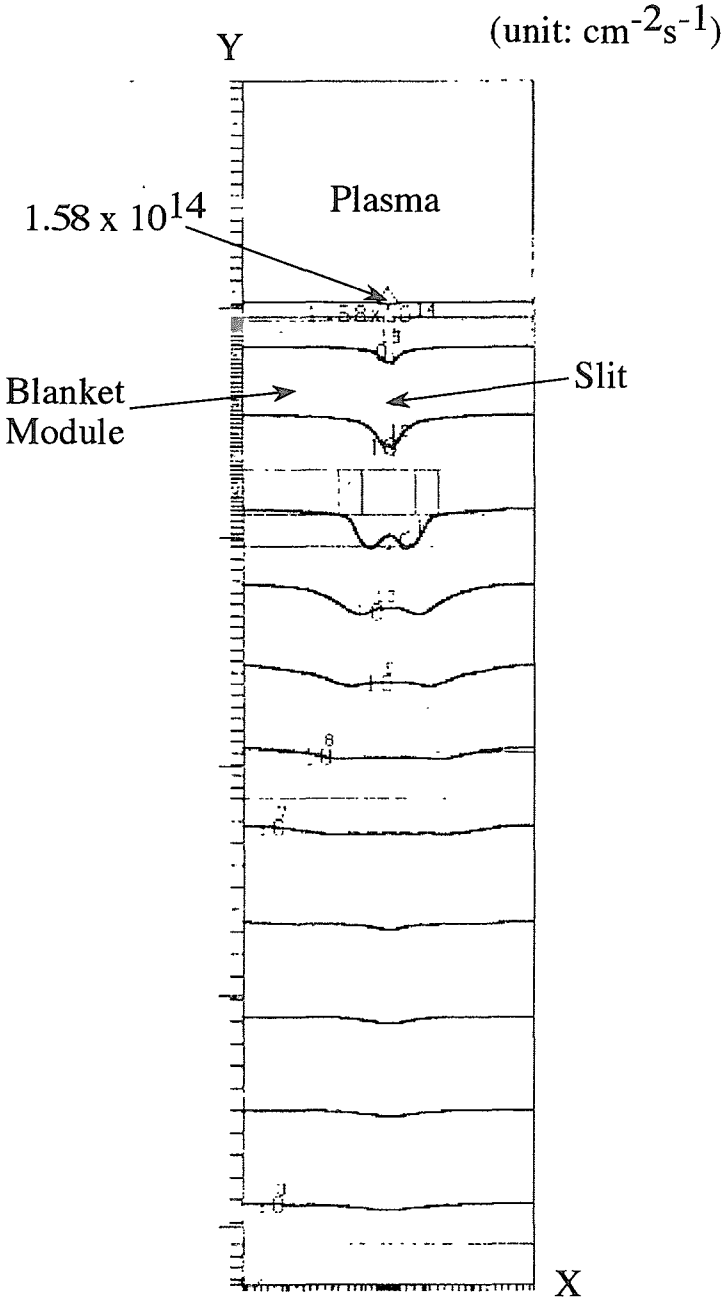

Fig. 2.5 Contour of neutron flux with the energy of 14 MeV.

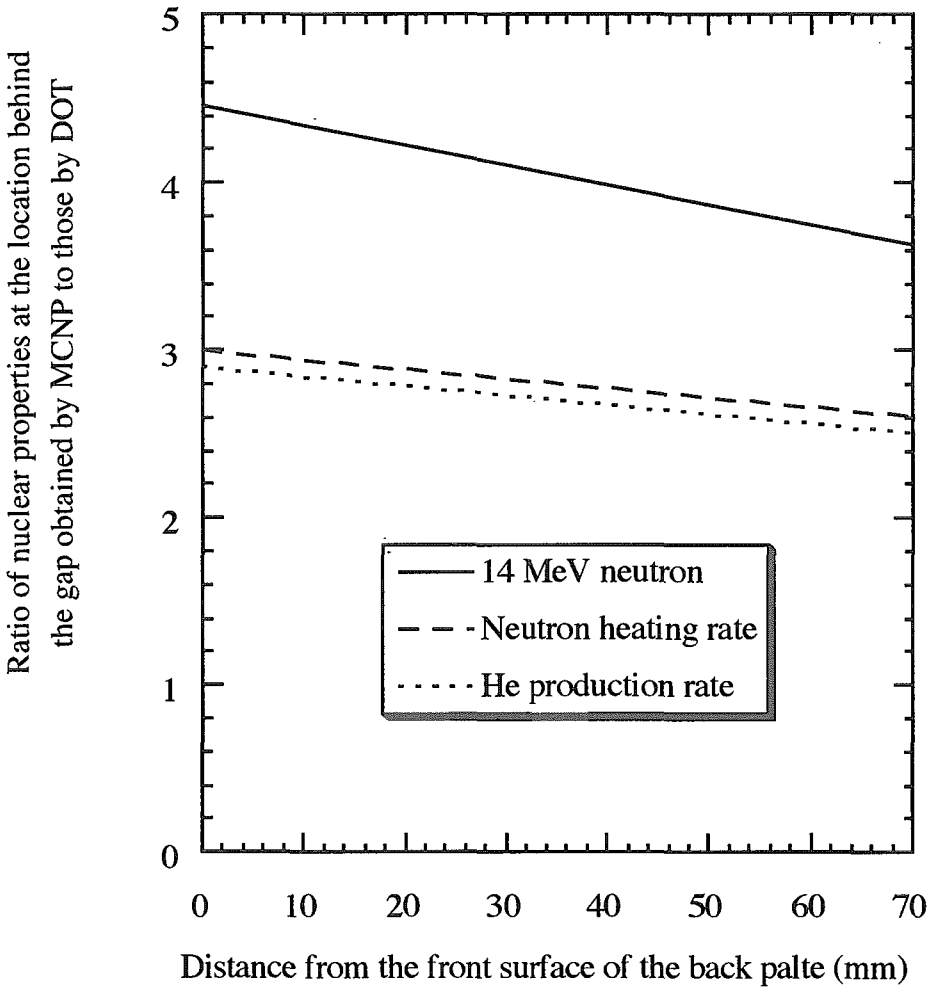

Fig. 2.6 Ratio of the nuclear properties at the location along the slit obtained by MCNP to those by DOT3.5 as a function of the distance from the front surface of the back plate.

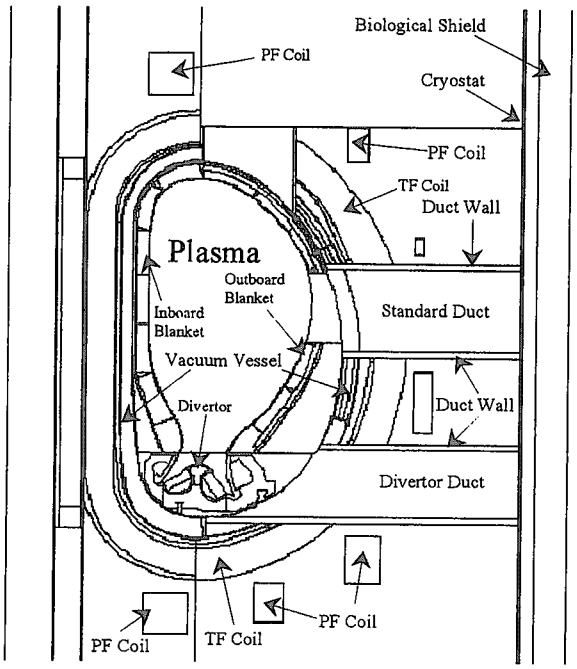

Fig. 2.7 Vertical cross section view of the MCNP calculational geometry.

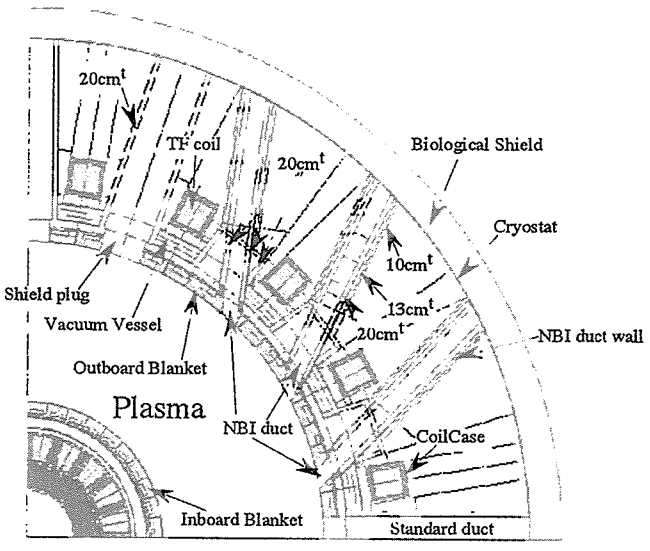

Fig. 2.8 Horizontal cross section view of the MCNP calculational geometry.

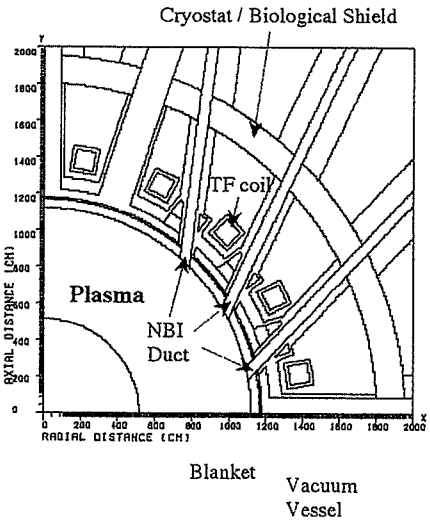

Fig. 2.9 DOT calculational geometry (XY coordinate).

This is a blank page.

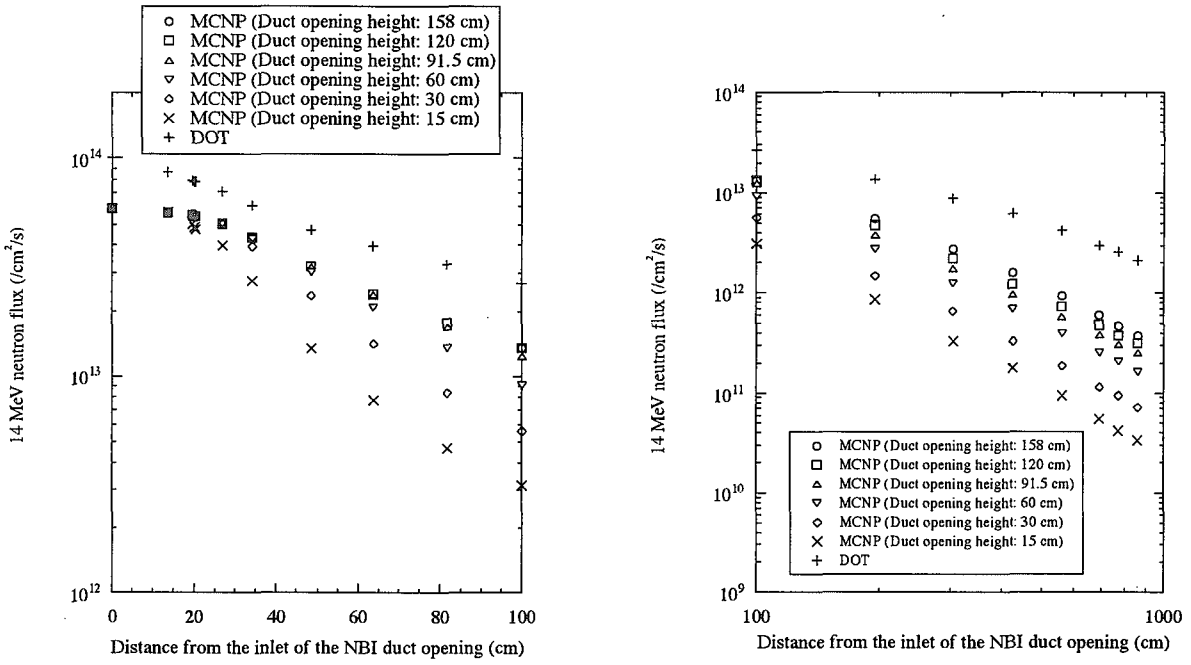

(a) 0 - 100 cm distance from the inlet of the NBI duct opening

(b) 100 - 1000 cm distance from the inlet of the NBI duct opening

Fig. 2.10 Distribution of 14 MeV neutron flux along the center axis in the NBI duct.

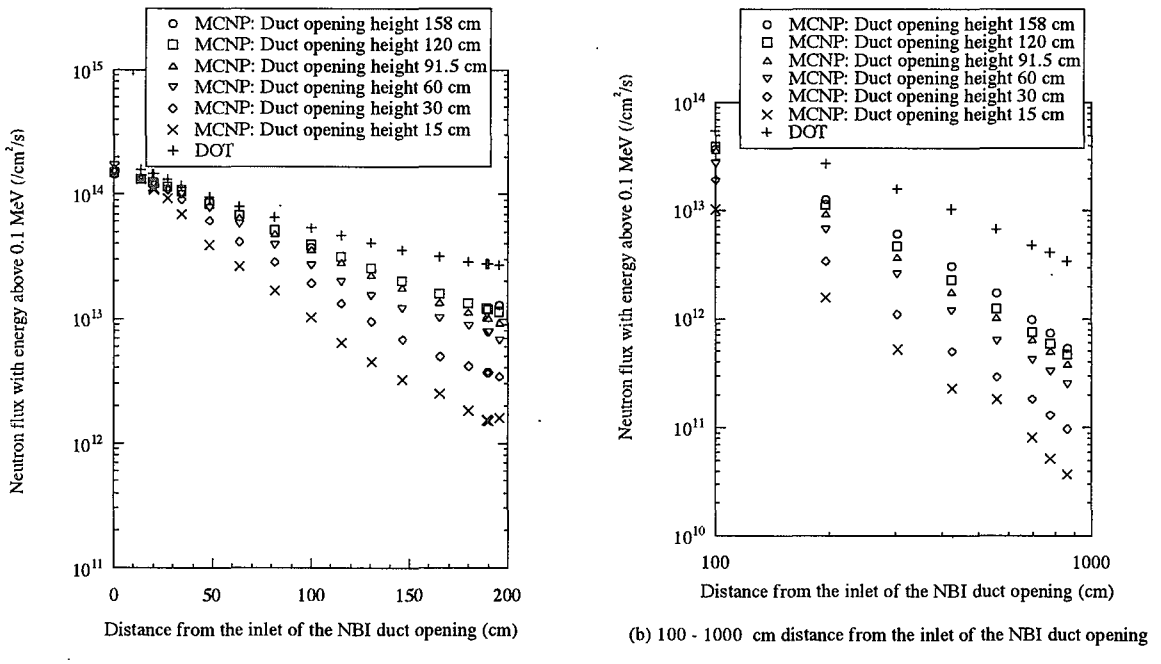

(a) 30 - 100 cm distance from the inlet of the NBI duct opening

(b) 100 - 1000 cm distance from the inlet of the NBI duct opening

Fig. 2.11 Distribution of neutron flux with the energy above 0.1 MeV along the center axis in the NBI duct.

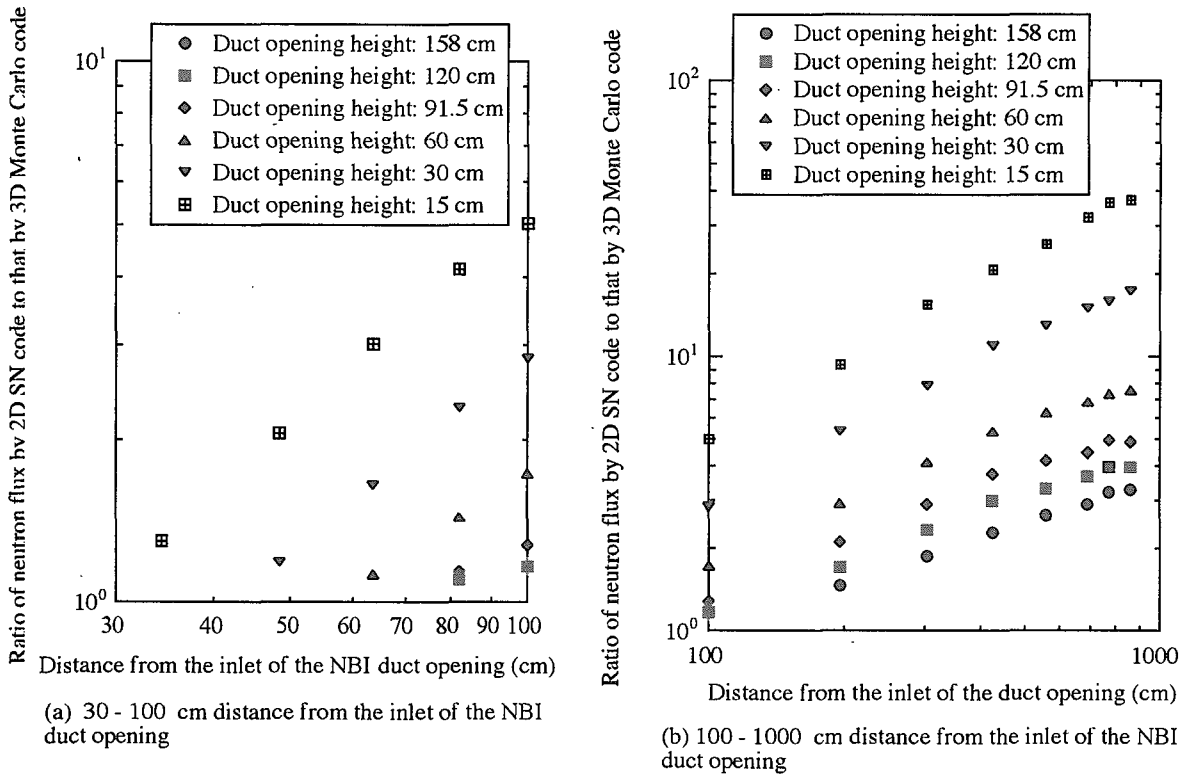

(a) 30 - 100 cm distance from the inlet of the NBI duct opening

(b) 100 - 1000 cm distance from the inlet of the NBI duct opening

Fig. 2.12 Ratio of the result for the 14 MeV neutron flux distribution along the center axis in the NBI duct obtained by 2D Sn code to that by 3D Monte Carlo code.

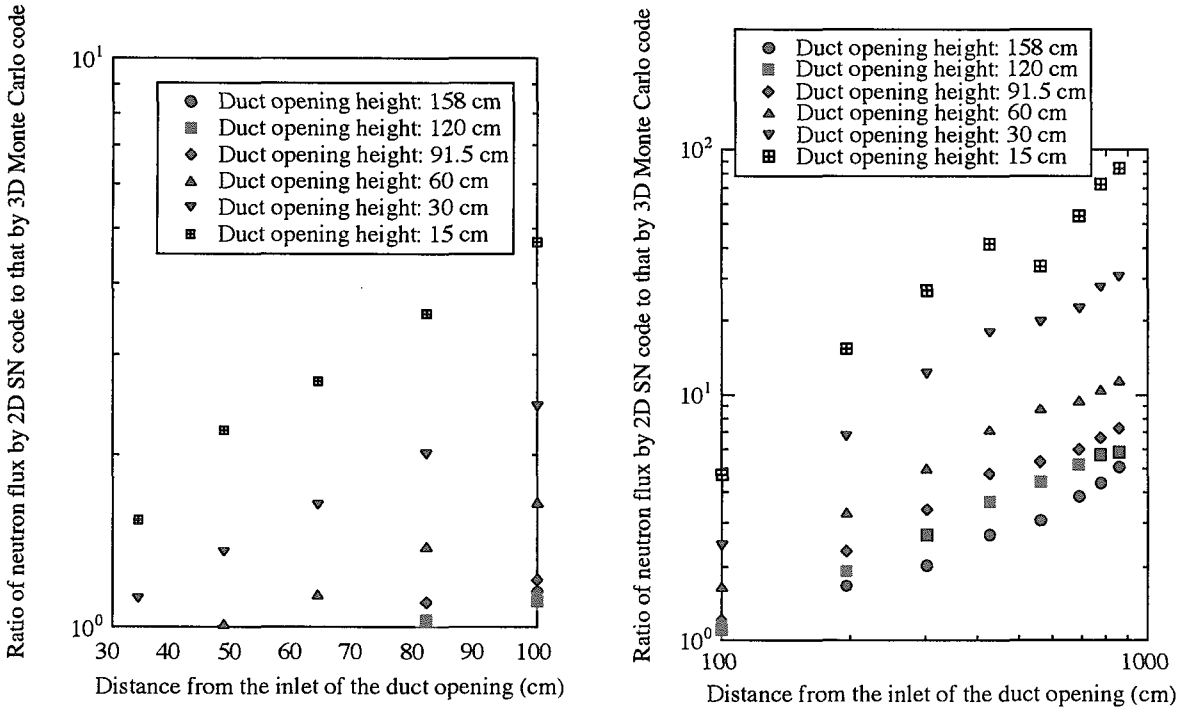

(a) 30 - 100 cm distance from the inlet of the NBI duct opening

(b) 100 - 1000 cm distance from the inlet of the NBI duct opening

Fig. 2.13 Ratio of the result for the neutron flux distribution of the energy above 0.1 MeV along the center axis in the NBI duct obtained by 2D Sn code to that by 3D Monte Carlo code.

3. Streaming through Slit between Blanket Modules [3.1]

3.1 Introduction

As discussed in Chapter 2, the three-dimensional Monte Carlo method is the most suitable method for the analysis of the neutron streaming through a few centimeter wide slits between the adjacent blanket modules, however, it requires a lot of calculation time. The analytical representations that can give the nuclear properties along the slit are very useful from the view point of the engineering design application. In this Chapter, the nuclear properties in the vacuum vessel and the TF coil along the slit are calculated by taking into account the neutron streaming through the slit by using the three dimensional Monte Carlo code MCNP4B, and their analytical representations are established based on the Monte Carlo results. By changing systematically the slit width, the blanket and the vacuum vessel thicknesses, and the boron content in the vacuum vessel, the analytical representations of the nuclear properties along the slit are established as functions of these parameters. The helium production in the vacuum vessel made of SS is caused from fast neutron reactions with the Ni, Fe and Cr elements, and thermal neutron reaction with the boron. It is then expected that the helium production in the vacuum vessel strongly depend on the boron, though the boron is trace element in SS. The dependencies of the nuclear properties on the blanket and the vacuum vessel compositions are also clarified by changing the blanket and the vacuum vessel composition. The analytical formula thus-obtained is applied to clarify the shielding design constraint required to satisfy the shielding design criteria for the DT fusion reactor.

3.2 Calculation Method

The three-dimensional Monte Carlo calculational geometry used in the calculation is shown in Fig. 3.1 with the dimensions, and the calculational condition is shown in Table 3.1. The configuration of the model and the conditions are based on the ITER design. The ITER design has been studied in the extent of 31 to 45 cm thick blankets, ~ 40 cm thick vacuum vessel, 1 to 2 cm wide slits and 10 to 20 parts per million by weight (wppm) boron. In this Chapter, the Monte Carlo calculations are performed for the conditions of the wider extent compared with the ITER conditions.

The helium production in the vacuum vessel, the nuclear heating rates in the coil case made of stainless steel (SS) and at the coil winding pack, and the radiation damage in the TF coil are calculated by using the Monte Carlo calculation code MCNP-4A with the fusion evaluated nuclear data library FENDL-1. As for the radiation damage, the absorbed dose rate in the insulator, the neutron damage in the stabilizer copper and the neutron fluence in the winding pack are evaluated.

Volumetric source neutrons in the plasma region shown in Fig. 3.1 are sampled from an isotropic neutron distribution having a Muir velocity Gaussian fusion energy spectrum shown in Fig. 3.2. Source neutrons normalized to a number of 14-MeV source neutrons of 4.439 x 10^{13} cm^{-2} s^{-1} averaged on a blanket surface, which corresponds to a neutron wall loading of 1

MW/m^2 at the blanket surface and a typical neutron first wall loading in fusion experimental reactors such as ITER (1 MW/m^2/ = 10^6 J/m^2 / (14.06 MeV x 1.602 x 10^{-13} J/MeV) / 10^4 cm^2 = 4.439 x 10^{13} cm^{-2} s^{-1}).

The track length estimator is applied as the detector. The helium production, Y_h, is estimated by multiplying the neutron spectrum, $\phi_n(E)$, by the helium production cross-section, $\Sigma_{h,i}(E)$, in FENDL library as follows;

$$Y_h = \sum_i \int \phi_n(E)\, \Sigma_{h,i}(E)\, dE \qquad (3.1),$$

where i and E are each element in SS and the neutron energy, respectively. The nuclear heating rate, Y_{NH}, is estimated by multiplying the neutron and the gamma-ray spectra, $\phi_n(E)$ and $\phi_\gamma(E)$, by the kerma factor, $\Sigma_{k,i}(E)$, in FENDL library as follows;

$$Y_{NH} = \sum_i \int \left(\phi_n(E) + \phi_\gamma(E)\right) \Sigma_{k,i}(E)\, dE \qquad (3.2).$$

The absorbed dose rate, Y_a, in the insulator is estimated by dividing the integrated nuclear heating rate with the specific gravity, ρ, of the insulator as follows;

$$Y_a = P_s\, Y_{NH} / \rho \qquad (3.3),$$

where P_s is the effective operation period (second). The neutron damage, Y_d, is estimated by multiplying the neutron spectrum by the displacement cross-section, $\Sigma_{d,i}(E)$ [3.2], as follows;

$$Y_d = \int_i \phi_n(E)\, \Sigma_{d,i}(E)\, dE \qquad (3.4).$$

Their peak nuclear properties are most critical concern in the shielding design. The nuclear properties in the vacuum vessel surface, the coil case surface, the winding pack surface and the insulator surface along the poloidal slit are evaluated as their peak nuclear properties. The calculations are done to get average values of the helium production in 0 to 1.1 cm depth of the 5.5 cm-thick front wall of the vacuum vessel along the slit, and those of the nuclear heating rate and the radiation damage in 0 to 1 cm depth of the coil case, the insulator and the coil winding pack along the slit.

The weight window technique is applied as the variance reduction method. Reducing the value of the weight window along the track of the neutron streaming from the plasma to the target along the slit results in a large number of neutrons with low weight that reach the target region. By assigning the target location, the optimized weight window table is automatically generated in the MCNP-4A. To generate the table, a considerable number of neutrons must reach the target location. An enormous number of histories and long calculation time is required to generate the weight window table in a single step. In this process, the target locations are sequentially moved from the plasma to the target along the slit in steps and the weight window table for each target location is generated. The weight window table for the

final target location, i.e. the vacuum vessel and the TF coil surface toward the plasma along the slit is then prepared in the final step of this process.

3.3 Results and Discussions

From the Monte Carlo calculation results, the analytical representations are established for the blanket and the vacuum vessel shield compositions of 80 % SS/20 % water and 60 % SS/40 % water, respectively. The condition of the composition is the typical one in the experimental reactor such as ITER.

3.3.1 Neutron flux along the slit

In the case of the 45 cm thick blanket and the 40 cm thick vacuum vessel, distributions of the 14 MeV neutron flux and the energy-integrated total neutron flux along the slit as a function of the distance from the blanket surface behind the plasma are shown for slit widths of 0 to 8 cm in Figs. 3.3 and 3.4, respectively. In the blanket without the slit, the 14 MeV neutron flux and the energy-integrated total neutron flux in the vacuum vessel surface toward the plasma are reduced by about four and two orders of magnitude, respectively, compared with those at the blanket surface toward the plasma. They are also reduced by factors of 20 to 200 and 6 to 70, respectively, in the blankets with decreasing the slit width from 8 cm to 1 cm.

It is found that the energy integrated total neutron flux distribution, $\phi_{fl}(x)$, along the 1 to 8 cm wide slits can be expressed approximately only by an exponential function of the distance from the blanket surface, x (cm), as follows;

$$\phi_{fl}(x) = C_{fl} \exp (- \lambda_{eff} x) \qquad (3.5),$$

where λ_{eff} can be defined as the effective linear attenuation coefficient. Similarly to the exponential attenuation of the neutron flux in the shield, the neutron flux in the blanket along the slit may decrease exponentially. The values of λ_{eff} are shown in Table 3.2 with the values of C_{fl}. The errors given in Table 3.2 are the maximum values of the ratio between the neutron flux obtained by the analytical representation (3.5) with the values shown in Table 3.2 and those by the Monte Carlo calculation. Disagreement of the neutron flux obtained by the analytical representation (3.5) is 7 to 19 % compared with those by the Monte Carlo calculation.

3.3.2 Helium productions along the slit

In the case of SS with 20 wppm boron, distributions of the helium productions in SS along the slit as a function of the distance from the blanket surface are shown in Fig. 3.5 for slit widths of 0 to 8 cm. Neutron transport calculations are first conducted for no material in the slit, and the helium productions along the slit are calculated by multiplying the neutron

spectrum in void by the helium production cross-section of SS existing in the slit. The helium production in the vacuum vessel wall made of SS adjacent to the vacuum vessel shield which is composed of SS and water increases due to enhancement of the thermal neutron flux in the water. In the case of the blanket without the slit, the helium production in the vacuum vessel surface toward the plasma is reduced by a factor of about 600 compared with that at the blanket surface toward the plasma. In the case of the blanket with the slit, they are reduced by 1 to 2 orders of magnitude with decreasing the slit width from 8 to 1 cm.

3.3.3 Helium productions in the vacuum vessel

In this Chapter, the helium productions are discussed in the vacuum vessel front wall surface toward the plasma along the slit.

3.3.3.1 Dependency on the slit width

Some calculated results are shown in Table 3.3 with the statistical error for the 10 wppm boron content, the 45 cm thick blanket and the integrated neutron wall loading of 1 MWa/m^2. Dependencies of the helium productions on the slit width are shown in Fig. 3.6 with the error bar corresponding to the range of the statistical error for the 10, 20, 50 and 100 wppm boron content. It was found that the helium productions along the slit increased linearly with the slit width. The incident 14 MeV neutron flux to the slit increase linearly with the slit width, therefore the helium productions along the slit may increase linearly with the slit width. The analytical representation on the helium production along the slit can be given as a function of the slit width, X_s (cm), as follows;

$$Y_h = N P (A_s + B_s (X_s - 1)) \quad (3.6),$$

where N and P are the neutron wall loading (MW/m^2), the effective operation period (year), respectively. The value of N * P corresponds to the integrated neutron wall loading (MWa/m^2). The values of A_s and B_s obtained by the least squares fitting to Eq. (3.6) are shown in Table 3.4 for various blanket thicknesses and boron contents. The values of A_s correspond to the helium productions in the vacuum vessel surface along the 1 cm wide slit at the integrated neutron wall loading of 1 MWa/m^2. Disagreement of the helium productions obtained by the analytical representation (3.6) are 3 to 7, 6 to 13 and 4 to 19 % compared with those by the Monte Carlo calculation for the 30, 45 and 60 cm thick blankets, respectively. The values of A_s and B_s increase linearly with the boron content, and they decrease exponentially with the blanket thickness as seen in Table 3.4. Detailed discussions on the values of A_s and B_s are described in Chapter 3.3.3.4.

3.3.3.2 Dependency on the boron content

Dependencies on the boron content are shown in Fig. 3.7 for the 1, 2, 4 and 8 cm wide slits. It was found that the helium productions increased linearly with the boron content. The

helium production in the vacuum vessel made of SS is caused from fast neutron reactions with Ni, Fe and Cr elements, and thermal neutron reaction with boron as mentioned above. The helium production caused from the thermal neutron reaction with elements except for boron is negligibly small, therefore the helium production caused from the thermal neutron reaction increases linearly with the boron content. The analytical representation on the helium production can be given as a function of the boron content, X_{bo} (appm), as follows;

$$Y_h = N P (A_{bo} + B_{bo} X_{bo}) \quad (3.7).$$

The values of A_{bo} and B_{bo} obtained by the least squares fitting to Eq. (3.7) are shown in Table 3.5 for various slit widths and blanket thicknesses. The values of N P A_{bo} and N P B_{bo} X_{bo} correspond to the helium productions by the fast and thermal neutrons, respectively. Disagreement of the helium productions obtained by the analytical representation Eq. (3.7) with the values in Table 3.5 is less than 18 % compared with those by the Monte Carlo calculation. The values of A_{bo} and B_{bo} increase linearly with the slit width, and they decrease exponentially with the blanket thickness as seen in Table 3.5.

3.3.3.3 Dependency on the blanket thickness

Dependencies on the blanket thickness are shown in Fig. 3.8 for the 10, 20, 50 and 100 wppm boron content. It was found that the helium productions decreased exponentially with the blanket thickness. Similarly to the exponential attenuation of the neutron flux in the blanket along the slit shown in Chapter 3.3.1, the helium productions along the slit may decrease exponentially with the blanket thickness. The analytical representation on the helium production can be given as a function of the blanket thickness, X_b (cm), as follows;

$$Y_h = N P A_b \exp (-B_b X_b) \quad (3.8),$$
$$T_{h/b} = \ln 10 / B_b \quad (3.9).$$

The values of A_b and B_b obtained by the least squares fitting to Eq. (3.8) are shown in Table 3.6 for various boron contents and slit widths. The B_b values, 1/cm, correspond to the effective linear attenuation coefficient of the blanket for the helium production in the vacuum vessel front wall surface along the slit. Disagreement of the helium productions obtained by the analytical representation Eq. (3.8) with the values in Table 3.6 is 1 to 16 % compared with those by the Monte Carlo calculation. The values of A_b and B_b almost increase linearly with the slit width and the boron content as seen in Table 3.6. The values of $T_{h/b}$ correspond to blanket thickness required to reduce the helium production by one order of magnitude, which are also shown in Table 3.6. In the case of the blanket without the slit, about 17 - 18 cm thick blanket is required to reduce the helium productions by one order of magnitude, but with increasing the slit width from 1 to 8 cm, the values of $T_{h/b}$ rapidly increase from 31 - 44 to 77 - 84 cm. The enhancement of the fast neutron flux along the slit due to the neutron streaming through the slit is expected to be much larger than that of the thermal neutron flux along the slit due to the neutron streaming through the slit, since the thermal neutrons are generated as a

result of fast neutron scattering and moderation in the blanket. The values of $T_{h/b}$ are expected to be enhanced by the fast neutron streaming through the slit. The smaller is the boron content in steel, the smaller is the thermal neutron contribution in the helium production due to the $^{10}B(n, \alpha)$ reaction and the larger is the fast neutron contribution. Therefore it is expected that the values of $T_{h/b}$ increase with decreasing the boron content. With decreasing the boron content from 100 to 10 wppm, the values of $T_{h/b}$ increase from 31 - 77 to 44 - 84 cm.

3.3.3.4 Establishment of analytical representation

Similarly to Eq. (3.7), it was found that the A_s and B_s values in Eq. (3.6) representing a function of the slit width also increased linearly with the boron content as seen in Table 3.4. The values of A_s and B_s can then be given approximately by a function of the boron content X_b as follows;

$$A_s = A'_s + A'_{bo} X_{bo} \quad (3.10),$$
$$B_s = B'_s + B'_{bo} X_{bo} \quad (3.11).$$

From the analytical representation Eq. (3.6) and the formulae Eqs. (3.10) and (3.11), the analytical representation on the helium productions can be given as function of the slit width X_{slit} and the boron content X_{boron} as follows;

$$Y_h = N P (A'_s + A'_{bo} X_{bo} + (B'_s + B'_{bo} X_{bo}) (X_{sl} - 1)) \quad (3.12).$$

The values of A'_s, A'_{bo}, B'_{sl} and B'_{bo} obtained by the least squares fitting to Eq. (3.12) are shown in Table 3.7 for various blanket thicknesses. Disagreements of the helium productions obtained by the analytical representation Eq. (3.12) with the values shown in Table 3.7 are less than 9, 14 and 20 % for the 30, 45 and 60 cm thick blankets, respectively, compared with those by the Monte Carlo calculation.

Dependencies of the values of A'_s, A'_{bo}, B'_{sl} and B'_{bo} on the blanket thickness are shown in Fig. 3.9. Similarly to Eq. (3.8), it was found that the A'_s, A'_{bo}, B'_{sl} and B'_{bo} values decreased exponentially with the blanket thickness as seen in Fig. 3.9. The values of A'_s, A'_{bo}, B'_s and B'_{bo} can then be given approximately by an exponential function of the blanket thickness X_{blt} as follows;

$$A'_s = A''_s \exp (- A'_b X_b) \quad (3.13),$$
$$A'_{bo} = A''_{bo} \exp (- A''_b X_b) \quad (3.14),$$
$$B'_s = B''_s \exp (- B'_b X_b) \quad (3.15),$$
$$B'_{bo} = B''_{bo} \exp (- B''_b X_b) \quad (3.16).$$

From the analytical representation Eq. (3.12) and the formulae Eqs. (3.13) - (3.16), the analytical representation on the helium production can be given as functions of the slit width X_s, the boron content X_{bo} and the blanket thickness X_b as follows;

$$Y_h = N P A''_s \exp(- A'_b X_b) + A''_{bo} \exp(- A''_b X_b) X_{bo} + (B''_{sl} \exp(- B'_b X_b) + B''_{bo} \exp(- B''_b X_b) X_{bo}) (X_s - 1)) \quad (3.17).$$

The values of A''_s, A'_b , A''_{bo}, A''_b, B''_{sl}, B'_b, B''_{bo}, B''_b obtained by the least squares fitting to Eq. (3.17) are shown in Table 3.8. By applying the values in Table 3.8, the helium productions can be obtained within 18 % difference by using the analytical representation Eq. (3.17) compared with those by the Monte Carlo calculation. The analytical representation Eq. (3.17) can be applied with good accuracy in the range of 1 to 8 cm wide slits, 0.1 to 100 wppm boron and 30 to 60 cm thick blankets.

3.3.4 Nuclear properties in the super-conductive magnet

In this Chapter, the nuclear properties such as the nuclear heating rate and the radiation damage are discussed in the TF coil surface toward the plasma along the slit.

3.3.4.1 Dependency on slit width

In the TF coil surface along the 1 - 8 cm wide slits in the 45 cm thick blanket and the 40 cm thick vacuum vessel, some calculated results are shown in Table 3.9 with the statistical error for the nuclear heating rate in the coil case surface, the nuclear heating rate in the winding pack, the absorbed dose rates in the insulator, the neutron damage in the stabilizer copper, the neutron fluence of the energy above 0.1 MeV in the winding pack. Dependencies of these nuclear properties on the slit width are shown in Figs. 3.10 - 3.14 in the TF coil surface along the slit in the range of the 30, 40 and 45 thick blankets, the 20, 30 and 40 cm thick vacuum vessels. Dependencies of the nuclear heating rate in the coil case, the nuclear heating rate in the winding pack, the absorbed dose rates in the insulator, the neutron damage in the stabilizer copper, the neutron fluence of the energy above 0.1 MeV in the winding pack are shown in Figs. 3.10, 3.11, 3.12, 3.13 and 3.14, respectively. Dependencies on the slit width are shown in Figs. 3.15 - 3.19 in the range of the 45, 50 and 60 thick blankets. Dependencies of the nuclear heating rate in the coil case, the nuclear heating rate in the winding pack, the absorbed dose rates in the insulator, the neutron damage in the stabilizer copper, the neutron fluence of the energy above 0.1 MeV in the winding pack are shown in Figs. 3.15, 3.16, 3.17, 3.18 and 3.19, respectively.

It was found that all nuclear properties in the TF coil along the slit increased exponentially with the slit width in the range of 30 – 45 thick blankets as seen in Figs. 3.10 – 3.14. The neutron flux in the blanket along the slit decrease exponentially with the blanket thickness as mentioned in Chapter 3.3.1. It is discussed that the increase of the slit width may corresponds to the decrease of the blanket thickness and all nuclear properties in the TF coil along the slit may increase exponentially with the slit width. Since the 14 MeV neutrons streaming pass directly through the slit to the vacuum vessel wall, the helium production in the vacuum vessel wall along the slit may increase linearly with the slit width as mentioned in Chapter 3.3.3.1. The TF coil along the slit is hidden by the vacuum vessel against the plasma,

and the 14 MeV neutrons streaming do not pass directly through the slit to the TF coil. Therefore the nuclear properties in the TF coil along the slit may increase exponentially with the slit width.

On the other hand, it is found that the all nuclear properties in the TF coil along the slit increase in proportion to the power function of the slit width in the range of 45 – 60 cm thick blankets as seen in Figs. 3.15 – 3.19. The comparison is shown in Fig. 3.20 about the least squares fittings for the exponential and power functions of the slit width in the 60 cm thick blanket and 40 cm thick vacuum vessel. Fig. 3.20 shows the example of the nuclear heating rate in the coil case. In the range of 1 – 10 cm wide slits, the values by the exponential function of the slit width do not match the values by the Monte Carlo calculation code so well. On the other hand, the values by the power function of the slit width match the values by the Monte Carlo calculation code so well. In case the blanket thickness is more than 45 cm, the increase of the slit width may corresponds to the decrease of the blanket thickness and further effects. Therefore it is discussed that the nuclear properties in the TF coil along the slit may increase in proportion to the power function of the slit width.

The analytical representation on all nuclear properties can be given as a function of the slit width as follows;

$$Y_c = N\,P\,C_s \exp(D_s X_s), \qquad 30 \le X_b \le 45, \quad 1 \le X_s \le 8 \qquad (3.18),$$

$$Y_c = N\,P\,C_s X_s^{D_s}, \qquad 45 \le X_b \le 60, \quad 1 \le X_s \le 8 \qquad (3.19),$$

where Y_{coil} are the nuclear properties such as the nuclear heating rates in the coil case and the winding pack (mW/cm^3), the absorbed dose rates in the insulator (rad), the fast neutron fluence of the energy above 0.1 MeV in the winding pack (n/cm^2) and the neutron damage in the stabilizer copper (dpa). The values of C_s and D_s obtained by the least squares fitting to Eqs. (3.18) and (3.19) are shown in Tables 3.10 and 3.11, respectively, for various blanket and vacuum vessel thicknesses. The D_s value are factors of a dependency on the the slit width. Disagreement of the nuclear properties obtained by the analytical representations (3.22) and (3.23) with the values in Tables 3.9 and 3.10 are 2 to 33 and 7 to 21 %, respectively, compared with those by the Monte Carlo calculation. The values of C_{slit} and D_{slit} decrease exponentially with the blanket thickness and the vacuum vessel thickness as seen in Tables 3.9 and 3.10. Detailed discussions on the values of C_{slit} and D_{slit} are described in Chapter 3.3.4.4.

3.3.4.2 Dependency on blanket thickness

Dependencies on the blanket thickness are shown in Figs. 3.21 -3.25 in the range of the 1, 2, 3, 4 and 8 cm wide slits, the 20, 30 and 40 cm thick vacuum vessels. Dependencies of the nuclear heating rate in the coil case, the nuclear heating rate in the winding pack, the absorbed dose rates in the insulator, the neutron damage in the stabilizer copper, the neutron fluence of the energy above 0.1 MeV in the winding pack are shown in Figs. 3.21, 3.22, 3.23, 3.24 and 3.25, respectively. It was found that all nuclear properties in the TF coil along the slit

decreased exponentially with the blanket thickness. In Chapter 3.3.3.3, it is discussed that the helium production in the vacuum vessel wall along the slit decreases exponentially with the blanket thickness. Similarly to the dependency of the helium production on the blanket thickness, it is discussed that all nuclear properties in the TF coil along the slit decrease exponentially with the blanket thickness. The analytical representations on all nuclear properties in the TF coil along the slit can be given as a function of the blanket thickness as follows;

$$Y_c = N\,P\,C_b \exp(-D_b X_b) \quad (3.20),$$
$$T_{c/b} = \ln 10/D_b \quad (3.21).$$

The values of C_b and D_b obtained by the least squares fitting to Eq. (3.20) are shown in Table 3.12 for various slit widths and vacuum vessel thicknesses. The D_b values, 1/cm, correspond to the effective linear attenuation coefficient of the blanket for the nuclear properties in the TF coil along the slit. Disagreement of the nuclear properties obtained by the analytical representation Eq. (3.24) with the values shown in Table 3.12 is less than 25 % compared with those by the Monte Carlo calculation. The values of C_b decrease exponentially with the vacuum vessel thickness as seen in Table 3.11. Detailed discussions on the values of C_b and D_b are described in Chapter 3.3.3.4. The values of $T_{c/b}$ correspond to blanket thickness required to reduce the nuclear properties by one order of magnitude, and they are also shown in Table 3.11. In the case of the blanket with the 1 cm wide slit, about 21 - 22 cm thick blanket is required to reduce the nuclear properties by one order of magnitude, but with increasing the slit width from 2 to 8 cm, the values of $T_{c/b}$ rapidly increase from 27 - 32 to 58 - 70 cm thickness as seen in Table 3.11.

3.3.4.3 Dependency on vacuum vessel thickness

Dependencies on the vacuum vessel thickness are shown in Figs. 3.26 - 3.30 in the range of the 1, 2, 3, 4 and 8 cm wide slits, the 30, 45 and 60 cm thick blankets. Dependencies of the nuclear heating rate in the coil case, the nuclear heating rate in the winding pack, the absorbed dose rates in the insulator, the neutron damage in the stabilizer copper, the fast neutron fluence of the energy above 0.1 MeV in the winding pack are shown in Figs. 3.26, 3.27, 3.28, 3.29 and 3.30, respectively. Similarly to dependencies on the blanket thickness, it was found that the all nuclear properties in the TF coil along the slit decreased exponentially with the vacuum vessel thickness. The analytical representations on all nuclear properties in the TF coil along the slit can be given as a function of the vacuum vessel thickness, X_v (cm), as follows;

$$Y_c = N\,P\,C_v \exp(-D_v X_v) \quad (3.22),$$
$$T_v = \ln 10/D_v \quad (3.23).$$

The values of C_v and D_v obtained by the least squares fitting to Eq. (3.22) are shown in Table 3.13 for various slit widths and blanket thicknesses. The D_v values, 1/cm, correspond to the

effective linear attenuation coefficient of the vacuum vessel for the nuclear properties in the TF coil along the slit. Disagreement of the nuclear properties obtained by the analytical representation Eq. (3.26) with the values shown in Table 3.13 is less than 5 % compared with those by the Monte Carlo calculation results. The values of C_v decrease exponentially with the blanket thickness as seen in Table 3.13. Detailed discussions on the values of C_v and D_v are described in Chapter 3.3.4.4. The values of T_v correspond to vacuum vessel thickness required to reduce the nuclear properties by one order of magnitude, and they are also shown in Table 3.13. They are in the range of 16 to 20 cm. The blanket thickness required to reduce these nuclear properties by one order of magnitude strongly depends on the slit width, while no significant difference is found in the range of 1 to 8 cm wide slits for the vacuum vessel thickness required. The vacuum vessel is bulk shield without the slit, and the slits exist only in the blanket. Therefore it can be discussed that the dependency of the attenuation of the neutron flux along the slit in the vacuum vessel on the slit width is very little. The radiation streaming through the slit in the blanket is enhanced with increasing the slit width, and the attenuation of the neutron flux along the slit in the blanket is weaken. Therefore it can be discussed that the blanket thickness required strongly depends on the slit width.

3.3.3.4 Establishment of analytical representation

Dependencies of the C_b values in Eq. (3.20) on the vacuum vessel thickness are shown in Fig. 3.31. Figure 3.31 show the example for the nuclear heating rate in the coil case. Similarly to Eq. (3.22), it is found that all C_b values in Eq. (3.20) representing a function of the blanket thickness also decrease exponentially with the vacuum vessel thickness as seen in Fig. 3.31. The values of C_b can be expressed approximately by an exponential function of the vacuum vessel thickness X_v as follows;

$$C_b = C_{b/v} \exp (- C'_{b/v} X_v) \qquad (3.24).$$

The values of $C_{b/v}$ and $C'_{b/v}$ are shown in Table 3.14 for various slit widths. It is found that the D_b values in Eq. (3.20) are almost constant in the range of 20 – 40 cm thick vacuum vessel as seen in Table 3.12. The average effective linear attenuation coefficients $D_{b/v}$ for three vacuum vessel thicknesses of 20, 30 and 40 cm calculated by the following formula Eq. (3.25) are also shown in Table 3.13 with the average $T_{b/v}$ calculated by the following formula Eq. (3.26);

$$D_{b/v} = \sum D_b(m) / 3, \quad m = 20, 30, 40 \qquad (3.25),$$

$$T_{b/v} = \ln 10 / D_{b/v} \qquad (3.26).$$

where $D_b(m)$ are the value of D_b shown in Table 3.12 in the case of the m cm thick vacuum vessel.

From the analytical representation Eq. (3.20), and the formulae Eqs. (3.24) and (3.25), the analytical representation on the nuclear properties in the TF coil along the slit can be

given as functions of the blanket thickness X_b and the vacuum vessel thickness X_v as follows;

$$Y_c = N P C_{b/v} \exp (- C'_{b/v} X_v) \exp (- D_{b/v} X_b) \quad (3.27).$$

Disagreement of the nuclear properties obtained by the analytical representation Eq. (3.27) with the values in Table 3.14 is less than 28 % compared with those by the Monte Carlo calculation results.

Dependencies of the C_s values in Eqs. (3.18) and (3.19) on the blanket thickness are shown in Figs. 3.32 and 3.33, respectively, and the D_s values in Eqs. (3.18) and (3.19) on the blanket thickness are shown in Figs. 3.34 and 3.35, respectively. Figures 3.32 - 3.35 show the example for the nuclear heating rate in the coil case. Similarly to Eq. (3.20), it was found that all C_s values in Eqs. (3.18) and (3.19) representing a function of the slit width also decreased exponentially with the blanket thickness. On the other hand, it was found that all D_s values in Eqs. (3.18) and (3.19) increased exponentially with the blanket thickness. With increasing the blanket thickness, the difference between the attenuation of the neutron flux in the bulk shield and that in the slit increases. Therefore with increasing the blanket thickness, the factor of the slit width dependency may also increases. The D_s values are factors of a dependency on the slit width as mentioned above, therefore they are expected to be increased as the blanket thickness is increased. The values of C_s and D_s can be expressed approximately by an exponential function of the blanket thickness X_b as follows;

$$C_s = C'_s \exp (-C'_b X_b) \quad (3.28),$$
$$D_s = D'_s \exp (D'_b X_b) \quad (3.29).$$

From the analytical representations Eqs. (3.18) and (3.19), and the formulae Eqs. (3.28) and (3.29), the analytical representation on the nuclear properties in the TF coil along the slit can be given as functions of the slit width X_s and the blanket thickness X_b as follows;

$$Y_c = N P C'_s \exp (- C'_b X_b) \exp (D'_s X_s \exp (D'_b X_b)), \quad 30 \le X_b \le 45, \quad (3.30),$$
$$Y_c = N P C'_s \exp (- C'_b X_b) X_s^{D'_s \exp (D'_b X_b)}, \quad 45 \le X_b \le 60, \quad (3.31).$$

The values of C'_s, C'_b, D'_s and D'_b obtained by the least squares fitting to Eqs. (3.30) and (3.31) are shown in Tables 3.15 and 3.16, respectively, for various vacuum vessel thicknesses. Disagreement of the nuclear properties obtained by the analytical representations Eqs. (3.30) and (3.31) with the values in Tables 3.15 and 3.16 are within 33 and 20 %, respectively, compared with those by the Monte Carlo calculation.

Dependencies of the C'_s values in Eqs. (3.30) and (3.31) on the vacuum vessel thickness are shown in Fig. 3.36. Figure 3.36 shows the example for the nuclear heating rate in the coil case. Similarly to the C_b values in Eq. (3.20), it was found that all C'_s values in Eqs. (3.30) and (3.31) representing functions of the slit width and the blanket thickness also decrease exponentially with the vacuum vessel thickness. The C'_s values can be given approximately by an exponential function of the vacuum vessel thickness X_v as follows;

$$C'_s = C'_{s/v} \exp (- C''_{s/v} X_v) \quad (3.32).$$

The values of $C'_{s/v}$ and $C''_{s/v}$ obtained by the least squares fitting to Eq. (3.32) are shown in Table 3.17. Also similarly to D_{blt} values in Eq. (3.20), it is found that all C'_b, D'_s and D'_b values are almost constant in the range of 20 – 40 cm thick vacuum vessel as seen in Tables 3.15 and 3.16. The average values $C'_{b/v}$, $D'_{s/v}$ and $D'_{b/v}$ for three vacuum vessel thicknesses of 20, 30 and 40 cm calculated by the following formulae Eqs. (3.33) – (3.35) are also shown in Table 3.17;

$$C'_{b/v} = \sum C'_b(m) / 3, \quad m = 20, 30, 40 \quad (3.33),$$

$$D'_{s/v} = \sum D'_s(m) / 3, \quad m = 20, 30, 40 \quad (3.34),$$

$$D'_{b/v} = \sum D'_b(m) / 3, \quad m = 20, 30, 40 \quad (3.35).$$

where $C'_b(m)$, $D'_s(m)$ and $D'_b(m)$ are the values of C'_b, D'_s and D'_b shown in Tables 3.15 and 3.16 in the case of the m cm thick vacuum vessel.

From the analytical representations Eqs. (3.30) and (3.31) representing functions of the slit width X_s and the blanket thickness X_b, the formulae (3.33) – (3.35), the analytical representation can be given as functions of the slit width X_s, the blanket thickness X_b and the vacuum vessel thickness X_v as follows;

$$Y_c = N P C'_{s/v} \exp (- C''_{s/v} X_v) \exp (- C'_{b/v} X_b) \exp (D'_{s/v} X_s \exp (D'_{b/v} X_b)),$$
$$1 \le X_s \le 8, \quad 30 \le X_b \le 45, \quad 20 \le X_v \le 40, \quad (3.36),$$

$$Y_c = N P C'_{s/v} \exp (- C''_{s/v} X_v) \exp (- C'_{b/v} X_b) X_s^{D'_{s/v} \exp (D'_{b/v} X_b)},$$
$$1 \le X_{slit} \le 8, \quad 45 \le X_{blt} \le 60, \quad 20 \le X_{vv} \le 40, \quad (3.37).$$

Disagreement of the nuclear properties obtained by the analytical representations Eqs. (3.36) and (3.37) with the values in Table 3.17 are less than 37 and 22 %, respectively, compared with those by the Monte Carlo calculation. The representations Eqs. (3.36) and (3.37) can be applied with good accuracy in the range of 1 – 8 cm wide slits, 30 – 60 cm thick blankets and 20 – 40 cm thick vacuum vessels.

3.3.4 Dependencies on blanket and vacuum vessel composition

Dependency of the helium production on the blanket composition is shown in Fig. 3.37 in the vacuum vessel front wall surface toward the plasma along the slit. The horizontal axis corresponds to the volume fraction of SS in the blanket composition. Dependencies of the nuclear heating rate on the blanket and vacuum vessel shield composition are also shown in Fig. 3.37 in the TF coil surface toward the plasma along the slit. It was found that the optimized composition to minimize these nuclear properties were range from 70 % SS/30 %

water to 90 % SS/10 % water.

The difference between the helium production obtained by the blanket composition down to 50 % SS/50 % water and that by 80 % SS/20 % water is only 9 %. It is therefore expected that the helium productions can also be estimated within 9 % difference for the blanket composition in the range from 50 % SS/50 % water to 90 % SS/10 % water by using the values in Table 3.8 based on the blanket composed of 80 % SS/20 % water.

The difference between the nuclear properties in the TF coil obtained by the blanket composition down to 60 % SS/40 % water and that by 80 % SS/20 % water is only 23 %, and it is therefore expected that the nuclear properties in the TF coil can also be estimated within 23 % difference for the blanket composition in the range from 60 % SS/40 % water to 90 % SS/10 % water.

The difference between the nuclear properties in the TF coil obtained by the vacuum vessel shield region composition down to 50 % SS/50 % water and that by 60 % SS/40 % water is only 24 %, and it is therefore expected that the nuclear properties in the TF coil can also be estimated within 24 % difference for the vacuum vessel shield composition in the range from 50 % SS/50 % water to 80 % SS/20 % water.

3.4 Application to Establishment of Shielding Design Constraint

3.4.1 Helium production in the vacuum vessel

The analytical representation Eq. (3.17) for the helium production in the vacuum vessel front wall surface toward the plasma along the slit as functions of the slit width X_s, the boron content X_{bo} and the blanket thickness X_b can be applied to clarify the shielding design constraint required to satisfy the shielding design criteria by using the following formulae;

$$Y_h \leq L_h / S_h \qquad (3.38),$$

where Y_h, L_h and S_h are the helium production (appm) obtained by the analytical representation Eq. (3.17), shielding design criteria capable for rewelding and a safety factor in the shielding calculation, respectively. Using Eq. (3.38) and the analytical representation Eq. (3.13), the shielding design constraint can be easily selected as follows;

$$A''_s \exp (- A'_b X_b) + A''_{bo} \exp (- A''_b X_b) X_{bo} + (B''_{sl} \exp (- B'_b X_b) + B''_{bo} X_{bo} \exp (- B''_b X_b)) (X_{sl} - 1) \leq L_h / (S_h N P) \qquad (3.39).$$

The formula Eq. (3.39) is applied to the ITER shielding design with the values in Table 3.8. In the ITER, 1 - 2 cm wide slits are to be designed, and the integrated neutron wall loading of 0.3 MWa/m^2 is planned at the end-of-life. It is assumed that the rewelding of SS in the vacuum vessel wall can be accomplished if the integrated helium production is less than 1 appm [1.3]. From the shielding experiment results for the slit streaming of the blanket by Maekawa et al., it is expected that the calculation uncertainty by MCNP with FENDL is less than 30 % [3.3]. Disagreement of the helium production obtained by the analytical

representation Eq. (3.17) is less than 18 % compared with that by MCNP with FENDL, therefore a safety factor of 1.6, which corresponds to the value of 1.3 x 1.18, is considered in this Chapter. The values of L_h, S_h, and N P applied to the shielding design are 1 appm, 1.6 and 0.3 MWa/m^2, respectively. By inputting these values into Eq. (3.39), the shielding design constraint for the slit width X_s, the boron content X_{bo} and the blanket thickness X_b required to satisfy the shielding design criteria can be given as shown in Fig. 3.38. If a combination of the boron content and the blanket thickness exists in the lower region of each curve, the helium production can satisfy the criteria for the respective slit width. In the case of the 45 cm thick blankets with 1, 1.5 and 2 cm wide slits, it is found that the required boron contents are less than 47, 15 and 0.6 wppm, respectively, to satisfy the shielding design criteria.

3.4.2 Nuclear properties in the TF coil

Similarly to the formula (3.39), the analytical representations Eqs. (3.36) and (3.37) for the nuclear properties in the TF coil along the slit as functions of the slit width X_s, the the blanket thickness X_b and the vacuum vessel thickness X_v can be applied to clarify the shielding design constraint required to satisfy the shielding design criteria by using the following formulae;

$$Y_c \leq L_c / S_c \qquad (3.40),$$

where Y_c, L_c and S_c are the nuclear properties obtained by the analytical representations Eqs. (3.36) and (3.37), shielding design criteria capable for soundness of the TF coil and a safety factor in the shielding calculation, respectively. Using Eq. (3.40) and the analytical representation Eqs. (3.36) and (3.37), the shielding design constraint can be easily selected as follows;

$$C'_{s/v} \exp (- C''_{s/v} X_v) \exp (- C'_{b/v} X_b) \exp (D'_{s/v} X_s \exp (D'_{b/v} X_b)) \leq L_c / (S N P),$$
$$30 \leq X_{blt} \leq 45, \qquad (3.41),$$

$$C'_{s/v} \exp (- C''_{s/v} X_v) \exp (- C'_{b/v} X_b) X_s^{D'_{s/v} \exp (D'_{b/v} X_{blt})} \leq L_c / (S N P),$$
$$45 \leq X_{blt} \leq 60, \qquad (3.42).$$

The formulae Eqs. (3.41) and (3.42) are applied to the ITER shielding design for the 40 cm thick vacuum vessel. Here, it is assumed that the nuclear wall loading and the integrated nuclear wall loading are 0.7 MW/m^2 and 0.3 MWa/m^2, respectively. The assumed shielding design criteria are shown in Table 1.1. From the shielding experiment results for the slit streaming of the blanket by Konno et al., it is expected that the calculation uncertainty by MCNP with FENDL is less than 40 % [3.4]. Disagreement of the nuclear properties obtained by the analytical representations Eqs. (3.36) and (3.37) are less than 37 and 22 %, respectively, compared with those by MCNP with FENDL, therefore a safety factor of 1.9 and 1.7 are considered in this Chapter. By inputting these values into Eqs. (3.41) and (3.42), the shielding

design constraint for the slit width X_s, the blanket thickness X_b and the vacuum vessel thickness X_v required to satisfy the shielding design criteria can be given as shown in Fig. 3.39. If the combination of the slit width and the blanket thickness exists in the lower region of each curve, the nuclear properties can satisfy the criteria. In the case of the 40 cm thick vacuum vessel with 4 cm wide slits, it is found that the required blanket thickness is more than 49 cm to satisfy the shielding design criteria.

3.5 Conclusion

Three dimensional Monte Carlo calculations are performed taking into account the radiation streaming through the slit between the adjacent blanket modules.

(1) The analytical representations on the helium productions in the vacuum vessel are established as functions of the slit width, the blanket thickness and the boron content.
(2) By using the analytical representation, the helium production can be estimated within 18 difference compared with the results by the Monte Carlo calculation in the compositions of 80 % SS/20 % water in the blanket.
(3) The analytical representations on the nuclear properties in the TF coil such as the nuclear heating rate and the radiation damage along the slit are established as functions of the slit width, the blanket thickness and the vacuum vessel thickness.
(4) By using the analytical representation, the nuclear properties in the TF coil can be estimated within 37 % difference compared with the results by the Monte Carlo calculation in the compositions of 80 % SS/20 % water and 60 % SS/40 % water in the blanket and the vacuum vessel shield, respectively.
(5) Dependencies of these nuclear properties along the slit on the blanket and the vacuum vessel shield composition are also clarified. By using the analytical representation, the helium productions can be estimated in the blanket composed of the region of 50 % SS/50 % water to 90 % SS/10 % water within only 9 % difference compared with that in 80 % SS/20 % water.
(6) The analytical representation is applied to clarify the shielding design constraint required to satisfy the shielding design criteria.
(7) In case the shielding design conditions were applied to the ITER one, it was found that the required boron contents were less than 47, 17 and 0.6 wppm in the 45 cm thick blanket with 1, 1.5 and 2 cm wide slits, respectively.
(8) In the case of the 40 cm thick vacuum vessel with 4 cm wide slits, it was found that the required blanket thickness were more than 49 cm to satisfy the shielding design criteria of the TF coil.
(9) These analytical representations will be useful for the shield design of DT fusion reactors.

References

[3.1] S. Sato, K. Maki, Analytical Representation for Neutron Streaming through Slits in Fusion Reactor Blanket by Monte Carlo Calculation, Fusion Eng. Design, 65, 501-524 (2003).

[3.2] K. Maki, S. Sato, H. Kawasaki, Development of Displacement Cross Section Set for Evaluating Radiation Damage by Neutron Irradiation in Materials Used for Fusion Reactors, JAERI-Data/Code 97-002, February (1997).

[3.3] F. Maekawa, et al., Investigation on Prediction Capability of Nuclear Design Parameters for Gap Configuration in ITER through Analysis of the FNS Gap Streaming Experiment, J. Nucl. Sci. Technol., Supplement 1, 263-267 (2000).

[3.4] C. Konno, et al., Benchmark experiment on bulk shield of SS316/water with simulated superconducting magnet, Fusion Engineering and Design, 42, 267-273 (1998).

Table 3.1 Calculational condition

Blanket thickness (cm)	30, 40, 45, 50, 60
Boron content in the vacuum vessel surface (wppm)	0.1, 0.2, 0.3, 0.5, 1, 2, 3, 5, 10, 20, 30, 50, 100
Slit width (cm)	0, 1, 2, 3, 4, 6, 8
Vacuum vessel thickness (cm)	20, 30, 40
Blanket composition (%)	SS/H_2O = 0/100, 10/90, 20/80, 30/70, 40/60, 50/50, 60/40, 70/30, 80/20, 90/10, 100/0
Vacuum vessel shield composition (%)	SS/H_2O = 0/100, 10/90, 20/80, 30/70, 40/60, 50/50, 60/40, 70/30, 80/20, 90/10, 100/0

Table 3.2 The value of Cn and the effective line reduction factor λ_{eff} in the analytical representation (3.1) on the energy integrated total neutron flux distribution along the 1 - 8 cm wide slit as a function of the distance from the blanket surface. The blanket thickness is 45 cm, and the blanket composition is 80% SS and 20% water. The neutron wall loading is 1 MW/m^2.

Slit width (cm)	Extent (cm)*	C_{sl}	λ_{eff}	Error**
1	0 < x < 45	2.92×10^{14}	9.40E-02	1.145
2	0 < x < 45	2.64×10^{14}	7.91E-02	1.122
3	0 < x < 45	2.43×10^{14}	6.70E-02	1.194
4	1 < x < 45	2.37×10^{14}	5.95E-02	1.071
8	1 < x < 45	2.22×10^{14}	4.22E-02	1.182

Error**: Maximum values of the ratio between the helium productions obtained by the analytically using Eq. (3.6) to those by the Monte Carlo calculation.

Table 3.3 Calculation results for the helium production in the vacuum vessel surface with 10 wppm boron content along the slit in the 45 cm thick blanket. (Integarated neutron wall loading: 1MWa/m^2)

Slit width (cm)	Helium production (appm)	Statistical error
1	1.26	0.0892
2	2.19	0.0481
3	3.56	0.0499
4	5.09	0.0435
8	10.01	0.0340

Table 3.4 The value of A_S and B_S in the analytical representation (3.6) on the helium production in the vacuum vessel front wall surface along the slit as a function of the slit width. The slit width is 1 to 8 cm.

	Blanket thickness (cm)					
	30			45		
Boron content (wppm)	A_S	B_S	Error*	A_S	B_S	Error*
100	1.22E+01	5.06	1.068	3.63E+00	3.67	1.081
50	7.15E+00	3.28	1.058	2.23E+00	2.34	1.058
30	5.11E+00	2.57	1.048	1.67E+00	1.81	1.069
20	4.09E+00	2.22	1.040	1.39E+00	1.54	1.077
10	3.08E+00	1.86	1.031	1.12E+00	1.27	1.131

	Blanket thickness (cm)		
	60		
Boron content (wppm)	A_S	B_S	Error*
100	9.97E-01	2.60	1.192
50	7.99E-01	1.67	1.090
30	7.19E-01	1.29	1.044
20	6.80E-01	1.11	1.048
10	6.40E-01	0.92	1.054

Error*: Maximum values of the ratio between the helium productions obtained by the analytically using Eq. (3.6) to those by the Monte Carlo calculation.

Table 3.5 The value of A_{bo} and B_{bo} in the analytical representation (3.7) on the helium production in the vacuum vessel front wall surface along the slit as a function of the boron content. The blanket composition is 80 % SS and 20 % water. The boron content is 0.1 to 100 wppm.

	Blanket thickness (cm)					
	30			45		
Slit width (cm)	A_{bo}	B_{bo}	Error*	A_{bo}	B_{bo}	Error*
0	7.31E-01	7.11E-02		8.41E-02	1.10E-02	
1	2.05E+00	9.40E-02	1.004	1.02E+00	2.34E-02	1.003
2	3.52E+00	1.37E-01	1.020	1.97E+00	4.85E-02	1.181
3	5.12E+00	1.86E-01	1.009	2.71E+00	8.55E-02	1.000
4	6.72E+00	2.05E-01	1.011	3.97E+00	1.13E-01	1.000
8	1.29E+01	3.43E-01	1.025	7.90E+00	2.11E-01	1.000

	Blanket thickness (cm)		
	60		
Slit width (cm)	A_{bo}	B_{bo}	Error*
0	9.76E-03	1.66E-03	
1	5.53E-01	6.35E-03	1.000
2	1.46E+00	2.01E-02	1.156
3	1.94E+00	4.07E-02	1.000
4	2.83E+00	6.07E-02	1.000
8	5.72E+00	1.35E-01	1.000

Error*: Maximum values of the ratio between the helium productions obtained by the analytically using Eq. (3.7) to those by the Monte Carlo calculation.

Table 3.6 The values of A_b and B_b in the analytical representation (3.8) on the helium production in the vacuum vessel front wall surface along the slit as an exponential function of the blanket thickness, and the required blanket thickness $T_{h/b}$ to reduce the helium productions by one order of magnitude. The blanket composition is 80 % SS and 20 % water. The blanket thickness is 30 to 60 cm.

Slit width (cm)	Boron content (wppm)	A_b	B_b (cm^{-1})	Error*	$T_{h/b}$ (cm)
0	10	7.98E+01	1.34E-01		17.2
	100	3.50E+02	1.27E-01		18.2
1	10	1.42E+01	5.28E-02	1.046	43.6
	20	2.21E+01	5.85E-02	1.064	39.4
	30	3.10E+01	6.27E-02	1.068	36.7
	50	5.06E+01	6.83E-02	1.067	33.7
	100	1.06E+02	7.53E-02	1.065	30.6
2	10	1.40E+01	3.79E-02	1.160	60.8
	20	1.97E+01	4.08E-02	1.152	56.4
	30	2.56E+01	4.28E-02	1.145	53.8
	50	3.77E+01	4.54E-02	1.131	50.7
	100	6.96E+01	4.85E-02	1.125	47.4
3	10	2.01E+01	3.65E-02	1.092	63.1
	20	2.75E+01	3.89E-02	1.077	59.1
	30	3.49E+01	4.06E-02	1.065	56.8
	50	5.07E+01	4.29E-02	1.053	53.7
	100	9.16E+01	4.57E-02	1.041	50.4
4	10	2.15E+01	3.10E-02	1.046	74.4
	20	2.82E+01	3.27E-02	1.039	70.4
	30	3.47E+01	3.38E-02	1.031	68.2
	50	4.86E+01	3.54E-02	1.029	65.0
	100	8.30E+01	3.74E-02	1.012	61.6
8	10	3.59E+01	2.74E-02	1.045	83.9
	20	4.44E+01	2.80E-02	1.038	82.2
	30	5.31E+01	2.85E-02	1.034	80.8
	50	7.09E+01	2.92E-02	1.032	78.9
	100	1.14E+02	2.99E-02	1.023	77.1

Error*: Maximum values of the ratio between the helium productions obtained by the analytically using Eq. (3.8) to those by the Monte Carlo calculation.

Table 3.7 The values of A'_s, A'_{bo}, B'_s and B'_{bo} in the analytical representation (3.12) on the helium production in the vacuum vessel front wall surface along the slit as functions of the slit width and the boron content. The blanket composition is 80 % SS and 20 % water. The slit width is 1 to 8 cm. The boron content is 0.1 to 100 wppm.

Blanket thickness	A_s	A'_{bo}	B'_s	B'_{bo}	Error*
30 cm	2.12E+00	1.03E-01	1.50E+00	3.51E-02	1.085
45 cm	8.36E-01	2.79E-02	1.01E+00	2.66E-02	1.131
60 cm	6.00E-01	3.96E-03	7.31E-01	1.87E-02	1.193

Error*: Maximum values of the ratio between the helium productions obtained by theanalytically using Eq. (3.12) to those by the Monte Carlo calculation.

Table 3.8 The values of A''_s, A'_b, A''_{bo}, A''_b, B''_{sl}, B'_b, B''_{bo}, B''_b in the analytical representation (3.17) on the helium production in the vacuum vessel front wall surface along the slit as functions of the slit width, the blanket thickness and the boron content. The blanket composition is 80 % SS and 20 % water. The slit width is 1 to 8 cm. The boron content is 0.1 to 100 wppm.

A''_s	A'_b	A''_{bo}	A''_b	B''_s	B'_b	B''_{bo}	B''_b
6.77	0.042	2.99	0.109	3.02	0.0238	0.0668	0.021

Table 3.9 (a) Calculation results for the nuclear properties in the TF coil surface with the 45 cm thick blanket and 40 cm thick vacuum vessel. (Neutron wall loading: 1MW/m^2, Integarated neutron wall loading: 1MWa/m^2)

Slit width (cm)	Nuclear heating rate in the magnet case (w/cm^3)	Statistical error
1	3.69E-04	0.0605
2	7.22E-04	0.0423
3	1.15E-03	0.0325
4	1.72E-03	0.0280
8	4.93E-03	0.0215

Table 3.9 (b) Calculation results for the nuclear properties in the TF coil surface with the 45 cm thick blanket and 40 cm thick vacuum vessel. (Neutron wall loading: 1MW/m^2, Integarated neutron wall loading: 1MWa/m^2)

Slit width (cm)	Nuclear heating rate in the winding pack (w/cm^3)	Statistical error
1	1.20E-04	0.0748
2	2.40E-04	0.0491
3	3.76E-04	0.0399
4	5.50E-04	0.0349
6	1.00E-03	0.0308
8	1.61E-03	0.0279

Slit width (cm)	Absorbed dose rate in the insulator (rad)	Statistical error
1	1.28E+08	0.0592
2	2.45E+08	0.042
3	3.99E+08	0.0339
4	6.07E+08	0.0301
6	1.10E+09	0.0282
8	1.74E+09	0.0246

Slit width (cm)	Neutron damage in the stbilizer copper (dpa)	Statistical error
1	7.81E-05	0.0738
2	1.41E-04	0.0537
3	2.40E-04	0.0459
4	3.64E-04	0.0382
8	1.01E-03	0.0288

Slit width (cm)	Fast (> 0.1 MeV) neutron fluence in the winding pack (n/cm^2)	Statistical error
1	1.06E+17	0.064
2	1.86E+17	0.0483
3	3.18E+17	0.0402
4	4.87E+17	0.0356
8	1.40E+18	0.0285

Table 3.10 (a) The values of C_s and D_s in the analytical representation (3.18) on the nuclear properties such as the nuclear heating density and the radiation damage in the TF coil surface along the slit as an exponential function of the slit width. The blanket and the vacuum vessel shield compositions are 80 % SS/20 % water and 60 % SS/40 % water, respectively. The slit width is 1 to 8 cm.

Vacuum vessel thickness (cm)	20			30		
Blanket thickness: 30cm	C_s	D_s	Error*	C_s	D_s	Error*
1)*	3.19E-02	0.155	1.042	8.01E-03	0.174	1.044
2)*	1.14E-02	0.166	1.032	2.40E-03	0.191	1.025
3)*	1.11E+10	0.174	1.041	2.42E+09	0.199	1.042
4)*	5.92E-03	0.184		1.33E-03	0.207	
5)*	9.06E+18	0.183	1.073	1.94E+18	0.200	1.066

Vacuum vessel thickness (cm)	20			30		
Blanket thickness: 40cm	C_s	D_s	Error*	C_s	D_s	Error*
1)*	9.24E-03	0.256	1.111	2.37E-03	0.274	1.132
2)*	3.29E-03	0.263	1.107	7.33E-04	0.286	1.146
3)*	3.19E+09	0.277	1.118	7.43E+08	0.294	1.178
4)*	1.70E-03	0.291		4.23E-04	0.298	
5)*	2.55E+18	0.281	1.113	5.93E+17	0.293	1.159

Vacuum vessel thickness (cm)	20			30		
Blanket thickness: 45cm	C_s	D_s	Error*	C_s	D_s	Error*
1)*	5.20E-03	0.307	1.162	1.36E-03	0.326	1.222
2)*	1.81E-03	0.321	1.121	4.00E-04	0.344	1.257
3)*	1.84E+09	0.327	1.200	4.23E+08	0.347	1.247
4)*	1.02E-03	0.337		2.42E-04	0.355	
5)*	1.48E+18	0.331	1.190	3.34E+17	0.349	1.226

1)*: Nuclaer heating rate on the coil case (w/cm^3)
2)*: Nuclaer heating rate on the winding pack (w/cm^3)
3)*: Absorbed dose rate in the insulator (rad)
4)*: Neutron damage in the stbilizer copper (dpa)
5)*: Fast (> 0.1 MeV) neutron fluence in the winding pack ($n/cm^2/s$)

Error*: Maximum values of the ratio between the nuclear properties obtained by the analytically using Eq. (3.18) to those by the Monte Carlo calculation.

Table 3.10 (b) The values of C_s and D_s in the analytical representation (3.18) on the nuclear properties such as the nuclear heating density and the radiation damage in the TF coil surface along the slit as an exponential function of the slit width. The blanket and the vacuum vessel shield compositions are 80 % SS/20 % water and 60 % SS/40 % water, respectively. The slit width is 1 to 8 cm.

Vacuum vessel thickness (cm)	40		
Blanket thickness: 30 cm	C_s	D_s	Error*
1)*	2.14E-03	0.186	1.034
2)*	6.07E-04	0.205	1.061
3)*	6.38E+08	0.207	1.068
4)*	3.53E-04	0.214	1.077
5)*	4.96E+17	0.207	1.055

Vacuum vessel thickness (cm)	40		
Blanket thickness: 40 cm	C_s	D_s	Error*
1)*	6.38E-04	0.283	1.172
2)*	1.89E-04	0.297	1.212
3)*	1.93E+08	0.308	1.231
4)*	1.11E-04	0.313	1.224
5)*	1.50E+17	0.311	1.224

Vacuum vessel thickness (cm)	40		
Blanket thickness: 45 cm	C_s	D_s	Error*
1)*	3.41E-04	0.352	1.236
2)*	1.11E-04	0.356	1.325
3)*	1.16E+08	0.361	1.298
4)*	7.04E-05	0.352	1.282
5)*	9.28E+16	0.357	1.258

1)*: Nuclaer heating rate on the coil case (w/cm^3)
2)*: Nuclaer heating rate on the winding pack (w/cm^3)
3)*: Absorbed dose rate in the insulator (rad)
4)*: Neutron damage in the stbilizer copper (dpa)
5)*: Fast (> 0.1 MeV) neutron fluence in the winding pack ($n/cm^2/s$)

Error*: Maximum values of the ratio between the nuclear properties obtained by the analytically using Eq. (3.18) to those by the Monte Carlo calculation.

Table 3.11 (a) The values of C_s and D_s in the analytical representation (3.19) on thenuclear properties such as the nuclear heating density and the radiation damage in the TF coil surface along the slit as an exponential function of the slit width. The blanket and the vacuum vessel shield compositions are 80 % SS/20 % water and 60 % SS/40 % water, respectively. The slit width is 1 to 8 cm.

Vacuum vessel thickness (cm)	20			30		
Blanket thickness: 45 cm	C_s	D_s	Error*	C_s	D_s	Error*
1)*	5.10E-03	1.07	1.173	1.32E-03	1.14	1.164
2)*	1.78E-03	1.11	1.190	3.86E-04	1.21	1.163
3)*	1.80E+09	1.14	1.183	4.11E+08	1.22	1.168
4)*	9.94E-04	1.18		2.33E-04	1.25	
5)*	1.46E+18	1.15	1.202	3.27E+17	1.22	1.181

Vacuum vessel thickness (cm)	20			30		
Blanket thickness: 50 cm	C_s	D_s	Error*	C_s	D_s	Error*
1)*	3.12E-03	1.19	1.189	7.79E-04	1.29	1.150
2)*	1.04E-03	1.28	1.154	2.34E-04	1.36	1.158
3)*	1.07E+09	1.30	1.154	2.44E+08	1.39	1.133
4)*	5.92E-04	1.35		1.36E-04	1.44	
5)*	8.43E+17	1.32	1.142	1.87E+17	1.41	1.136

Vacuum vessel thickness (cm)	20			30		
Blanket thickness: 60 cm	C_s	D_s	Error*	C_s	D_s	Error*
1)*	1.37E-03	1.47	1.141	3.47E-04	1.58	1.118
2)*	4.55E-04	1.56	1.129	1.14E-04	1.60	1.129
3)*	4.80E+08	1.58	1.097	1.16E+08	1.65	1.087
4)*	2.73E-04	1.61		6.48E-05	1.71	
5)*	3.54E+17	1.63	1.084	8.25E+16	1.71	1.070

1)*: Nuclaer heating rate on the coil case (w/cm^3)
2)*: Nuclaer heating rate on the winding pack (w/cm^3)
3)*: Absorbed dose rate in the insulator (rad)
4)*: Neutron damage in the stbilizer copper (dpa)
5)*: Fast (> 0.1 MeV) neutron fluence in the winding pack ($n/cm^2/s$)

Error*: Maximum values of the ratio between the nuclear properties obtained by the analytically using Eq. (3.19) to those by the Monte Carlo calculation.

Table 3.11 (b) The values of C_s and D_s in the analytical representation (3.19) on the nuclear properties such as the nuclear heating density and the radiation damage in the TF coil surface along the slit as an exponential function of the slit width. The blanket and the vacuum vessel shield compositions are 80 % SS/20 % water and 60 % SS/40 % water, respectively. The slit width is 1 to 8 cm.

Vacuum vessel thickness (cm)	40		
Blanket thickness: 45 cm	C_s	D_s	Error*
1)*	3.27E-04	1.24	1.134
2)*	1.07E-04	1.24	1.140
3)*	1.12E+08	1.26	1.144
4)*	6.76E-05	1.24	1.155
5)*	8.96E+16	1.26	1.178

Vacuum vessel thickness (cm)	40		
Blanket thickness: 50 cm	C_s	D_s	Error*
1)*	2.03E-04	1.36	1.141
2)*	6.51E-05	1.37	1.162
3)*	7.08E+07	1.39	1.109
4)*	3.92E-05	1.43	1.129
5)*	5.03E+16	1.44	1.144

Vacuum vessel thickness (cm)	40		
Blanket thickness: 60 cm	C_s	D_s	Error*
1)*	9.39E-05	1.65	1.110
2)*	2.86E-05	1.68	1.122
3)*	2.97E+07	1.72	1.066
4)*	1.77E-05	1.74	1.103
5)*	2.34E+16	1.73	1.109

1)*: Nuclaer heating rate on the coil case (w/cm^3)
2)*: Nuclaer heating rate on the winding pack (w/cm^3)
3)*: Absorbed dose rate in the insulator (rad)
4)*: Neutron damage in the stbilizer copper (dpa)
5)*: Fast (> 0.1 MeV) neutron fluence in the winding pack ($n/cm^2/s$)

Error*: Maximum values of the ratio between the nuclear properties obtained by the analytically using Eq. (3.19) to those by the Monte Carlo calculation.

Table 3.12 (a) The values of C_b and D_b in the analytical representation Eq. (3.20) on the nuclear properties such as the nuclear heating density and the radiation damage in the TF coil surface along the slit as an exponential function of the blanket thickness, and the required blanket thickness $T_{c/b}$ to reduce the nuclear properties by one order of magnitude. The blanket thickness is 30 - 60 cm. The blanket and the vacuum vessel shield compositions are 80 % SS/20 % water and 60 % SS/40 % water, respectively.

Slit width	1 cm			2 cm			3 cm		
	C_b	D_b (cm^{-1})	$T_{c/b}$ (cm)	C_b	D_b (cm^{-1})	$T_{c/b}$ (cm)	C_b	D_b (cm^{-1})	$T_{c/b}$ (cm)
Vacuum vessel:		20cm							
1)*	7.86E-01	0.105	22.0	5.01E-01	0.085	27.2	4.07E-01	0.071	32.4
2)*	3.08E-01	0.108	21.4	1.91E-01	0.086	26.8	1.44E-01	0.070	32.9
3)*	2.87E+11	0.106	21.7	1.69E+11	0.082	28.0	1.32E+11	0.067	34.3
4)*	1.49E-01	0.105	21.9	8.38E-02	0.079	29.1	6.65E-02	0.064	36.1
5)*	2.77E+20	0.111	20.8	1.51E+20	0.085	27.2	1.17E+20	0.069	33.4
Vacuum vessel:		30cm							
1)*	2.20E-01	0.107	21.5	1.20E-01	0.082	28.2	9.52E-02	0.067	34.2
2)*	5.89E-02	0.104	22.1	3.43E-02	0.079	29.0	3.02E-02	0.067	34.5
3)*	5.78E+10	0.103	22.3	3.50E+10	0.078	29.3	2.91E+10	0.065	35.6
4)*	3.26E-02	0.104	22.2	1.79E-02	0.076	30.4	1.56E-02	0.062	36.9
5)*	5.44E+19	0.108	21.3	2.98E+19	0.080	28.7	2.51E+19	0.066	34.7
Vacuum vessel:		40cm							
1)*	5.44E-02	0.106	21.7	3.10E-02	0.080	28.8	2.69E-02	0.067	34.4
2)*	1.50E-02	0.104	22.1	8.54E-03	0.077	29.9	8.24E-03	0.066	34.7
3)*	1.73E+10	0.106	21.6	8.43E+09	0.076	30.5	7.67E+09	0.063	36.5
4)*	8.89E-03	0.104	22.2	4.41E-03	0.073	31.7	4.26E-03	0.062	37.2
5)*	1.29E+19	0.105	22.0	7.10E+18	0.077	29.8	6.02E+18	0.063	36.4

1)*: Nuclaer heating rate on the coil case (w/cm^3)
2)*: Nuclaer heating rate on the winding pack (w/cm^3)
3)*: Absorbed dose rate in the insulator (rad)
4)*: Neutron damage in the stbilizer copper (dpa)
5)*: Fast (> 0.1 MeV) neutron fluence in the winding pack ($n/cm^2/s$)

Error*: Maximum values of the ratio between the nuclear properties obtained by the analytically using Eq. (3.20) to those by the Monte Carlo calculation.

Table 3.12 (b) The values of C_b and D_b in the analytical representation Eq. (3.20) on the nuclear properties such as the nuclear heating density and the radiation damage in the TF coil surface along the slit as an exponential function of the blanket thickness, and the required blanket thickness $T_{c/b}$ to reduce the nuclear properties by one order of magnitude. The blanket thickness is 30 - 60 cm. The blanket and the vacuum vessel shield compositions are 80 % SS/20 % water and 60 % SS/40 % water, respectively.

Slit width	4 cm			8 cm		
	C_b	D_b (cm^{-1})	$T_{c/b}$ (cm)	C_b	D_b (cm^{-1})	$T_{c/b}$ (cm)
Vacuum vessel: 20 cm						
1)*	3.51E-01	0.060	38.3	3.48E-01	0.040	57.8
2)*	1.29E-01	0.060	38.5	1.34E-01	0.040	58.2
3)*	1.23E+11	0.058	39.9	1.33E+11	0.038	60.4
4)*	6.43E-02	0.055	41.6	7.31E-02	0.037	63.1
5)*	1.07E+20	0.059	38.9	1.17E+20	0.040	58.1
Vacuum vessel: 30 cm						
1)*	8.51E-02	0.056	41.0	9.90E-02	0.039	59.4
2)*	2.59E-02	0.055	42.0	3.32E-02	0.038	60.1
3)*	2.60E+10	0.053	43.2	3.33E+10	0.037	62.9
4)*	1.46E-02	0.052	44.1	1.85E-02	0.035	66.1
5)*	2.23E+19	0.055	41.6	2.79E+19	0.038	61.4
Vacuum vessel: 40 cm						
1)*	2.27E-02	0.055	42.0	2.59E-02	0.035	65.1
2)*	6.67E-03	0.053	43.5	8.20E-03	0.035	65.8
3)*	6.83E+09	0.051	44.7	8.42E+09	0.034	67.9
4)*	3.83E-03	0.050	45.9	4.80E-03	0.033	70.3
5)*	5.08E+18	0.050	45.9	6.97E+18	0.035	66.7

1)*: Nuclaer heating rate on the coil case (w/cm^3)
2)*: Nuclaer heating rate on the winding pack (w/cm^3)
3)*: Absorbed dose rate in the insulator (rad)
4)*: Neutron damage in the stbilizer copper (dpa)
5)*: Fast (> 0.1 MeV) neutron fluence in the winding pack ($n/cm^2/s$)

Error*: Maximum values of the ratio between the nuclear properties obtained by the analytically using Eq. (3.20) to those by the Monte Carlo calculation.

Table 3.13 (a) The values of C_v and D_v in the analytical representation Eq. (3.22) on the nuclear properties such as the nuclear heating density and the radiation damage in the TF coil surface along the slit as an exponential function of the vacuum vessel thickness, and the required vacuum vessel thickness T_v to reduce the nuclear properties by one order of magnitude. The vacuum vessel thickness is 20 - 40 cm. The blanket and the vacuum vessel shield compositions are 80 % SS/20 % water and 60 % SS/40 % water, respectively.

Blanket: 30 cm									
Slit width	1 cm			2 cm			3 cm		
	C_v	D_v (cm^{-1})	T_v (cm)	C_v	D_v (cm^{-1})	T_v (cm)	C_v	D_v (cm^{-1})	T_v (cm)
1)*	0.53459	0.134	17.2	0.59153	0.132	17.5	0.66945	0.129	17.8
2)*	0.23535	0.146	15.8	0.27296	0.144	16.0	0.29688	0.139	16.6
3)*	2.08E+11	0.142	16.3	2.56E+11	0.141	16.4	2.90E+11	0.137	16.8
4)*	0.11094	0.141	16.3	0.12909	0.137	16.8	0.16027	0.136	16.9
5)*	1.85E+20	0.145	15.9	2.12E+20	0.141	16.3	2.71E+20	0.142	16.2
Blanket: 45 cm									
1)*	0.098083	0.139	16.5	0.1255	0.129	17.9	0.19023	0.128	18.0
2)*	0.03613	0.144	16.0	0.045702	0.132	17.4	0.073319	0.132	17.4
3)*	3.44E+10	0.14	16.4	4.93E+10	0.133	17.3	7.34E+10	0.131	17.6
4)*	0.016757	0.135	17.0	0.028277	0.133	17.3	0.041314	0.129	17.8
5)*	2.81E+19	0.141	16.4	4.24E+19	0.136	16.9	5.95E+19	0.131	17.5
Blanket: 60 cm									
1)*	0.023513	0.136	16.9	0.040803	0.125	18.5	0.07165	0.123	18.7
2)*	0.008506	0.14	16.4	0.016291	0.13	17.7	0.033097	0.133	17.3
3)*	9.00E+09	0.142	16.2	1.79E+10	0.131	17.6	3.44E+10	0.131	17.6
4)*	0.00462	0.139	16.5	0.009914	0.128	18.0	0.022433	0.134	17.2
5)*	5.67E+18	0.137	16.9	1.34E+19	0.13	17.7	2.87E+19	0.133	17.3

1)*: Nuclaer heating rate on the coil case (w/cm^3)
2)*: Nuclaer heating rate on the winding pack (w/cm^3)
3)*: Absorbed dose rate in the insulator (rad)
4)*: Neutron damage in the stbilizer copper (dpa)
5)*: Fast (> 0.1 MeV) neutron fluence in the winding pack ($n/cm^2/s$)

Error*: Maximum values of the ratio between the nuclear properties obtained by the analytically using Eq. (3.22) to those by the Monte Carlo calculation.

Table 3.13 (b) The values of C_v and D_v in the analytical representation Eq. (3.22) on the nuclear properties such as the nuclear heating density and the radiation damage in the TF coil surface along the slit as an exponential function of the vacuum vessel thickness, and the required vacuum vessel thickness T_v to reduce the nuclear properties by one order of magnitude. The vacuum vessel thickness is 20 - 40 cm. The blanket and the vacuum vessel shield compositions are 80 % SS/20 % water and 60 % SS/40 % water, respectively.

Blanket: 30 cm						
Slit width	4 cm			8 cm		
	C_v	D_v (cm^{-1})	T_v (cm)	C_v	D_v (cm^{-1})	T_v (cm)
1)*	0.81888	0.129	17.8	1.2604	0.123	18.8
2)*	0.34986	0.138	16.7	0.59723	0.133	17.3
3)*	3.41E+11	0.136	17.0	6.01E+11	0.132	17.5
4)*	0.18294	0.133	17.3	0.33296	0.13	17.8
5)*	3.12E+20	0.14	16.5	5.20E+20	0.133	17.3
Blanket: 45 cm						
1)*	0.24986	0.124	18.5	0.61276	0.121	19.1
2)*	0.1057	0.132	17.5	0.27642	0.129	17.8
3)*	1.08E+11	0.13	17.7	2.89E+11	0.128	18.0
4)*	0.06025	0.128	18.0	0.17761	0.129	17.8
5)*	8.68E+19	0.131	17.6	2.49E+20	0.13	17.7
Blanket: 60 cm						
1)*	0.11704	0.122	19.0	0.32977	0.116	19.8
2)*	0.048052	0.128	18.0	0.15728	0.126	18.3
3)*	5.08E+10	0.126	18.2	1.68E+11	0.125	18.4
4)*	0.029786	0.125	18.3	0.099323	0.124	18.6
5)*	4.00E+19	0.126	18.2	1.35E+20	0.126	18.3

1)*: Nuclaer heating rate on the coil case (w/cm^3)
2)*: Nuclaer heating rate on the winding pack (w/cm^3)
3)*: Absorbed dose rate in the insulator (rad)
4)*: Neutron damage in the stbilizer copper (dpa)
5)*: Fast (> 0.1 MeV) neutron fluence in the winding pack ($n/cm^2/s$)

Error*: Maximum values of the ratio between the nuclear properties obtained by the analytically using Eq. (3.22) to those by the Monte Carlo calculation.

Table 3.14 (a) The values of $C_{b/v}$, $C'_{b/v}$, $D_{b/v}$ and $T_{b/v}$ in the analytical representation (3.24) on the nuclear heating density and the radiation damage in the TF coil surface along the slit as functions of the blanket thickness and the vacuum vessel thickness. The blanket and the vacuum vessel shield composition are 80 % SS/20 % water and 60 % SS/40 % water, respectively. The slit width is 1 to 8 cm.

Slit width (cm)	1			
	$C_{b/v}$	$C'_{b/v}$ (cm^{-1})	$D_{b/v}$ (cm^{-1})	$T_{b/v}$ (cm)
1)*	1.16E+01	0.134	0.106	21.7
2)*	6.06E+00	0.151	0.105	21.9
3)*	4.46E+12	0.140	0.105	21.9
4)*	2.41E+00	0.141	0.104	22.1
5)*	5.76E+21	0.153	0.108	21.4

Slit width (cm)	2			
	$C_{blt/vv}$	$C'_{blt/vv}$ (cm^{-1})	$D_{blt/vv}$ (cm^{-1})	$T_{blt/vv}$ (cm)
1)*	7.99E+00	0.139	0.082	28.1
2)*	4.03E+00	0.155	0.081	28.5
3)*	3.30E+12	0.150	0.079	29.2
4)*	1.55E+00	0.147	0.076	30.4
5)*	3.11E+21	0.153	0.081	28.5

Slit width (cm)	3			
	$C_{blt/vv}$	$C'_{blt/vv}$ (cm^{-1})	$D_{blt/vv}$ (cm^{-1})	$T_{blt/vv}$ (cm)
1)*	5.97E+00	0.136	0.068	33.6
2)*	2.41E+00	0.143	0.068	34.0
3)*	2.21E+12	0.142	0.065	35.5
4)*	1.01E+00	0.137	0.063	36.7
5)*	2.23E+21	0.148	0.066	34.8

1)*: Nuclaer heating rate on the coil case (w/cm^3)
2)*: Nuclaer heating rate on the winding pack (w/cm^3)
3)*: Absorbed dose rate in the insulator (rad)
4)*: Neutron damage in the stbilizer copper (dpa)
5)*: Fast (> 0.1 MeV) neutron fluence in the winding pack ($n/cm^2/s$)

Table 3.14 (b) The values of $C_{b/v}$, $C'_{b/v}$, $D_{b/v}$ and $T_{b/v}$ in the analytical representation (3.24) on the nuclear heating density and the radiation damage in the TF coil surface along the slit as functions of the blanket thickness and the vacuum vessel thickness. The blanket and the vacuum vessel shield composition are 80 % SS/20 % water and 60 % SS/40 % water, respectively. The slit width is 1 to 8 cm.

Slit width (cm)	4			
	$C_{b/v}$	$C'_{b/v}$ (cm^{-1})	$D_{b/v}$ (cm^{-1})	$T_{b/v}$ (cm)
1)*	5.33E+00	0.137	0.057	40.4
2)*	2.38E+00	0.148	0.056	41.2
3)*	2.14E+12	0.145	0.054	42.5
4)*	1.05E+00	0.141	0.053	43.8
5)*	2.22E+21	0.152	0.055	42.0

Slit width (cm)	8			
	$C_{b/v}$	$C'_{bl/v}$ (cm^{-1})	$D_{b/v}$ (cm^{-1})	$T_{b/v}$ (cm)
1)*	4.74E+00	0.130	0.038	60.6
2)*	2.19E+00	0.140	0.038	61.2
3)*	2.10E+12	0.138	0.036	63.6
4)*	1.11E+00	0.136	0.035	66.3
5)*	1.95E+21	0.141	0.037	61.9

1)*: Nuclaer heating rate on the coil case (w/cm^3)
2)*: Nuclaer heating rate on the winding pack (w/cm^3)
3)*: Absorbed dose rate in the insulator (rad)
4)*: Neutron damage in the stbilizer copper (dpa)
5)*: Fast (> 0.1 MeV) neutron fluence in the winding pack ($n/cm^2/s$)

Table 3.15 The values of C's, C'b, D's and D'b in the analytical representations Eq. (3.28) on the nuclear heating density and the radiation damage in the TF coil surface along the slit as functions of the slit width and the blanket thickness. The blanket and the vacuum vessel shield compositions are 80 % SS/20 % water and 60 % SS/40 % water, respectively. The slit widths are 1 to 8 cm, and the blanket thicknesses are 30 to 45 cm.

Vacuum vessel thickness (cm)	20			
	C's	C'b (cm^{-1})	D's (cm^{-1})	D'b (cm^{-1})
1)*	1.21E+00	1.21E-01	3.88E-02	4.64E-02
2)*	4.48E-01	1.23E-01	4.43E-02	4.42E-02
3)*	4.08E+11	1.21E-01	4.87E-02	4.28E-02
4)*	2.03E-01	1.18E-01	5.39E-02	4.12E-02
5)*	3.44E+20	1.22E-01	5.58E-02	3.99E-02

Vacuum vessel thickness (cm)	30			
	C's	C'b (cm^{-1})	D's (cm^{-1})	D'b (cm^{-1})
1)*	2.80E-01	1.19E-01	4.93E-02	4.23E-02
2)*	8.68E-02	1.19E-01	5.84E-02	3.95E-02
3)*	7.95E+10	1.17E-01	6.50E-02	3.74E-02
4)*	4.03E-02	1.14E-01	7.08E-02	3.59E-02
5)*	6.56E+19	1.17E-01	6.59E-02	3.72E-02

Vacuum vessel thickness (cm)	40			
	C's	C'b (cm^{-1})	D's (cm^{-1})	D'b (cm^{-1})
1)*	8.41E-02	1.22E-01	5.19E-02	4.25E-02
2)*	1.83E-02	1.14E-01	6.82E-02	3.67E-02
3)*	1.95E+10	1.14E-01	6.71E-02	3.77E-02
4)*	9.07E-03	1.09E-01	7.81E-02	3.39E-02
5)*	1.44E+19	1.13E-01	6.92E-02	3.69E-02

1)*: Nuclaer heating rate on the coil case (w/cm^3)
2)*: Nuclaer heating rate on the winding pack (w/cm^3)
3)*: Absorbed dose rate in the insulator (rad)
4)*: Neutron damage in the stbilizer copper (dpa)
5)*: Fast (> 0.1 MeV) neutron fluence in the winding pack ($n/cm^2/s$)

Table 3.16 The values of C'_s, C'_b, D'_s and D'_b in the analytical representations Eq. (3.29) on the nuclear heating density and the radiation damage in the TF coil surface along the slit as functions of the slit width and the blanket thickness. The blanket and the vacuum vessel shield compositions are 80 % SS/20 % water and 60 % SS/40 % water, respectively. The slit widths are 1 to 8 cm, and the blanket thicknesses are 30 to 45 cm.

Vacuum vessel thickness (cm)	20			
	C'_s	C'_b (cm^{-1})	D'_s (cm^{-1})	D'_b (cm^{-1})
1)*	2.50E-01	8.70E-02	4.14E-01	2.11E-02
2)*	9.72E-02	8.97E-02	4.20E-01	2.19E-02
3)*	8.72E+10	8.70E-02	4.43E-01	2.13E-02
4)*	4.36E-02	8.48E-02	4.73E-01	2.06E-02
5)*	9.43E+19	9.34E-02	4.13E-01	2.29E-02

Vacuum vessel thickness (cm)	30			
	C'_s	C'_b (cm^{-1})	D'_s (cm^{-1})	D'_b (cm^{-1})
1)*	6.72E-02	8.81E-02	4.40E-01	2.13E-02
2)*	1.35E-02	8.00E-02	5.44E-01	1.80E-02
3)*	1.64E+10	8.29E-02	5.03E-01	1.99E-02
4)*	9.55E-03	8.36E-02	5.13E-01	2.02E-02
5)*	1.83E+19	9.04E-02	4.62E-01	2.19E-02

Vacuum vessel thickness (cm)	40			
	C'_s	C'_b (cm^{-1})	D'_s (cm^{-1})	D'_b (cm^{-1})
1)*	1.30E-02	8.24E-02	5.31E-01	1.89E-02
2)*	5.27E-03	8.71E-02	5.01E-01	2.02E-02
3)*	5.90E+09	8.83E-02	4.92E-01	2.09E-02
4)*	3.39E-03	8.79E-02	4.73E-01	2.18E-02
5)*	4.38E+18	8.77E-02	4.94E-01	2.10E-02

1)*: Nuclaer heating rate on the coil case (w/cm^3)
2)*: Nuclaer heating rate on the winding pack (w/cm^3)
3)*: Absorbed dose rate in the insulator (rad)
4)*: Neutron damage in the stbilizer copper (dpa)
5)*: Fast (> 0.1 MeV) neutron fluence in the winding pack ($n/cm^2/s$)

Table 3.17 The values of $C'_{s/v}$, $C''_{s/v}$, $C'_{b/v}$, $D'_{s/v}$ and $D'_{b/v}$ in the analytical representations Eqs. (3.36) and (3.37) on the nuclear heating density and the radiation damage in the TF coil surface along the slit as functions of the slit width, the blanket thickness and the vacuum vessel thickness. The blanket and the vacuum vessel shield compositions are 80 % SS/20 % water and60 % SS/40 % water, respectively. The slit widths are 1 to 8 cm, the blanket thicknesses are 30 to 60 cm and the vacuum vessel thicknesses are 20 to 40 cm.

Blanket thickness (cm)	30 - 45				
	$C'_{s/v}$	$C''_{s/v}$ (cm^{-1})	$C'_{b/v}$ (cm^{-1})	$D'_{s/v}$ (cm^{-1})	$D'_{b/v}$ (cm^{-1})
1)*	1.67E+01	1.33E-01	1.21E-01	4.67E-02	4.37E-02
2)*	1.08E+01	1.60E-01	1.19E-01	5.70E-02	4.02E-02
3)*	8.22E+12	1.52E-01	1.17E-01	6.03E-02	3.93E-02
4)*	4.45E+00	1.55E-01	1.14E-01	6.76E-02	3.70E-02
5)*	8.03E+21	1.59E-01	1.17E-01	6.36E-02	3.80E-02

Blanket thickness (cm)	45 - 60				
	$C'_{s/v}$	$C''_{s/v}$ (cm^{-1})	$C'_{b/v}$ (cm^{-1})	$D'_{s/v}$ (cm^{-1})	$D'_{b/v}$ (cm^{-1})
1)*	5.10E+00	1.48E-01	8.58E-02	4.62E-01	2.04E-02
2)*	1.51E+00	1.46E-01	8.56E-02	4.88E-01	2.01E-02
3)*	1.16E+12	1.35E-01	8.60E-02	4.79E-01	2.07E-02
4)*	5.17E-01	1.28E-01	8.55E-02	4.86E-01	2.08E-02
5)*	1.96E+21	1.53E-01	9.05E-02	4.56E-01	2.19E-02

1)*: Nuclaer heating rate on the coil case (w/cm^3)
2)*: Nuclaer heating rate on the winding pack (w/cm^3)
3)*: Absorbed dose rate in the insulator (rad)
4)*: Neutron damage in the stbilizer copper (dpa)
5)*: Fast (> 0.1 MeV) neutron fluence in the winding pack ($n/cm^2/s$)

This is a blank page.

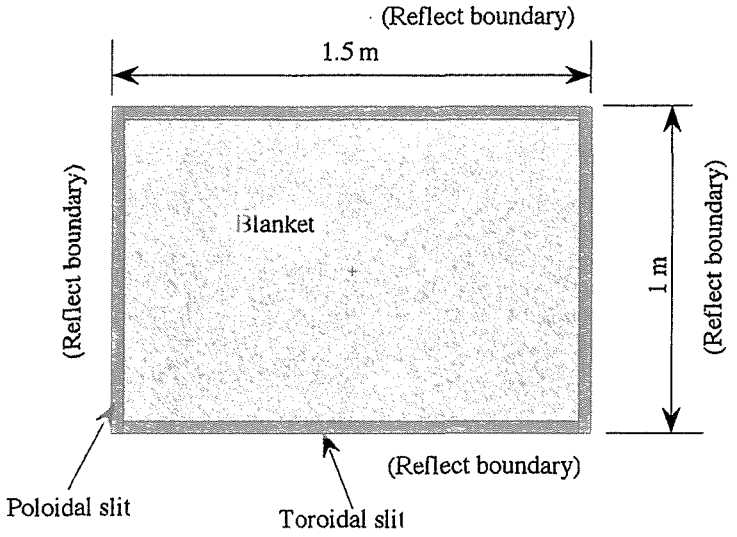

Vertical view (A-A cross section in horizontal view)

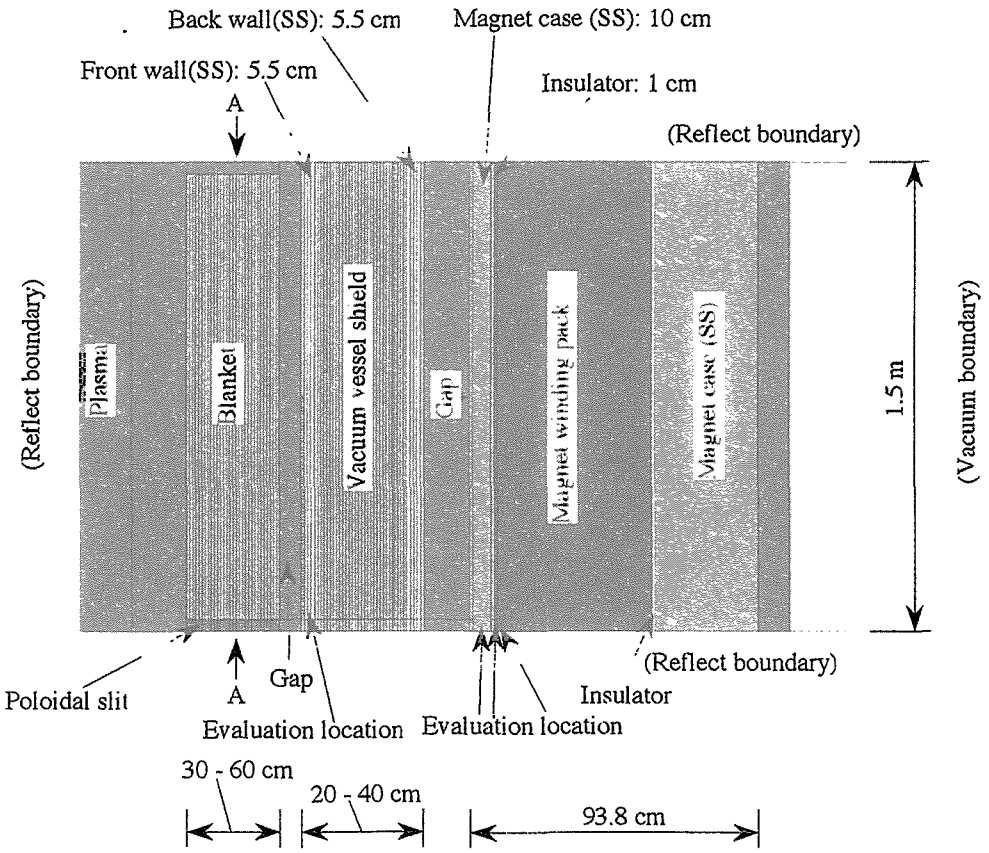

Horizontal view

Fig. 3.1 Three-dimensional Monte Carlo calculation model used in the study about the streaming through slit between blanket module.

This is a blank page.

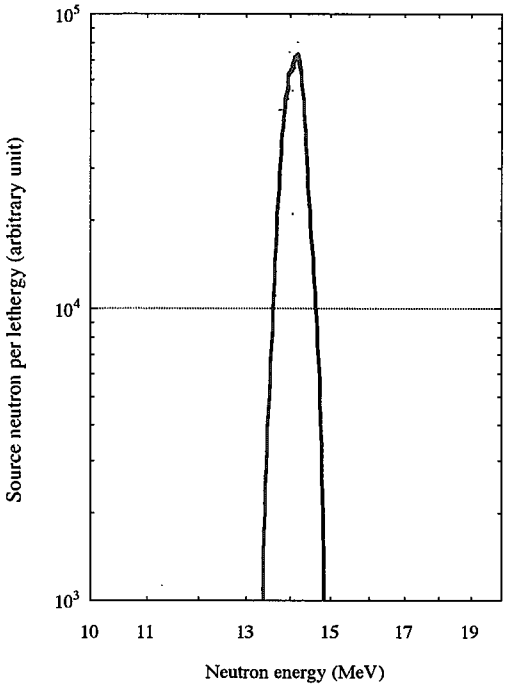

Fig. 3.2 Spectrum of source neutrons having a Muir velocity Gaussian fusion energy spectrum used in the present study.

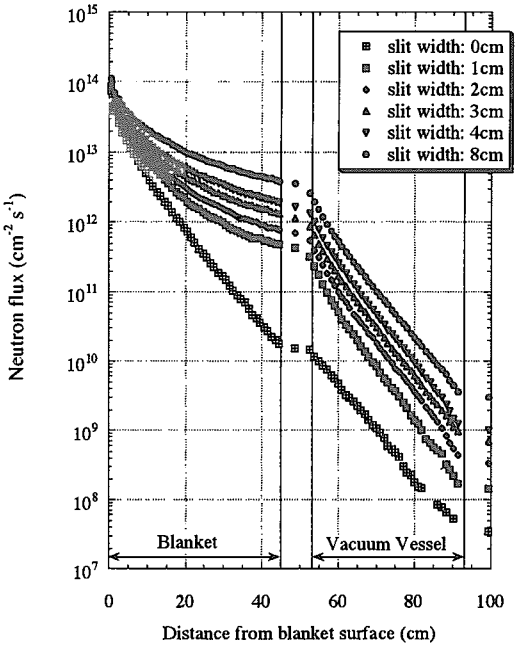

Fig. 3.3 Distributions of the 14 MeV neutron flux along the slit between the blanket modules under the neutron wall loading of 1 MW/m^2, the blanket thickness of 45 cm, the blanket composition of 80 % SS and 20 % water, the vacuum vessel thickness of 40 cm, and the vacuum vessel shield composition of 60 % SS and 40 % water.

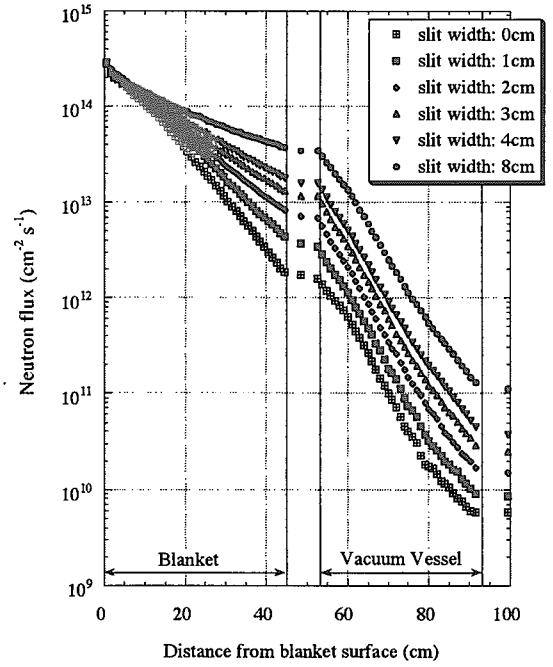

Fig. 3.4 Distributions of the energy-integrated total neutron flux along the slit between the blanket modules under the neutron wall loading of 1 MW/m^2, the blanket thickness of 45 cm, the blanket composition of 80 % SS and 20 % water, the vacuum vessel thickness of 40 cm, and the vacuum vessel shield composition of 60 % SS and 40 % water.

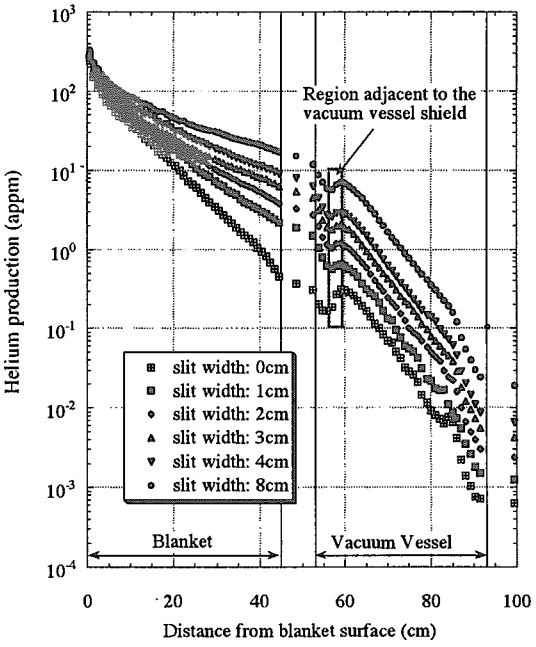

Fig. 3.5 Distributions of the helium production along the slit between the blanket modules. The integrated neutron wall loading is 1 MWa/m^2, the blanket thickness is 45 cm, the blanket composition is 80 % SS and 20 % water, the vacuum vessel thickness is 40 cm, the vacuum vessel shield composition is 60 % SS and 40 % water, and the boron content in SS is 20 wppm.

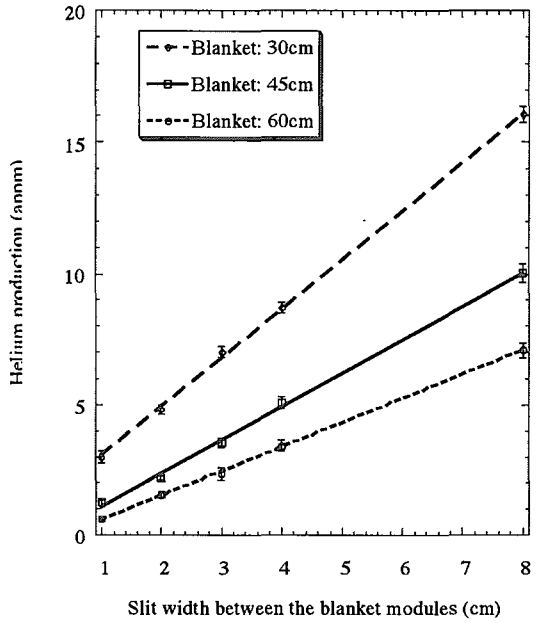

(a) Boron content in the vacuum vessel surface: 10 wppm.

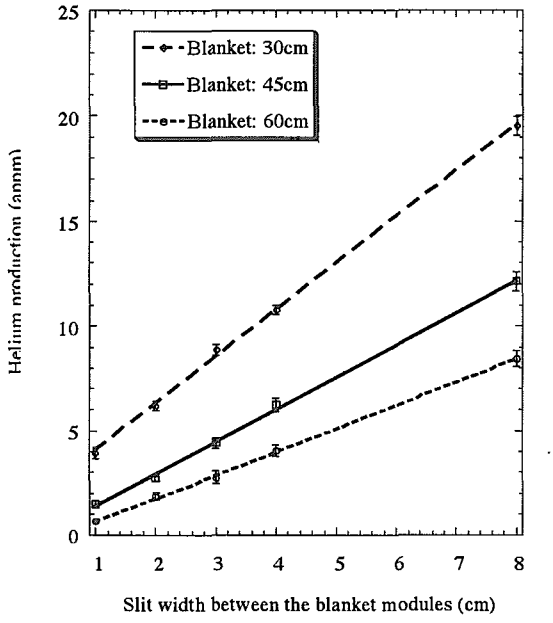

(b) Boron content in the vacuum vessel surface: 20 wppm.

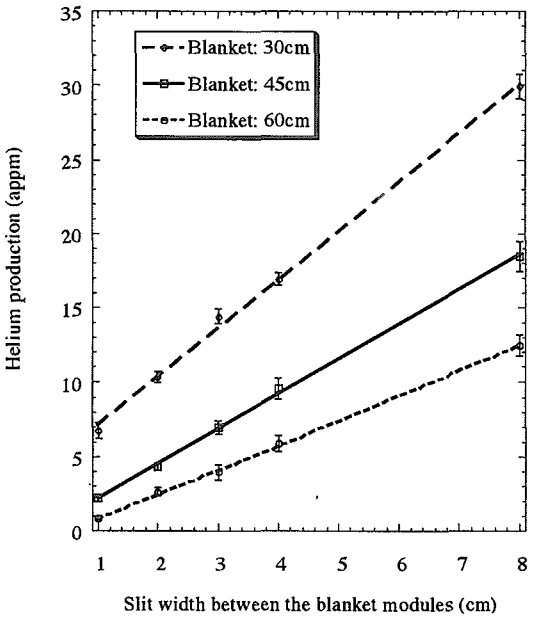

(c) Boron content in the vacuum vessel surface: 50 wppm.

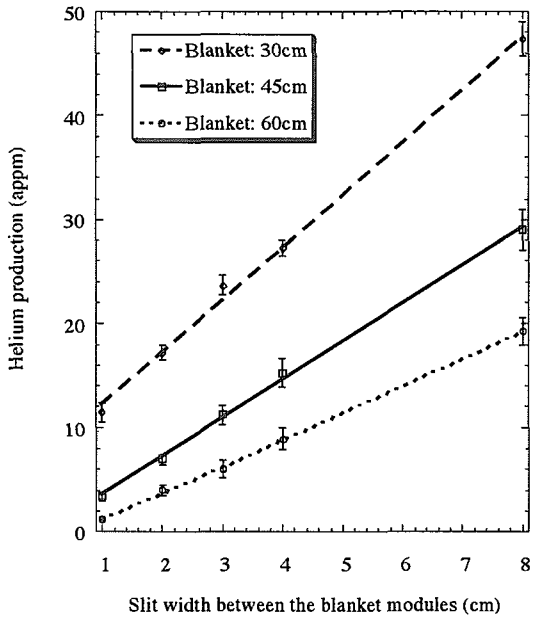

(d) Boron content in the vacuum vessel surface: 100 wppm.

Fig. 3.6 Dependencies of the helium productions on the slit width in the vacuum vessel front wall surface along the slit for the 10, 20, 50 and 100 wppm boron content of the vacuum vessel surface.

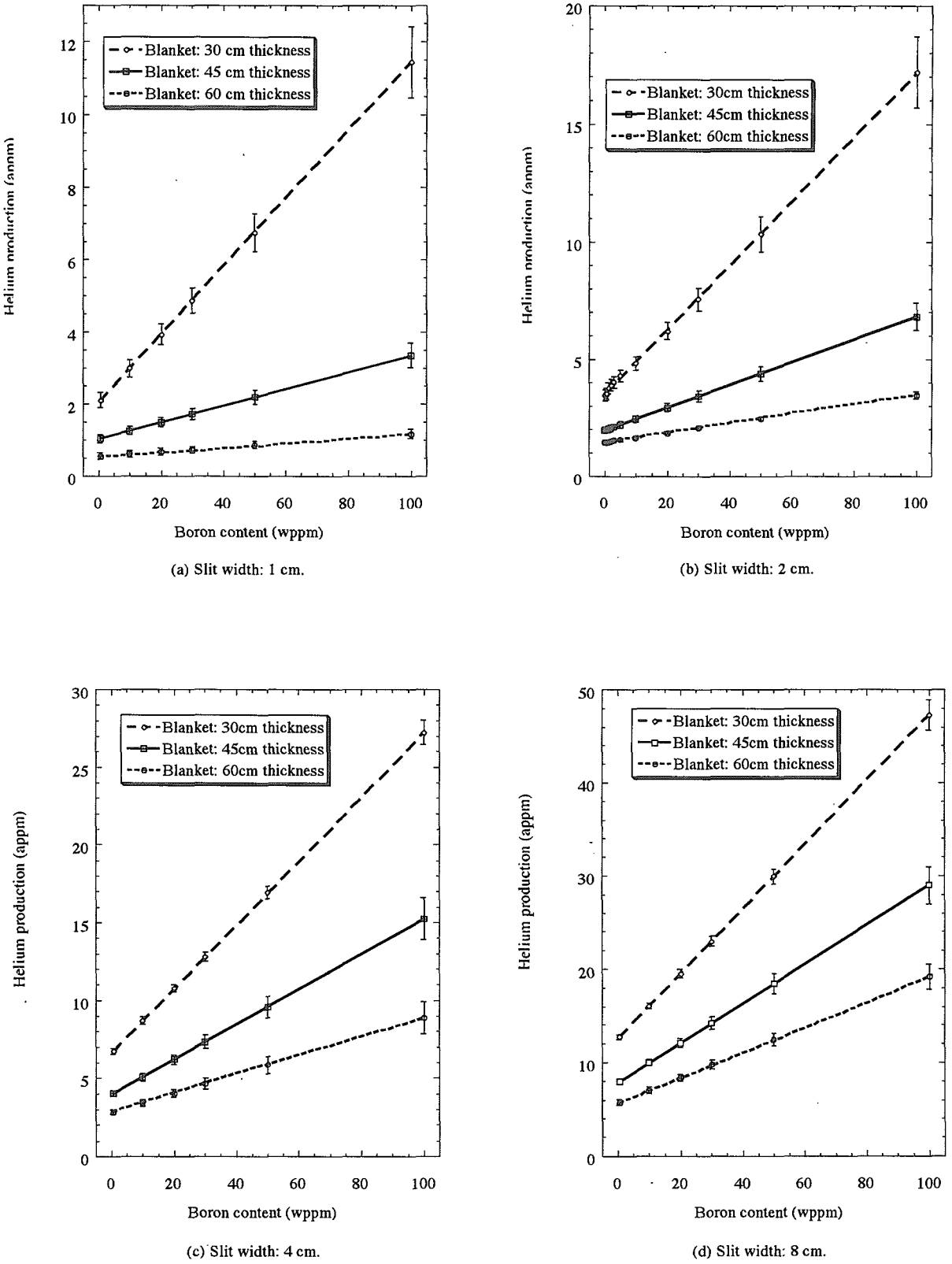

Fig. 3.7 Dependencies of the helium productions on the boron content for the 1, 2, 4 and 8 cm wide slits

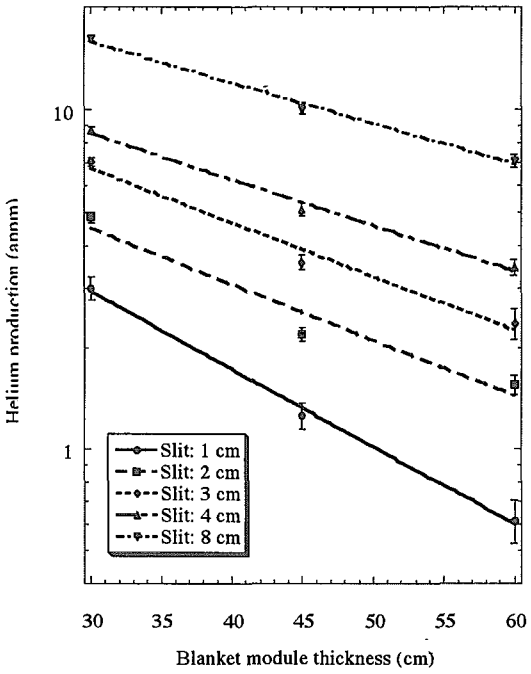

(a) Boron content in the vacuum vessel surface: 10 wppm.

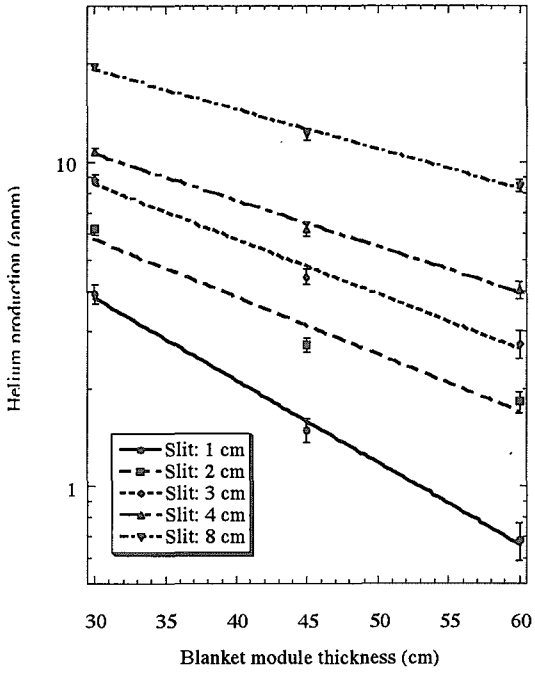

(b) Boron content in the vacuum vessel surface: 20 wppm.

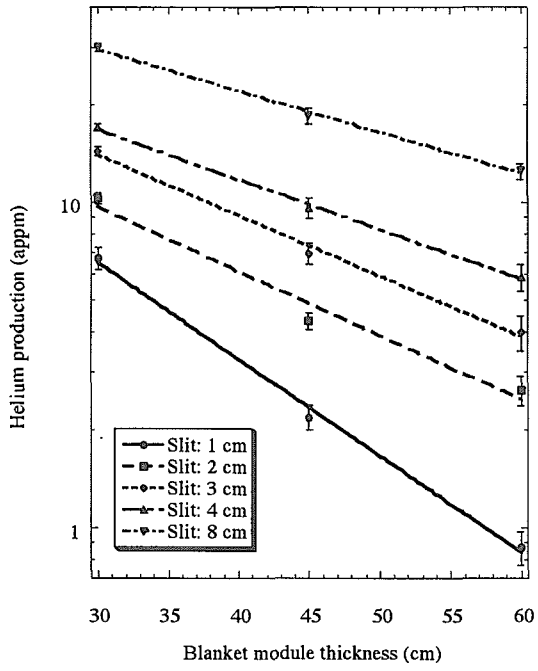

(c) Boron content in the vacuum vessel surface: 50 wppm.

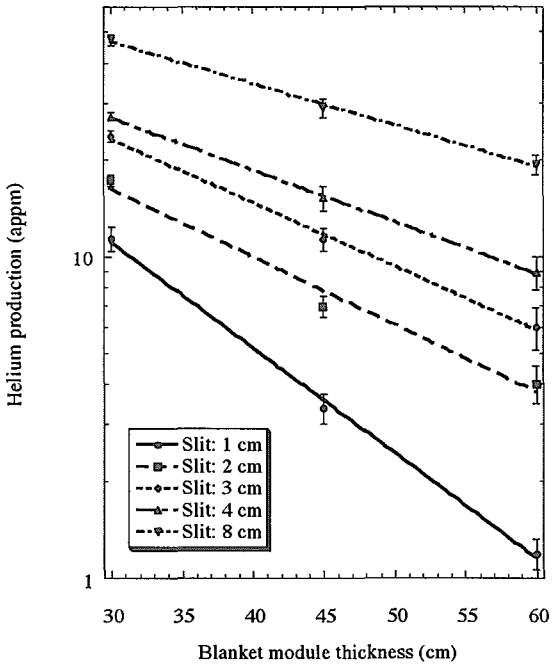

(d) Boron content in the vacuum vessel surface: 100 wppm.

Fig. 3.8 Dependencies of the helium productions on the blanket thickness in the vacuum vessel front wall surface along the slit for the 10, 20, 50 and 100 wppm boron content of the vacuum vessel surface.

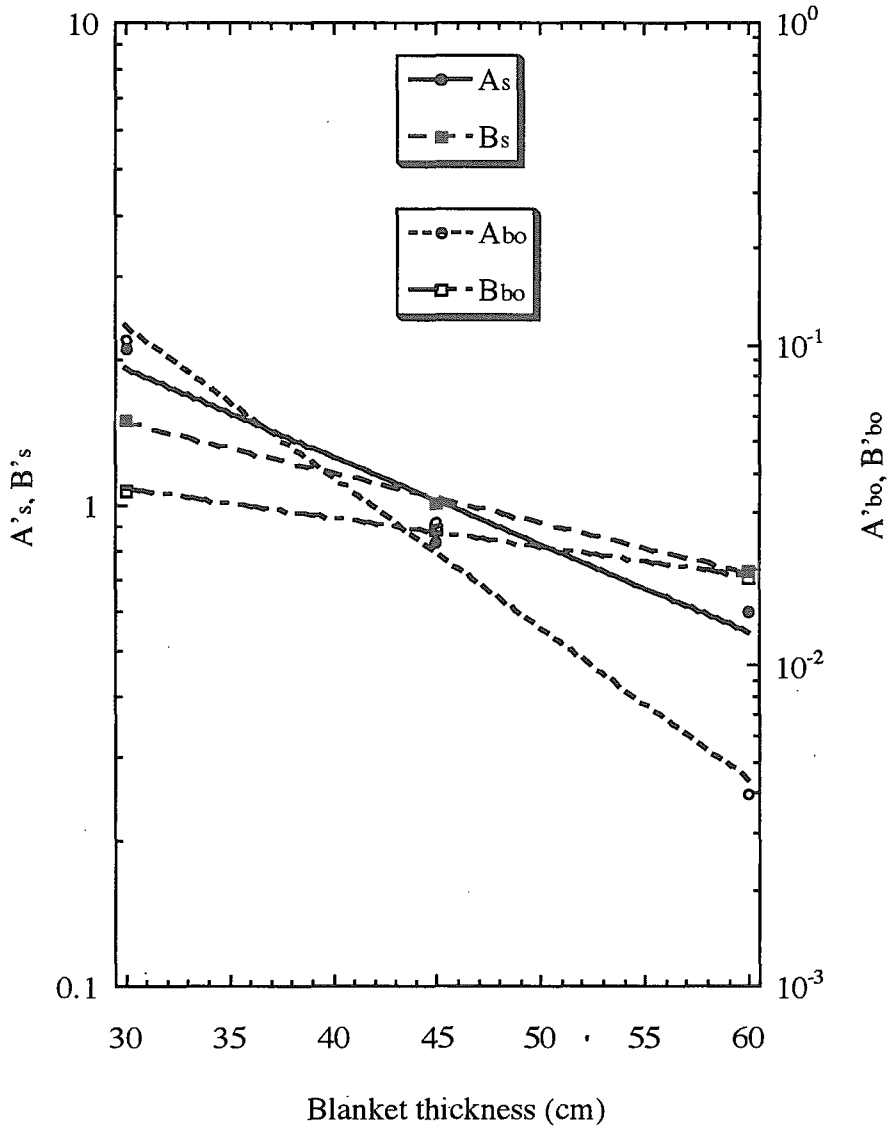

Fig. 3.9 Dependencies of the values of A's, A'bo, B's and B'bo on the blanket thickness

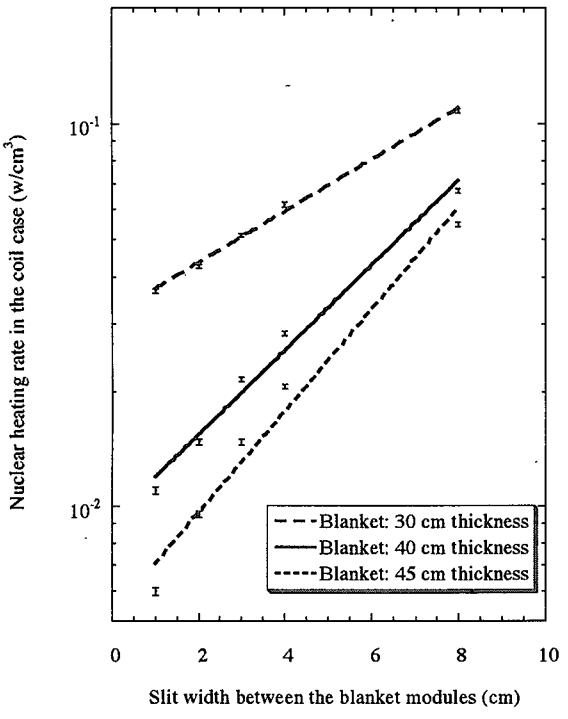

(a) Vacuum vessel thickness: 20 cm

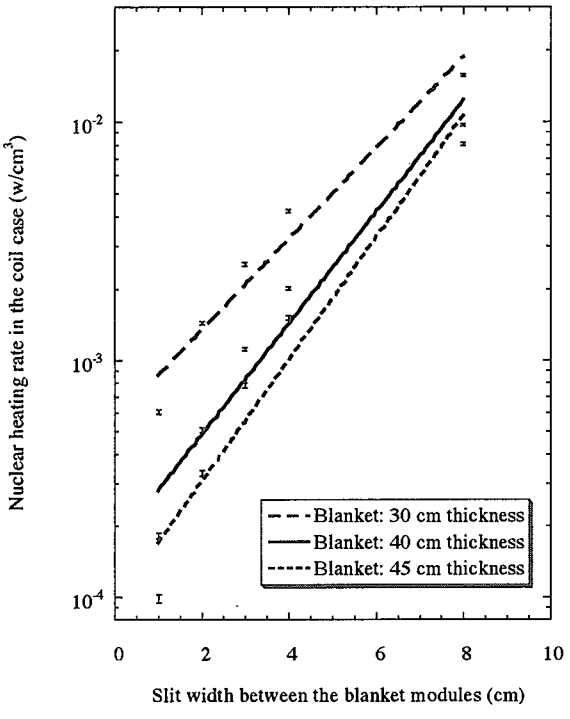

(b) Vacuum vessel thickness: 30 cm

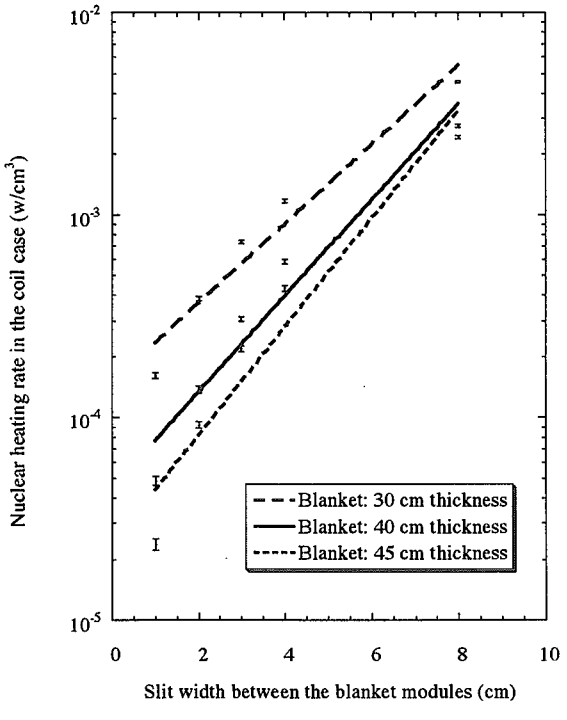

(c) Vacuum vessel thickness: 40 cm

Fig. 3.10 Dependency of nuclear heating rate in the TF coil case on the slit width adjacent blanket module. (Neutron wall load: 1MW/m^2, Blanket composition: SS/H_2O=80/20, Vacuum vessel shield composition: SS/H_2O=60/40)

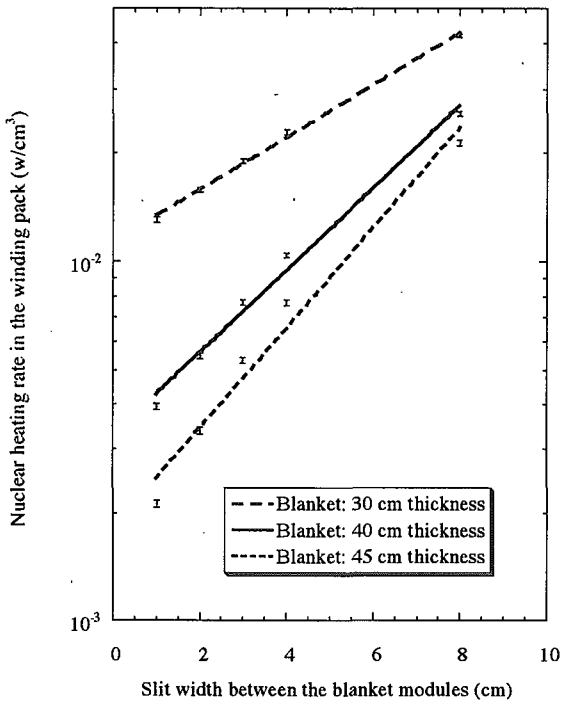

(a) Vacuum vessel thickness: 20 cm

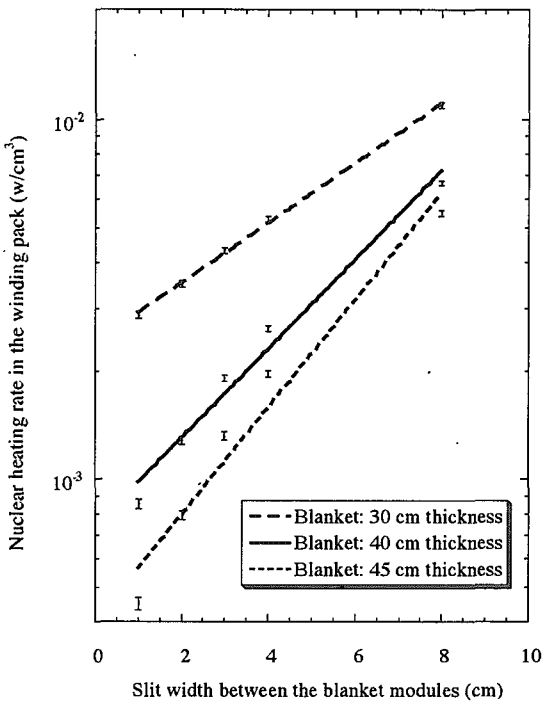

(b) Vacuum vessel thickness: 30 cm

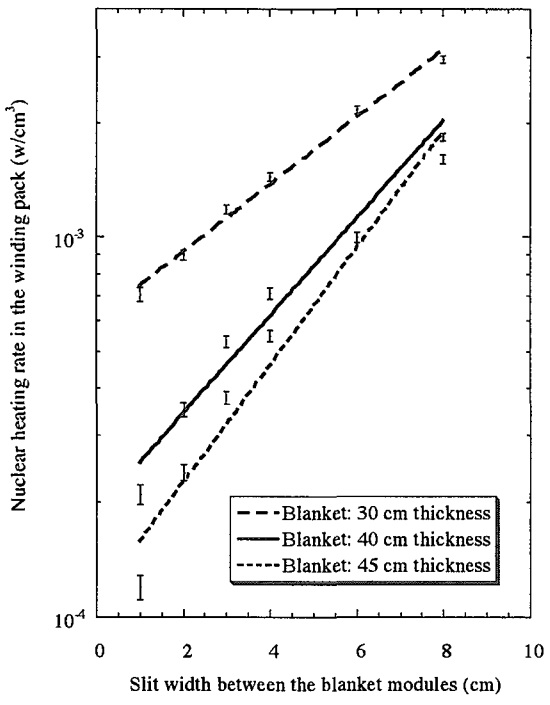

(c) Vacuum vessel thickness: 40 cm

Fig. 3.11 Dependency of nuclear heating rate in the TF coil winding pack on the slit width adjacent blanket module. (Neutron wall load: 1MW/m^2, Blanket composition: SS/H_2O=80/20, Vacuum vessel shield composition: SS/H_2O=60/40)

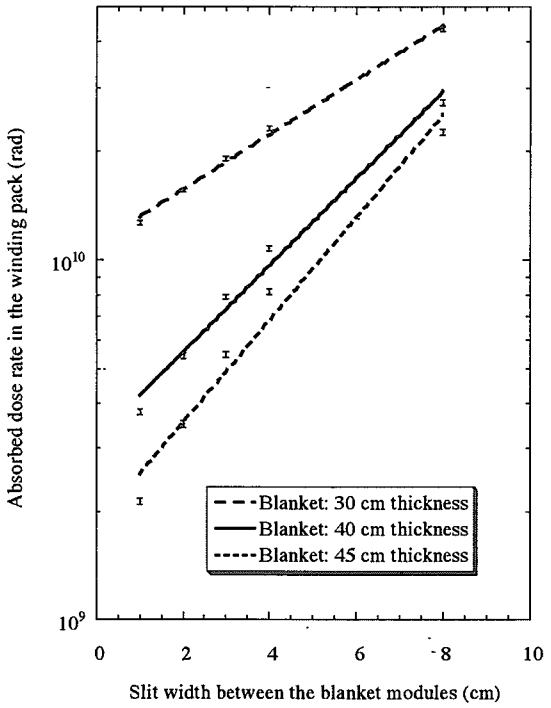

(a) Vacuum vessel thickness: 20 cm

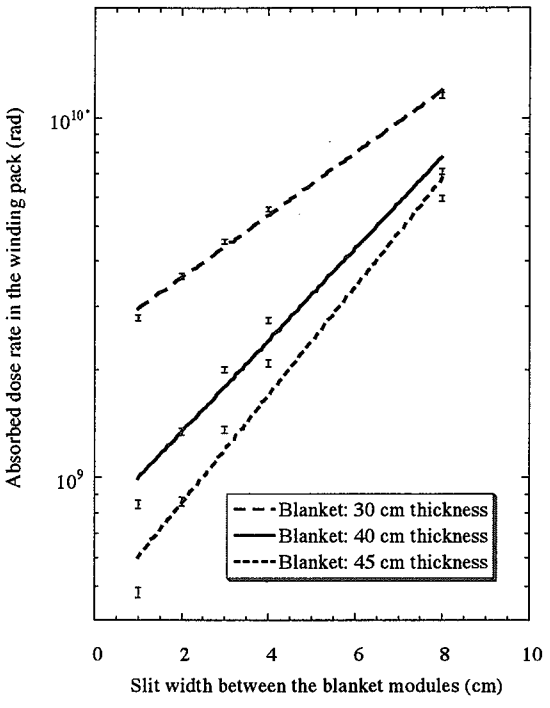

(b) Vacuum vessel thickness: 30 cm

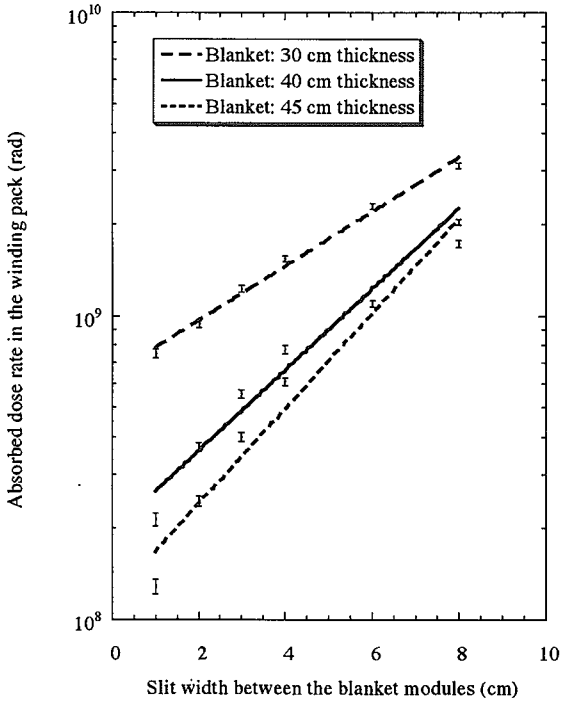

(c) Vacuum vessel thickness: 40 cm

Fig. 3.12 Dependency of absorbed dose rate in the TF coil winding pack on the slit width adjacent blanket module. (Neutron wall load: 1MW/m^2, Blanket composition: SS/H2O=80/20, Vacuum vessel shield composition: SS/H2O=60/40)

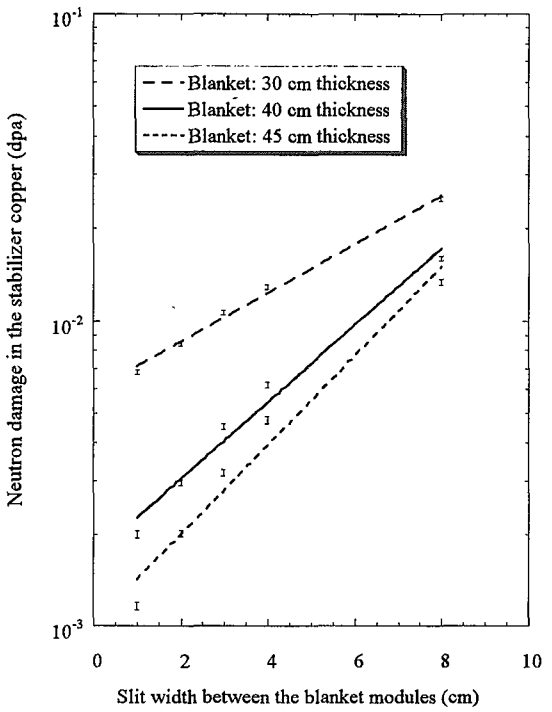

(a) Vacuum vessel thickness: 20 cm

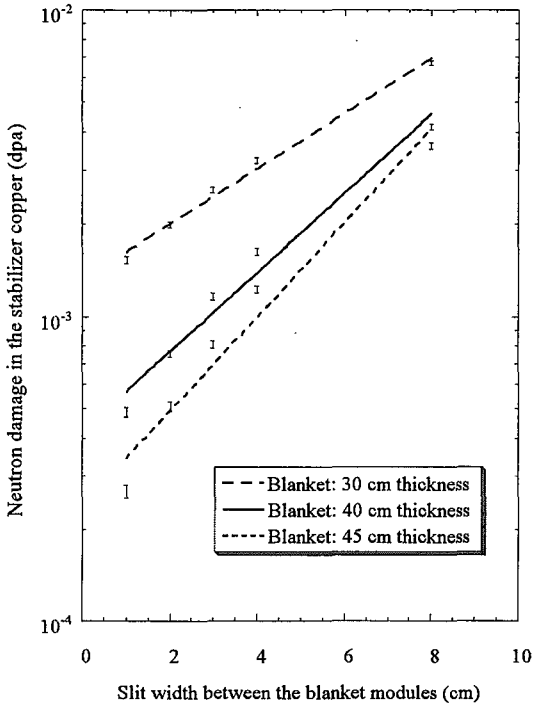

(b) Vacuum vessel thickness: 30 cm

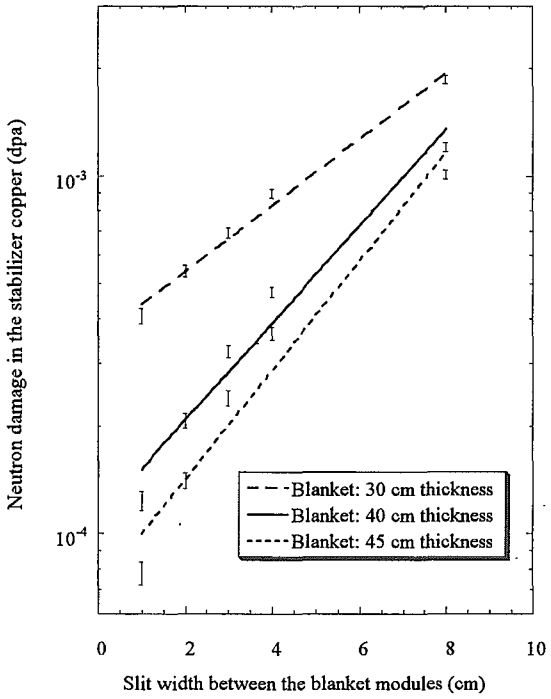

(c) Vacuum vessel thickness: 40 cm

Fig. 3.13 Dependency of neutron damage in the stabilizer copper on the slit width adjacent blanket module. (Neutron wall load: 1MW/m^2, Blanket composition: SS/H2O=80/20, Vacuum vessel shield composition: SS/H2O=60/40)

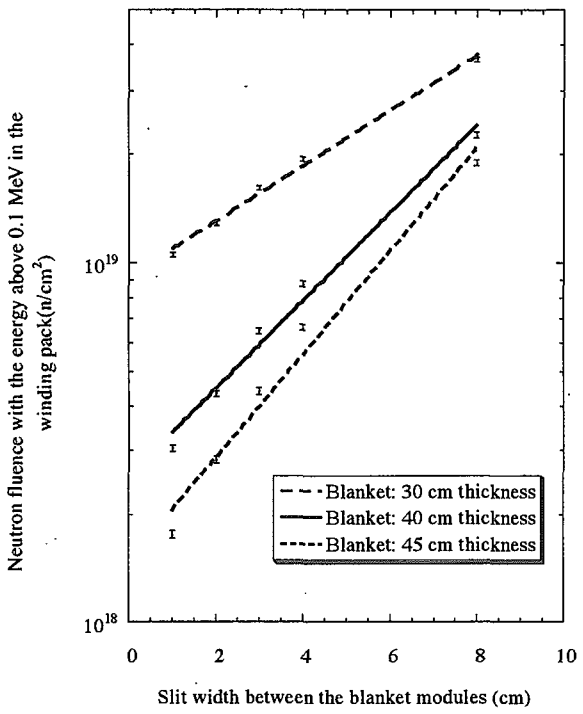

(a) Vacuum vessel thickness: 20 cm

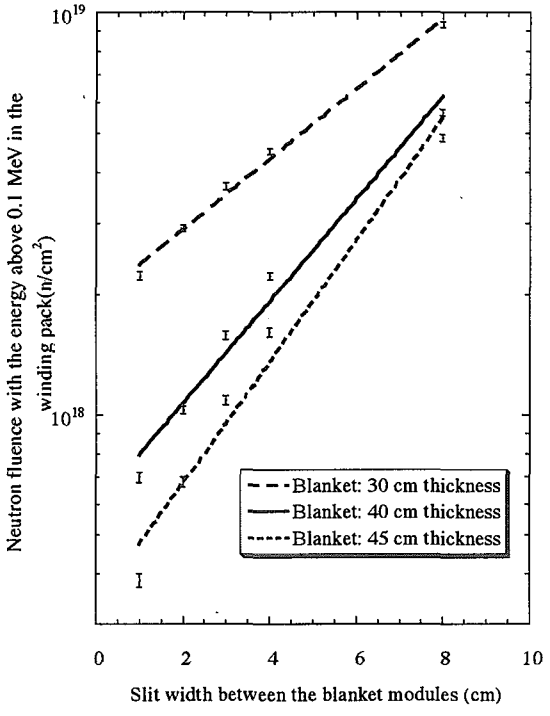

(b) Vacuum vessel thickness: 30 cm

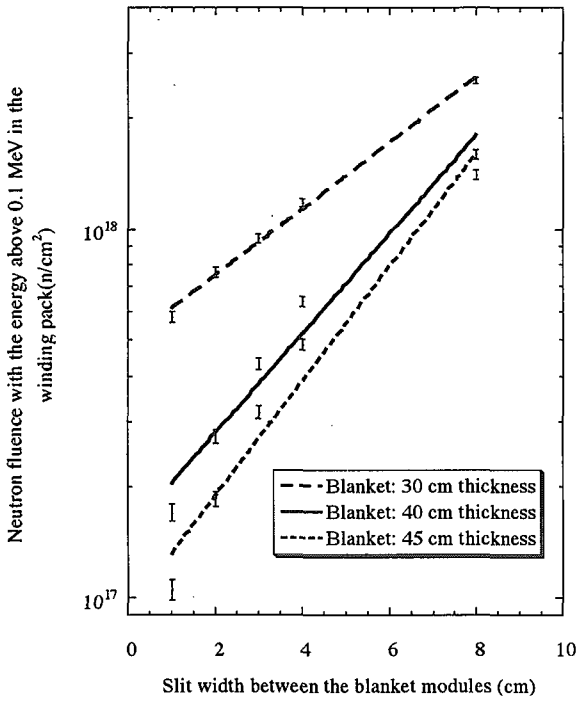

(c) Vacuum vessel thickness: 40 cm

Fig. 3.14 Dependency of neutron fluence with the energy above 0.1 MeV in the winding pack on the slit width adjacent blanket module. (Neutron wall load: 1MW/m^2, Blanket composition: SS/H2O=80/20, Vacuum vessel shield composition: SS/H2O=60/40)

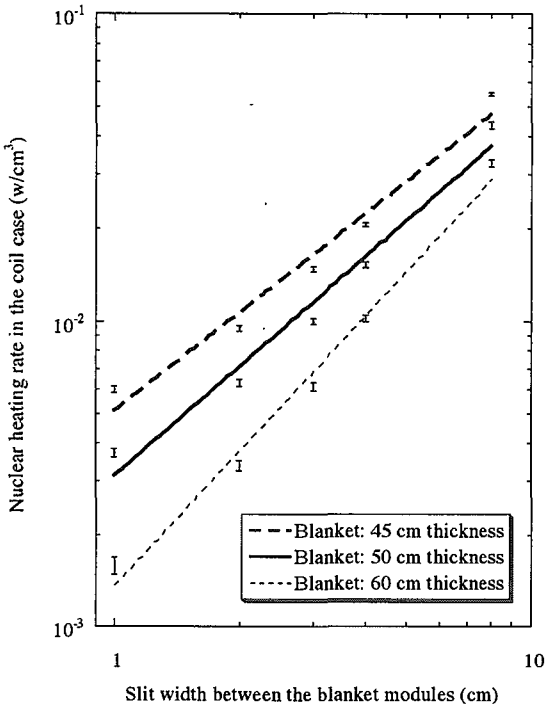

(a) Vacuum vessel thickness: 20 cm

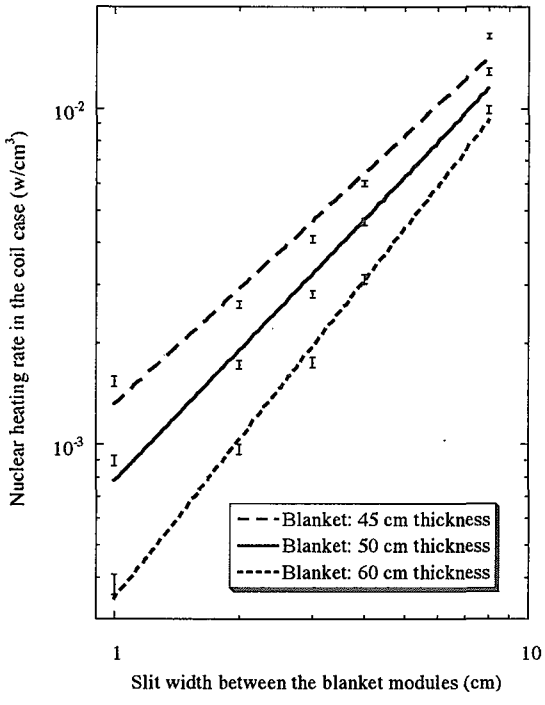

(b) Vacuum vessel thickness: 30 cm

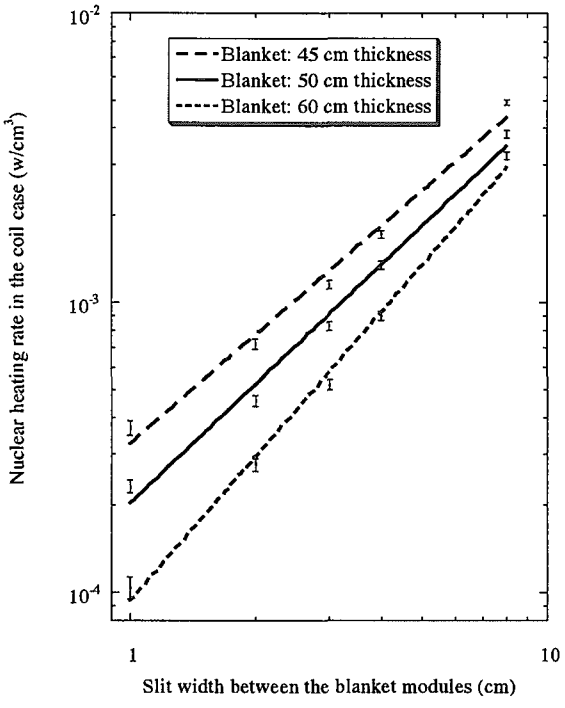

(c) Vacuum vessel thickness: 40 cm

Fig. 3.15 Dependency of nuclear heating rate in the TF coil case on the slit width adjacent blanket module. (Neutron wall load: 1MW/m^2, Blanket composition: SS/H$_2$O=80/20, Vacuum vessel shield composition: SS/H$_2$O=60/40)

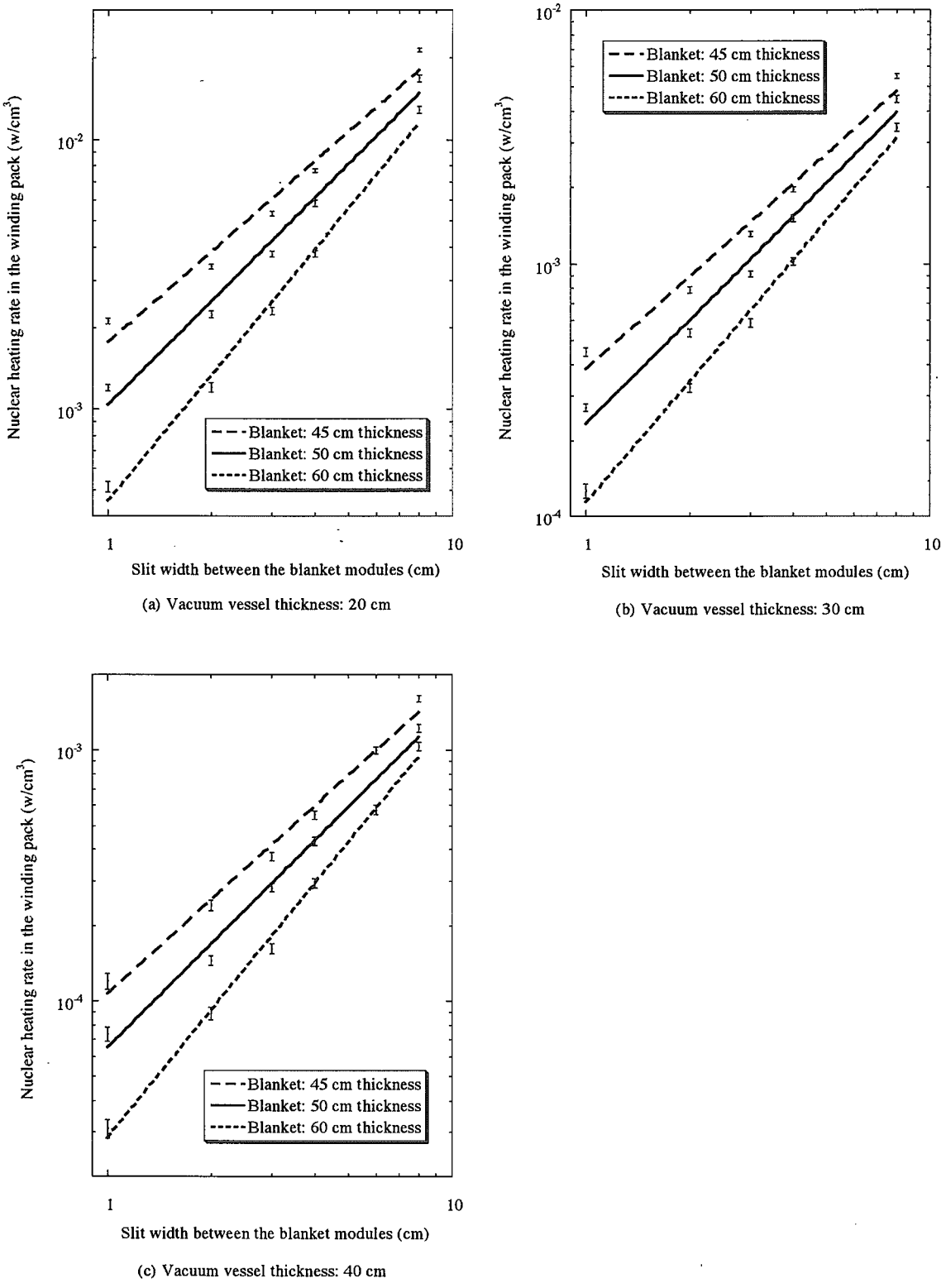

Fig. 3.16 Dependency of nuclear heating rate in the TF coil winding pack on the slit width adjacent blanket module. (Neutron wall load: 1MW/m^2, Blanket composition: SS/H_2O=80/20, Vacuum vessel shield composition: SS/H_2O=60/40)

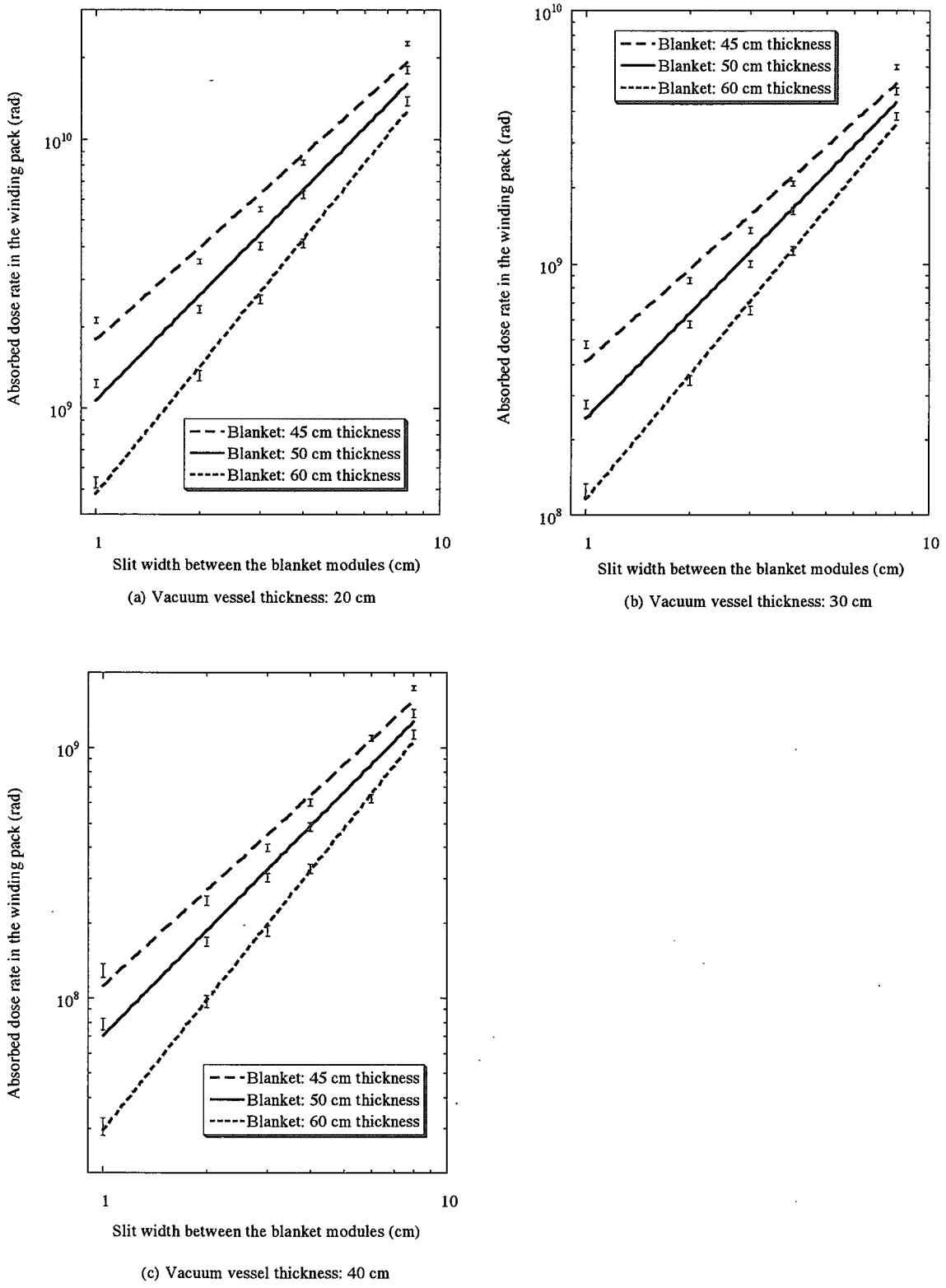

Fig. 3.17 Dependency of absorbed dose rate in the TF coil winding pack on the slit width adjacent blanket module. (Neutron wall load: 1MW/m^2, Blanket composition: SS/H2O=80/20, Vacuum vessel shield composition: SS/H2O=60/40)

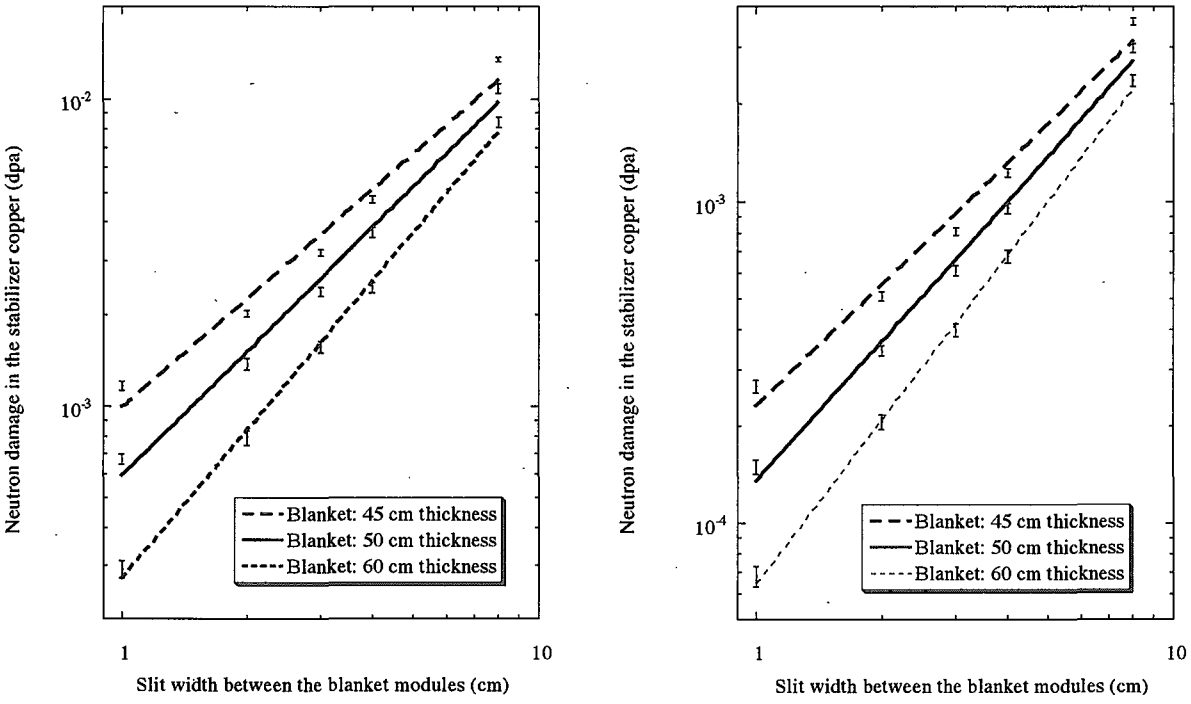

(a) Vacuum vessel thickness: 20 cm

(b) Vacuum vessel thickness: 30 cm

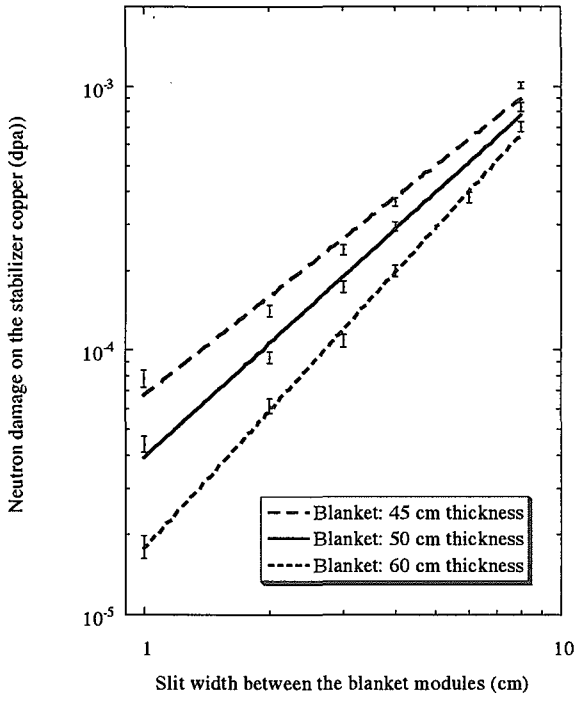

(c) Vacuum vessel thickness: 40 cm

Fig. 3.18 Dependency of neutron damage in the stabilizer copper on the slit width adjacent blanket module. (Neutron wall load: 1MW/m^2, Blanket composition: SS/H2O=80/20, Vacuum vessel shield composition: SS/H2O=60/40)

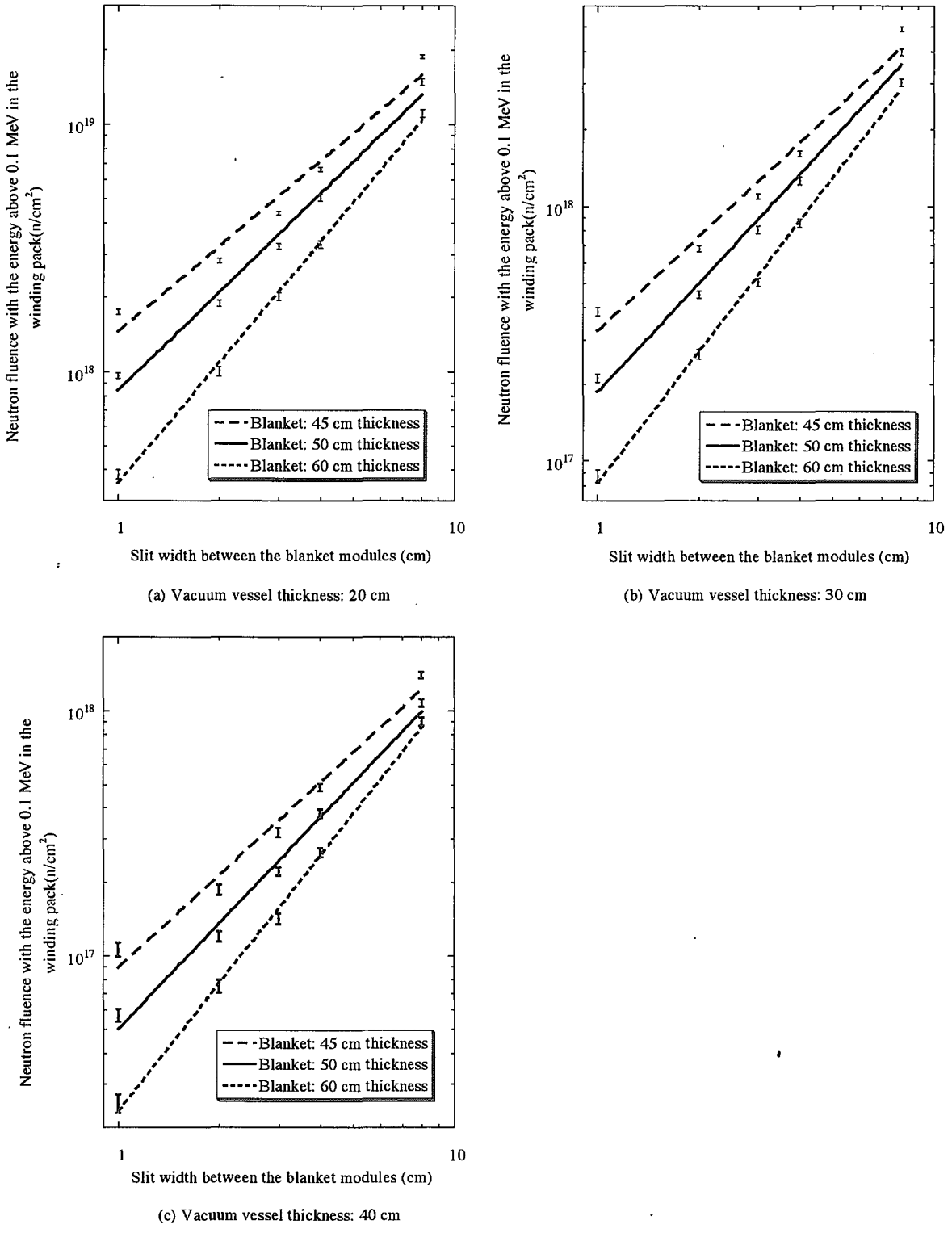

Fig. 3.19 Dependency of neutron fluence with the energy above 0.1 MeV in the winding pack on the slit width adjacent blanket module. (Neutron wall load: 1MW/m^2, Blanket composition: SS/H2O=80/20, Vacuum vessel shield composition: SS/H2O=60/40)

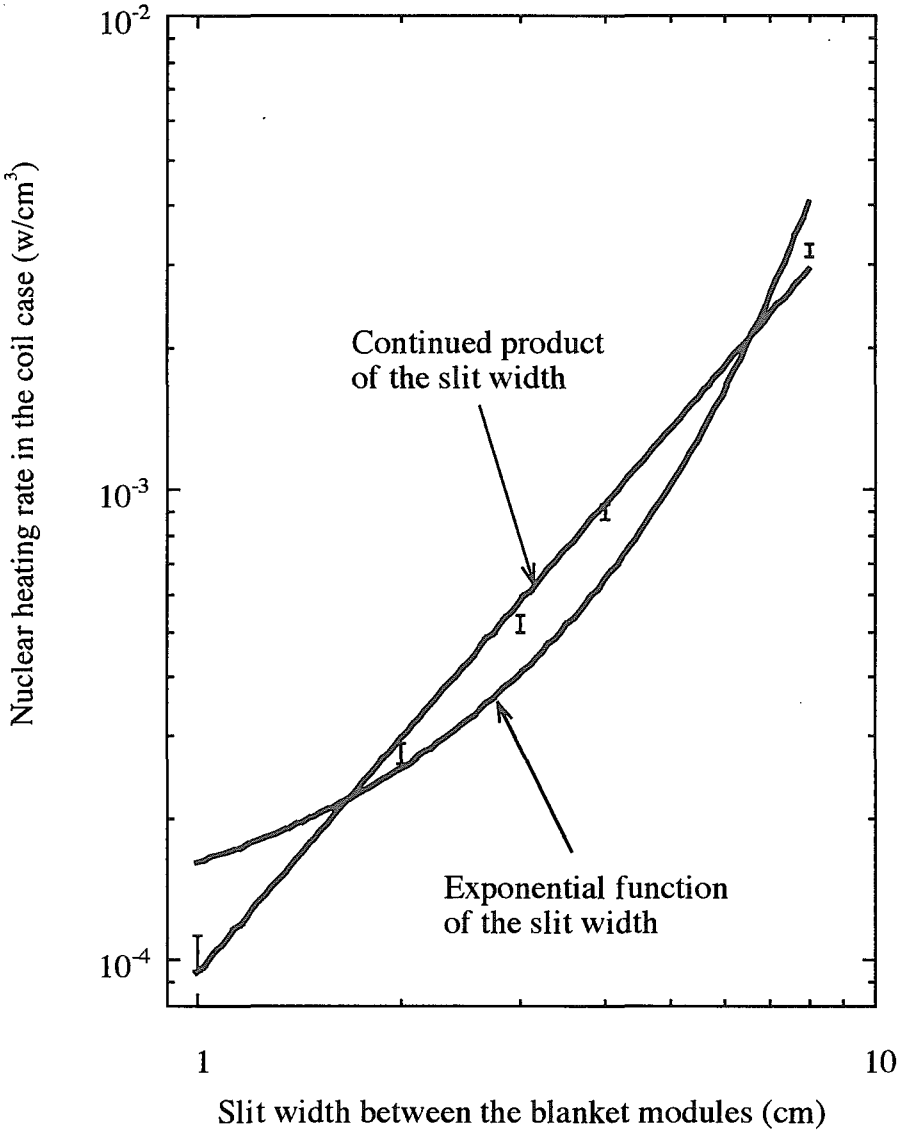

Fig. 3.20 Comparison for the fittings of the exponential and power functions of the slit width in the nuclear heating rate in the coil case in the 60 cm thick blanket and 40 cm thick vacuum vessel.

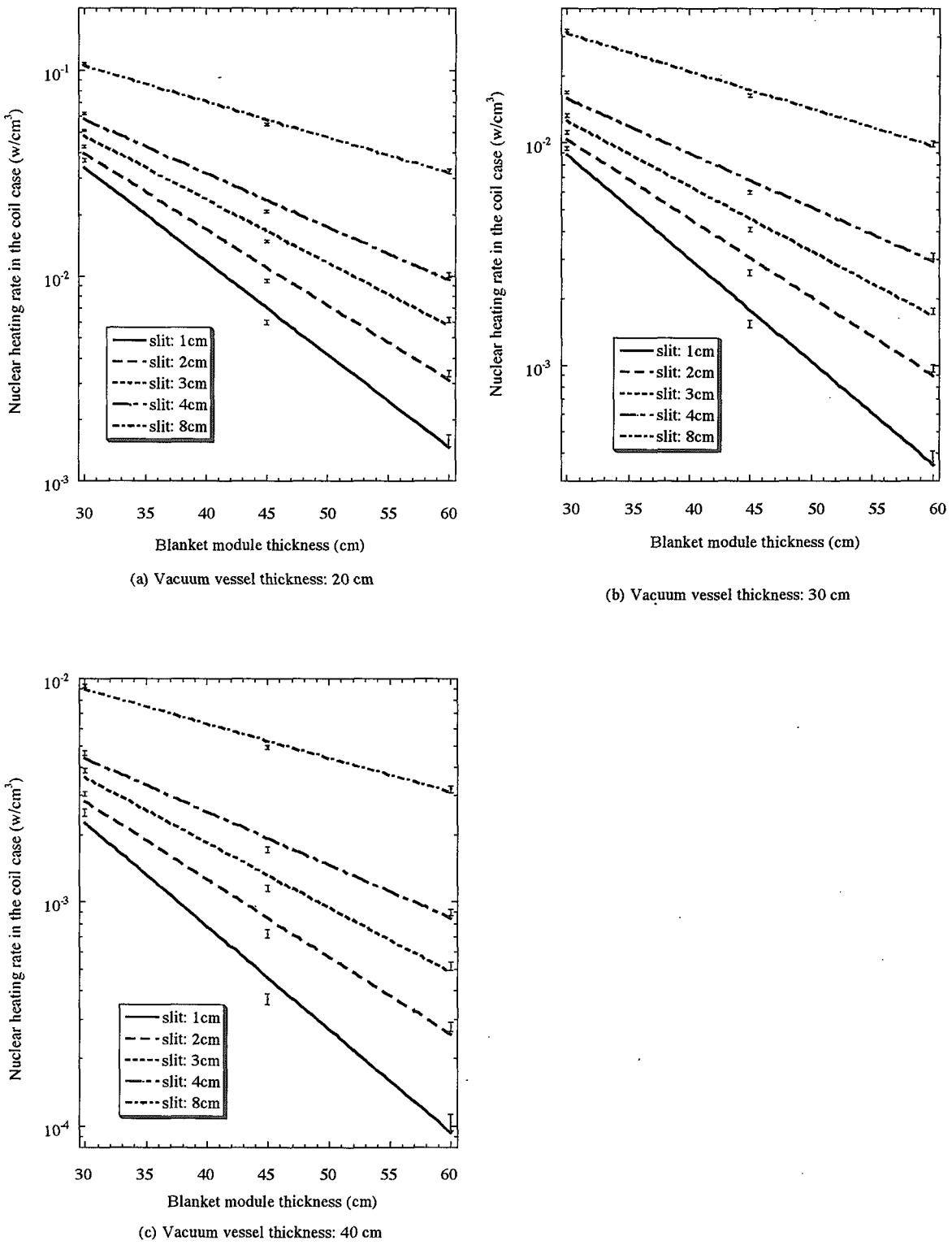

Fig. 3.21 Dependency of nuclear heating rate in the TF coil case on the blanket thickness. (Neutron wall load: 1MW/m^2, Blanket composition: SS/H_2O=80/20, Vacuum vessel shield composition: SS/H_2O=60/40)

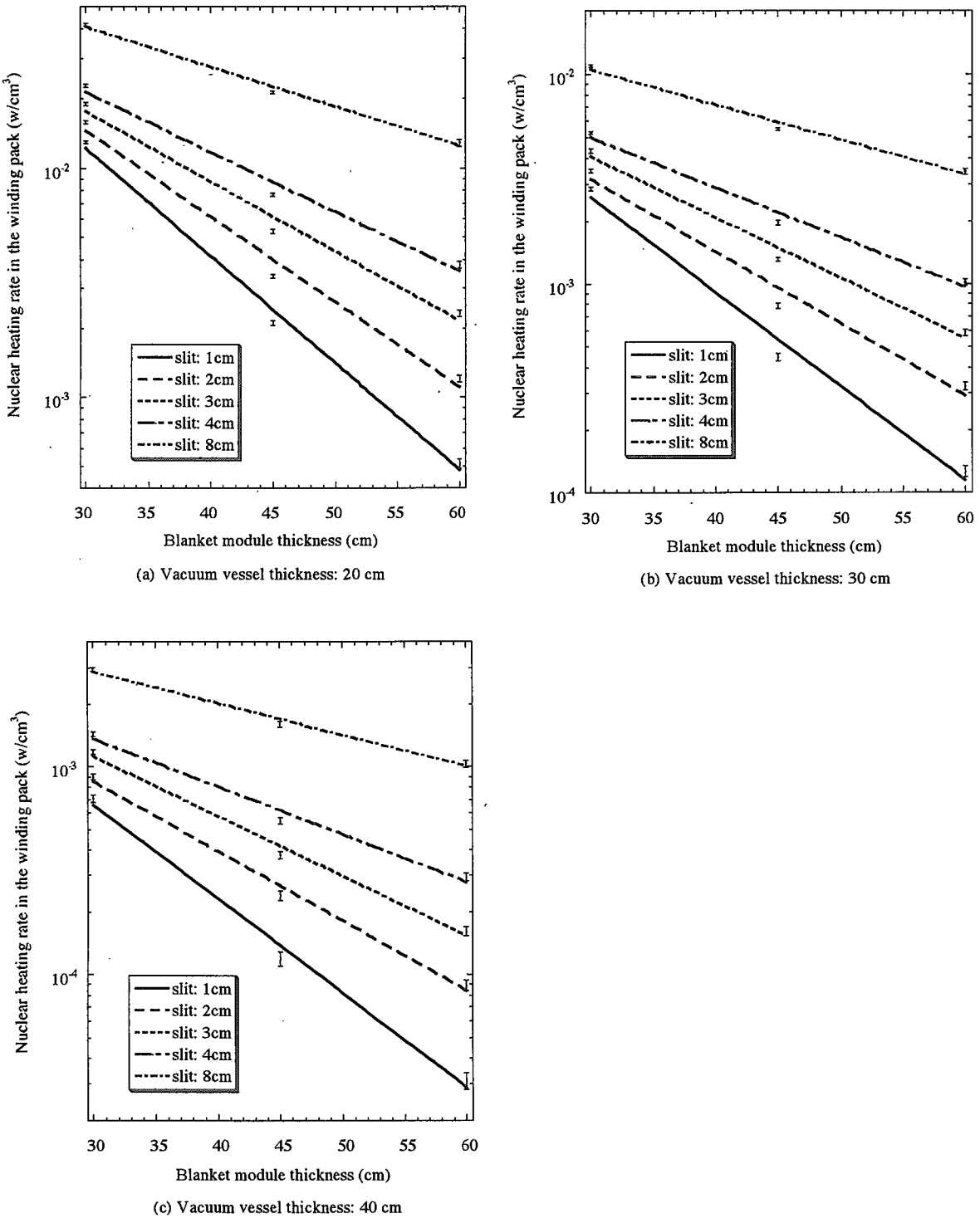

Fig. 3.22 Dependency of nuclear heating rate in the TF coil winding pack on the blanket thickness. (Neutron wall load: 1MW/m^2, Blanket composition: SS/H$_2$O=80/20, Vacuum vessel shield composition: SS/H$_2$O=60/40)

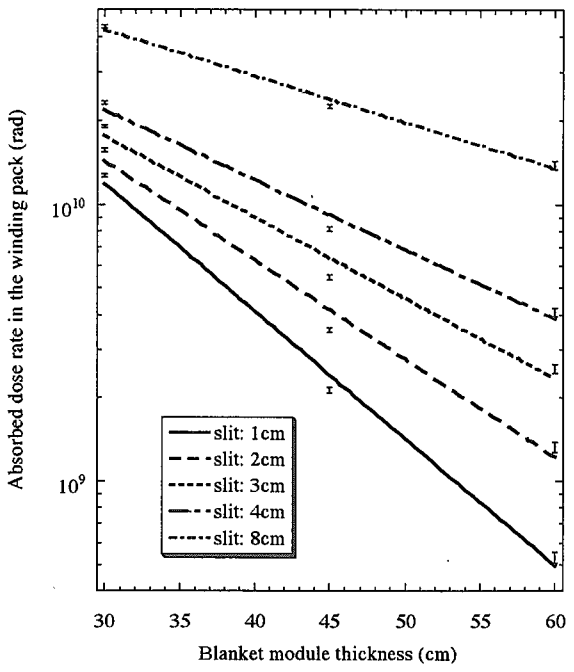

(a) Vacuum vessel thickness: 20 cm

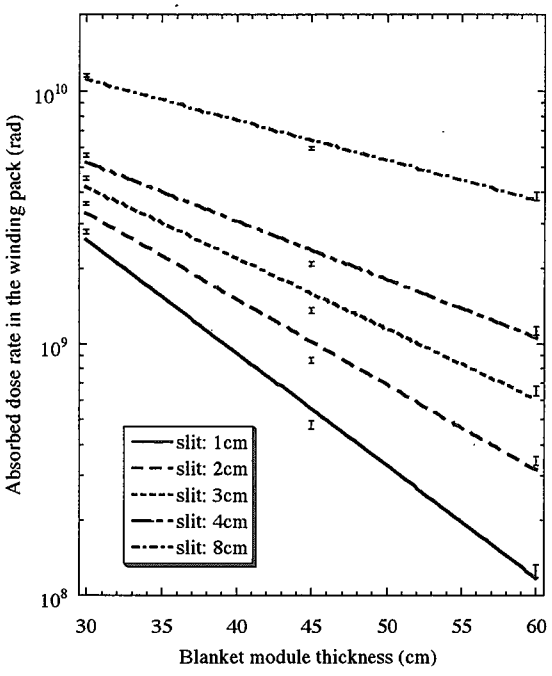

(b) Vacuum vessel thickness: 30 cm

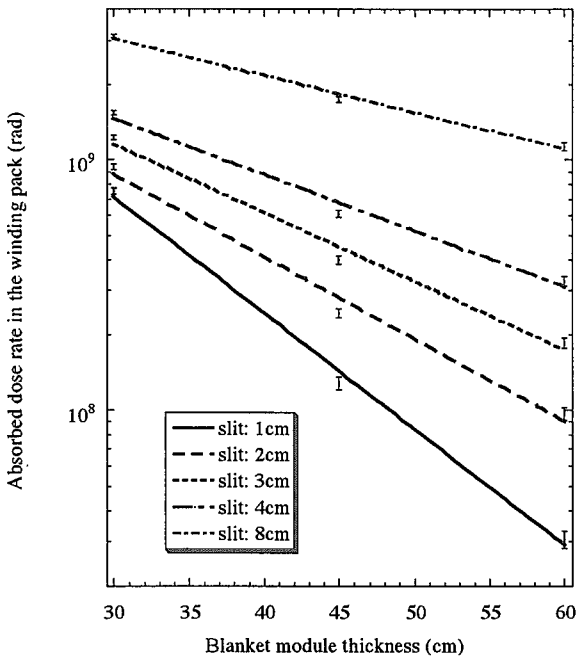

(c) Vacuum vessel thickness: 40 cm

Fig. 3.23 Dependency of absorbed dose rate in the TF coil winding pack on the blanket thickness. (Integrated neutron wall load: 1MWa/m^2, Blanket composition: SS/H2O=80/20, Vacuum vessel shield composition: SS/H2O=60/40)

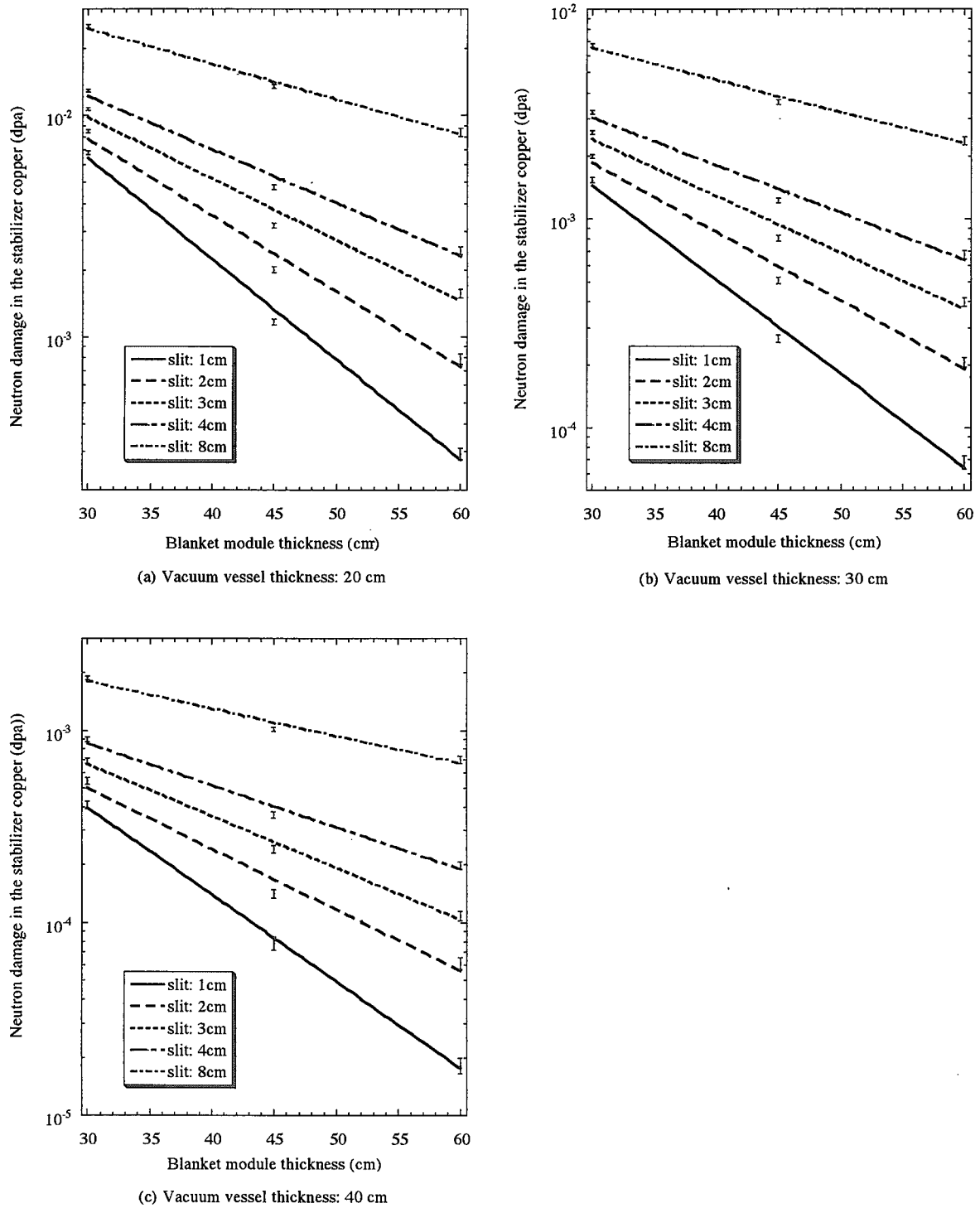

Fig. 3.24 Dependency of neutron damage in the stabilizer copper on the blanket thickness. (Integrated neutron wall load: 1MWa/m^2, Blanket composition: SS/H2O=80/20, Vacuum vessel shield composition: SS/H2O=60/40)

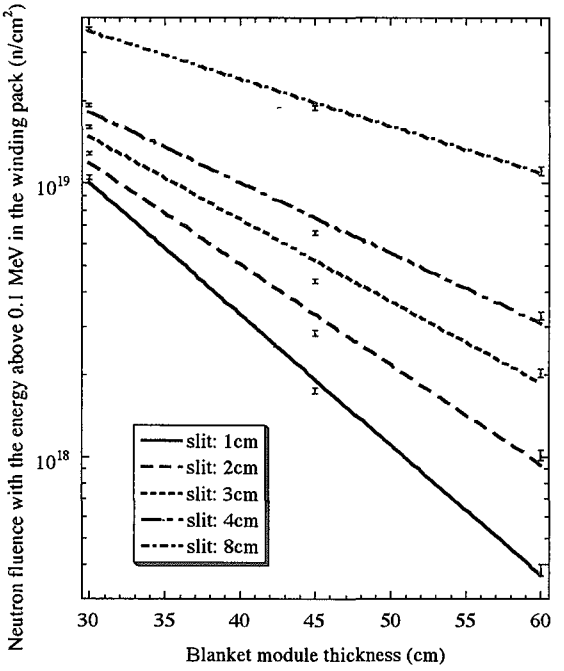

(a) Vacuum vessel thickness: 20 cm

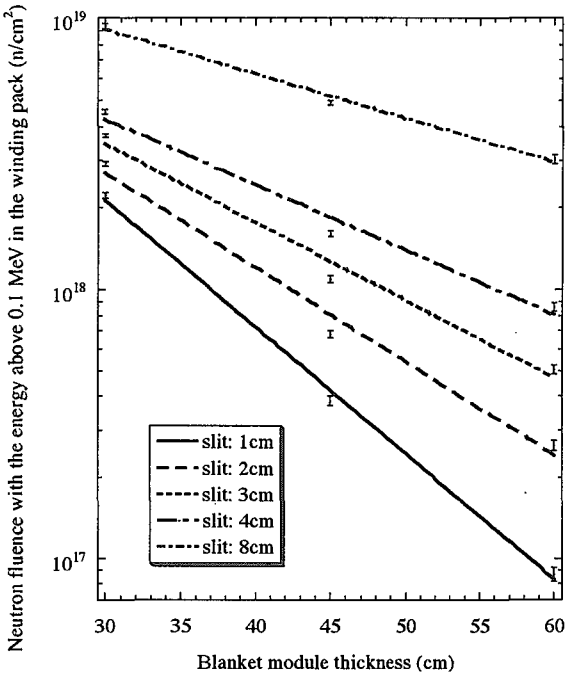

(b) Vacuum vessel thickness: 30 cm

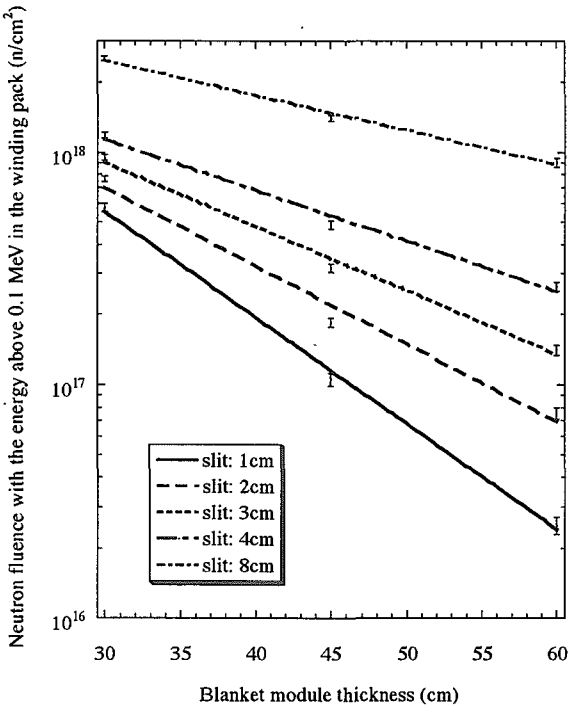

(c) Vacuum vessel thickness: 40 cm

Fig. 3.25 Dependency of neutron fluence with the energy above 0.1 MeV in the winding pack on the blanket thickness. (Integrated neutron wall load: 1MWa/m^2, Blanket composition: SS/H2O=80/20, Vacuum vessel shield composition: SS/H2O=60/40)

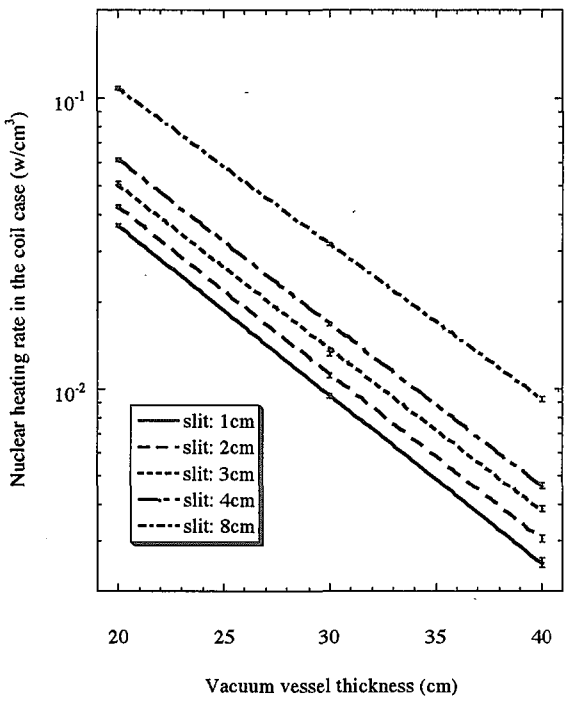

(a) Blanket module thickness: 30 cm

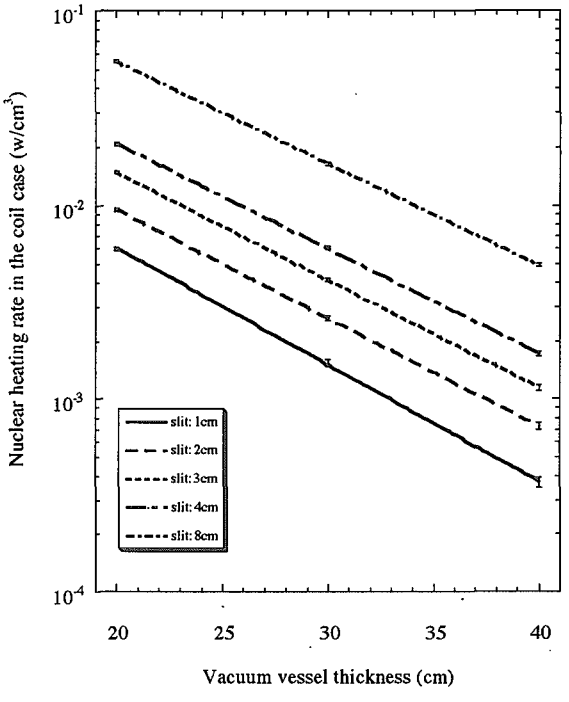

(b) Blanket module thickness: 45 cm

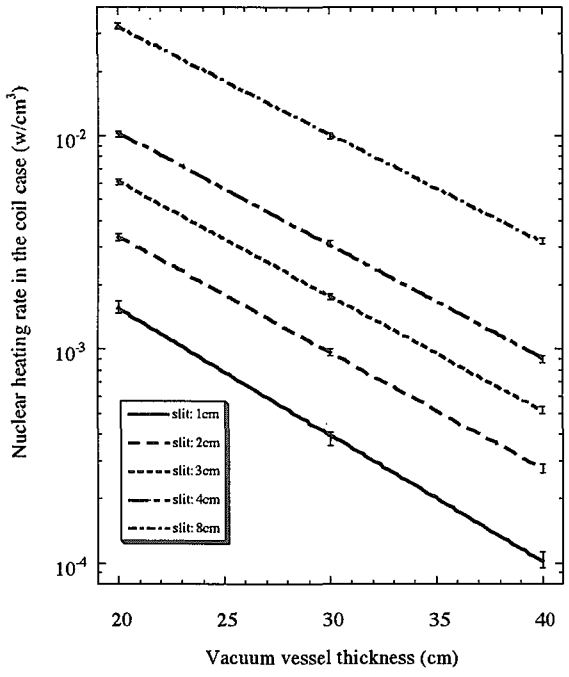

(c) Blanket module thickness: 60 cm

Fig. 3.26 Dependency of nuclear heating rate in the TF coil case on the vacuum vessel thickness. (Neutron wall load: 1MW/m^2, Blanket composition: SS/H_2O=80/20, Vacuum vessel shield composition: SS/H_2O=60/40)

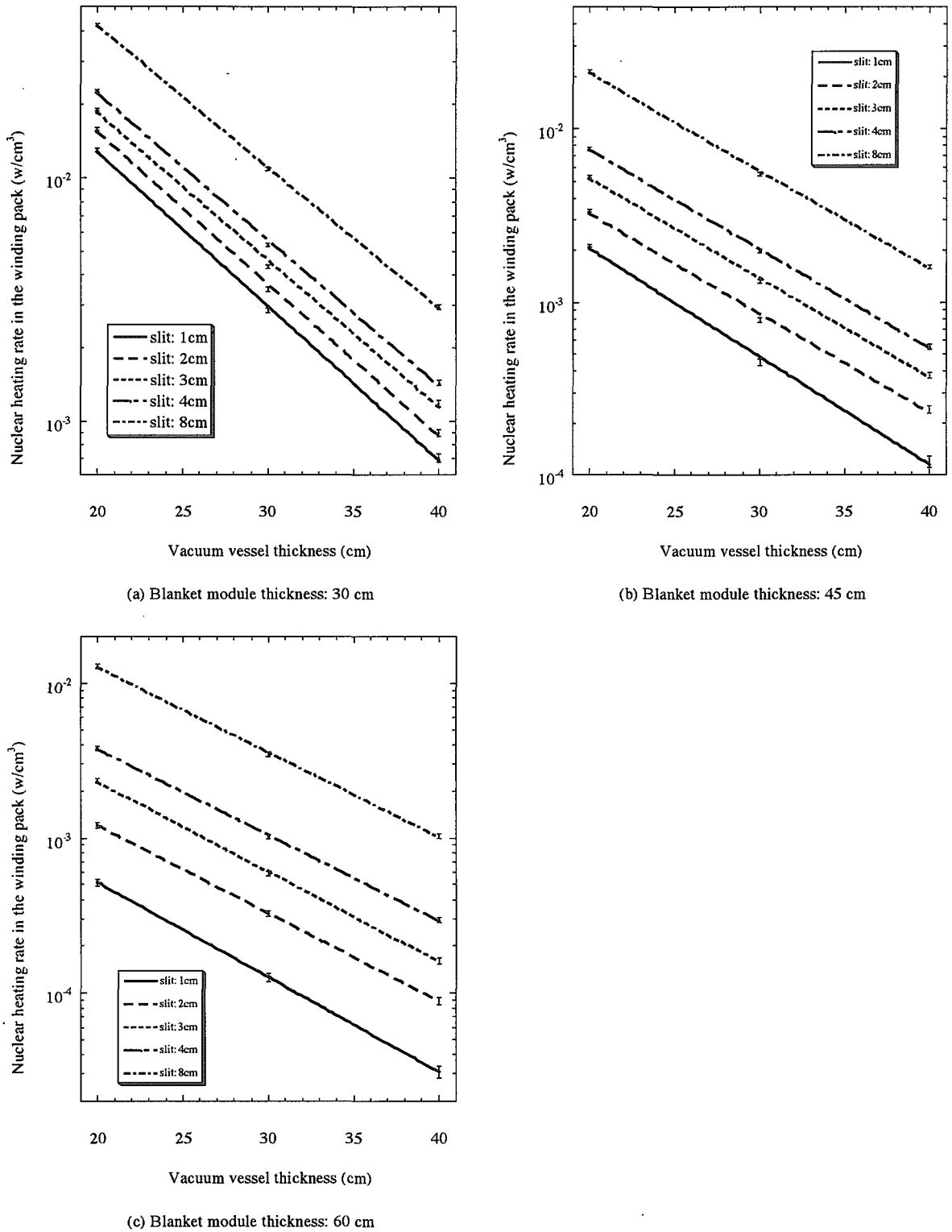

(a) Blanket module thickness: 30 cm

(b) Blanket module thickness: 45 cm

(c) Blanket module thickness: 60 cm

Fig. 3.27 Dependency of nuclear heating rate in the TF coil winding pack on the vacuum vessel thickness. (Neutron wall load: 1MW/m^2, Blanket composition: SS/H_2O=80/20, Vacuum vessel shield composition: SS/H_2O=60/40)

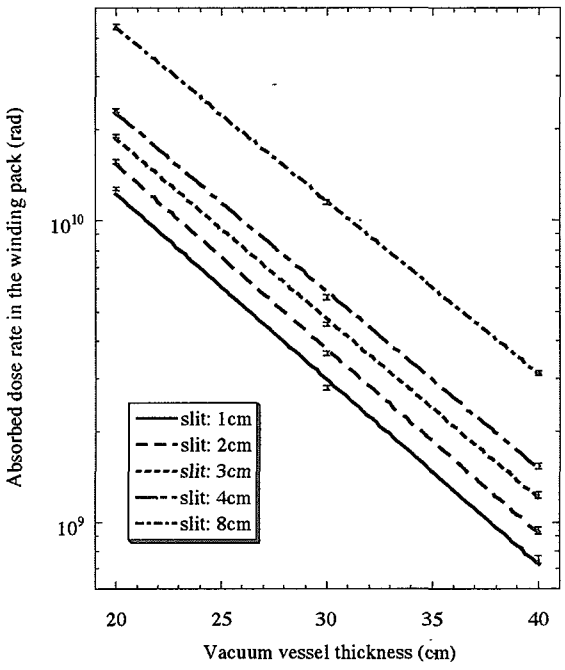

(a) Blanket module thickness: 30 cm

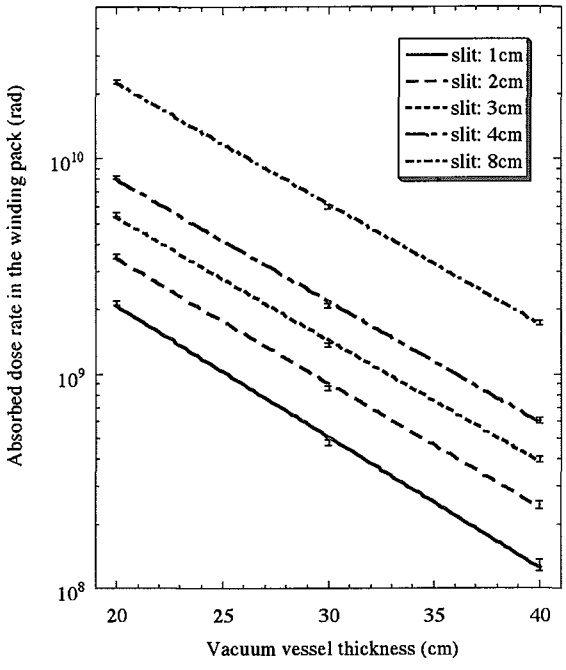

(b) Blanket module thickness: 45 cm

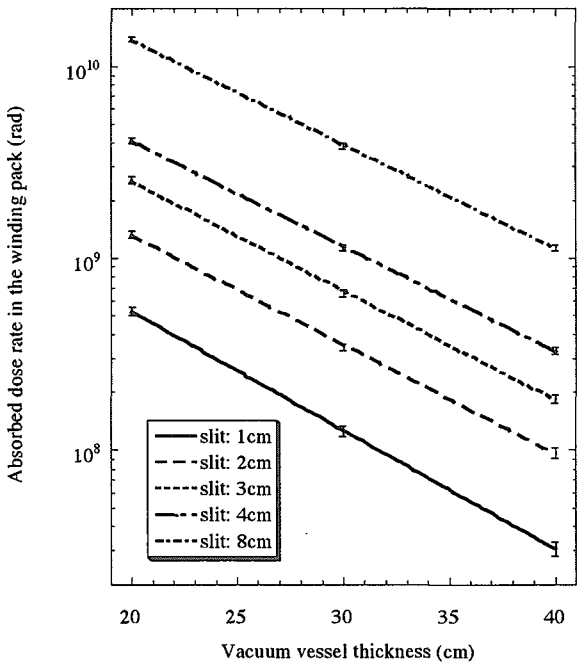

(c) Blanket module thickness: 60 cm

Fig. 3.28 Dependency of absorbed dose rate in the TF coil winding pack on the vacuum vessel thickness. (Integrated neutron wall load: 1MWa/m^2, Blanket composition: SS/H2O=80/20, Vacuum vessel shield composition: SS/H2O=60/40)

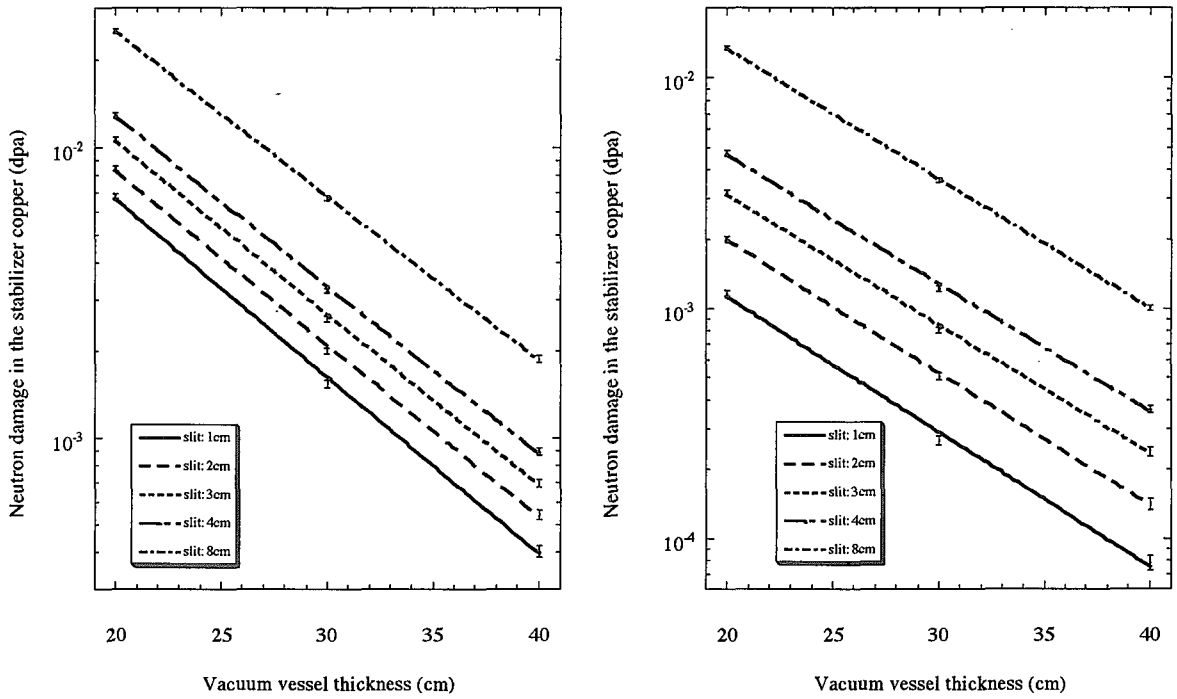

(a) Blanket module thickness: 30 cm

(b) Blanket module thickness: 45 cm

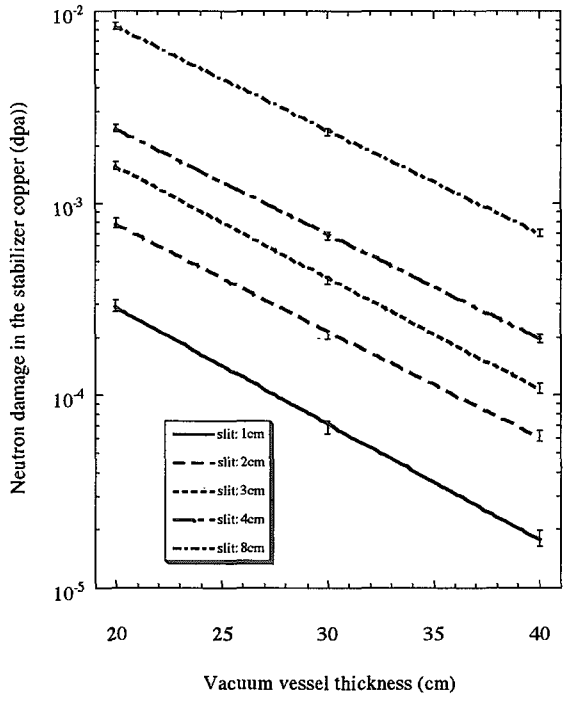

(c) Blanket module thickness: 60 cm

Fig. 3.29 Dependency of neutron damage in the stabilizer copper on the vacuum vessel thickness. (Integrated neutron wall load: 1MWa/m^2, Blanket composition: SS/H2O=80/20, Vacuum vessel shield composition: SS/H2O=60/40)

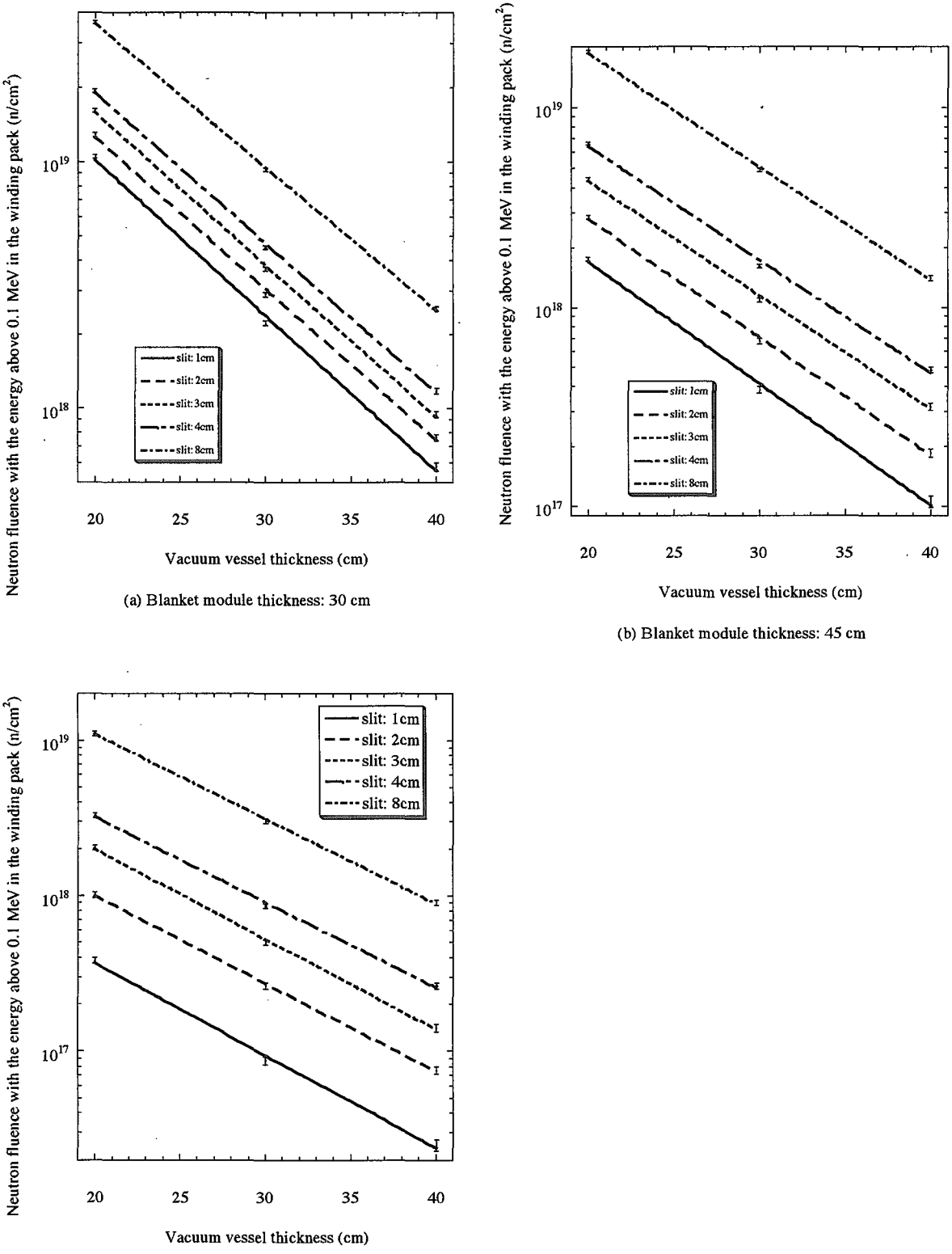

Fig. 3.30 Dependency of neutron fluence with the energy above 0.1 MeV in the winding pack on the vacuum vessel thickness. (Integrated neutron wall load: 1MWa/m^2, Blanket composition: SS/H2O=80/20, Vacuum vessel shield composition: SS/H2O=60/40)

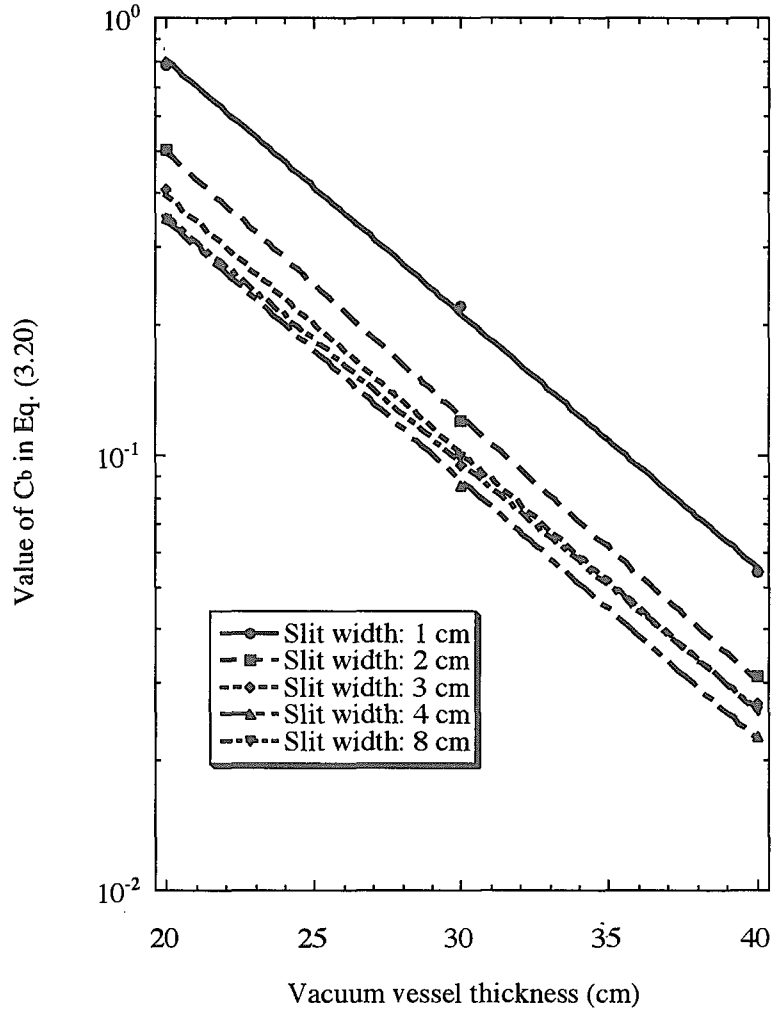

Fig. 3.31 Dependency of the values of C_b in Eq. (3.20) on the vacuum vessel thickness for the nuclear heating rate in the coil case.

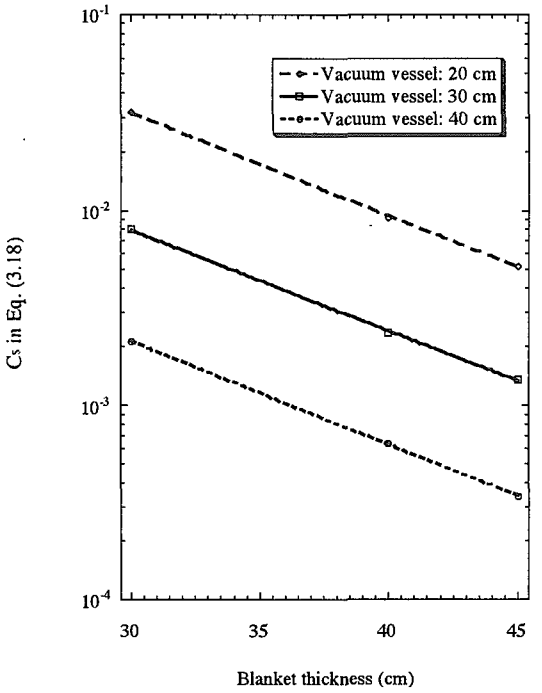

Fig. 3.32 Dependency of the values of Cs in Eq. (3.18) on the blanket thickness for the nuclear heating rate in the coil case.

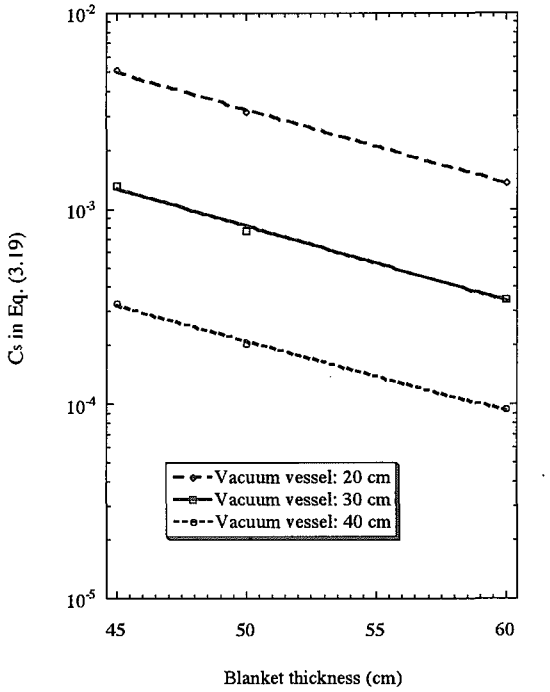

Fig. 3.33 Dependency of the values of Cs in Eq. (3.19) on the blanket thickness for the nuclear heating rate in the coil case.

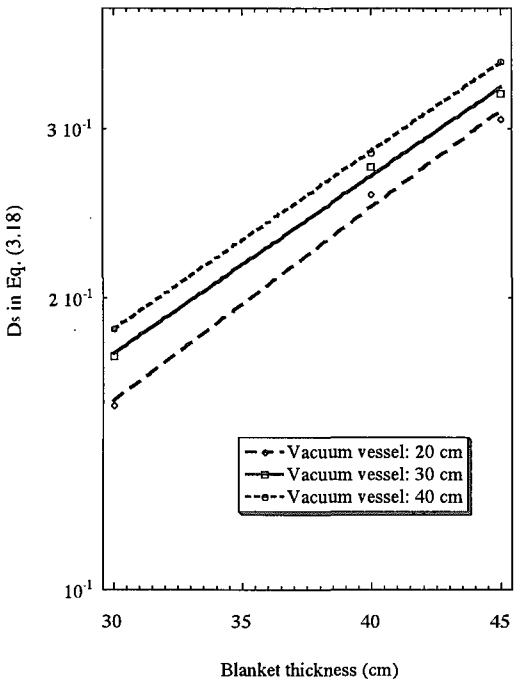

Fig. 3.34 Dependency of the values of Cs in Eq. (3.18) on the blanket thickness for the nuclear heating rate in the coil case.

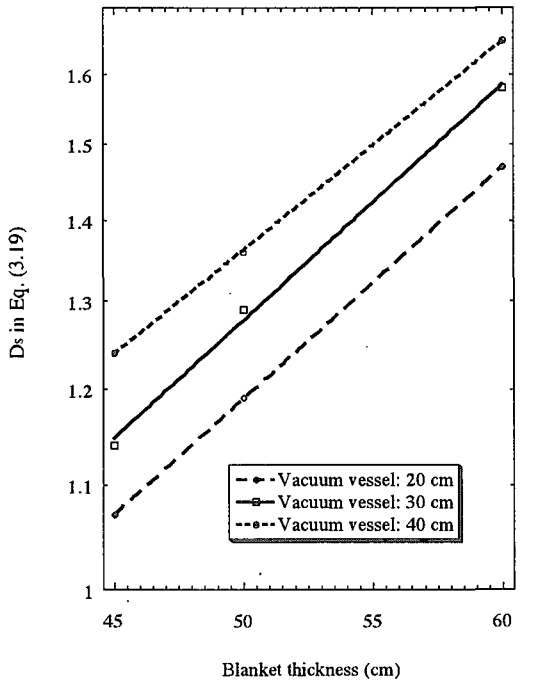

Fig. 3.35 Dependency of the values of Cs in Eq. (3.19) on the blanket thickness for the nuclear heating rate in the coil case.

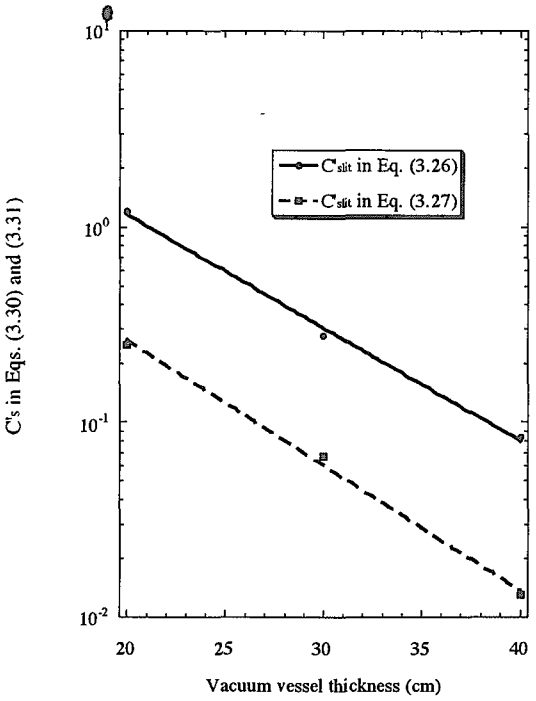

Fig. 3.36 Dependency of the values of C's in Eq. (3.30) and (3.31) on the vacuum vessel thickness for the nuclear heating rate in the coil case.

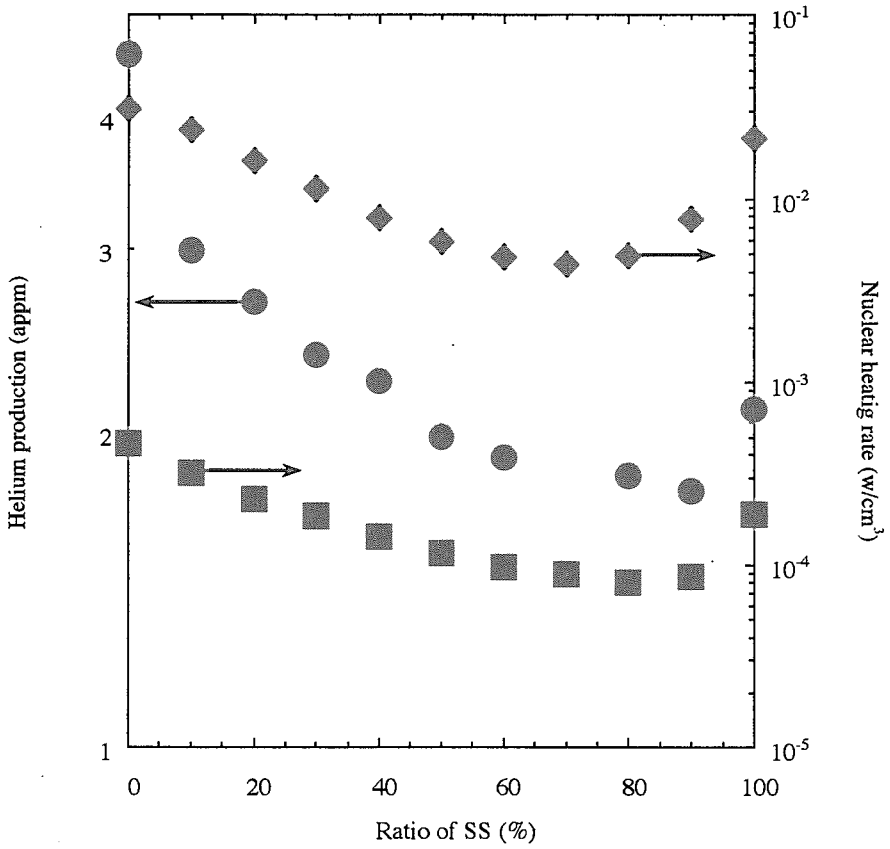

Fig. 3.37 Dependencies of the nuclear properties on the blanket and the vacuum vessel shield composition. The neutron wall loading and the integrated neutron wall loading are 1 MW/m2 and 1 MWa/m2, respectively. The blanket and the vacuum vessel shield are composed of SS and water.

● Helium productions in the vacuum vessel front wall surface along the slit on the blanket composition. The blanket thickness is 60 cm, the slit width is 2 cm and the boron content in the vacuum vessel front wall is 20 wppm.

■ Nuclear heating rate in the winding pack surface along the slit on the blanket composition. The vacuum vessel shiled composition is 60 % SS and 40 % water. The blanket and the vacuum vessel thicknesses are 60 and 40cm, respectively, and the slit width is 2 cm.

◆ Nuclear heating density in the super-conductive magnet case surface along the slit on the vacuum vessel shield composition. The blanket composition is 80 % SS and 20 % water. The blanket and the vacuum vessel thicknesses are 30 and 40cm, respectively, and the slit width is 4 cm.

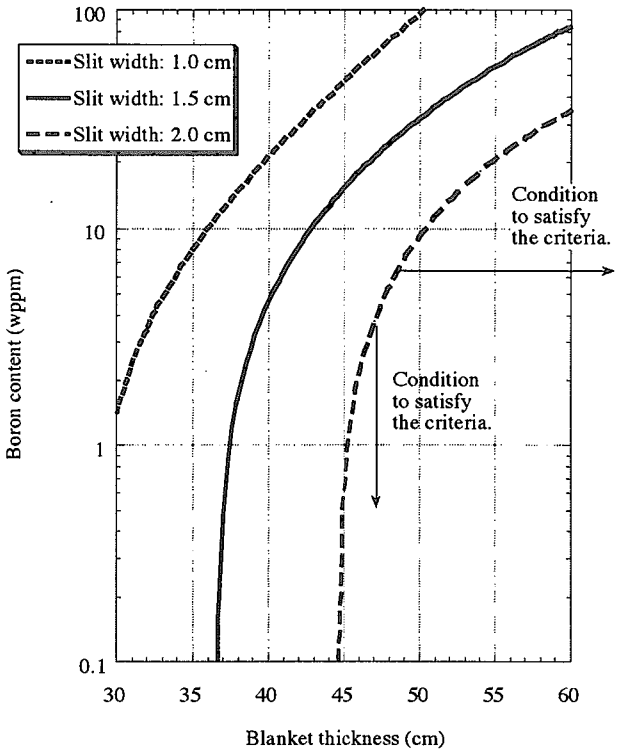

Fig. 3.38 Combinations of the boron content and the blanket thickness required to satisfy the shielding design criteria. The blanket composition is 80 % SS and 20 % water. The shielding design criteria is 1 appm for rewelding of SS, a safety factor is 1.6 and the integrated neutron wall loading is 0.3 MWa/m^2. In the lower region of each curve, the helium productions can satisfy the criteria.

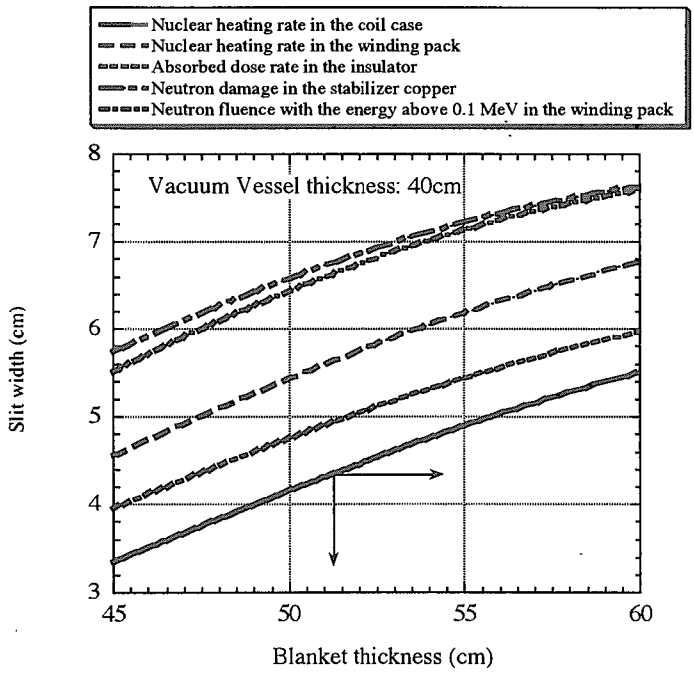

Fig. 3.39 Combinations of the slit width and the blanket thickness required to satisfy the shielding design criteria. The blanket composition is 80 % SS and 20 % water. A safety factor is 1.6 and the neutron wall loading and the integrated neutron wall loading are 0.7 MW/m^2 and 0.3 MWa/m^2, respectively. In the lower region of each curve, the nuclear properties of the TF coil can satisfy the criteria.

4. Streaming through Small Circular Duct in Blanket [4.1]

4.1 Introduction

Radiation streaming through the slit between the adjacent blanket modules is described in Chapter 3. In addition to the radiation streaming through the slit, there is a critical concern of the shielding design about the radiation streaming through the small circular duct in the blanket modules. In this Chapter, the radiation streaming through the small circular duct is described.

The cooling water branch pipes are connected to each blanket module to supply and drain the cooling water for the blanket, and they are connected to the common manifold, which are installed inside the vacuum vessel. The small circular ducts are bored through the face of the blanket in order to install the welding and cutting equipment for a replacement of the blanket module. A plug is installed at the boundary between the small circular duct and the branch pipe. The plug, which is made of stainless-steel (SS) and serves as a pressure boundary, and the branch pipes are to be cut and rewelded during a replacement of the blanket module.

The helium productions in the plug and the branch pipe are enhanced by neutron streaming through the small circular duct. The small circular ducts are 3 - 4 cm diameter in the ITER design [4.2, 4.3]. As long as the helium production can fully satisfy the design limit, it is desirable to widen the duct diameter from the view point of the maintenance process. The helium production is therefore required to be evaluated exactly. Also, the nuclear properties in the TF coil may be increased by neutron streaming through the small circular duct.

In this Chapter, these nuclear properties are calculated taking into account the neutron streaming through the small circular duct by using the three dimensional Monte Carlo code, and their analytical representations were established from the Monte Carlo results. By changing systematically the duct diameter, the blanket thickness and the boron content in the plug, the analytical representations of the nuclear properties along the slit are established as functions of these parameters. The dependencies of the nuclear properties on the blanket compositions are also clarified. The analytical formula thus-obtained is applied to clarify the shielding design constraint required to satisfy the shielding design criteria for the DT fusion reactor.

4.2 Calculation Method

By the same method as Chapter 3.2, the helium production and the nuclear properties in the TF coil are calculated using the Monte Carlo code MCNP-4B and the fusion evaluated nuclear data library FENDL-1. The three dimensional Monte Carlo calculational geometry used in the calculation is shown in Fig. 4.1 with the dimensions, and the calculational condition is shown in Table 4.1. The cooling water branch pipes are installed inside the blanket, and their length inside the blanket is 8 cm in ITER. Similarly to the ITER design, the length is fixed as 8cm in the present calculation. The ITER design has been studied in the extent of 31 to 45 cm thick blankets, 3 to 4 cm diametric ducts and 10 to 20 parts per million

by weight (wppm) boron. In this Chapter, the Monte Carlo calculations are performed for the conditions of the wider extent compared with the ITER conditions.

4.3 Results and Discussions

4.3.1 Helium production in the cooling water pipe

In this Chapter, the helium productions are discussed in the plug of the cooling water branch pipe along the duct. The helium productions are normalized to the integrated neutron wall loading of 1 MWa/m^2.

4.3.1.1 Dependency on duct diameter

Some calculated results are shown in Table 4.2 with the statistical error for the 10 wppm boron content and the 3 cm diametric duct. Dependencies on the duct diameter are shown in Fig. 4.2 with the error bar corresponding to the range of the statistical error for boron content in the plug of 100, 30, 10 wppm. It was found that the helium productions increased exponentially with the duct diameter. In Chapter 3.3.4.1, it is discussed that the nuclear properties in the TF coil along the slit increase exponentially with the slit width. Similarly to the dependency of the nuclear properties in the TF coil along the slit on the slit width, it is discussed that the helium productions increase exponentially with the duct diameter. The analytical representation on the helium production along the duct can be given as a function of the duct diameter, X_d (cm), as follows;

$$Y_h = N P A_d \exp (B_d X_d) \qquad (4.1).$$

The values of A_d and B_d obtained by the least squares fitting to Eq. (4.1) are shown in Table 4.3 for various blanket thicknesses and boron contents. The B_d values, 1/cm, are factors of a dependency on the duct diameter. Disagreement of the helium production obtained by the analytical representation (4.1) with the values in Table 4.3 is 1 to 8 % compared with those by the Monte Carlo calculation.

4.3.1.2 Dependency on blanket thickness

Dependencies on the blanket thickness are shown in Fig. 4.3 for the 10, 30 and 100 wppm boron content. It was found that the helium productions decreased exponentially with the blanket thickness. In Chapter 3.3.3.3, it is discussed that the helium production in the vacuum vessel wall along the slit decreases exponentially with the blanket thickness. Similarly to the dependency of the helium production in the vacuum vessel wall along the slit on the blanket thickness, it is discussed that the helium production in the plug of the cooling water branch pipe along the duct decreases exponentially with the blanket thickness. The analytical representation on the helium production in the plug of the cooling water branch pipe can be given as a function of the blanket thickness as follows;

$$Y_h = N\,P\,A_b \exp(-B_b X_b) \quad (4.2),$$
$$T_b = \ln 10 / B_b \quad (4.3).$$

where X_b is the blanket thickness to the plug (cm). The values of A_b and B_b obtained by the least squares fitting to Eq. (4.2) are shown in Table 4.4 for various duct diameters and boron contents. The B_b values, 1/cm, correspond to the effective linear attenuation coefficient of the blanket for the helium production in the plug of the cooling water branch pipe. Disagreement of the helium productions obtained by the analytical representation Eq. (4.2) with the values in Table 4.4 is 0.1 to 7 % compared with those by the Monte Carlo calculation. The values of A_{blt} and B_{blt} almost increase exponentially with the duct diameter, and they increase linearly with the boron content as seen in Table 4.4. The values of T_b correspond to the blanket thickness required to reduce the helium production by one order of magnitude, and they are also shown in Table 4.4. The larger is the boron content in steel, the larger is the thermal neutron contribution in the helium production due to the $^{10}B(n, \alpha)$ reaction. The thermal neutrons are generated as a result of fast neutron scattering and moderation, and the attenuation of the thermal neutron flux in the blanket is lower compared with that of the fast neutron flux, which may bring an increase of the T_{blt} values with increasing the boron contents. Since the helium production increases with the duct diameter as shown in Chapter 4.3.1.1, in the case of the 1 cm diametric duct, about 19.0 – 19.8 cm thick blanket is required to reduce the helium productions by one order of magnitude, but with increasing the duct diameter to 6 cm, the values of T_{blt} become 21.3 – 22.9 cm.

4.3.1.3 Dependency on boron content

Dependencies on the boron content are shown in Figs. 4.4 for the 25, 35 and 45 cm thick blankets. It was found that the helium productions increased linearly with the boron content. The helium productions by each element are shown in Fig. 4.5 as a function of neutron energy. The helium production caused from the thermal neutron reaction with elements except for boron is negligibly small, therefore the helium production caused from the thermal neutron reaction increases linearly with the boron content as mentioned in Chapter 3.3.3.2. The analytical representation on the helium production in the plug of the cooling water branch pipe can be given as a function of the boron content as follows;

$$Y_h = N\,P\,(A_{bo} + B_{bo} X_{bo}) \quad (4.4).$$

The values of A_{bo} and B_{bo} obtained by the least squares fitting to Eq. (4.4) are shown in Table 4.5 for various duct diameters and blanket thicknesses. Disagreement of the helium productions obtained by the analytical representation Eq. (4.4) with the values in Table 4.5 is less than 7 % compared with those by the Monte Carlo calculation. The values of A_{bo} and B_{bo} almost increase exponentially with the duct diameter, and they decrease exponentially with the blanket thickness as seen in Table 4.5.

4.3.1.4 Establishment of analytical representation

Dependencies of the values of A_d and B_d on the blanket thickness are shown in Figs. 4.6 and 4.7, respectively. Similarly to Eq. (4.2), it is found that the A_d values in Eq. (4.1) representing a function of a duct diameter also decrease exponentially with the blanket thickness. On the other hand, it is found that the B_d values in Eq. (4.1) increase exponentially with the blanket thickness. When the blanket becomes thicker, the difference between the neutron flux attenuation in the bulk shield and that in the duct becomes larger, then the dependency of helium production on the duct diameter becomes also larger. The B_d values are factors of a dependency on the duct diameter as mentioned above, and they increase with the blanket thickness. The A_d and B_d values can be given approximately by exponential functions of the blanket thickness X_b as follows;

$$A_d = A'_d \exp (- C_b X_b) \quad (4.5),$$

$$B_d = B'_d \exp (D_b X_b) \quad (4.6).$$

From the analytical representation Eq. (4.1) and the formulae Eqs. (4.5) and (4.6), the analytical representation on the helium production can be given as functions of the duct diameter X_d and the blanket thickness X_b as follows;

$$Y_h = N P A'_d \exp (- C_b X_b) \exp (B'_d X_d \exp (D_b X_b)) \quad (4.7).$$

The values of A'_{duct}, C_{blt}, B'_{duct} and D_{blt} obtained by the least squares fitting to Eq. (4.7) are shown in Table 4.6 for boron contents of 100, 30 and 10 wppm. Disagreement of the helium productions obtained by the analytical representation Eq. (4.7) with the values in Table 4.6 is 5 to 8 % compared with those by the Monte Carlo calculation.

Similarly to Eq. (4.4), it is found that the A_d values in Eq. (4.1) also increase linearly with the boron content as seen in Table 4.3. The A_d values can then be given approximately as a function of the boron content as follows;

$$A_d = A''_d + A'_{bo} X_{bo} \quad (4.8).$$

On the other hand, the B_d values, which are factors of a dependency on the duct diameter, slightly decreased with the boron content. With increasing the boron contents, the contribution of the helium production caused from thermal neutron reaction with boron also increases. Since the enhancement of the thermal neutron flux due to duct streaming is smaller than that of the fast neutron flux, the dependency of helium production on the duct diameter may decrease with increasing the boron content. Though the B_d values slightly decreased with the boron content, they show almost constant values. The B''_d values averaged for three boron contents are then applied to all blanket thicknesses in this Chapter. From the analytical representation Eq. (4.1) and the formula (4.8), the analytical representation on the helium

production can be given as functions of the duct diameter X_d and the boron content X_{bo} as follows;

$$Y_h = N P (A''_d + A'_{bo} X_{bo}) \exp (B''_d X_d) \quad (4.9).$$

The values of A''_d, A'_{bo} and B''_d obtained by the least squares fitting to Eq. (4.9) are shown in Table 4.7 for three blanket thicknesses of 25, 35 and 45 cm. Disagreement of the helium productions obtained by the analytical representation Eq. (4.9) with the values in Table 4.7 is 9 to 11 % compared with those by the Monte Carlo calculation.

Dependencies of the values of A''_d, A'_{bo} and B''_d on the blanket thickness are shown in Fig. 4.8. Similarly to Eqs. (4.5) and (4.6), it is found that the A''_d and A'_{bo} values in Eq. (4.9) also decrease exponentially with the blanket thickness, and the B''_d values increase exponentially with the blanket thickness. The A''_d, A'_{bo} and B''_d values can be given approximately by an exponential function of the blanket thickness X_b as follows;

$$A''_d = A'''_d \exp (-C'_b X_b) \quad (4.10),$$
$$A'_{bo} = A''_{bo} \exp (-E_b X_b) \quad (4.11),$$
$$B''_d = B'''_d \exp (D'_b X_b) \quad (4.12).$$

From the analytical representation Eq. (4.9) and the formulae (4.10), (4.11) and (4.12), the analytical representation on the helium production can be given as functions of the duct diameter X_d, the boron content X_{bo} and the blanket thickness X_b as follows;

$$Y_h = N P (A'''_d \exp (- C'_b X_b) + A''_{bo} X_{bo} \exp (- E_b X_b)) \exp (B'''_d X_d \exp (D'_b X_b)) \quad (4.13).$$

The values of A'''_d, C'_b, A''_{bo}, E_b, B'''_d and D'_b obtained by the least squares fitting to Eq. (4.13) are shown in Table 4.8. By applying the values in Table 4.8, the helium productions can be obtained within 8 % difference by using the analytical representation Eq. (4.13) compared with those by the Monte Carlo calculation. The analytical representation (4.13) can be applied with good accuracy in the range of 1 to 6 cm diametric ducts, 0.1 to 100 wppm boron contents and 30 to 50 cm thick blankets.

4.3.2 Nuclear properties in the super-conductive magnet

Dependencies of the nuclear heating rate in the TF coil case surface along the duct on the duct diameter are shown in Fig. 4.9 for the 35 and 45 cm thick blankets and 40 cm thick vacuum vessel. In Chapter 3.3.4.1, it is shown that the nuclear properties in the TF coil along the slit increase in proportion to the exponential or power functions of the slit width. On the other hand, significant differences are not found among the 1 – 6 diametric duct for the nuclear properties of the super conductive TF coil as seen in Fig. 4.9, though the nuclear

properties slightly increase with the duct diameter. Therefore it can be concluded that the nuclear properties can be evaluated without taking into account the radiation streaming through the 1 – 6 diametric duct.

4.3.3 Dependencies on the blanket composition

Dependency of the helium productions on the blanket composition is shown in Fig. 4.10. Figure 4.10 shows the examples for the case of 45 cm thick blanket with the 3 cm diametric duct, and the 10, 30 and 100 wppm boron contents. The horizontal axis corresponds to the volume fraction of SS in the blanket composition. It was found that the optimized composition to minimize the helium production in the cooling water pipe along the duct were range from 60 % SS/40 % water to 70 % SS/30 % water. The difference between the helium production obtained by the blanket compositions in the range from 50 % SS/50 % water to 90 % SS/10 % water and that from 60 % SS/40 % water to 70 % SS/30 % water is only 40 %. It is therefore expected that the helium productions can be estimated within 40 % difference for the blanket composition in the range from 50 % SS/50 % water to 90 % SS/10 % water by using the values in Table 4.8 based on the blanket composed of 70 % SS/30 % water.

4.4 Application to Establishment of Shielding Design Constraint

The analytical representation Eq. (4.13) for the helium production as functions of the duct diameter X_d, the boron content X_{bo} and the blanket thickness X_b can be applied to clarify the shielding design constraint required to satisfy the shielding design criteria by using the following formulae;

$$Y_h \leq L_h / S_h \qquad (4.14),$$

where Y_h, L_h and S_h are the helium production (appm) obtained by the analytical representation Eq. (4.13), the shielding design criteria specified for rewelding and a safety factor in the shielding calculation, respectively. Using Eq. (4.14) and the analytical representation Eq. (4.13), the shielding design constraint can be easily selected as follows;

$$(A'''_d \exp(-C'_b X_b) + A''_{bo} X_{bo} \exp(-E_b X_b)) \exp(B''_d X_d \exp(D'_b X_b)) \leq L_h / (S_h N P) \qquad (4.15).$$

The formula Eq. (4.15) is applied to the ITER shielding design with the values in Table 4.8. It is assumed that the rewelding of SS in the cooling water branch pipe can be accomplished if the integrated helium production is less than 3 appm. The integrated neutron wall loading of 0.5 MWa/m^2 is assumed in this Chapter. Similarly to Chapter 3.4.1, it is assumed that the calculation uncertainty by MCNP with FENDL is less than 30 % for the estimation of the helium production. Disagreement of the helium production obtained by the analytical representation Eq. (4.13) is less than 8 % compared with that by MCNP with FENDL, then a safety factor of 1.4, which corresponds to the value of 1.3 * 1.08, is considered in this Chapter.

The values of L_h, S_h and N P applied to the shielding design are 3 appm, 1.4 and 0.5 MWa/m^2, respectively. By inputting these values into Eq. (4.15), the shielding design constraint for combination of the duct diameter X_d, the boron content X_{bo} and the blanket thickness X_b required to satisfy the shielding design criteria can be given as shown in Fig. 4.11. If a combination of the duct diameter and boron content exist in the lower region of each curve, the helium production can satisfy the criteria for the respective blanket thickness. In case the 3 cm diametric duct is applied to the 25 and 35 cm thick blankets, it is found that SS with less than 10 and 49 wppm boron contents are required to be applied, respectively. In the case of the 45 cm thick blanket with the 100 wppm boron content, the helium production can fully satisfy the shielding design criteria. If the SS with less than 79 wppm boron content is applied, it is found that the duct diameter can be widen to 6 cm.

4.5 Conclusion

Three dimensional Monte Carlo calculations are performed taking into account the radiation streaming through the small circular duct in the blanket module.

(1) The analytical representations on the helium productions in the plug of cooling water branch pipes are established as functions of the duct diameter, the blanket thickness and the boron content.
(2) By using the analytical representation, the helium production can be estimated within 8 difference compared with the results by the Monte Carlo calculation in the compositions of 70 % SS/30 % water in the blanket.
(3) By using the analytical representation, the helium production can be estimated within 40 % difference compared with the results by the Monte Carlo calculation in the compositions of 50 % SS/50 % water and 90 % SS/10 % water in the blanket.
(4) The analytical representation is applied to clarify the shielding design conditions required to satisfy the shielding design criteria for the shielding design.
(5) Significant differences are not been found among the 1 – 6 diametric duct for the nuclear properties in the TF coil along the duct.
(6) The analytical representation is applied to clarify the shielding design constraint required to satisfy the shielding design criteria.

References

[4.1] S. Sato, T. Nakamura, T. Nishitani, Helium Production due to Neutron Streaming through Small Circular Ducts in Fusion Reactor Blanket by Analytical Fitting from Monte Carlo Calculation Results, Fusion Sci. Technol., 43, 559-568 (2003).

[4.2] S. Sato, H. Iida, R. Plenteda, R. T. Santoro, Monte Carlo Analysis of Helium Production in the ITER Shielding Blanket Module, Fusion Eng. Design, 46, 1-9 (1999).

[4.3] S. Sato, Establishment of Shielding Design Conditions in Fusion Shielding Blanket by 3-D Monte Carlo Calculation, J. Nucl. Sci. Technol., Supplement 1, 253-257 (2000).

Table 4.1 Calculational condition

Blanket thickness (cm)	25, 35, 45
Boron content in the plug (wppm)	0.1, 0.2, 0.3, 0.5, 1, 2, 3, 5, 10, 20, 30, 50, 100
Duct diameter (cm)	0, 1, 2, 3, 4, 5, 6
Blanket composition (%)	SS/H_2O = 0/100, 10/90, 20/80, 30/70, 40/60, 50/50, 60/40, 70/30, 80/20, 90/10, 100/0

Table 4.2 Calculation results for the helium production at the plug of the cooling water branch pipe with 10 wppm boron content along the 3 cm diametric hole.

Blanket thickness (cm)	Helium production (appm)	Relative error
25	4.40E+00	0.0370
35	1.38E+00	0.0391
45	4.04E-01	0.0553

Table 4.3 The values of A_d and B_d in the analytical representation Eq. (4.1) on the helium production at the plug of the cooling water branch pipe along the small circular duct as a function of the duct diameter for various blanket thicknesses and boron contents. The blanket composition is 70 % SS and 30 % water.

Blanket thickness (cm)	Boron content (wppm)	A_d (appm/MWa/m^2)	B_d (cm^{-1})	Error*
25	100	1.44E+01	0.164	1.015
	30	5.34E+00	0.166	1.108
	10	2.58E+00	0.172	1.078
35	100	4.81E+00	0.176	1.032
	30	1.59E+00	0.189	1.029
	10	7.38E-01	0.195	1.053
45	100	1.32E+00	0.222	1.020
	30	4.53E-01	0.226	1.019
	10	2.01E-01	0.239	1.037

Error*: Maximum values of the ratio between the helium productions obtained by the analytically using Eq. (4.1) to those by the Monte Carlo calculation.

Table 4.4 The values of A_b and B_b in the analytical representation (4.2) on the helium production at the plug of the cooling water branch pipe along the small circular duct as a function of the blanket thickness for various duct diameters and boron contents, and the required blanket thickness T_b to reduce the helium production by one order of magnitude. The blanket composition is 70 % SS and 30 % water.

Duct diameter	Boron content (wppm)	A_b	B_b	T_b	Error*
1 cm	100	1.24E+02	0.116	19.8	1.045
	30	4.99E+01	0.121	19.0	1.005
	10	2.24E+01	0.121	19.0	1.015
3 cm	100	1.60E+02	0.111	20.7	1.021
	30	6.17E+01	0.114	20.1	1.024
	10	3.39E+01	0.119	19.3	1.027
5 cm	100	2.01E+02	0.106	21.8	1.041
	30	7.45E+01	0.107	21.5	1.016
	10	3.85E+01	0.110	21.0	1.001
6 cm	100	2.10E+02	0.101	22.9	1.019
	30	7.59E+01	0.102	22.7	1.028
	10	4.52E+01	0.108	21.3	1.068

Error*: Maximum values of the ratio between the helium productions obtained by the analytically using Eq. (4.2) to those by the Monte Carlo calculation.

Table 4.5 The values of A_{bo} and B_{bo} in the analytical representation Eq. (4.4) on the helium production at the plug of the cooling water branch pipe along the small circular duct as a function of the boron content for various duct diameters and blanket thicknesses. The blanket composition is 70 % SS and 30 % water.

Blanket thickness	Duct diameter	A_{bo}	B_{bo}	Error*
25 cm	1 cm	1.47E+00	1.55E-01	1.063
	2 cm	1.82E+00	1.80E-01	1.000
	3 cm	2.23E+00	2.17E-01	1.001
	4 cm	2.35E+00	2.81E-01	1.001
	5 cm	2.96E+00	2.99E-01	1.001
	6 cm	3.94E+00	3.43E-01	1.000
35 cm	1 cm	3.14E-01	5.34E-02	1.004
	2 cm	3.93E-01	6.59E-02	1.063
	3 cm	6.37E-01	7.45E-02	1.001
	4 cm	7.35E-01	8.88E-02	1.001
	5 cm	8.78E-01	1.11E-01	1.001
	6 cm	1.04E+00	1.26E-01	1.004
45 cm	1 cm	1.01E-01	1.56E-02	1.051
	2 cm	1.43E-01	1.92E-02	1.010
	3 cm	1.65E-01	2.41E-02	1.016
	4 cm	2.49E-01	2.85E-02	1.001
	5 cm	2.92E-01	3.69E-02	1.001
	6 cm	3.73E-01	4.73E-02	1.002

Error*: Maximum values of the ratio between the helium productions obtained by the analytically using Eq. (4.4) to those by the Monte Carlo calculation.

Table 4.6 The values of A'_d, C_b, B'_d and D_b in the analytical representation Eq. (4.7) on the helium production at the plug of the cooling water branch pipe along the small circular duct as functions of the duct diameter and the blanket thickness for various boron contents. The blanket composition is 70 % SS and 30 % water.

Boron content	A'_d	C_b	B'_d	D_b	Error*
100 wppm	1.14E+02	0.120	0.124	0.0151	1.055
30 wppm	4.38E+01	0.123	0.126	0.0155	1.061
10 wppm	2.28E+01	0.128	0.129	0.0165	1.080

Error*: Maximum values of the ratio between the helium productions obtained by The analytically using Eq. (4.7) to those by the Monte Carlo calculation.

Table 4.7 The values of A''_d, A'_{bo} and B''_d in the analytical representation Eq. (4.9) on the helium production at the plug of the cooling water branch pipe along the small circular duct as functions of the duct diameter and the boron contents for various blanket thicknesses. The blanket composition is 70 % SS and30 % water.

Blanket thickness (cm)	A''_d	A'_{bo}	B''_d	Error*
25	1.33E+00	1.31E-01	0.167	1.098
35	2.60E-01	4.54E-02	0.187	1.104
45	8.07E-02	1.24E-02	0.234	1.107

Error*: Maximum values of the ratio between the helium productions obtained by The analytically using Eq. (4.9) to those by the Monte Carlo calculation.

Table 4.8 The values of A'''_d, C'_b, A''_{bo}, E_b, B'''_d and D'_b in the analytical representation Eq. (4.13) on the helium production at the plug of the cooling water branch pipe along the small circular duct as functions of the duct diameter, the blanket thickness and the boron contents for various blanket thicknesses. The blanket composition is 70 % SS and30 % water.

A'''_d	C'_b	A''_{bo}	E_b	B'''_d	D'_b
13.3	0.14	1.01	0.118	0.126	0.0157

This is a blank page.

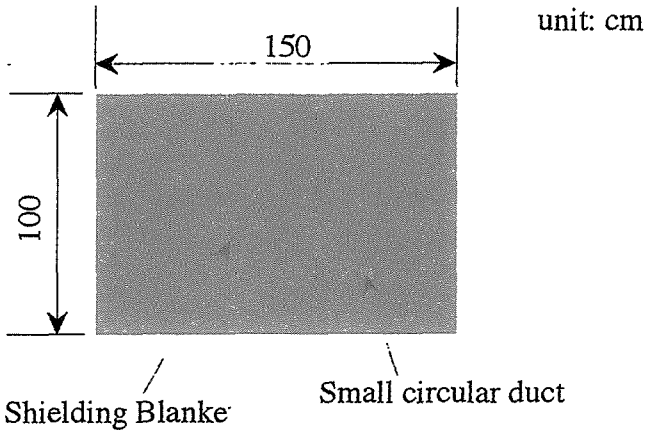

Vertical view

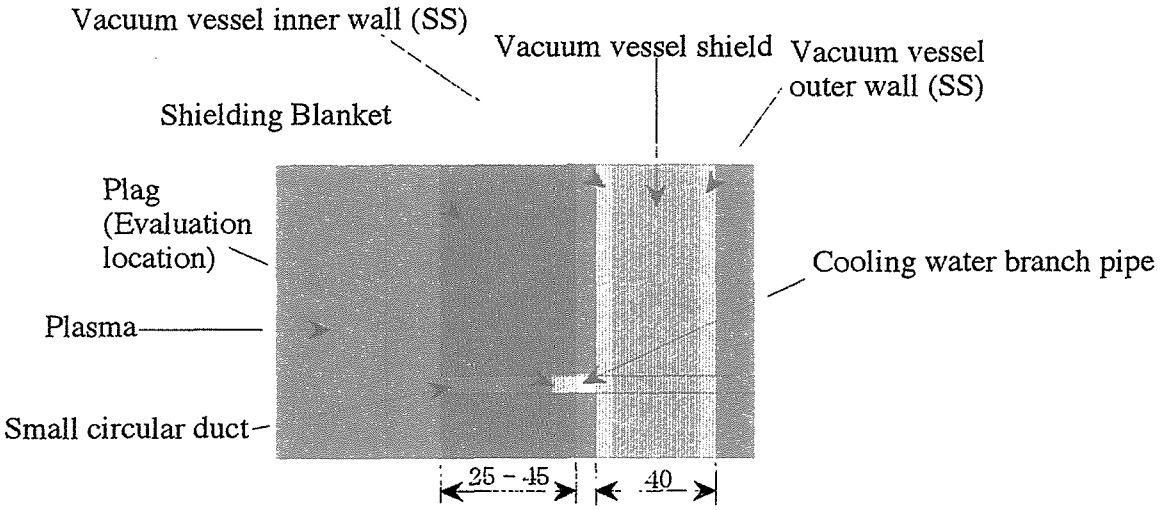

Horizontal view

Fig. 4.1 Three dimensional Monte Carlo calculational geometry used in the study about the streaming through small circular duct in blanket.

This is a blank page.

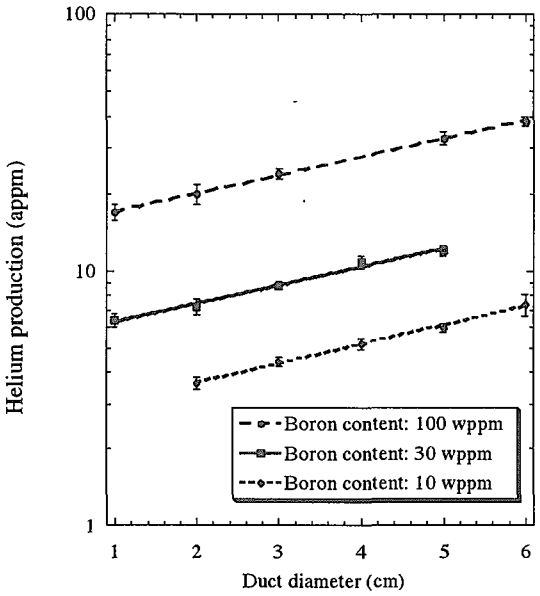

(a) Blanket thickness: 25 cm,
Blanket thickness to the plug: 17 cm

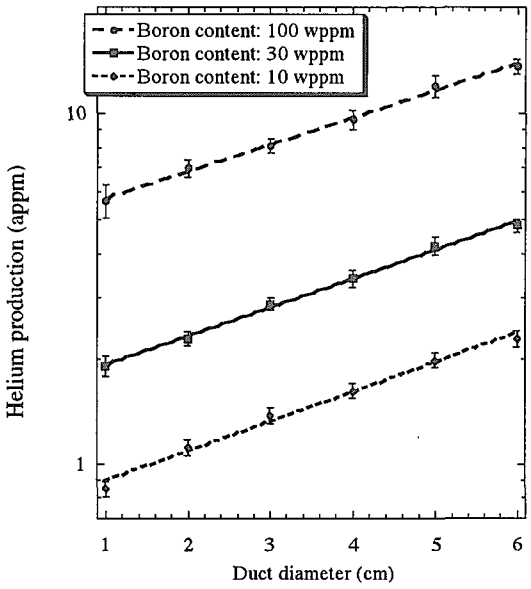

(b) Blanket thickness: 35 cm,
Blanket thickness to the plug: 27 cm

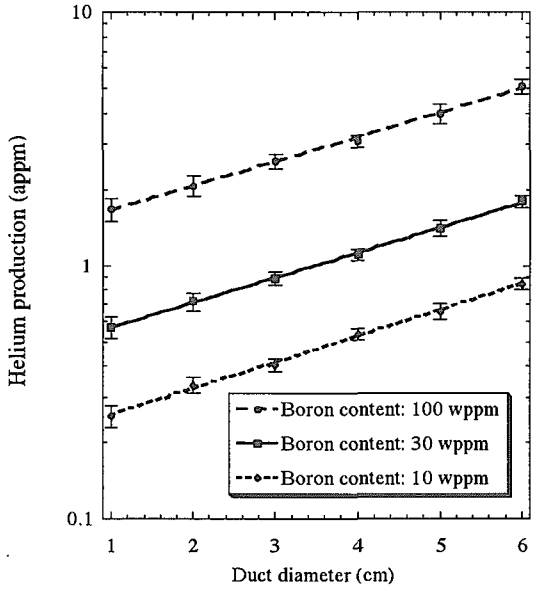

(c) Blanket thickness: 45 cm,
Blanket thickness to the plug: 37 cm

Fig. 4.2 Dependency of the helium production on the duct diameter at the plug of the cooling water branch pipe along the small circular duct. The integrated neutron wall loading is 1 MWa/m^2, the blanket composition is 70 % SS and 30 % water.

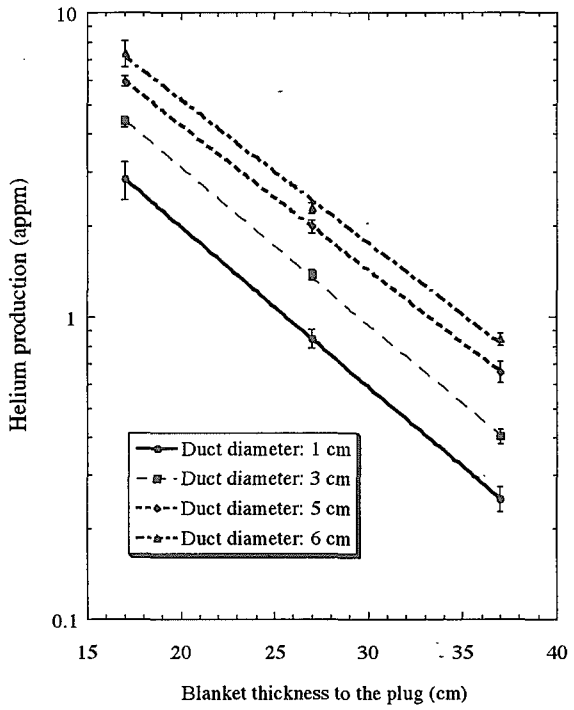

(a) Boron content in the plug: 10 wppm

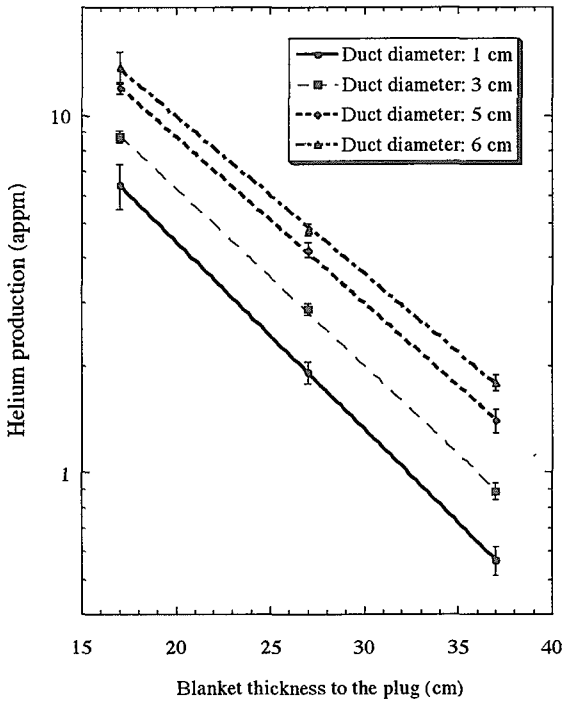

(b) Boron content in the plug: 30 wppm

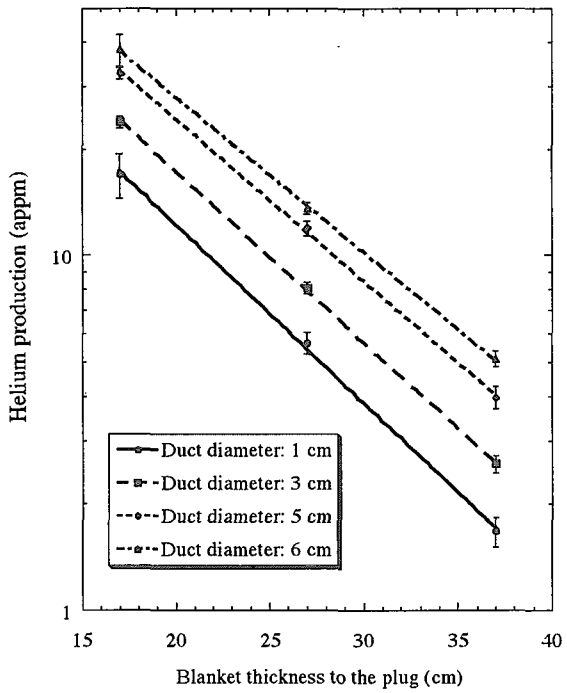

(c) Boron content in the plug: 100 wppm

Figs. 4.3 Dependency of the helium production on the blanket thickness at the plug of the cooling water branch pipe along the small circular duct. The integrated neutron wall loading is 1 MWa/m^2, the blanket composition is 70 % SS and 30 % water.

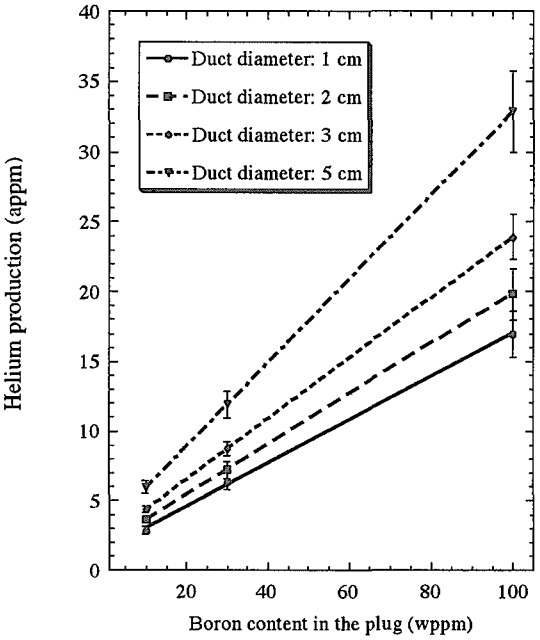

(a) Blanket thickness: 25 cm,
Blanket thickness to the plug: 17 cm

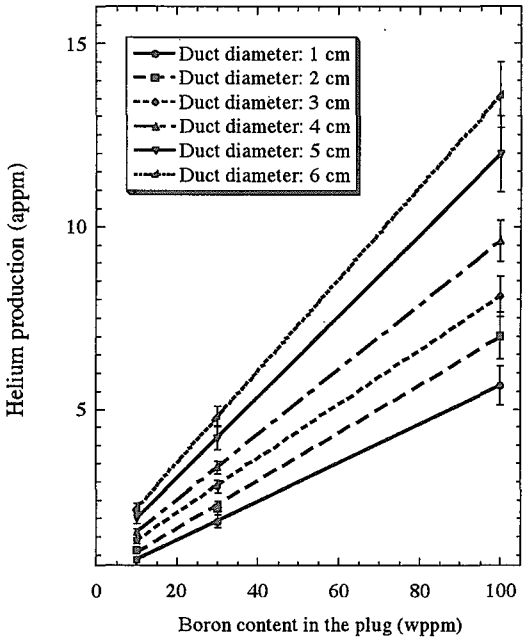

(b) Blanket thickness: 35 cm,
Blanket thickness to the plug: 27 cm

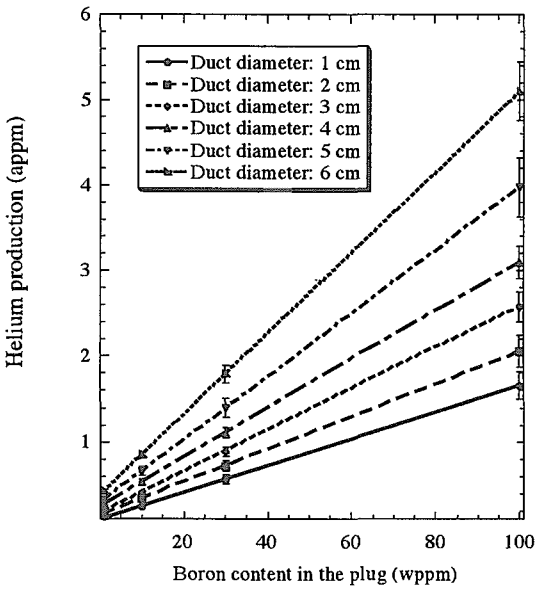

(c) Blanket thickness: 45 cm,
Blanket thickness to the plug: 37 cm

Figs. 4.4 Dependency of the helium production on the boron content at the plug of the cooling water branch pipe along the small circular duct. The integrated neutron wall loading is 1 MWa/m^2, the blanket composition is 70 % SS and 30 % water.

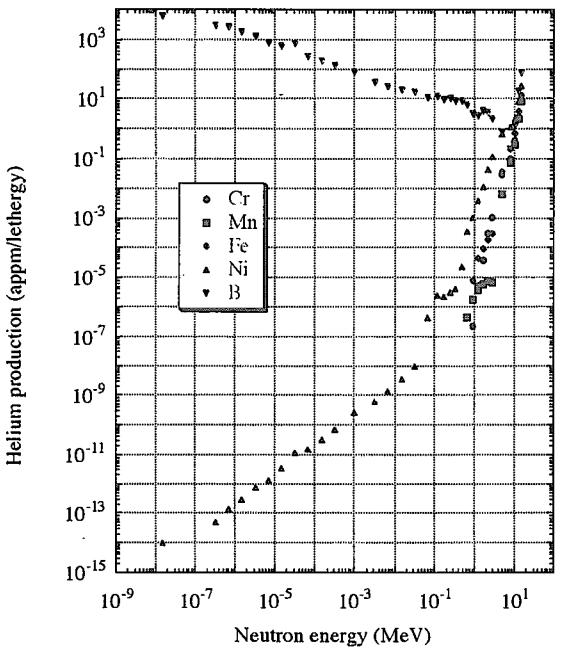

Fig. 4.5 Helium productions at the plug of the cooling water branch pipe by each element with 10 wppm boron. The blanket thickness is 45 cm, and the blanket thickness to the plug is 37 cm.

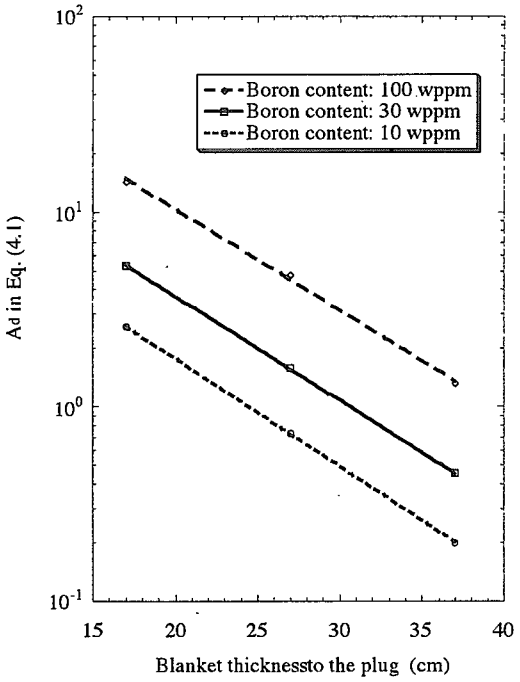

Fig. 4.6 Dependency of the values of Ad in Eq. (4.1) on the blanket thickness.

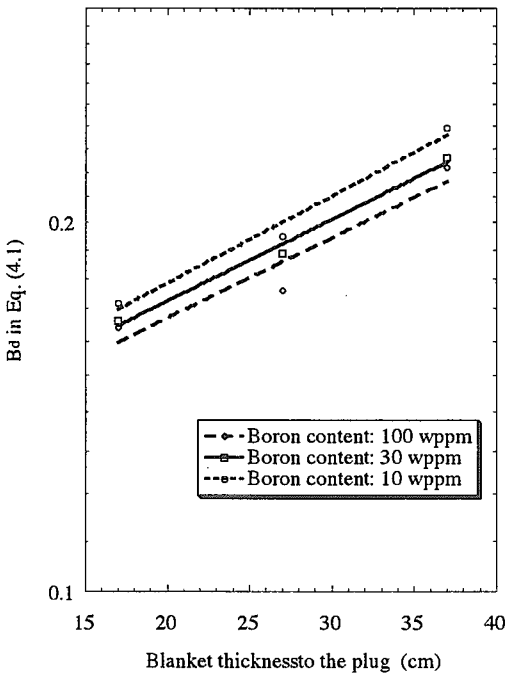

Fig. 4.7 Dependency of the values of Bd in Eq. (4.1) on the blanket thickness.

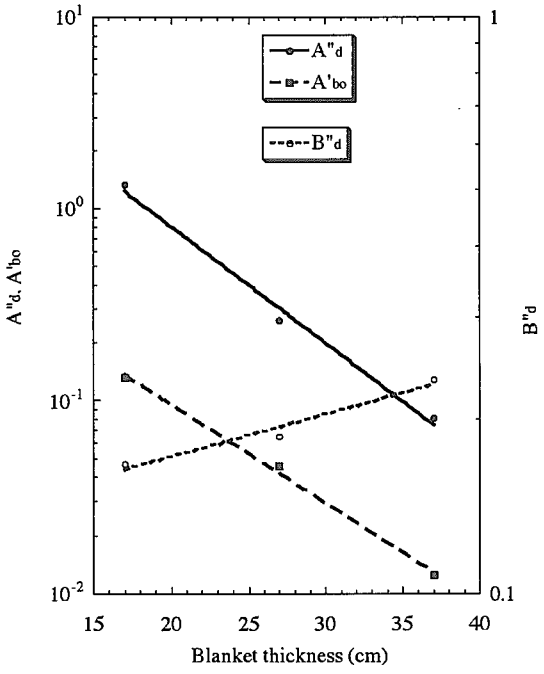

Fig. 4.8 Dependencies of the values in A"d, A'bo and B"d on the blanket thickness.

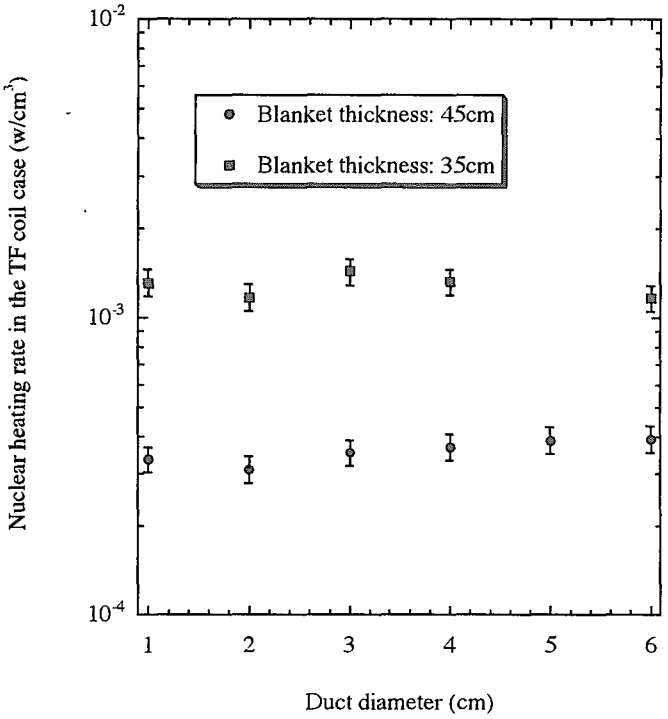

Fig. 4.9 Dependency of the peak nuclear heating rate on the duct diameter in the TF coil case along the small circular duct. The neutron wall loading is 1 MW/m^2, the blanket composition is 70 % SS and 30 % water, the blanket thickness is 45 cm, and the vacuum vessel thickness is 40 cm.

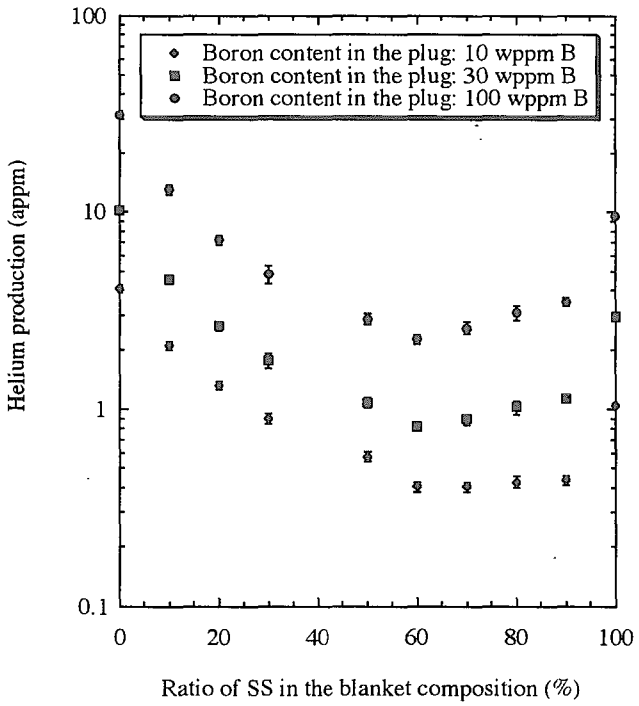

Fig. 4.10 Dependency of the helium production on the blanket composition at the plug of the cooling water branch pipe along the small circular duct. The integrated neutron wall loading is 1 MWa/m^2, the duct diameter is 3 cm, the blanket thickness is 45 cm, and the blanket thickness to the plug is 37 cm.

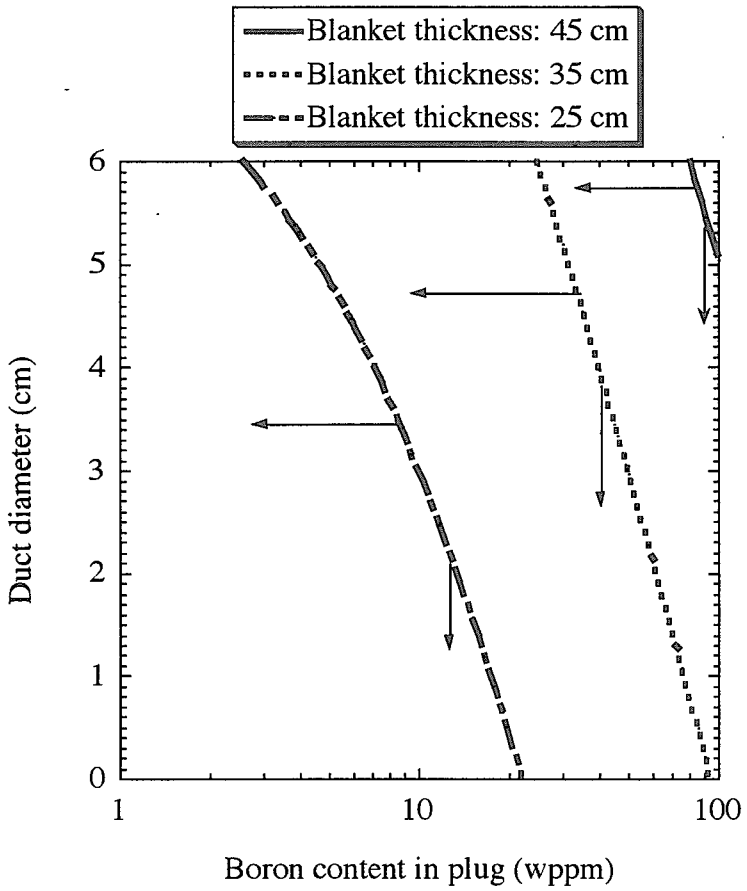

Fig. 4.11 The shielding design conditions about combination of the duct diameter, the boron content and the blanket thickness required to satisfy the shielding design criteria. In the left and lower region of the curved line, the helium productions can satisfy the criteria. The blanket composition is 70 % SS and 30 % water. The shielding design criteria is 3 appm for rewelding of SS, a safety factor is 1.41 and the integrated neutron wall loading is 0.5 MWa/m^2.

5 Nuclear Properties in the TF Coil around Large Opening Duct in Vacuum Vessel

5.1 Introduction

Radiation streaming through the small circular duct in the blanket modules is discussed in Chapter 4, and the nuclear properties are discussed in the blanket, the vacuum vessel and the TF coil along the slit and duct. In addition to the small circular duct in the blanket modules, there are large opening ducts penetrating the blanket and the vacuum vessel as shown in Figs 1.1, 2.7 and 2.8. The nuclear properties are enhanced in the TF coil adjacent to the duct by the radiation streaming through the large opening duct in the vacuum vessel. In this Chapter, the radiation streaming through the large opening duct in the vacuum vessel is described.

In the tokamak-type DT fusion reactor, large opening ducts are located in the confined space between the adjacent to TF coils as mentioned in Chapter 1 [5.1 – 5.10]. These ducts are used for the beam injection, exhausting the impurity, diagnostics, maintenance for the blanket and divertor, and so on. Because of the space limitation due to the reactor configuration, TF coils locate close to the duct and would be damaged by the radiation streaming through the duct. The nuclear heating and the radiation damage in the TF coils are enhanced by the radiation streaming through the duct, therefore they cause a critical concern with sound operation of the TF coils.

In order to reduce the radiation streaming through the duct, the shield plug will be installed inside the duct as shown in Fig. 5.1, if possible [5.9, 5.10]. The adjacent duct wall and shield plug are separated by a few centimeter wide slits in the poloidal (vertical) and toroidal (horizontal) directions. It is expected that the nuclear properties in the TF coil adjacent to the duct are drastically reduced by installing the shield plug, while they are enhanced by the radiation streaming through the slit between the duct wall and the shield plug. Therefore in order to also reduce the radiation streaming through the slit, the step configuration is applied to the slit, if possible [5.11, 5.12].

In this Chapter, these nuclear properties are calculated taking into account the radiation streaming through the duct without and with the shield plug by using the three dimensional Monte Carlo code, and their analytical representations are established from the Monte Carlo results.

By changing systematically the calculational geometry, the peak nuclear properties in the TF coil adjacent to the duct without the shield plug are calculated for the following parameters;

1) the duct opening height,
2) the duct opening width,
3) the duct wall thickness,
4) the shield thickness, which corresponds to the sum of the blanket and the vacuum vessel thickness adjacent to the duct.

The analytical representations on the peak nuclear properties in the TF coil adjacent to the

duct are established as functions of these parameters. Dependencies of the nuclear properties on the duct wall and the shield compositions are also clarified. The analytical formula thus-obtained is applied to clarify the shielding design conditions required to satisfy the shielding design criteria for the DT fusion reactor.

Also for the duct with the shield plug, the peak nuclear properties are calculated for the following parameters;

1) the slit width between the duct wall and the shield plug,
2) the shield plug thickness installed inside the duct opening,
3) the duct wall thickness.

The analytical representations on the peak nuclear properties in the TF coil adjacent to the duct with the shield plug are established as functions of these parameters.

In case the step configuration is applied to the slit between the duct wall and the shield plug, the peak nuclear properties in the TF coil adjacent to the duct are calculated for the following parameters;

1) the step width,
2) the step thickness,
3) the step position.

Dependencies on these parameters are clarified, the effective step configuration is proposed from view point of the shielding design.

In Chapter 5.3, the radiation streaming is described for the duct without the shield plug inside the duct. In the case of the NBI duct, the shield plug can not be installed inside the duct due to the direct beam injection to the plasma. In Chapter 5.4, the radiation streaming is described for the duct with the shield plug inside the duct, and the slit between the shield plug and the duct wall is not step configuration. In the maintenance duct, it is possible to install the shield duct inside the duct as shown in Fig. 5.1, and the shield plug is pulled out during the maintenance. In Chapter 5.5, the radiation streaming is evaluated for the duct with the shield plug inside the duct, and the step configuration is applied to the slit between the shield plug and the duct wall. Although the structural design becomes difficult in the case of application of the step configuration, the radiation streaming through the slit is expected to be drastically reduced.

5.2 Calculation Method

By the same method as Chapter 3.2, the nuclear properties in the TF coil are calculated using the Monte Carlo calculation code MCNP-4B and the fusion evaluated nuclear data library FENDL-2. The calculational geometry used in the calculation are shown in Figs. 5.2 – 5.4. The calculational geometry is shown in Fig. 5.2 for the duct without the shield plug. The calculational geometry is shown in Fig. 5.3 for the duct with the shield plug

without the step configuration, and it is shown in Fig. 5.4 for the duct with the shield plug with the step configuration. The calculational condition is shown in Table 5.1.

5.3 Duct without Shield Plug

In case the shield plug is not installed inside the duct opening, the peak nuclear properties in the TF coil adjacent to the duct are calculated at the neutron wall loading and the integrated one of 1 MW/m^2 and 1 MWa/m^2, respectively, in this Chapter.

5.3.1 Dependency on duct opening height

Some calculated results are shown in Table 5.2 with the statistical error for the 50, 80, 120, 200 and 280 cm high and 80 cm wide duct openings, the 30 cm thick duct wall, and the 200 cm thick shield just adjacent to the duct. The duct wall and the shield plug are composed of 60 % SS/40 % water and 80% SS/20 % water, respectively.

Dependencies on the duct opening height are shown in Figs. 5.5 – 5.8. Figure 5.5 shows an example for the case of the 120 cm wide duct opening, the 20 cm thick duct wall and the 100 cm thick shield adjacent to the duct. Figure 5.6 shows an example for the case of the 160 cm wide duct opening, the 30 cm thick duct wall and the 100 cm thick shield adjacent to the duct. Figure 5.7 shows an example for the case of the 80 cm wide duct opening, the 40 cm thick duct wall and the 100 cm thick shield adjacent to the duct. Figure 5.8 shows an example for the case of the 80 cm wide duct opening, the 40 cm thick duct wall and the 200 cm thick shield adjacent to the duct. It was found that all peak nuclear properties in the TF coil adjacent to the duct increased linearly with the duct opening height in the range of 50 – 280 cm high duct opening. In Chapter 3.3.3.1, it is discussed that the helium productions in the vacuum vessel wall along the slit increase linearly with the slit width between the adjacent blanket modules due to the increase of the incident 14 MeV neutron flux to the slit. Similarly to the dependency of the helium productions along the slit on the slit width, it is discussed that all peak nuclear properties in the TF coil adjacent to the duct increase linearly with the duct opening height due to the increase of the incident 14 MeV neutron flux to the duct. The analytical representation on the nuclear properties in the TF coil adjacent to the duct can be given as a function of the duct opening height, X_h (cm), as follows;

$$Y_c = N P (C_h + D_h (X_h - 50)) \quad (5.1).$$

The values of C_h and D_h obtained by the least squares fitting to Eq. (5.1) are shown in Tables 5.3 – 5.6 for various duct opening widths, duct wall thicknesses and shield thicknesses. The values of C_h correspond to the nuclear properties in the 50 cm high duct opening at the neutron wall loading and the integrated one of 1 MW/m^2 and 1 MWa/m^2, respectively. Disagreement of the nuclear properties obtained by the analytical representation Eq. (5.1) with the values in Tables 5.3 – 5.6 are 6 to 31, 6 to 42 and 6 to 50 % compared with those by the Monte Carlo calculation for the 20. 30 and 40 cm thick duct walls, respectively. The values of C_h and D_h increase in proportion to the power function of the duct opening width,

and they decrease exponentially with the duct wall thickness and the shield thickness adjacent to the duct. Detailed discussions on the values of C_h and D_h are described in Chapters 5.3.2 – 5.3.4.

5.3.2 Dependency on duct opening width

Dependencies on the duct opening width are shown in Figs. 5.9 – 5.11. Figures 5.9 and 5.10 show the nuclear heating rate in the winding pack, the neutron damage in the stabilizer copper, the neutron fluence of the energies above 0.1 and 1 MeV in the winding pack for the 30 cm thick duct wall, the 100 cm thick shield adjacent to the duct, and the 50 and 160 cm high duct opening, respectively. Figure 5.11 shows the nuclear heating rate in the winding pack for the 30 cm thick duct wall, the 200 cm thick shield adjacent to the duct, and the 50, 80, 120, 200 and 280 cm high duct openings. It was found that all nuclear properties in the TF coil adjacent to the duct increased in proportion to the power function of the duct opening width in the range of 50 – 160 cm wide duct opening. In Chapter 3.3.4.1, it is discussed that the nuclear properties in the TF coil along the slit between adjacent blanket modules increase in proportion to the power function of the slit width. Similarly to the dependency of the nuclear properties in the TF coil along the slit on the slit width, it is discussed that the nuclear properties in the TF coil adjacent to the duct increase in proportion to the power function of the duct opening width. The analytical representation on the nuclear properties adjacent to the duct can be established as a function of the duct opening width, X_w (cm), as follows;

$$Y_c = N P C_w X_w^{D_w} \quad (5.2).$$

The values of C_w and D_w obtained by the least squares fitting to Eq. (5.2) are shown in Table 5.7 for various high duct openings, the 30 cm thick duct wall and the 100 and 200 cm thick shields adjacent to the duct. Disagreement of the nuclear properties obtained by the analytical representation Eq. (5.2) with the values shown in Table 5.7 is 0.6 to 9 % compared with those by the Monte Carlo calculation.

Dependencies of the C_h and D_h values in Eq. (5.1) on the duct opening width are shown in Fig. 5.12. Figure 5.12 shows the example of the nuclear heating rate in the winding pack for the 20 cm thick duct wall and the 130 cm thick shield adjacent to the duct. Similarly to Eq. (5.2), it was found that all C_h and D_h values in Eq. (5.1) also increased in proportion to the power function of the duct opening width. The values of C_h and D_h can be given approximately by a function of the duct opening width X_w as follows;

$$C_h = C_{h/w} X_w^{C'_{h/w}} \quad (5.3),$$

$$D_h = D_{h/w} X_w^{D'_{h/w}} \quad (5.4).$$

From the analytical representation (5.1), and the formulae (5.3) and (5.4), the analytical representation on the nuclear properties can be given as functions of the duct opening height

X_h and the width X_w as follows;

$$Y_c = N\,P\,(C_{h/w}\, X_w^{\,C'_{h/w}} + D_{h/w}\, X_w^{\,D'_{h/w}\,(X_h - 50)}) \qquad (5.5).$$

The values of $C_{h/w}$, $C'_{h/w}$, $D_{h/w}$ and $D'_{h/w}$ obtained by the least squares fitting to Eq. (5.5) are shown in Table 5.8 for various duct wall thicknesses and shield thicknesses. Disagreement of the nuclear properties obtained by the analytical representation Eq. (5.5) with the values shown in Table 5.8 is 27 to 42 % compared with those by the Monte Carlo calculation.

5.3.3 Dependency on duct wall thickness

Dependency on the duct wall thickness is shown in Fig. 5.13 for various duct opening heights, the 80 cm wide duct opening and the 130 cm thick shield adjacent to the duct. It was found that the nuclear properties in the TF coil adjacent to the duct decreased exponentially with the duct wall thickness. In Chapter 3.3.4.2, it is discussed that the nuclear properties in the TF coil along the slit between the adjacent blanket modules decrease exponentially with the blanket thickness. Similarly to the dependency of the nuclear properties in the TF coil along the slit on the blanket thickness, it is discussed that all nuclear properties in the TF coil adjacent to the duct decrease exponentially with the duct wall thickness. The analytical representation on the nuclear properties can be given as a function of the duct wall thickness, X_{wa} (cm), as follows;

$$Y_c = N\,P\,C_{wa} \exp (- D_{wa}\, X_{wa}) \qquad (5.6),$$
$$T_{wa} = \ln 10 / D_{wa} \qquad (5.7).$$

The values of C_{wa} and D_{wa} obtained by the least squares fitting to Eq. (5.6) are shown in Tables 5.9 for various duct opening heights, the 80 cm wide duct opening and the 130 cm thick shield. Disagreement of the nuclear properties obtained by the analytical representation (5.6) with the values in Tables 5.9 is 0.2 to 6 % compared with those by the Monte Carlo calculation. The values of T_{wa} correspond to the duct wall thickness required to reduce the nuclear properties by one order of magnitude, and they are also shown in Tables 5.8. The T_{wa} values are almost constant, and they are 15 - 17 cm thickness.

Dependencies of the C_h and D_h values in Eq. (5.1) on the duct wall thickness are shown in Fig. 5.14. Figure 5.14 shows the example of the nuclear heating rate in the winding pack for the 80 cm wide duct opening and the 130 cm thick shield adjacent to the duct. Similarly to Eq. (5.6), it was found that the C_h and D_h values in Eq. (5.1) also decreased exponentially with the duct wall thickness. The values of C_h and D_h can be given approximately by an exponential function of the duct wall thickness X_{wall} as follows;

$$C_h = C_{h/wa} \exp (- C'_{h/wa}\, X_{wa}) \qquad (5.8),$$
$$D_h = D_{h/wa} \exp (- D'_{h/wa}\, X_{wa}) \qquad (5.9).$$

From the analytical representation Eq. (5.1), and the formulae (5.8) and (5.9), the analytical representation on the nuclear properties can be given as functions of the duct opening height X_h and the duct wall thickness X_{wa} as follows;

$$Y_c = N P (C_{h/wa} \exp (- C'_{h/wa} X_{wa}) + D_{h/wa} \exp (- D'_{h/wa} X_{wa}) (X_h - 50)) \quad (5.10).$$

The values of $C_{h/wa}$, $C'_{h/wa}$, $D_{h/wa}$ and $D'_{h/wa}$ obtained by the least squares fitting to Eq. (5.10) are shown in Tables 5.10 – 5.13 for various duct opening widths and the 130 and 200 cm thick shields. Disagreement of the nuclear properties obtained by the analytical representation Eq. (5.10) with the values shown in Tables 5.10 – 5.13 is less than 32 % compared with those by the Monte Carlo calculation.

5.3.4 Dependency on shield thickness

Dependencies on the shield thickness are shown in Fig. 5.15 for the 80 cm wide duct opening and the 30 cm thick duct wall. It was found that the nuclear properties in the TF coil adjacent to the duct decreased exponentially with the shield thickness. Although most of the peak nuclear heating rate in the TF coil winding pack adjacent to the duct are generated by the radiation streaming through the duct, it is expected that some of the radiation streaming through the shield adjacent to the duct may contribute the peak nuclear heating rate. Similarly to the dependency on the duct wall thickness shown in Chapter 5.3.3, it is expected that some of the radiation streaming decrease exponentially with the shield thickness. Therefore, it is discussed that the nuclear properties in the TF coil adjacent to the duct decrease exponentially with the shield thickness. The analytical representation on the nuclear properties can be given as a function of the shield thickness, X_{sh} (cm), as follows;

$$Y_c = N P C_{sh} \exp (- D_{sh} X_{sh}) \quad (5.11),$$
$$T_{sh} = \ln 10 / D_{sh} \quad (5.12).$$

The values of C_{sh} and D_{sh} obtained by the least squares fitting to Eq. (5.11) are shown in Table 5.14 for various duct opening heights, 80 cm wide duct opening and 30 cm thick duct wall. Disagreement of the nuclear properties obtained by the analytical representation Eq. (5.11) with the values shown in Table 5.14 is 0.4 to 6 % compared with those by the Monte Carlo calculation. The T_{sh} values correspond to the shield thickness required to reduce the nuclear properties by one order of magnitude, and they are also shown in Tables 5.14. The T_{sh} values are 200 - 250 cm thickness. The T_{sh} values are much large compared with the T_{wa} values shown in Chapter 5.3.3 because the neutron streaming through the duct is much lower than that through the shield adjacent to the duct as mentioned above. Therefore in order to enhance the shielding performance, i. e. reduction of the nuclear properties in the TF coil adjacent to the duct, it is not so effective to increase the shield thickness adjacent to the duct.

Dependencies of the C_h and D_h values in Eq. (5.1) representing on the shield thickness adjacent to the duct are shown in Fig. 5.16. Figure 5.16 shows the example of the nuclear heating rate in the winding pack for the 80 cm wide duct opening and the 20 cm thick duct

wall. Similarly to Eq. (5.11), it was found that the C_h and D_h values in Eq. (5.1) also decreased exponentially with the shield thickness. The values of C_h and D_h can be given approximately by an exponential function of the shield thickness X_{sh} as follows;

$$C_h = C_{h/sh} \exp (- C'_{h/sh} X_{sh}) \quad (5.13),$$
$$D_h = D_{h/sh} \exp (- D'_{h/sh} X_{sh}) \quad (5.14).$$

From the analytical representation Eq. (5.1), and the formulae (5.13) and (5.14), the analytical representation on the nuclear properties can be given as functions of the duct opening height X_h and the shield thickness X_{sh} as follows;

$$Y_c = N P (C_{h/sh} \exp (- C'_{h/sh} X_{sh}) + D_{h/sh} \exp (- D'_{h/sh} X_{sh}) * (X_h - 50)) \quad (5.15).$$

The values of $C_{h/sh}$, $C'_{h/sh}$, $D_{h/sh}$ and $D'_{h/sh}$ obtained by the least squares fitting to Eq. (5.15) are shown in Tables 5.15 – 5.18 for various wide duct openings, the 20 and 30 cm thick duct walls. Disagreement of the nuclear properties obtained by the analytical representation Eq. (5.15) with the values shown in Tables 5.15 – 5.18 is 15 to 41 % compared with those by the Monte Carlo calculation.

5.3.5 Dependency on duct wall composition

Dependencies on the duct wall composition are shown in Fig. 5.17. Figure 5.17 shows an example for the case of the 160 cm high and 160 cm wide duct opening, the 40 cm thick duct wall and the 100 cm thick shield. The shield adjacent to the duct is composed of 70 % SS/30 % water. It was found that the optimized composition to minimize the nuclear properties were range from 60 % SS/40 % water to 80 % SS/20 % water. In Chapters 5.3.1 – 5.3.4, the analytical representations on the nuclear properties in the TF coil adjacent to the duct as functions of the duct opening height, the duct opening width, the duct wall thickness and the shield thickness adjacent to the duct are given for the duct wall composition of 60 % SS/40 % water. The differences between the peak nuclear properties in the TF coil obtained by the duct wall composition in the range from 50 % SS/50 % water to 80 % SS/20 % water and that obtained by the duct wall composition with 60 % SS/40 % water are within 40 %. It is therefore expected that the peak nuclear properties in the TF coil can be estimated within 40 % difference for the duct wall composition in the range from 50 % SS/50 % water to 80 % SS/20 % water by using the established analytical representation based on the duct wall composition in 60 % SS/40 % water.

5.3.6 Dependency on shield composition

Dependencies on the shield composition adjacent to the duct is shown in Fig. 5.18. Figure 5.18 shows the example for the case of the 80 cm high and 80 cm wide duct opening, the 30 cm thick duct wall and the 200 cm thick shield. The duct wall is composed of 60 % SS/ 40 % water. The peak nuclear properties in the TF coil are almost constant for the shield

composition in the range from 10 % SS/90 % water to 90 % SS/10 % water, and the differences are within only 14 %. It can be concluded that the dependencies on the shield composition adjacent to the duct is very little for the peak nuclear properties in the TF coil adjacent to the duct.

5.3.7 Application to establishment of shielding design constraint

The analytical representations Eqs. (5.5), (5.10), (5.15) for the peak nuclear properties in the TF coil adjacent to the duct can be applied to clarify the shielding design constraint required to satisfy the shielding design criteria by using the following formulae;

$$Y_c \leq L_c / S_c \qquad (5.16),$$

Using Eq. (5.16) and the analytical representation Eqs. (5.5), (5.10), (5.15), the shielding design constraint can be easily selected as follows;

$$L_c / (S_c N P) \geq C_{h/w} X_w^{C'_{h/w}} + D_{h/w} (X_h - 50) X_{wa}^{D'_{h/w}} \qquad (5.17),$$

$$L_c / (S_c N P) \geq C_{h/wa} \exp (- C'_{h/wa} X_{wa}) + D_{h/wa} (X_h - 50) \exp (- D'_{h/wa} X_{wa}) \qquad (5.18),$$

$$L_c / (S_c N P) \geq C_{h/sh} \exp (- C'_{h/sh} X_{sh}) + D_{h/sh} (X_h - 50) \exp (- D'_{h/sh} * X_{sh}) \qquad (5.19).$$

5.4 Duct with Shield Plug without Step Configuration

In case the shield plug is installed inside the duct opening with the slit between the duct wall and the shield plug, the peak nuclear properties in the TF coil adjacent to the duct are calculated in this Chapter.

5.4.1 Dependency on slit width

Dependencies on the slit width are shown in Figs. 5.19 – 5.21. Figures 5.19 and 5.20 show the nuclear heating rate in the winding pack, the neutron damage in the stabilizer copper, the neutron fluence of the energies above 0.1 and 1 MeV in the winding pack for the 20 and 30 cm thick duct walls, respectively, and the 100 cm thick shield plug. Figure 5.21 shows the nuclear heating rate in the winding pack for the 10 cm thick duct wall and the 70, 100, 130, 160 and 200 cm thick shield plugs. It was found that the peak nuclear properties in the TF coil adjacent to the duct increased in proportion to the power function of the slit width. In Chapter 3.3.4.1, it is discussed that the nuclear properties in the TF coil along the slit between adjacent blanket modules increase in proportion to the power function of the slit width. Similarly to the dependency of the nuclear properties on the slit width in the TF coil along the slit, it is discussed that the peak nuclear properties in the TF coil adjacent to the duct with the shield plug increase in proportion to the power function of the slit width between the duct wall and the shield plug. The analytical representation on the nuclear properties can be given as a function of the slit width as follows;

$$Y_c = N P E_s X_s^{F_s}, \quad (5.20).$$

The values of E_s and F_s obtained by the least squares fitting to Eq. (5.20) are shown in Tables 5.19 – 5.22, for various duct walls and shield thicknesses. Disagreement of the nuclear properties obtained by the analytical representations Eq. (5.20) with the values shown in Tables 5.19 – 5.22 are 2 to 27 % compared with those by the Monte Carlo calculation. The F_s values are almost constant, therefore the more handy analytical representation on the nuclear properties can be given as a function of the slit width as follows;

$$Y_c = N P E_s X_s^{2.1}, \quad (5.21).$$

Disagreement of the nuclear properties obtained by the analytical representation Eq. (5.21) with the values in Tables 5.19 – 5.22 within are 5 to 45 % compared with those by the Monte Carlo calculation.

5.4.2 Dependency on duct wall thickness

Dependency on the duct wall thickness is shown in Fig. 5.22. Figure 5.22 shows the nuclear heating rate in the TF coil winding pack for the 80 cm high duct opening and the 100 cm thick shield plug. It was found that the nuclear properties in the TF coil adjacent to the duct decreased exponentially with the duct wall thickness. The analytical representation on the nuclear properties in the TF coil can be given as a function of the duct wall thickness as follows;

$$Y_c = N P E_{wa} \exp (- F_{wa} X_{wa}) \quad (5.22),$$
$$T_{wa} = \ln 10 / F_{wa} \quad (5.23).$$

The values of E_{wa} and F_{wa} obtained by the least squares fitting to Eq. (5.22) are shown in Table 5.22 for various slit widths and the 100 cm thick shield plug. Disagreement of the peak nuclear properties obtained by the analytical representation Eq. (5.22) with the values shown in Table 5.23 is 0.2 to 10 % compared with those by the Monte Carlo calculation. The T_{wa} values correspond to the duct wall thickness required to reduce the nuclear properties by one order of magnitude, and they are also shown in Table 5.23. The T_{wa} values are almost constant values, and they are 16 - 18 cm thickness.

Dependency of the E_s values in Eq. (5.21) on the duct wall thickness is shown in Fig. 5.23. Figure 5.23 shows the example of the nuclear heating rate in the winding pack for the 80 cm high duct opening and the 70 and 100 cm thick shield adjacent to the duct. Similarly to Eq. (5.22), it is found that the E_s values in Eq. (5.21) also decrease exponentially with the duct wall thickness. The E_s values can be given approximately by an exponential function of the duct wall thickness X_{wa} as follows;

$$E_s = E_{s/wa} \exp (- F_{s/wa} X_{wa}) \quad (5.24),$$

From the analytical representation Eq. (5.21) and the formula (5.24), the analytical representation on the nuclear properties in the TF coil can be given as functions of the slit width X_s and the duct wall thickness X_{wa} as follows;

$$Y_c = N P E_{s/wa} \exp (- F_{s/wa} X_{wa}) X_s^{2.1} \quad (5.25).$$

The $E_{s/wa}$ and $F_{s/wa}$ values obtained by the least squares fitting to Eq. (5.25) are shown in Table 5.24 for the 70 and 100 cm thick shield plugs. Disagreement of the peak nuclear properties obtained by the analytical representation Eq. (5.25) with the values shown in Table 5.24 are 50 and 22 % compared with those by the Monte Carlo calculation for the 70 and 100 cm thick shield plugs, respectively.

5.4.3 Dependency on shield plug thickness

Dependencies on the shield plug thickness installed inside the duct opening is shown in Fig. 5.24. Figure 5.24 shows the peak nuclear heating rate in the winding pack for the case of the 80 cm high duct opening and the 10 cm thick duct wall. It was found that the peak nuclear heating rate on the TF coil winding pack adjacent to the duct decreased exponentially with the shield plug thickness. The analytical representation on the nuclear heating rate in the TF coil winding pack can be given as a function of the shield plug thickness, X_p (cm), as follows;

$$Y_c = N P E_p \exp (- F_p X_p) \quad (5.26),$$
$$T_p = \ln 10 / D_p \quad (5.27).$$

The values of E_p and F_p obtained by the least squares fitting to Eq. (5.26) are shown in Table 5.25 for various slit widths. Disagreement of the peak nuclear heating rate in the TF coil winding pack obtained by the analytical representation Eq. (5.26) with the values shown in Table 5.25 is 0.3 to 15 % compared with those by the Monte Carlo calculation results. The T_p values correspond to the shield plug thickness required to reduce the nuclear properties by one order of magnitude, and they are also shown in Table 5.25. The T_p values are about 220 to 290 cm, and they are larger than the T_{wa} values shown in Eq. (5.23) by more than one order of magnitude.

Similarly to Eq. (5.26), the E_s values in Eq. (5.21) also decrease exponentially with the shield plug thickness as seen in Table 5.18. The E_s values can be given approximately by an exponential function of the shield plug thickness X_p as follows;

$$E_s = E_{s/p} \exp (- F_{s/p} X_p) \quad (5.28).$$

From the analytical representation Eq. (5.26) and the formula (5.28), the analytical representation on the nuclear heating rate in the TF coil winding pack can be given as

functions of the slit width X_s and the shield plug thickness X_p as follows;

$$Y_c = N P E_{s/p} \exp (- F_{s/p} X_p) X_s^{2.1}, \quad (5.29).$$

The $E_{s/p}$ and $F_{s/p}$ values obtained by the least squares fitting to Eq. (5.29) are 1.2×10^{-2} and 1.12×10^{-2}, respectively, in the 10 cm thick duct wall. Disagreement of the peak nuclear heating rate in the TF coil winding pack obtained by the analytical representation Eq. (5.29) with these values is less than 38 % compared with those by the Monte Carlo calculation.

5.5 Duct with Shield Plug with Step Configuration

In case the shield plug is installed inside the duct opening and the step configuration is applied to the slit between the duct wall and the shield plug, the peak nuclear properties in the TF coil adjacent to the duct are calculated in this Chapter.

5.5.1 Dependency on step width

Dependency on the step width is shown in Fig. 5.25. Figure 5.25 shows the peak nuclear heating rate in the winding pack for the 80 cm high duct opening, the 100 cm thick shield plug, the 20 cm thick duct wall and the 200 cm thick shield adjacent to the duct. The horizontal axis corresponds to the ratio of the step width to the slit width. The step configuration is installed in the middle of the shield plug, i. e. 50 cm thickness in the shield plug, and the step thickness equals to the slit width. The nuclear properties in the TF coil adjacent to the duct are drastically reduced by applying the step configuration to the slit. The nuclear properties in the TF coil decrease with the step widths. It was found that the nuclear properties in the TF coil showed constant values when the step width was more than four times larger than the slit width. By installing the step width more than four times larger than the slit width, the nuclear properties are reduced to be the values of about 1/30 compared with those without step configuration in the case of 100 cm thick shield plug.

5.5.2 Dependency on step thickness

Dependencies on the step thickness are shown in Figs. 5.26 – 5.30 for the 80 cm high duct opening, the 100 cm thick shield plug, the 20 cm thick duct wall and the 200 cm thick shield adjacent to the duct. The step configuration is installed in the middle of the shield plug, i. e. 50 cm thickness in the shield plug. Figures 5.26 and 5.27 show dependencies of the nuclear heating rate in the TF coil winding pack for the 2 and 3 cm wide slits, respectively. Figure 5.28, 5.29 and 5.30 show dependency of the neutron damage in the stabilizer copper, that of the neutron fluence of the energy above 0.1 MeV and that above 1 MeV in the 3 cm wide slits, respectively. These figures show the example for the step width of same width as the slit width and that of four times of the slit width. It was found that dependencies on the step thickness are much smaller compared with those on the step width, though the nuclear

properties slightly increased with the step thicknesses.

5.5.3 Dependency on step position

Dependency on the step position is shown in Fig. 5.31 for the 80 cm high duct opening, the 100 cm thick shield plug, the 20 cm thick duct wall and the 200 cm thick shield adjacent to the duct. The step widths are 2, 3, 4 and 6 cm. The step configuration is installed in the positions with 1/4, 1/2, 3/4 of the shield plug thickness, i. e. 25, 50, 75 cm distances from the shield plug surface, respectively. The step widths are four times of the slit widths, and the step thicknesses equal to the slit widths. The horizontal axis corresponds to the ratio of the shield thickness to the step position, which is the distance from the shield plug surface to the step position, to the shield plug thickness. The values of 0 and 1 correspond to the shield plug without the step configuration in the horizontal axis, and those of 0.25, 0.5 and 0.75 correspond to the step position with 1/4, 1/2, 3/4 of the shield plug thickness, respectively. The peak nuclear heating rates in the winding pack in the step configuration installed in the positions with 1/2 of the shield plug thickness are lower that those with 1/4 and 3/4 of the shield plug thickness by factors of 3 – 6. It was found that the peak nuclear properties were minimized ones by installing the step configuration at the middle of the shield plug. It can be concluded that applying the step at the middle of the shield plug is optimized position from the view point of the shielding design.

5.6 Conclusion

Three dimensional Monte Carlo calculations are performed taking into account the radiation streaming through the large opening duct penetrating the blanket and the vacuum vessel, and the peak nuclear properties in the TF coil adjacent to the duct are calculated.

1) For case the shield plug is not installed in the duct opening, the analytical representations on the peak nuclear properties are established as functions of the duct opening height, the duct opening width, the duct wall thickness and the shield thickness adjacent to the duct.
2) Dependencies on the duct wall and the shield composition adjacent to the duct are also clarified. It was found that the peak nuclear properties were almost constant for the shield composed of the region of 10 % SS/90 % water to 90 % SS/10 % water.
3) For case the shield plug is installed in the duct opening, the slit is installed between the duct wall and the shield plug installed in the duct, and the step configuration is not applied to the slit, the analytical representations on the nuclear properties in the TF coil adjacent to the duct are established as functions of the slit width, the duct wall thickness, the shield plug thickness.
4) For the application of the step configuration to the slit, dependencies on the step width, the step thickness and the step position are clarified.
5) The nuclear properties are drastically reduced by applying the step configuration to the slit between the shield plug and the duct wall.

6) It can be concluded that applying the step configuration with the step width of four times of the slit width at the middle of the shield plug is most effective from the view point of the shield design.

References

[5.1] K. Maki, et al., Biological shield around the neutral beam injector duct in the ITER conceptual design, Fusion Eng. Design, 24, 315-325 (1994).

[5.2] K. Maki et al., Radiation shielding for superconductive toroidal field coils around the neutral beam injector duct in the ITER design, Fusion Eng. Design. 22, 427-434 (1993).

[5.3] S. Sato, R. Plenteda, D. Valenza, et. al., SHIELDING ANALYSES OF THE ITER NBI PORTS, Fusion Technol., 34, 1002-1007 (1998)

[5.4] S. Sato, H. Iida, R. Plenteda, D. Valenza, R. T. Santoro, Evaluation of Biological Dose Rates around the ITER NBI Ports by 2-D SN/Activation and 3-D Monte Carlo Analyses, Fusion Eng. Design, 47, 425-435 (2000).

[5.5] S. Sato, H. Iida, Monte Carlo Analyses for ITER NBI Duct by 1/4 Tokamak Model," J. Ncul. Sci. Technol., Supplement 1, 258-262 (2000).

[5.6] T. Inoue, et al., Design and R&D of high power negative ion source/accelerator for ITER NBI, Proc. 19th Symp. on Fusion Technol., Lisbon, Portugal, Sep. 16-20, 1996, p. 701, Portugal (1996).

[5.7] A. Krylov, et al., General design of the neutral beam injection system and integration with ITER, Proc. 19th Symp. on Fusion Technol., Lisbon, Portugal, Sep. 16-20, 1996, p. 697, Portugal (1996).

[5.8] K. Shibata, et al., Design analysis for reducing dose rate in the NBI to realize direct access by workers for a fusion experimental reactor, Proc. 19th Symp. on Fusion Technol., Lisbon, Portugal, Sep. 16-20, 1996, p. 1799, Portugal (1996).

[5.9] S. Sato, K. Maki, H. Takatsu and Y. Seki, SHIELDING ANALYSIS FOR TOROIDAL FIELD COILS AROUND EXHAUST DUCT IN FUSION EXPERIMENTAL REACTOR, Fusion Technol., 30, 1076-1080 (1996)

[5.10] S. Sato, H. Takatsu, T. Utsumi, et. al., STREAMING ANALYSIS FOR RADIATION THROUGH ITER MID-PLANE PORT, Fusion Eng. Design, 42, 213-219 (1998).

[5.11] S. Sato, et. al., JAERI-M 93-093 (1993).

[5.12] S. Sato et al., Evaluation of radiation streaming through the annular gaps around divertor cooling pipes in fusion experimental reactors, Proceedings of 8th International Conference on Radiation Shielding, Arlington, Texas USA, April 24-28, 1039-1046 (1994).

Table 5.1 Calculation conditions

Duct opening height (cm)	50, 60, 70, 80, 100, 120, 160, 200, 240, 280
Duct opening width (cm)	50, 80, 120, 160, 200
Duct wall thickness (cm)	10, 20, 30, 40
Shield thickness adjacent to the duct (cm)	100, 130, 200
Slit width between the shield plug and the dcut wall (cm)	1, 2, 3, 4, 5, 6, 8
Shiel plug thickness installed in the duct(cm)	70, 100, 160, 130, 200
Step width in the slit (times to the slit width)	0.5, 1.0, 1.1, 1.3, 1.5, 1.7, 1.9, 2.0, 2.5, 3.0, 3.5, 4.0, 4.5, 5.0, 5.5, 6.0
Step thickness in the slit (cm)	1, 2, 3, 4, 5, 6
Step position (ratio of the thickness from the shield plug surface to the shield plug thickness)	0.25, 0.50, 0.75
Duct wall composition (%)	SS/H_2O = 0/100, 10/90, 20/80, 30/70, 40/60, 50/50, 60/40, 70/30, 80/20, 90/10, 100/0
Shield composition adjacent to the duct(%)	SS/H_2O = 0/100, 10/90, 20/80, 30/70, 40/60, 50/50, 60/40, 70/30, 80/20, 90/10, 100/0

Table 5.2 Calculation results for the nuclear properties in the TF coil surface with the 45 cm thick blanket and 40 cm thick vacuum vessel. (Neutron wall loading: 1MW/m^2, Integrated neutron wall loading: 1MWa/m^2)

Duct opening height (cm)	Nuclear heating rate in the coil case (w/cm^3)	Statistical error
50	6.97E-05	0.0763
80	1.68E-04	0.0458
120	2.90E-04	0.0315
200	5.76E-04	0.0450
280	7.11E-04	0.0321

Duct opening height (cm)	Fast (> 0.1 MeV) neutron fluence in the winding pack (n/cm^2)	Statistical error
50	5.98E+16	0.0427
80	1.45E+17	0.0408
120	2.59E+17	0.0358
200	4.69E+17	0.0321
280	6.59E+17	0.0324

Duct opening height (cm)	Fast (> 0.1 MeV) neutron fluence in the winding pack (n/cm^2)	Statistical error
50	1.12E+16	0.0530
80	2.83E+16	0.0551
120	4.43E+16	0.0420
200	8.22E+16	0.0429
280	1.06E+17	0.0410

Duct opening height (cm)	Neutron damage in the stbilizer copper (dpa)	Statistical error
50	3.81E-05	0.0437
80	9.25E-05	0.0439
120	1.61E-04	0.0335
200	2.98E-04	0.0324
280	4.03E-04	0.0316

Table 5.3 (a) The values of Ch and Dh in the analytical representation Eq. (5.1) on the nuclear heating rate in the winding pack in the TF coil just adjacent to the duct as a function of the duct opening height. The duct wall and the shield compositions are 60 % SS and 40 % water and 70 % SS and 30 % water, respectively.

Duct wall thickness: 20 cm				
Duct opening width (cm)	Shield thickness (cm)	Ch	Dh	Error*
50	100	3.02E-04	7.96E-06	1.122
	130	2.03E-04	5.63E-06	1.194
	200	8.66E-05	2.88E-06	1.242
80	100	6.32E-04	1.94E-05	1.108
	130	4.54E-04	1.40E-05	1.127
	200	1.77E-04	7.42E-06	1.187
120	100	1.17E-03	3.75E-05	1.145
	130	8.71E-04	2.92E-05	1.138
	200	3.87E-04	1.44E-05	1.128
160	100	1.96E-03	5.31E-05	1.130
	130	1.67E-03	4.62E-05	1.116
	200	6.46E-04	2.29E-05	1.167

Duct wall thickness: 30 cm				
Duct opening width (cm)	Shield thickness (cm)	Ch	Dh	Error*
50	100	7.29E-05	1.79E-06	
	130	5.21E-05	1.22E-06	1.167
	200	2.31E-05	7.22E-07	1.403
80	100	1.37E-04	4.54E-06	1.084
	130	1.15E-04	3.13E-06	1.235
	200	5.21E-05	1.76E-06	1.226
120	100	2.93E-04	8.60E-06	1.283
	130	2.39E-04	6.56E-06	1.292
	200	1.42E-04	3.37E-06	
160	100	3.96E-04	1.42E-05	1.053
	130	3.37E-04	1.21E-05	1.068
	200	1.81E-04	6.30E-06	1.136

Error*: Maximum values of the ratio between the nuclear heating rate obtained by the analytically using Eq. (5.1) to those by the Monte Carlo calculation.

Table 5.3 (b) The values of C_h and D_h in the analytical representation Eq. (5.1) on the nuclear heating rate in the winding pack in the TF coil just adjacent to the duct as a function of the duct opening height. The duct wall and the shield compositions are 60 % SS and 40 % water and 70 % SS and 30 % water, respectively.

Duct wall thickness: 40 cm				
Duct opening width (cm)	Shield thickness (cm)	C_h	D_h	Error*
50	130	1.09E-05	3.24E-07	1.338
	200	5.92E-06	1.81E-07	1.244
80	100	3.47E-05	9.23E-07	1.245
	130	2.52E-05	8.13E-07	1.245
	200	1.43E-05	4.42E-07	1.142
120	100	7.06E-05	1.84E-06	1.341
	130	6.41E-05	1.57E-06	
	200	4.08E-05	9.21E-07	1.464
160	100	1.11E-04	3.47E-06	1.067
	130	1.02E-04	2.72E-06	1.230
	200	5.50E-05	1.70E-06	1.061

Error*: Maximum values of the ratio between the nuclear heating rate obtained by the analytically using Eq. (5.1) to those by the Monte Carlo calculation.

Table 5.4 (a) The values of C_h and D_h in the analytical representation Eq. (5.1) on the neutron fluence of the energy above 0.1 MeV in the winding pack in the TF coil just adjacent to the duct as a function of the duct opening height. The duct wall and the shield compositions are 60 % SS and 40 % water and 70 % SS and 30 % water, respectively.

Duct wall thickness: 20 cm				
Duct opening width (cm)	Shield thickness (cm)	C_h	D_h	Error*
50	100	3.27E+17	8.02E+15	1.166
	130	1.73E+17	5.63E+15	1.095
	200	6.80E+16	2.61E+15	1.137
80	100	6.60E+17	2.06E+16	1.126
	130	4.50E+17	1.45E+16	1.109
	200	1.59E+17	6.57E+15	1.067
120	100	1.21E+18	4.18E+16	1.084
	130	9.16E+17	3.04E+16	1.065
	200	3.76E+17	1.41E+16	1.075
160	100	2.04E+18	5.87E+16	1.141
	130	1.82E+18	4.84E+16	1.184
	200	6.07E+17	2.34E+16	1.114

Duct wall thickness: 30 cm				
Duct opening width (cm)	Shield thickness (cm)	C_h	D_h	Error*
50	100	7.14E+16	1.66E+15	1.317
	130	4.39E+16	1.20E+15	1.167
80	100	1.29E+17	4.45E+15	1.061
	130	1.03E+17	3.12E+15	1.233
	200	4.38E+16	1.51E+15	1.120
120	100	2.61E+17	9.66E+15	1.086
	130	2.22E+17	6.90E+15	1.156
	200	1.13E+17	3.35E+15	1.194
160	100	4.14E+17	1.55E+16	1.075
	130	3.57E+17	1.27E+16	1.064
	200	1.85E+17	6.00E+15	1.144

Error*: Maximum values of the ratio between the neutron fluence obtained by the analytically using Eq. (5.1) to those by the Monte Carlo calculation.

Table 5.4 (b) The values of C_h and D_h in the analytical representation Eq. (5.1) on the neutron fluence of the energy above 0.1 MeV in the winding pack in the TF coil just adjacent to the duct as a function of the duct opening height. The duct wall and the shield compositions are 60 % SS and 40 % water and 70 % SS and 30 % water, respectively.

Duct wall thickness: 40 cm				
Duct opening width (cm)	Shield thickness (cm)	C_h	D_h	Error*
50	130	9.32E+15	3.43E+14	1.229
	200	4.01E+15	1.60E+14	1.272
80	100	4.06E+16	8.53E+14	1.262
	130	2.52E+16	7.47E+14	1.263
120	100	6.37E+16	2.06E+15	1.138
	130	5.89E+16	1.69E+15	1.202
	200	3.16E+16	9.11E+14	1.279
160	100	1.11E+17	3.61E+15	1.131
	130	9.62E+16	2.69E+15	1.243
	200	5.76E+16	1.58E+15	1.324

Error*: Maximum values of the ratio between the neutron fluence obtained by the analytically using Eq. (5.1) to those by the Monte Carlo calculation.

Table 5.5 (a) The values of Ch and Dh in the analytical representation Eq. (5.1) on the neutron fluence of the energy above 1 MeV in the winding pack in the TF coil just adjacent to the duct as a function of the duct opening height. The duct wall and the shield compositions are 60 % SS and 40 % water and 70 % SS and 30 % water, respectively.

Duct wall thickness: 20 cm				
Duct opening width (cm)	Shield thickness (cm)	Ch	Dh	Error*
50	100	6.89E+16	1.53E+15	1.224
	130	3.52E+16	1.02E+15	1.085
	200	1.46E+16	4.14E+14	1.302
80	100	1.51E+17	4.21E+15	1.130
	130	1.05E+17	2.6436E+15	1.145
	200	3.19E+16	1.12E+15	1.126
120	100	3.06E+17	8.24E+15	1.182
	130	2.30E+17	5.78E+15	1.155
	200	7.66E+16	2.40E+15	1.125
160	100	4.74E+17	1.18E+16	1.171
	200	1.26E+17	4.26E+15	1.169

Duct wall thickness: 30 cm				
Duct opening width (cm)	Shield thickness (cm)	Ch	Dh	Error*
50	100	1.36E+16	3.31E+14	1.285
	130	8.54E+15	2.31E+14	1.239
	200	3.94E+15	1.02E+14	1.413
80	100	3.01E+16	8.58E+14	1.154
	130	2.36E+16	5.99E+14	1.279
	200	9.32E+15	2.74E+14	1.167
120	100	5.67E+16	1.98E+15	1.067
	130	5.22E+16	1.34E+15	1.248
	200	2.28E+16	6.45E+14	1.140
160	100	9.42E+16	3.21E+15	1.110
	130	8.43E+16	2.50E+15	1.077
	200	4.05E+16	1.12E+15	1.165

Error*: Maximum values of the ratio between the neutron fluence obtained by the analytically using Eq. (5.1) to those by the Monte Carlo calculation.

Table 5.5 (b) The values of C_h and D_h in the analytical representation Eq. (5.1) on the neutron fluence of the energy above 1 MeV in the winding pack in the TF coil just adjacent to the duct as a function of the duct opening height. The duct wall and the shield compositions are 60 % SS and 40 % water and 70 % SS and 30 % water, respectively.

Duct wall thickness: 40 cm				
Duct opening width (cm)	Shield thickness (cm)	C_h	D_h	Error*
50	130	2.47E+15	6.46E+13	1.496
	200	9.44E+14	2.90E+13	1.403
80	100	8.89E+15	1.48E+14	1.388
	130	6.03E+15	1.39E+14	1.343
	200	2.89E+15	6.83E+13	1.382
120	100	1.40E+16	3.86E+14	1.263
	130	1.24E+16	3.23E+14	1.174
	200	7.56E+15	1.67E+14	1.477
160	100	2.64E+16	6.96E+14	1.298
	130	2.28E+16	5.23E+14	1.327
	200	1.23E+16	3.15E+14	1.326

Error*: Maximum values of the ratio between the neutron fluence obtained by the analytically using Eq. (5.1) to those by the Monte Carlo calculation.

Table 5.6 (a) The values of C_h and D_h in the analytical representation Eq. (5.1) on the neutron damage in the winding pack stabilizer copper in the TF coil just adjacent to the duct as a function of the duct opening height. The duct wall and the shield compositions are 60 % SS and 40 % water and 70 % SS and 30 % water, respectively.

Duct wall thickness: 20 cm				
Duct opening width (cm)	Shield thickness (cm)	C_h	D_h	Error*
50	100	2.29E-04	5.28E-06	1.164
	130	1.19E-04	3.59E-06	1.100
	200	4.50E-05	1.60E-06	1.182
80	100	4.90E-04	1.39E-05	1.130
	130	3.26E-04	9.45E-06	1.093
	200	1.04E-04	4.09E-06	1.090
120	100	9.39E-04	2.79E-05	1.117
	130	6.97E-04	2.03E-05	1.100
	200	2.51E-05	8.80E-07	1.092
160	100	1.53E-03	4.03E-05	1.147
	130	1.35E-03	3.34E-05	1.152
	200	4.08E-04	1.50E-05	1.120

Duct wall thickness: 30 cm				
Duct opening width (cm)	Shield thickness (cm)	C_h	D_h	Error*
50	100	4.72E-05	1.12E-06	1.317
	130	2.97E-05	7.78E-07	1.194
	200	1.28E-05	3.60E-07	1.352
80	100	9.47E-05	2.96E-06	1.098
	130	7.43E-05	2.04E-06	1.256
	200	3.00E-05	9.65E-07	1.137
120	100	1.91E-04	6.51E-06	1.120
	130	1.65E-04	4.60E-06	1.188
	200	7.64E-05	2.18E-06	1.185
160	100	3.12E-04	1.04E-05	1.074
	130	2.66E-04	8.60E-06	1.076
	200	1.29E-04	3.95E-06	1.157

Error*: Maximum values of the ratio between the neutron damage obtained by the analytically using Eq. (5.1) to those by the Monte Carlo calculation.

Table 5.6 (b) The values of C_h and D_h in the analytical representation Eq. (5.1) on the neutron damage in the winding pack stabilizer copper in the TF coil just adjacent to the duct as a function of the duct opening height. The duct wall and the shield compositions are 60 % SS and 40 % water and 70 % SS and 30 % water, respectively.

		40 cm		
Duct wall thickness				
Duct opening width (cm)	Shield thickness (cm)	C_{height}	D_{height}	Error*
50	130	6.78E-06	2.10E-07	1.252
	200	2.98E-06	9.95E-08	1.348
80	100	2.85E-05	5.48E-07	1.328
	130	1.86E-05	4.85E-07	1.281
	200	8.47E-06	2.40E-07	1.298
120	100	4.63E-05	1.35E-06	1.213
	130	3.97E-05	1.12E-06	1.159
	200	2.29E-05	5.89E-07	1.371
160	100	7.89E-05	2.53E-06	1.144
	130	7.10E-05	1.80E-06	1.265
	200	3.96E-05	1.07E-06	1.287

Error*: Maximum values of the ratio between the neutron damage obtained by the analytically using Eq. (5.1) to those by the Monte Carlo calculation.

Table 5.7 The values of Cw and Dw in the analytical representation Eq. (5.2) on the nuclear properties in the TF coil just adjacent to the duct as a function of the duct opening height. The duct wall and the shield compositions are 60 % SS and 40 % water and 70 % SS and 30 % water, respectively.

Duct opening height (cm)	Shield thickness (cm)	Cw	Dw	Error*
Nuclear heating rate in the winding pack				
50	100	1.10E-07	1.61	1.055
80	200	3.65E-08	1.82	1.038
120	200	5.66E-08	1.84	1.017
160	100	4.92E-07	1.66	1.046
200	100	4.92E-07	1.66	1.046
	200	1.33E-07	1.79	1.006
280	200	1.22E-07	1.86	1.039
Neutron damage (DPA) in the stbilizer copper				
160	100	1.93E-07	1.78	1.060
Fast (> 0.1 MeV) neutron fluence in the winding pack				
160	100	3.19E+14	1.75	1.069
Fast (> 1 MeV) neutron fluence in the winding pack				
160	100	6.16E+16	1.74	1.083

Error*: Maximum values of the ratio between the nuclear properties obtained by the analytically using Eq. (5.2) to those by the Monte Carlo calculation.

Table 5.8 The values of $C_{h/w}$, $C'_{h/w}$, $D_{h/w}$ and $D'_{h/w}$ in the analytical representation Eq. (5.5) on the nuclear properties in the TF coil just adjacent to the duct as functions of the duct opening height and the duct opening width. The duct wall and the shield compositions are 60 % SS and 40 % water and 70 % SS and 30 % water, respectively.

Shield thickness (cm)	$C_{h/w}$	$C'_{h/w}$	$D_{h/w}$	$D'_{h/w}$	Error*
Nuclear heating rate in the winding pack					
100	2.00E-07	1.50	1.86E-09	1.76	1.340
200	1.61E-08	1.86	5.62E-10	1.83	1.413
Neutron damage (DPA) in the stbilizer copper					
100	7.83E-08	1.630	6.12E-10	1.93	1.297
Fast (> 0.1 MeV) neutron fluence in the winding pack					
100	1.74E+14	1.527	9.07E+11	1.93	1.278
Fast (> 1 MeV) neutron fluence in the winding pack					
100	2.13E+13	1.652	1.50E+11	1.97	1.295

Error*: Maximum values of the ratio between the nuclear properties obtained by the analytically using Eq. (5.5) to those by the Monte Carlo calculation.

Table 5.9 The values of C_{wa} and D_{wa} in the analytical representation Eq. (5.6) on the nuclear heating rate on the winding pack in the TF coil just adjacent to the duct as a function of the duct wall thicknessfor the80 cm wide duct opening and the 130 cm thick shield adjacent to the duct, and the required duct wall thickness T_{wa} to reduce the nuclear heating rate by one order of magnitude. The duct wall and the shield compositions are 60 % SS and 40 % water and 70 % SS and 30 % water, respectively.

Duct opening height (cm)	C_{wa}	D_{wa}	T_{wa}	Error*
50	8.86E-03	0.152	15.1	1.002
80	1.85E-02	0.152	15.2	1.044
120	2.58E-02	0.142	16.2	1.017
200	4.50E-02	0.142	16.3	1.016
280	6.26E-02	0.145	15.9	1.056

Error*: Maximum values of the ratio between the nuclear heating rate obtained by the analytically using Eq. (5.6) to those by the Monte Carlo calculation code.

Table 5.10 The values of $C_{h/wa}$, $C'_{h/wa}$, $D_{h/wa}$ and $D'_{h/wa}$ in the analytical representation Eq. (5.10) on the nuclear heating rate in the TF coil winding pack adjacent to the duct as functions of the duct opening height and the duct wall thickness. The duct wall and the shield compositions are 60 % SS and 40 % water and 70 % SS and 30 % water, respectively.

Duct opening width (cm)	Shield thickness (cm)	$C_{h/wa}$	$C'_{h/wa}$	$D_{h/wa}$	$D'_{h/wa}$
50	130	3.91E-03	0.146	9.46E-05	0.143
	200	1.28E-03	0.134	4.58E-05	0.138
Duct opening width (cm)	Shield thickness (cm)	Ch/wa	$C'_{h/wa}$	$D_{h/wa}$	$D'_{h/wa}$
80	130	8.37E-03	0.145	2.35E-04	0.142
Duct opening width (cm)	Shield thickness (cm)	Ch/wa	$C'_{h/wa}$	$D_{h/wa}$	$D'_{h/wa}$
120	130	1.19E-02	0.130	5.37E-04	0.146
	200	3.82E-03	0.112	2.18E-04	0.137
Duct opening width (cm)	Shield thickness (cm)	Ch/wa	$C'_{h/wa}$	$D_{h/wa}$	$D'_{h/wa}$
160	130	2.56E-02	0.140	8.05E-04	0.142
	200	7.49E-03	0.123	3.12E-04	0.130

Table 5.11 The values of $C_{h/wa}$, $C'_{h/wa}$, $D_{h/wa}$ and $D'_{h/wa}$ in the analytical representation Eq. (5.10) on the neutron fluence of the energy above 0.1 MeV in the winding pack in the TF coil adjacent to the duct as the function of the duct opening height and the duct wall thickness. The duct wall and the shield compositions are 60 % SS and 40 % water and 70 % SS and 30 % water, respectively.

Duct opening width (cm)	Shield thickness (cm)	$C_{h/wa}$	$C'_{h/wa}$	$D_{h/wa}$	$D'_{h/wa}$
80	130	7.95E+18	0.144	2.76E+17	0.148
120	130	1.40E+19	0.137	5.40E+17	0.144

Table 5.12 The values of $C_{h/wa}$, $C'_{h/wa}$, $D_{h/wa}$ and $D'_{h/wa}$ in the analytical representation Eq. (5.10) on the neutron fluence of the energy above 1 MeV in the winding pack in the TF coil adjacent to the duct as the function of the duct opening height and the duct wall thickness. The duct wall and the shield compositions are 60 % SS and 40 % water and 70 % SS and 30 % water, respectively.

Duct opening width (cm)	Shield thickness (cm)	$C_{h/wa}$	$C'_{h/wa}$	$D_{h/wa}$	$D'_{h/wa}$
80	130	1.79E+18	0.143	5.01E+16	0.147
120	130	4.23E+18	0.146	1.03E+17	0.144

Table 5.13 The values of $C_{h/wa}$, $C'_{h/wa}$, $D_{h/wa}$ and $D'_{h/wa}$ in the analytical representation Eq. (5.10) on the neutron damage in the stabilizer copper on the winding pack in the TF coil adjacent to the duct as functions of the duct opening height and the duct wall thickness. The duct wall and the shield compositions are60 % SS and 40 % water and 70 % SS and 30 % water, respectively.

Duct opening width (cm)	Shield thickness (cm)	$C_{h/wa}$	$C'_{h/wa}$	$D_{h/wa}$	$D'_{h/wa}$
80	130	5.62E-03	0.143	1.81E-04	0.148
120	130	1.22E-02	0.143	3.64E-04	0.145

Table 5.14 The values of C_{sh} and D_{sh} in the analytical representation Eq. (5.11) on the nuclear heating rate in the TF coil winding pack adjacent to the duct as a function of the shield thickness for the 80 cm wide duct opening and the 30 cm thick duct wall, and the required shield thickness T_{sh} adjacent to the duct to reduce the nuclear heating rate by one order of magnitude. The duct wall and the shield compositions are 60 % SS and 40 % water and 70 % SS and 30 % water, respectively.

Duct opening height (cm)	C_{sh}	D_{sh}	T_{sh}	Error*
50	3.90E-04	1.11E-02	208	1.004
80	6.82E-04	9.46E-03	243	1.017
120	1.28E-03	9.72E-03	237	1.023
200	2.16E-03	9.37E-03	246	1.010
280	2.79E-03	9.37E-03	246	1.053

Error*: Maximum values of the ratio between the nuclear heating rate obtained by the analytically using Eq. (5.11) to those by the Monte Carlo calculation

Table 5.15 The values of $C_{h/sh}$, $C'_{h/sh}$, $D_{h/sh}$ and $D'_{h/sh}$ in the analytical representation Eq. (5.15) on the nuclear heating rate in the TF coil winding pack adjacent to the duct as functions of the duct opening height and the shield thickness. The duct wall and the shield compositions are60 % SS and 40 % water and 70 % SS and 30 % water, respectively.

Duct opening width (cm)	Duct wall thickness (cm)	$C_{h/sh}$	$C'_{h/sh}$	$D_{h/sh}$	$D'_{h/sh}$	Error*
50	20	1.04E-03	1.24E-02	2.14E-05	1.01E-02	
	30	2.31E-04	1.15E-02	4.11E-06	8.80E-03	1.408
80	20	2.34E-03	1.29E-02	4.94E-05	9.52E-03	
	30	3.90E-04	9.96E-03	1.10E-05	9.25E-03	1.253
	40	8.11E-05	8.73E-03	2.06E-06	7.60E-03	
120	20	3.63E-03	1.12E-02	1.00E-04	9.66E-03	
	30	6.10E-04	7.28E-03	2.21E-05	9.39E-03	1.291
	40	1.28E-04	5.66E-03	3.80E-06	7.04E-03	
160	20	6.71E-03	1.15E-02	1.33E-04	8.70E-03	
	30	9.12E-04	8.02E-03	3.39E-05	8.34E-03	
	40	2.45E-04	7.34E-03	6.94E-06	7.06E-03	

Error*: Maximum values of the ratio between the nuclear heating rate obtained by the analytically using Eq. (5.15) to those by the Monte Carlo calculation.

Table 5.16 The values of $C_{h/sh}$, $C'_{h/sh}$, $D_{h/sh}$ and $D'_{h/sh}$ in the analytical representation Eq. (5.15) on the neutron damage in the stabilizer copper on the winding pack in the TF coil adjacent to the duct as functions of the duct opening height and the shield thickness. The duct wall and the shield compositions are60 % SS and 40 % water and 70 % SS and 30 % water, respectively.

Duct opening width (cm)	Duct wall thickness (cm)	$C_{h/sh}$	$C'_{h/sh}$	$D_{h/sh}$	$D'_{h/sh}$	Error*
50	30	1.66E-04	1.29E-02	3.43E-06	1.13E-02	1.330
80	30	3.21E-04	1.18E-02	8.85E-06	1.11E-02	1.178
120	30	5.22E-04	9.49E-03	1.92E-05	1.09E-02	1.214

Error*: Maximum values of the ratio between the neutron damage obtained by the analytically using Eq. (5.15) to those by the Monte Carlo calculation.

Table 5.17 The values of $C_{h/sh}$, $C'_{h/sh}$, $D_{h/sh}$ and $D'_{h/sh}$ in the analytical representation Eq. (5.15) on the neutron fluence of the energy above 0.1 MeV in the winding pack in the TF coil adjacent to the duct as functions of the duct opening height and the shield thickness. The duct wall and the shield compositions are60 % SS and 40 % water and 70 % SS and 30 % water, respectively.

Duct opening width (cm)	Duct wall thickness (cm)	$C_{h/sh}$	$C'_{h/sh}$	$D_{h/sh}$	$D'_{h/sh}$	Error*
50	20	1.40E+18	1.53E-02	2.44E+16	1.12E-02	
	30	2.59E+17	1.32E-02	4.77E+15	1.06E-02	1.328
80	20	2.82E+18	1.43E-02	6.42E+16	1.14E-02	
	30	4.07E+17	1.11E-02	1.28E+16	1.07E-02	1.153
120	20	4.09E+18	1.19E-02	1.25E+17	1.09E-02	
	30	6.42E+17	8.60E-03	2.75E+16	1.05E-02	1.217
	40	1.41E+17	7.34E-03	4.81E+15	8.28E-03	
160	20	8.16E+18	1.28E-02	1.56E+17	9.41E-03	
	30	9.89E+17	8.29E-03	4.25E+16	9.71E-03	
	40	2.22E+17	6.70E-03	7.99E+15	8.15E-03	

Error*: Maximum values of the ratio between the neutron fluence obtained by the analytically using Eq. (5.15) to those by the Monte Carlo calculation.

Table 5.18 The values of $C_{h/sh}$, $C'_{h/sh}$, $D_{h/sh}$ and $D'_{h/sh}$ in the analytical representation Eq. (5.15) on the neutron fluence of the energy above 1 MeV in the winding pack in the TF coil adjacent to the duct as functions of the duct opening height and the shield thickness. The duct wall and the shield compositions are60 % SS and 40 % water and 70 % SS and 30 % water, respectively.

Duct opening width (cm)	Duct wall thickness (cm)	$C_{h/sh}$	$C'_{h/sh}$	$D_{h/sh}$	$D'_{h/sh}$	Error*
50	30	4.40E+16	1.22E-02	1.07E+15	1.18E-02	1.387
80	30	1.05E+17	1.20E-02	2.66E+15	1.14E-02	1.211
120	30	1.61E+17	9.59E-03	5.85E+15	1.11E-02	1.185

Error*: Maximum values of the ratio between the neutron fluence obtained by the analytically using Eq. (5.15) to those by the Monte Carlo calculation.

Table 5.19 The values of E_s and F_s in the analytical representation Eqs. (5.20) and (5.21) on the nuclear heating rate in the TF coil winding pack adjacent to the duct with the shield plug installed in the duct as a function of the slit width between the shield plug and the duct wall for various shield plug thickness and duct wall thickness.

Shield plug thickness (cm)	Duct wall thickness (cm)	E_s	F_s	Error*	Error**
70	10	6.76E-03	2.01	1.062	1.192
	20	1.66E-03	2.06	1.072	1.148
	30	5.68E-04	1.91	1.271	1.566
100	10	3.21E-03	2.10	1.056	1.057
	20	8.62E-04	2.11	1.070	1.090
	30	2.43E-04	2.08	1.071	1.080
130	10	2.46E-03	2.15	1.023	1.141
160	10	2.22E-03	2.06	1.082	1.130
200	10	1.30E-03	2.24	1.053	1.352

Error*: Maximum values of the ratio between the nuclear heating rate obtained by the analytically using Eq. (5.20) to those by the Monte Carlo calculation.

Error**: Maximum values of the ratio between the nuclear heating rate obtained by the analytically using Eq. (5.21) to those by the Monte Carlo calculation.

Table 5.20 The values of E_s and F_s in the analytical representation Eqs. (5.20) and (5.21) on the neutron fluence of the energy above 0.1 MeV in the winding pack in the TF coil adjacent to the duct with the shield plug installed in the duct as a function of the slit width between the shield plug and the duct wall for various shield plug thickness and duct wall thickness.

Shield plug thickness (cm)	Duct wall thickness (cm)	E_s	F_s	Error*	Error**
70	10	3.78E+15	1.99	1.021	1.261
	20	9.22E+14	2.05	1.116	1.143
	30	2.42E+14	2.02	1.114	1.241
100	10	2.14E+15	2.01	1.065	1.249
	20	4.21E+14	2.21	1.205	1.339
	30	1.49E+14	2.08	1.080	1.104

Error*: Maximum values of the ratio between the neutron fluence obtained by the analytically using Eq. (5.20) to those by the Monte Carlo calculation.

Error**: Maximum values of the ratio between the neutron fluence obtained by the analytically using Eq. (5.21) to those by the Monte Carlo calculation.

Table 5.21 The values of E_s and F_s in the analytical representation Eqs. (5.20) and (5.21) on the neutron fluence of the energy above 1 MeV in the winding pack in the TF coil adjacent to the duct with the shield plug installed in the duct as a function of the slit width between the shield plug and the duct wall for various shield plug thickness and duct wall thickness.

Shield plug thickness (cm)	Duct wall thickness (cm)	E_s	F_s	Error*	Error**
70	10	3.62E+14	2.05	1.066	1.181
	20	1.01E+14	2.00	1.088	
	30	2.37E+13	1.98	1.196	
100	10	2.43E+14	1.96	1.107	1.441
	20	5.11E+13	2.11	1.266	
	30	1.50E+13	2.01	1.214	

Error*: Maximum values of the ratio between the neutron fluence obtained by the analytically using Eq. (5.20) to those by the Monte Carlo calculation.

Error**: Maximum values of the ratio between the neutron fluence obtained by the analytically using Eq. (5.21) to those by the Monte Carlo calculation.

Table 5.22 The values of E_s and F_s in the analytical representation Eqs. (5.20) and (5.21) on the neutron damage in the stabilizer copper on the winding pack in the TF coil adjacent to the duct with the shield plug installed in the duct as a function of the slit width between the shield plug and the duct wall for various shield plug thickness and duct wall thickness.

Shield plug thickness (cm)	Duct wall thickness (cm)	Eslit	Fslit	Error*	Error**
70	10	2.09E-06	2.00	1.025	1.244
	20	5.29E-07	2.04	1.100	1.174
	30	1.34E-07	2.02	1.106	1.227
100	10	1.18E-06	2.02	1.056	1.252
	20	2.44E-07	2.18	1.201	1.294
	30	8.17E-08	2.07	1.100	1.137

Error*: Maximum values of the ratio between the neutron damage obtained by the analytically using Eq. (5.20) to those by the Monte Carlo calculation.

Error**: Maximum values of the ratio between the neutron damage obtained by the analytically using Eq. (5.21) to those by the Monte Carlo calculation.

Table 5.23 The values of E_{wa} and F_{wa} in the analytical representation Eq. (5.22) on the nuclear heating rate in the TF coil winding pack adjacent to the duct with the shield plug installed in the duct as a function of the duct wall thickness for various slit widths between the shield plug and the duct wall, and the required duct wall thickness T_{wa} to reduce the nuclear properties by one order of magnitude.

Shield plug thickness (cm)	Slit width (cm)	Ewa	Ewa	Twa	Error*
100	2	5.39E-02	0.133	17.3	1.055
	3	1.63E-01	0.141	16.3	1.099
	4	2.50E-01	0.133	17.3	1.017
	6	5.34E-01	0.131	17.6	1.002
	8	1.12E+00	0.137	16.8	1.003
	10	1.97E+00	0.140	16.4	1.060

Error*: Maximum values of the ratio between the nuclear heating rate obtained by the analytically using Eq. (5.22) to those by the Monte Carlo calculation.

Table 5.24 The values of $E_{slit/wall}$ and $F_{slit/wall}$ in the analytical representation Eq. (5.25) on the nuclear heating rate in the TF coil winding pack adjacent to the duct as functions of the slit width and the duct wall thickness.

Shield plug thickness (cm)	$E_{slit/wall}$	$F_{slit/wall}$	Error*
70	1.99E-02	0.120	1.499
100	1.38E-02	0.133	1.216

Error*: Maximum values of the ratio between the nuclear heating rate obtained by the analytically using Eq. (5.25) to those by the Monte Carlo calculation.

Table 5.25 The values of C_p and D_p in the analytical representation Eq. (5.26) on the nuclear heating rate in the TF coil winding pack adjacent to the duct with the shield plug installed in the duct as a function of the shield plug thickness for the 10 cm thick duct wall and various the slit widths between the shield plug and the duct wall, and the required shield plug thickness T_p to reduce the nuclear properties by one order of magnitude.

Slit thickness (cm)	C_p	D_p	T_p	Error*
1	1.08E-02	8.92E-03	258	1.003
2	4.71E-02	1.04E-02	221	1.132
3	9.93E-02	9.69E-03	238	1.103
4	2.06E-01	1.02E-02	225	1.119
6	3.93E-01	9.01E-03	256	1.132
8	7.60E-01	9.07E-03	254	1.141
10	1.08E+00	8.16E-03	282	1.053

Error*: Maximum values of the ratio between the nuclear heating rate obtained by the analytically using Eq. (5.26) to those by the Monte Carlo calculation.

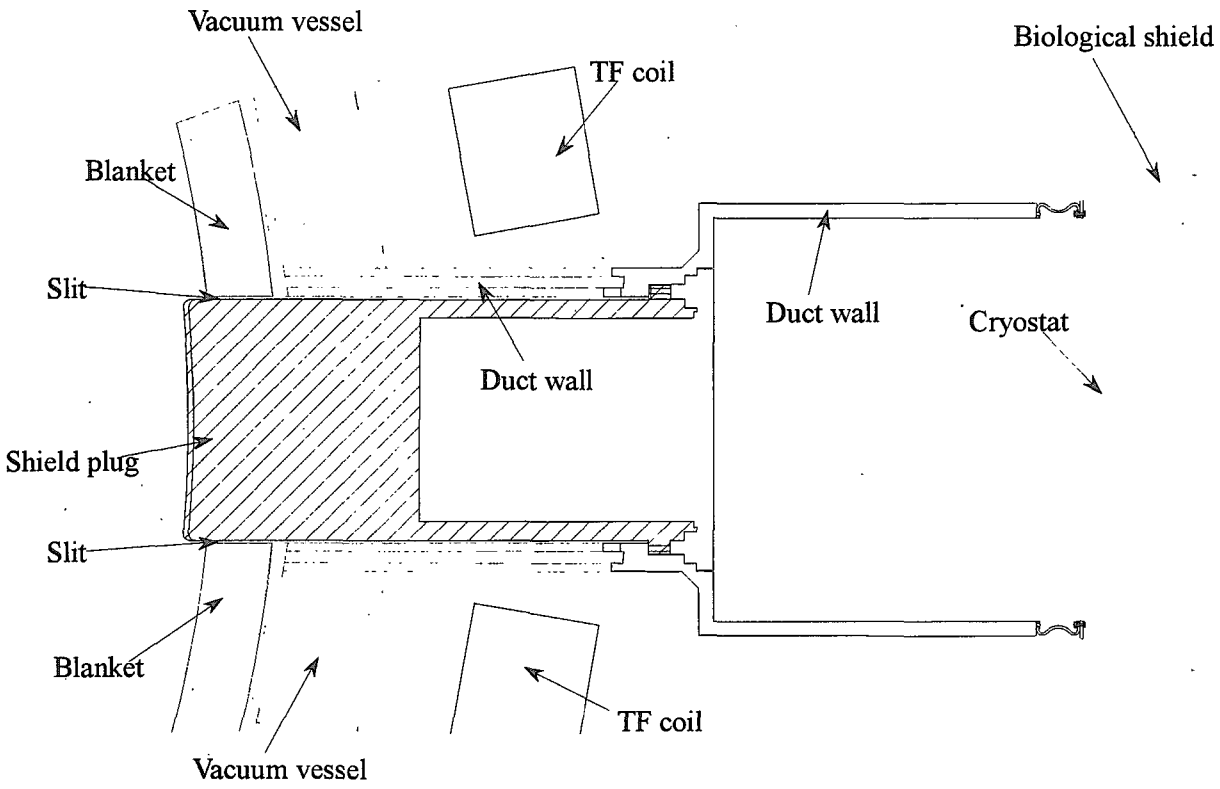

Fig. 5.1 Conceptual view of the horizontal cross section of the ITER maintenance duct

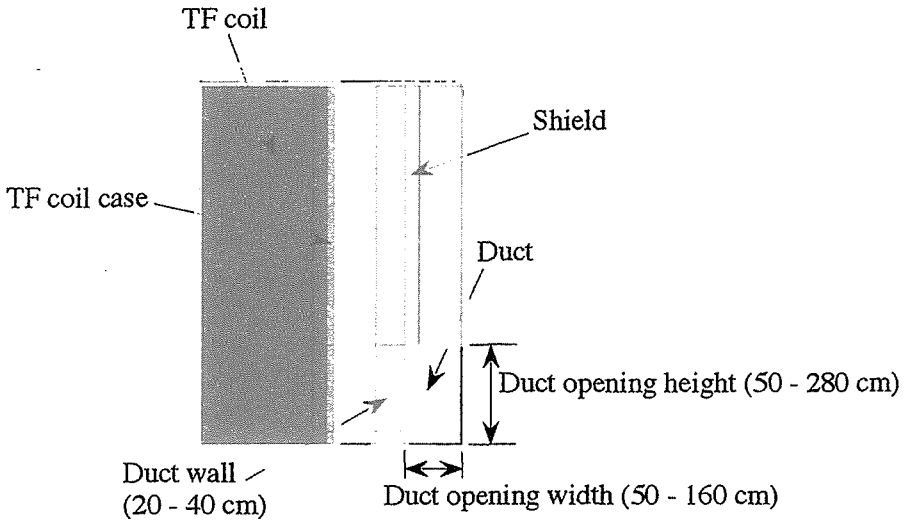

Vertical view

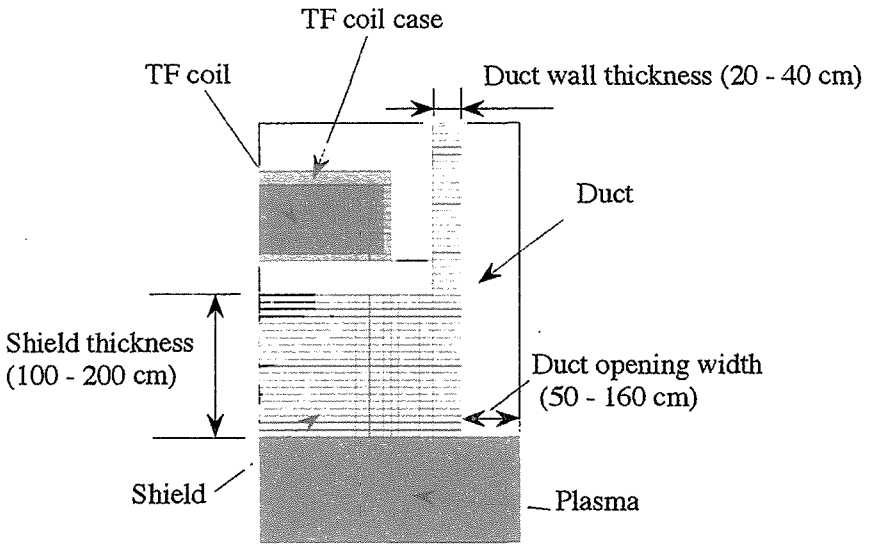

Horizontal view

Fig. 5.2 Three dimensional Monte Carlo calculational geometry used in the study about the streaming through the duct without the shield plug in the vacuum vessel.

This is a blank page.

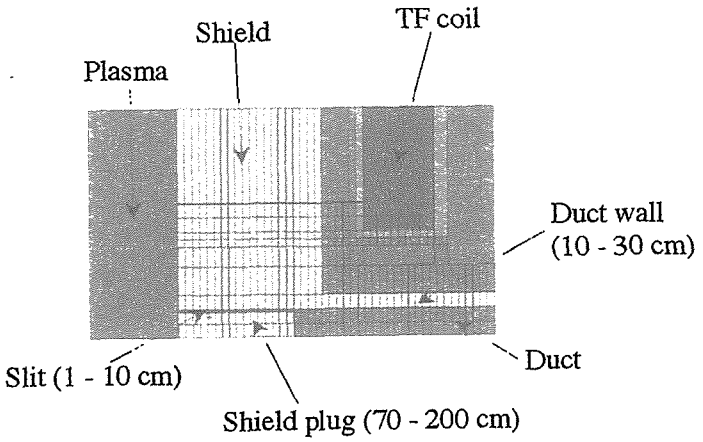

Fig. 5.3 Three dimensional Monte Carlo calculational geometry used in the study about the streaming through the slit between the duct wall and the shield plug installed in the duct.

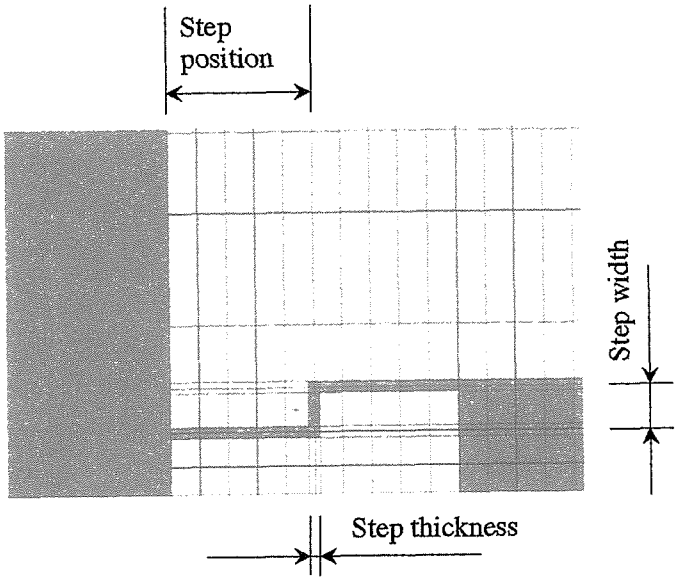

Fig. 5.4 Three dimensional Monte Carlo calculational geometry used in the study about the streaming through the slit with step configuration between the duct wall and the shield plug installed in the duct.

This is a blank page.

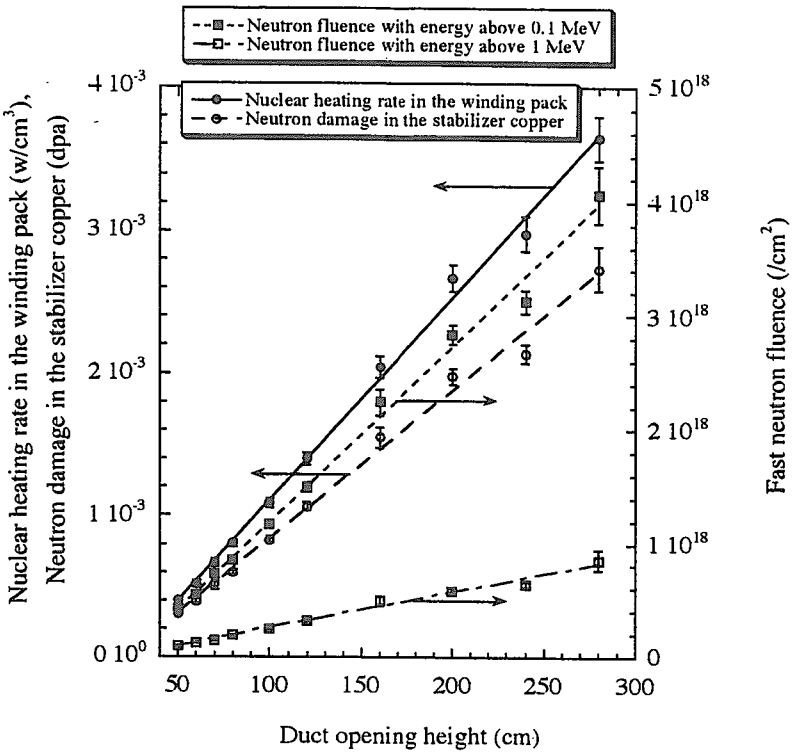

Fig. 5.5 Dependencies of the peak nuclear properties in the TF coil adjacent to the duct on the duct opening height with the error bar for the 120 cm wide duct opening, the 20 cm thick duct wall, the 100 cm thick shield adjacent to the duct under neutron wall loading of 1 MW/m^2 and integrated neutron wall loading of 1 MWa/m^2.

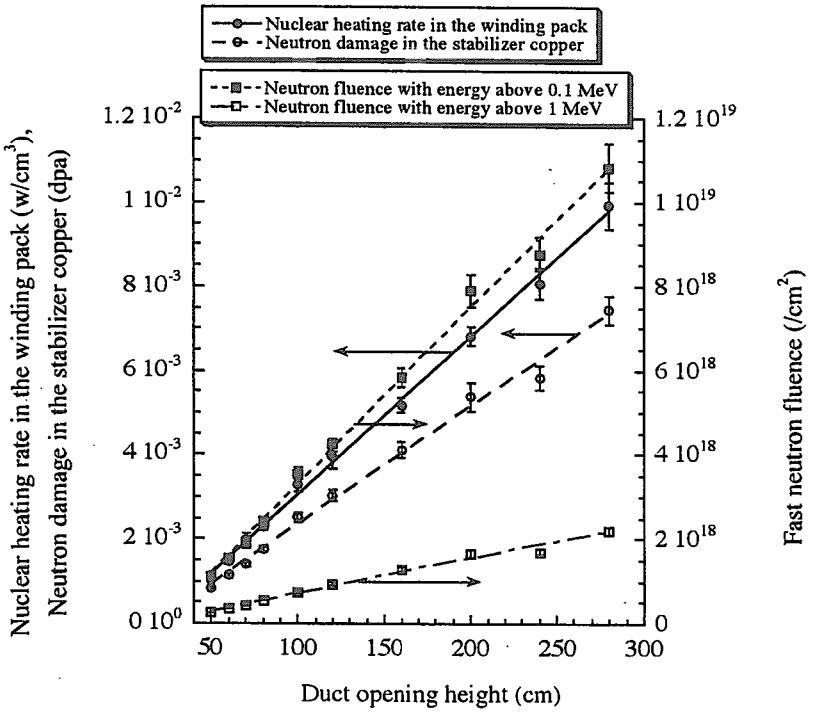

Fig. 5.6 Dependencies of the peak nuclear properties in the TF coil adjacent to the duct on the duct opening height with the error bar for the 160 cm wide duct opening, the 30 cm thick duct wall, the 100 cm thick shield adjacent to the duct under neutron wall loading of 1 MW/m^2 and integrated neutron wall loading of 1 MWa/m^2.

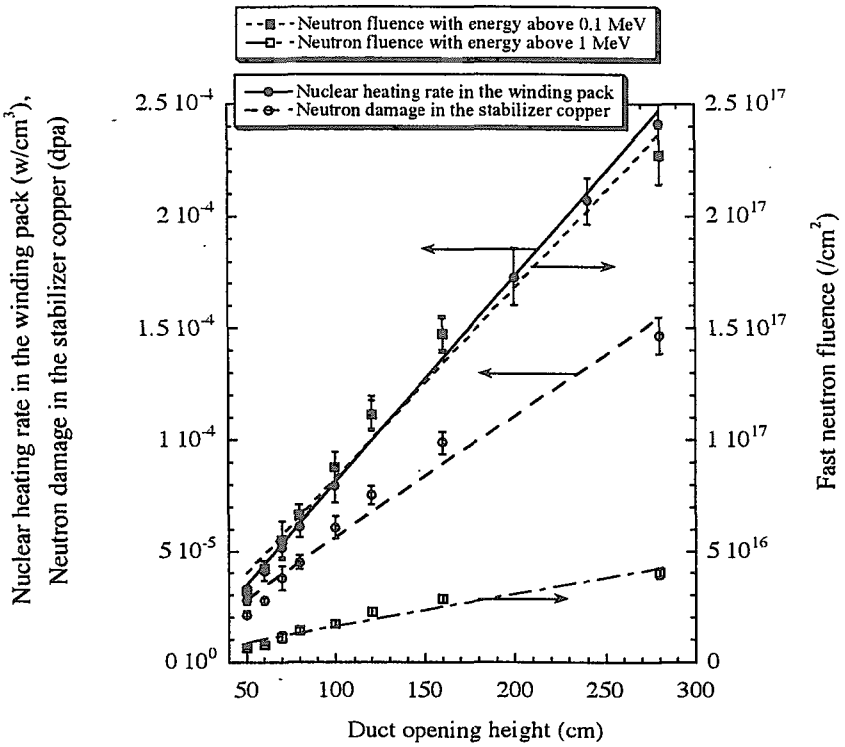

Fig. 5.7 Dependencies of the peak nuclear properties in the TF coil adjacent to the duct on the duct opening height with the error bar for the 80 cm wide duct opening, the 40 cm thick duct wall, the 100 cm thick shield adjacent to the duct under neutron wall loading of 1 MW/m^2 and integrated neutron wall loading of 1 MWa/m^2.

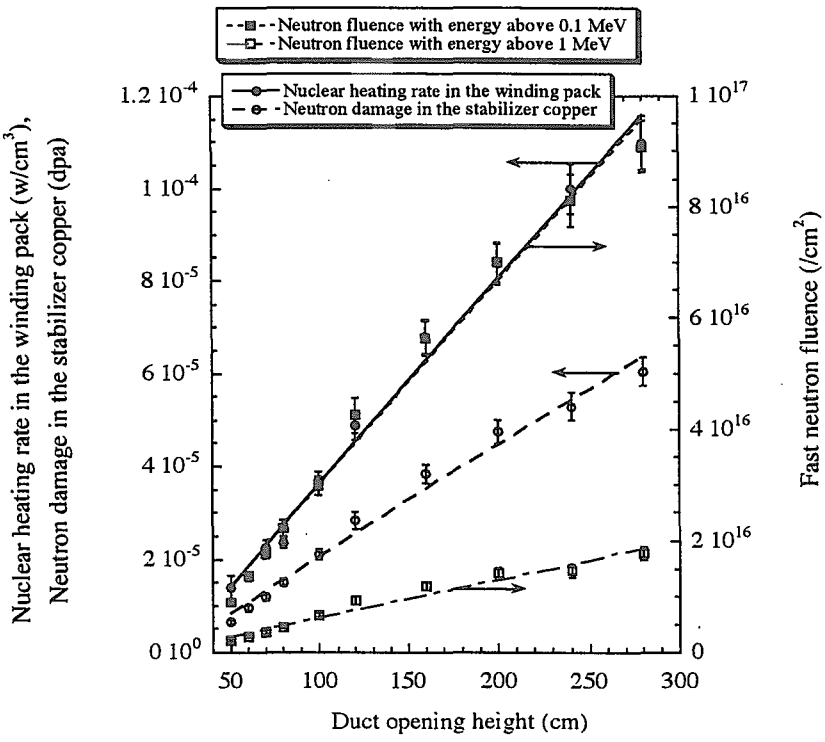

Fig. 5.8 Dependencies of the peak nuclear properties in the TF coil adjacent to the duct on the duct opening height with the error bar for the 80 cm wide duct opening, the 40 cm thick duct wall, the 200 cm thick shield adjacent to the duct under neutron wall loading of 1 MW/m^2 and integrated neutron wall loading of 1 MWa/m^2.

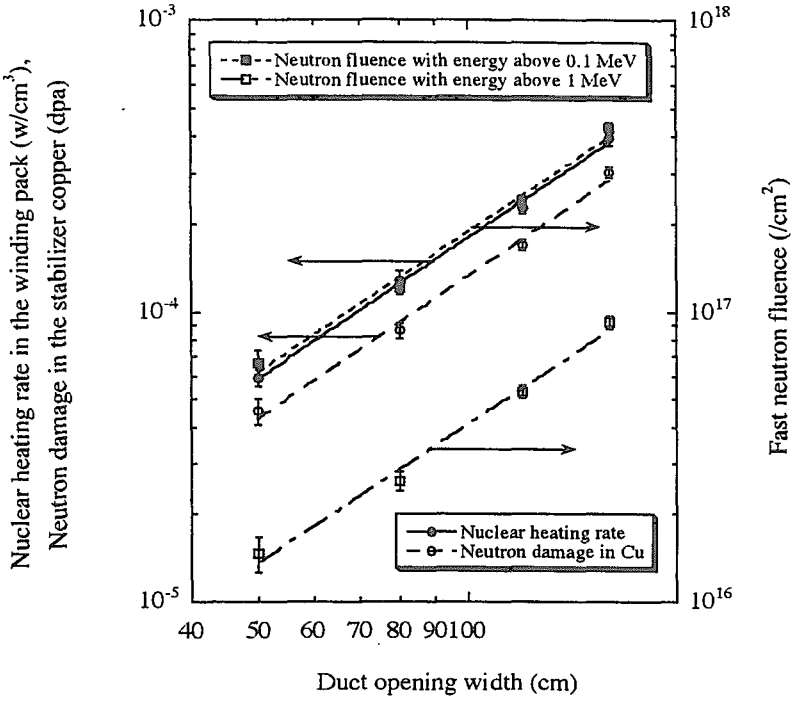

Fig. 5.9 Dependencies of the peak nuclear properties in the TF coil adjacent to the duct on the duct opening width with the error bar for the 50 cm high duct opening, the 30 cm thick duct wall, the 100 cm thick shield adjacent to the duct under neutron wall loading of 1 MW/m^2 and integrated neutron wall loading of 1 MWa/m^2.

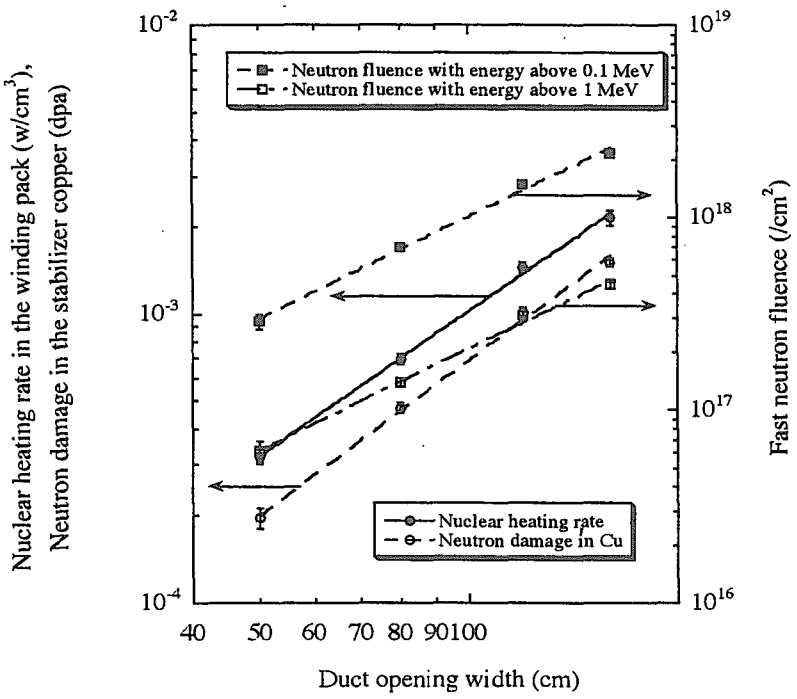

Fig. 5.10 Dependencies of the peak nuclear properties in the TF coil adjacent to the duct on the duct opening width with the error bar for the 160 cm high duct opening, the 30 cm thick duct wall, the 100 cm thick shield adjacent to the duct under neutron wall loading of 1 MW/m^2 and integrated neutron wall loading of 1 MWa/m^2.

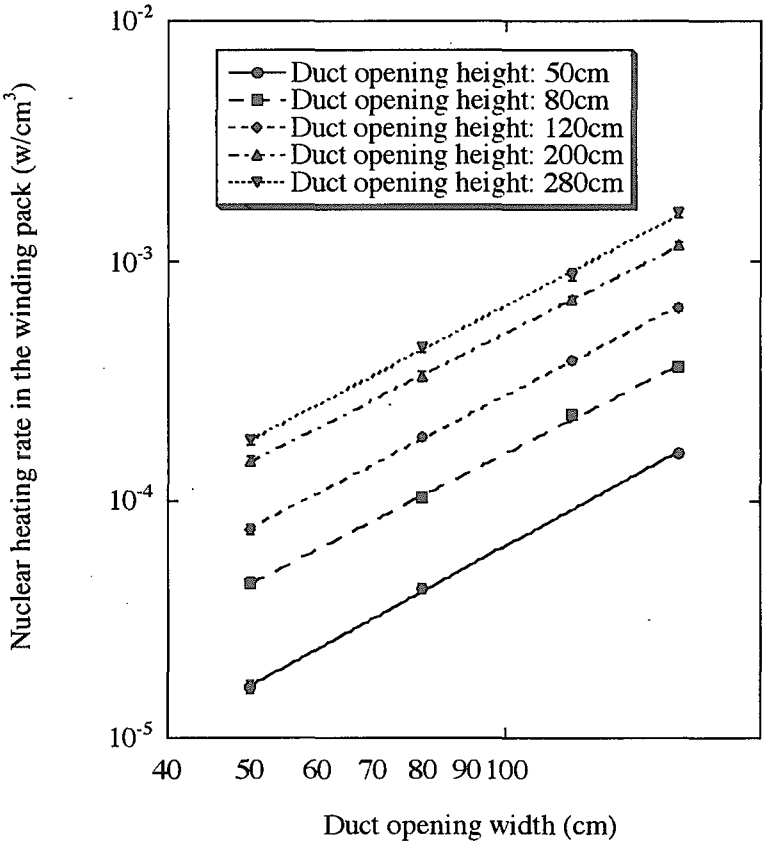

Fig. 5.11 Dependencies of the peak nuclear heating in the TF coil winding pack adjacent to the duct on the duct opening width with the error bar for the the 30 cm thick duct wall and the 200 cm thick shield adjacent to the duct under neutron wall loading of 1 MW/m^2.

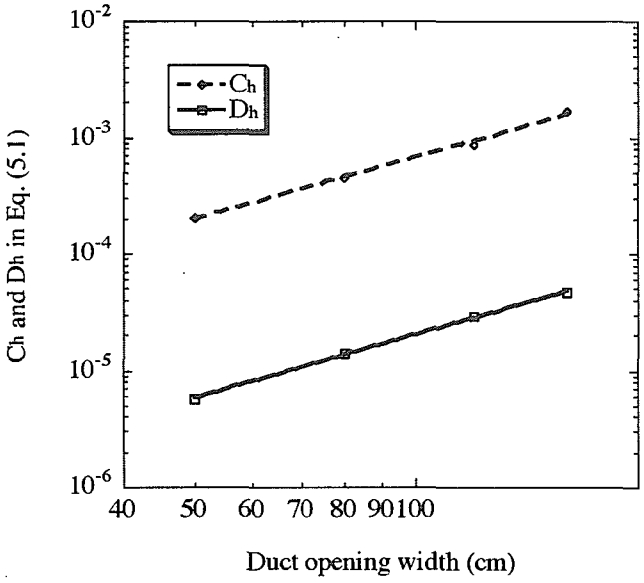

Fig. 5.12 Dependencies of the Ch and Dh values in Eq. (5.1) representing a function of the duct opening height on the duct opening width.

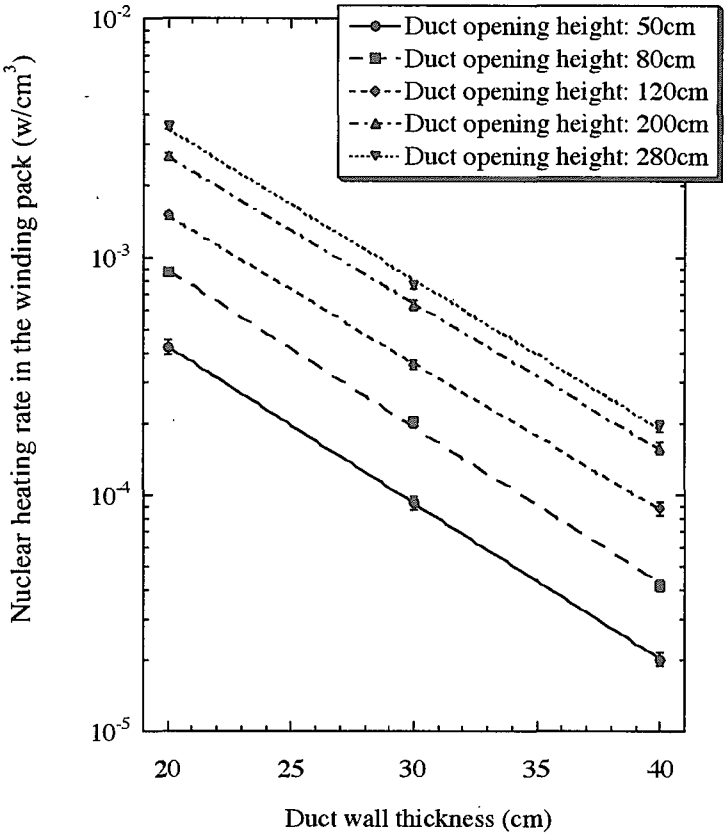

Fig. 5.13 Dependencies of the peak nuclear heating in the TF coil winding pack adjacent to the duct on the duct wall thickness with the error bar for the the 80 cm wide duct opening and the 130 cm thick shield adjacent to the duct under the neutron wall loading of 1 MW/m^2.

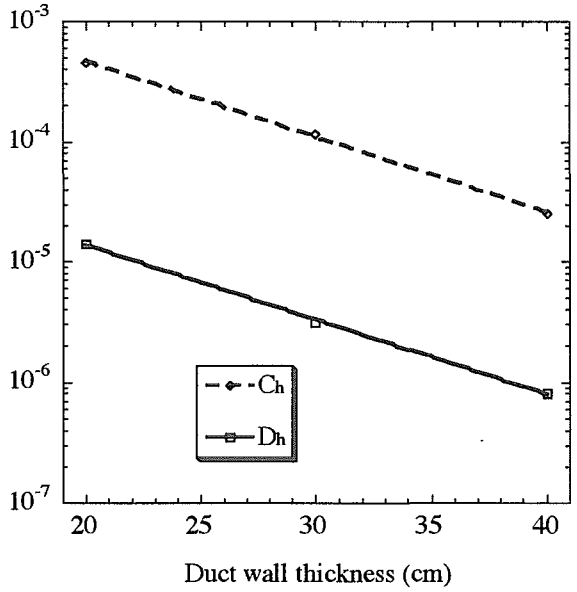

Fig. 5.14 Dependencies of the Ch and Dh values in Eq. (5.1) representing a function of the duct opening height on the duct wall thickness.

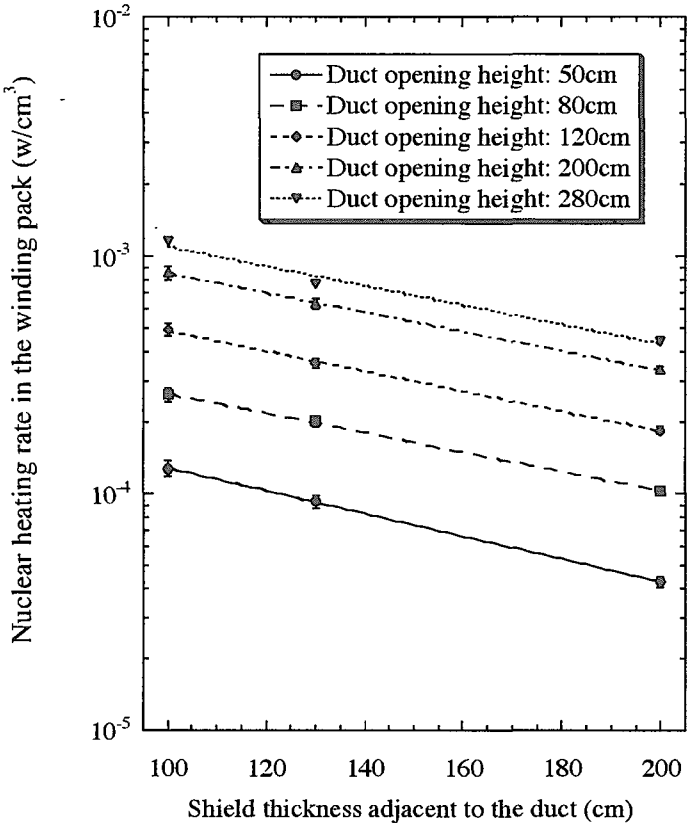

Fig. 5.15 Dependencies of the peak nuclear heating in the TF coil winding pack adjacent to the duct on the shield thickness adjacent to the duct with the error bar for the the 80 cm wide duct opening and the 30 cm thick duct wall under the neutron wall loading of 1 MW/m^2.

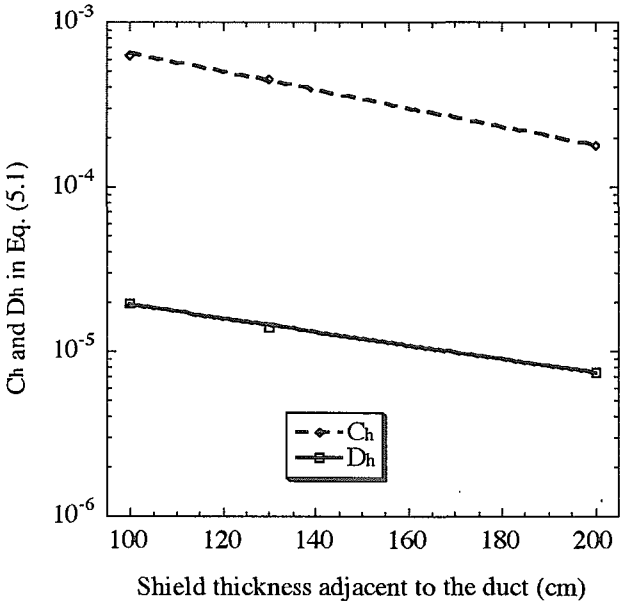

Fig. 5.16 Dependencies of the Ch and Dh values in Eq. (5.1) representing a function of the duct opening height on the shield thickness adjacent to the duct.

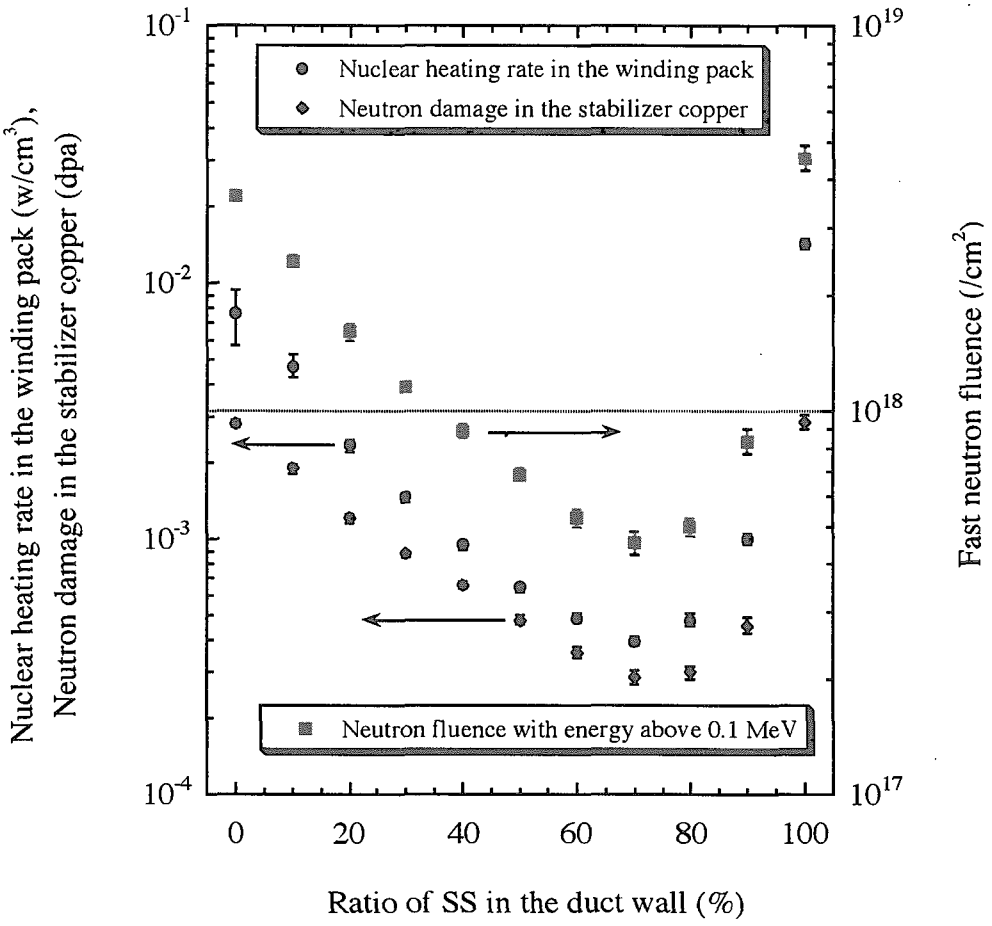

Fig. 5.17 Dependencies of the nuclear properties on the duct wall composition with the error bar for the 160 cm high and 160 cm wide duct opening, the 40 cm thick duct wall, the 100 cm thick shield adjacent to the duct under the neutron wall loading of 1 MW/m^2 and the integrated neutron wall loading of 1 MWa/m^2. The duct wall is composed of SS and water.

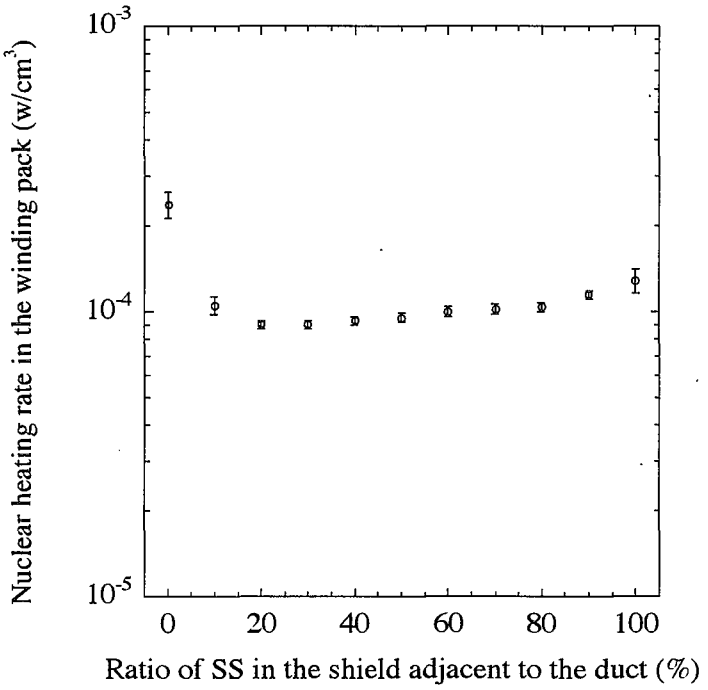

Fig. 5.18 Dependency of the nuclear heating rate in the TF coil winding pack adjacent to the duct on the shield composition adjacent to the duct with the error bar for the 80 cm high and 80 cm wide duct opening, the 30 cm thick duct wall, the 200 cm thick shield adjacent to the duct under the neutron wall loading of 1 MW/m^2. The shield is composed of SS and water.

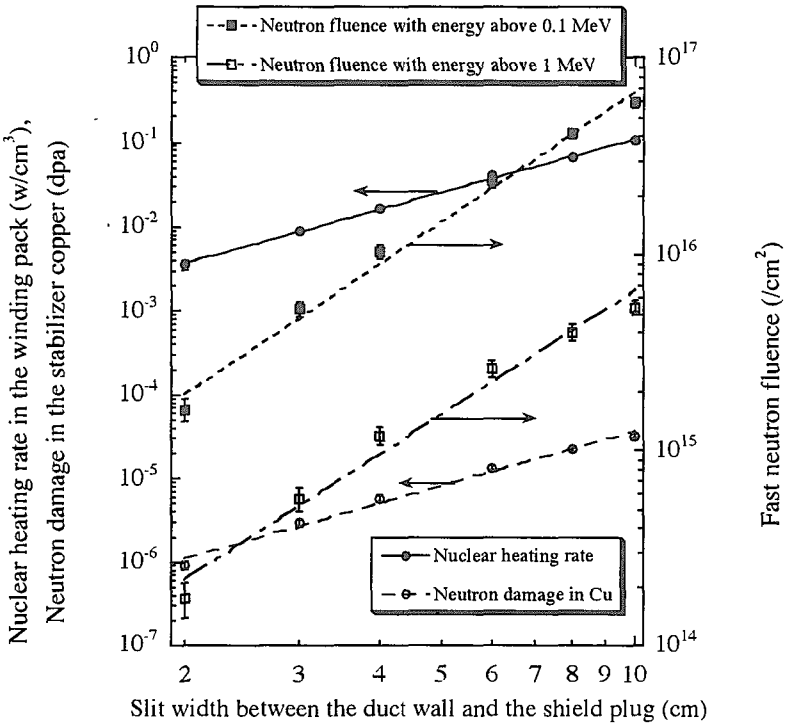

Fig. 5.19 Dependencies of the peak nuclear properties in the TF coil adjacent to the duct on the slit width between the duct wall and the shield plug installed in the duct with the error bar for the 20 cm thick duct wall with 100 cm thick shield plug under neutron wall loading of 1 MW/m^2 and integrated neutron wall loading of 1 MWa/m^2.

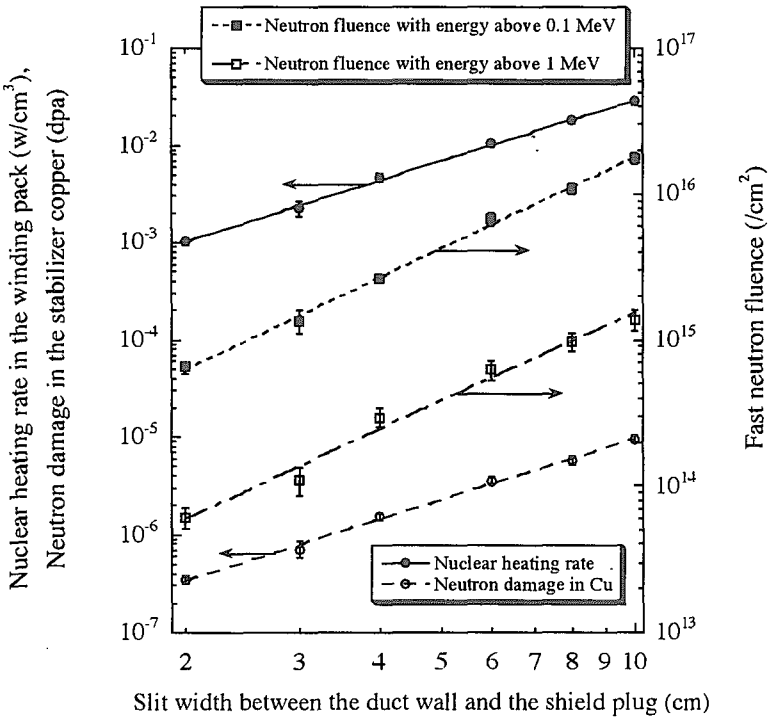

Fig. 5.20 Dependencies of the peak nuclear properties in the TF coil adjacent to the duct on the slit width between the duct wall and the shield plug installed in the duct with the error bar for the 30 cm thick duct wall with 100 cm thick shield plug under neutron wall loading of 1 MW/m^2 and integrated neutron wall loading of 1 MWa/m^2.

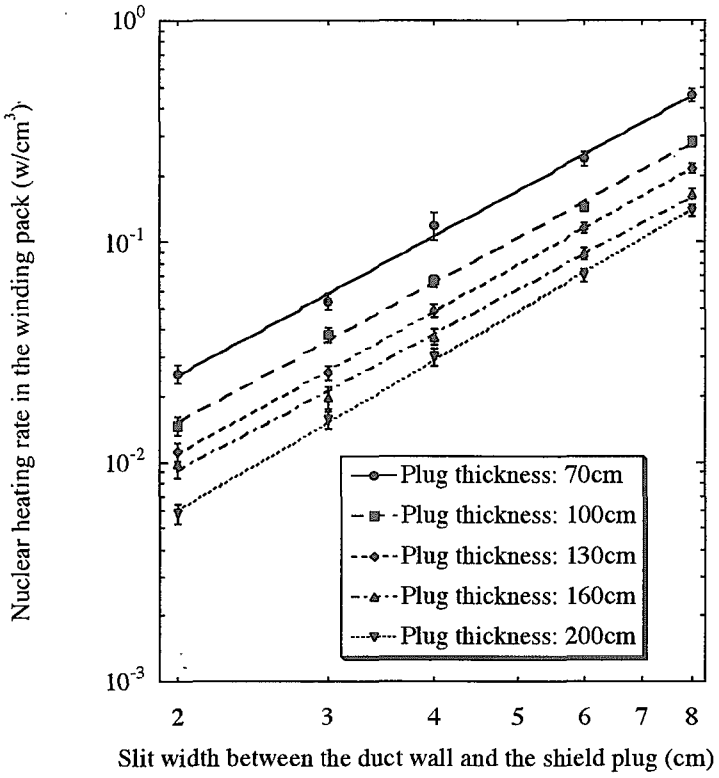

Fig. 5.21 Dependencies of the peak nuclear heating rate in the TF coil winding pack adjacent to the duct on the slit width between the duct wall and the shield plug installed in the duct with the error bar for the 10 cm thick duct wall under the neutron wall loading of 1 MW/m^2.

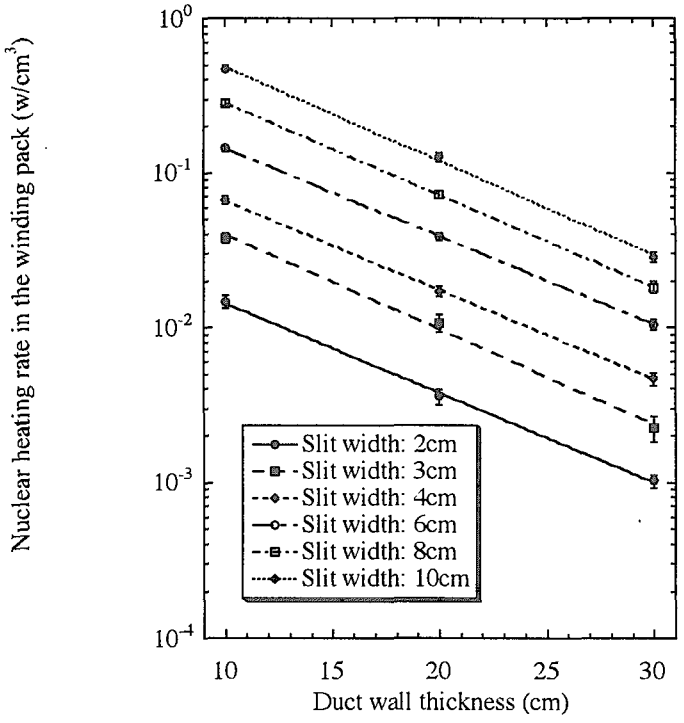

Fig. 5.22 Dependencies of the peak nuclear heating rate in the TF coil winding pack adjacent to the duct on the duct wall thickness with the error bar for the 100 cm thick shield plug installed in the duct under the neutron wall loading of 1 MW/m^2.

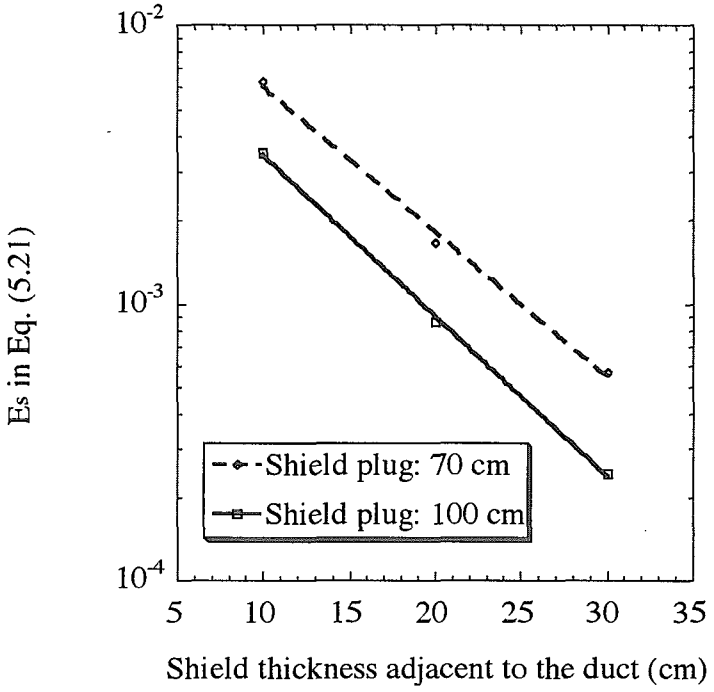

Fig. 5.23 Dependency of the E_S values in Eq. (5.21) representing a function of the slit width between the shield plug and the duct wall on the duct wall thickness for the nuclear heating rate on the winding pack with the 80 cm high duct opening and the 70 and 100 cm thick shield adjacent to the duct.

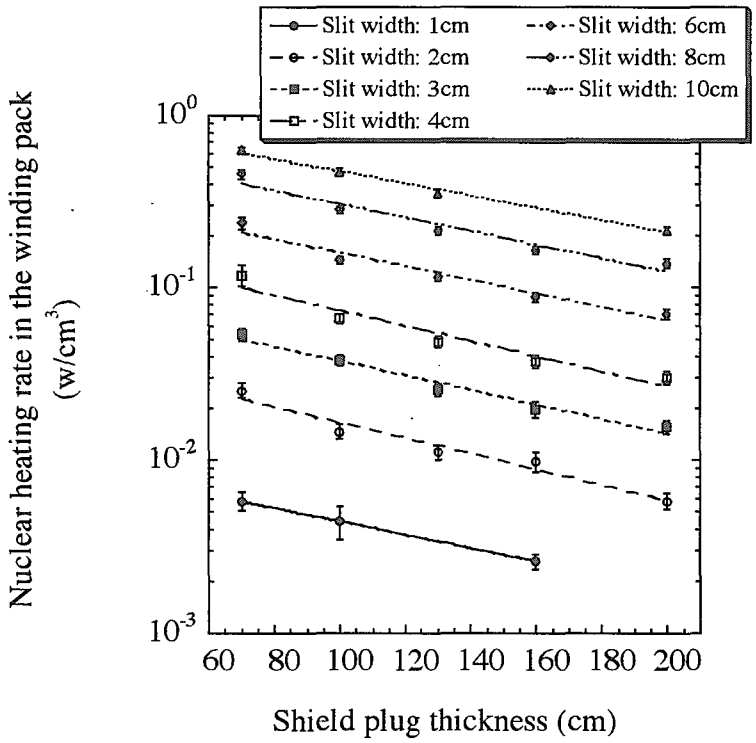

Fig. 5.24 Dependencies of the peak nuclear heating rate in the TF coil winding pack adjacent to the duct on the shield plug thickness installed in the duct with the error bar for the 10 cm thick duct wall under the neutron wall loading of 1 MW/m^2.

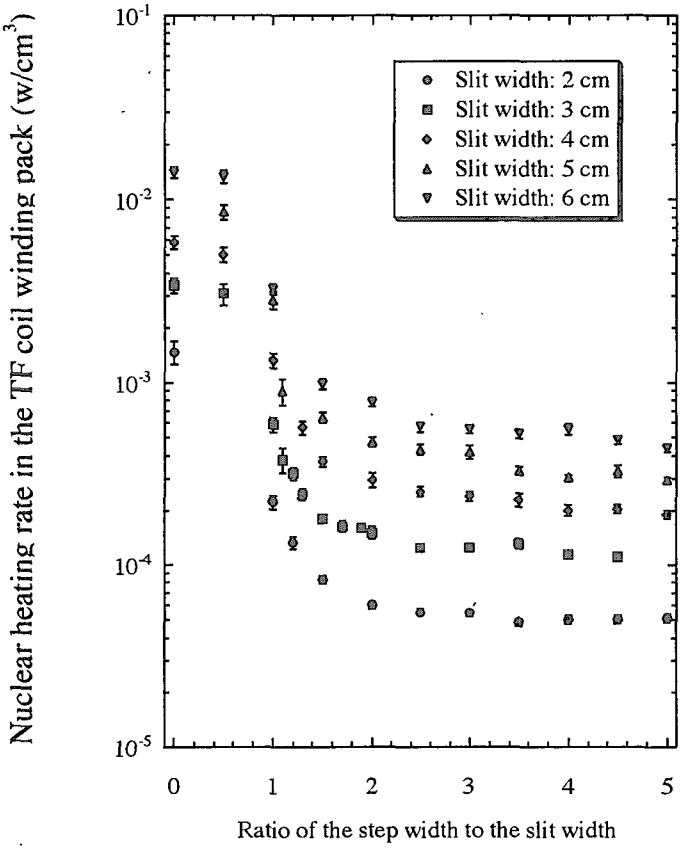

Fig. 5.25 Dependency of the peak nuclear heating rate in the TF coil winding pack adjacent to the duct on the step width under the neutron wall loading of 1 MW/m^2.

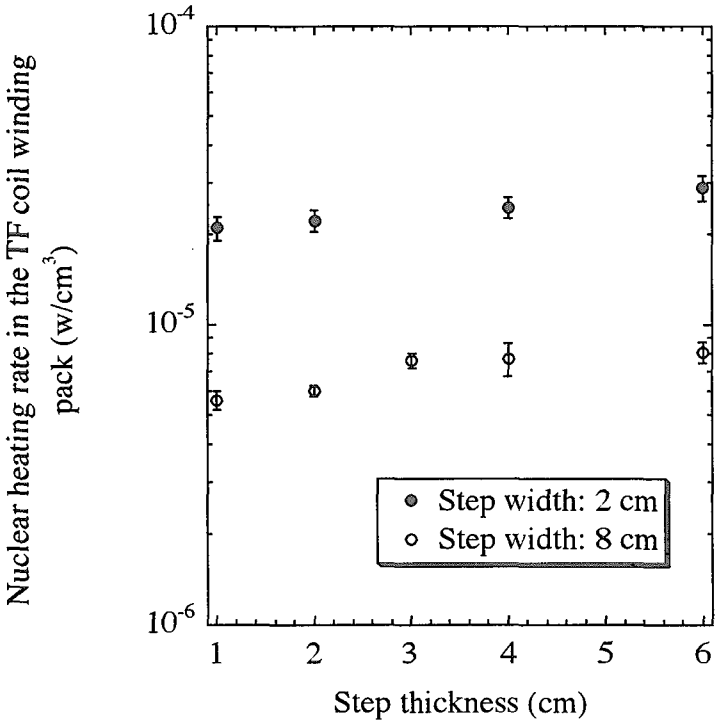

Fig. 5.26 Dependency of the peak nuclear heating rate in the TF coil winding pack adjacent to the duct on the step thickness under the 2 cm wide slit, 100 cm thick shield plug, 20 cm thick duct wall and the neutron wall loading of 1 MW/m^2.

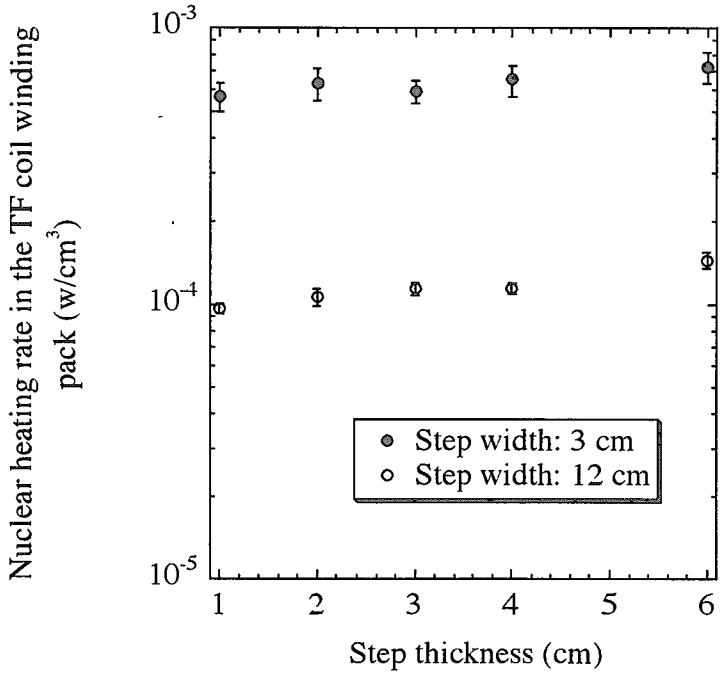

Fig. 5.27 Dependency of the peak nuclear heating rate in the TF coil winding pack adjacent to the duct on the step thickness under the 3 cm wide slit, 100 cm thick shield plug, 20 cm thick duct wall and the neutron wall loading of 1 MW/m^2.

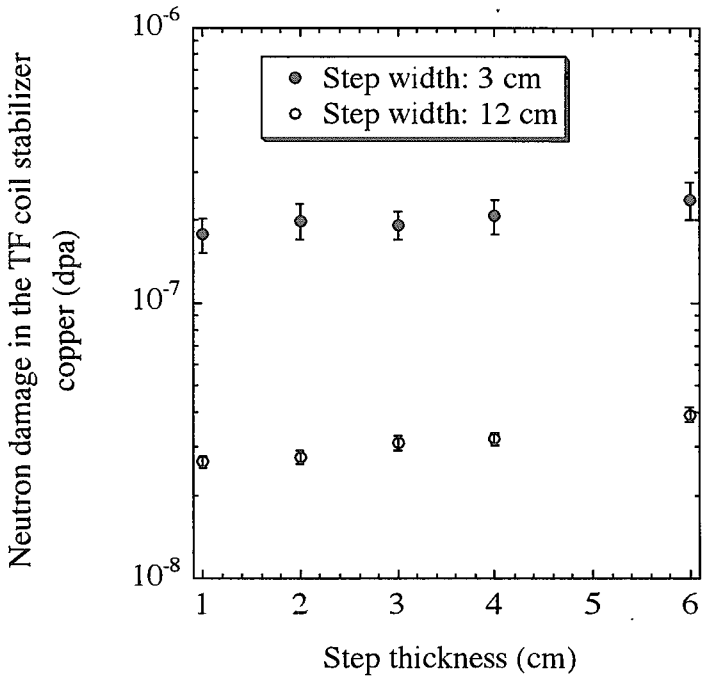

Fig. 5.28 Dependency of the peak neutron damage in the TF coil stabilizer copper adjacent to the duct on the step thickness under the 3 cm wide slit, 100 cm thick shield plug, 20 cm thick duct wall and the integrated neutron wall loading of 1 MWa/m^2.

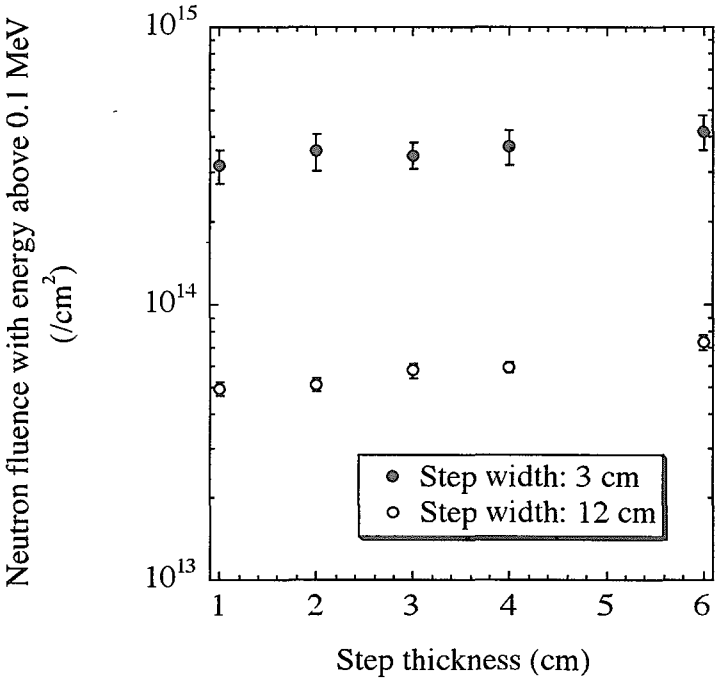

Fig. 5.29 Dependency of the peak neutron fluence in the TF oil winding pack with the energy above 0.1 MeV adjacent to the duct on the step thickness under the 3 cm wide slit, 100 cm thick shield plug, 20 cm thick duct wall and the integrated neutron wall loading of 1 MWa/m².

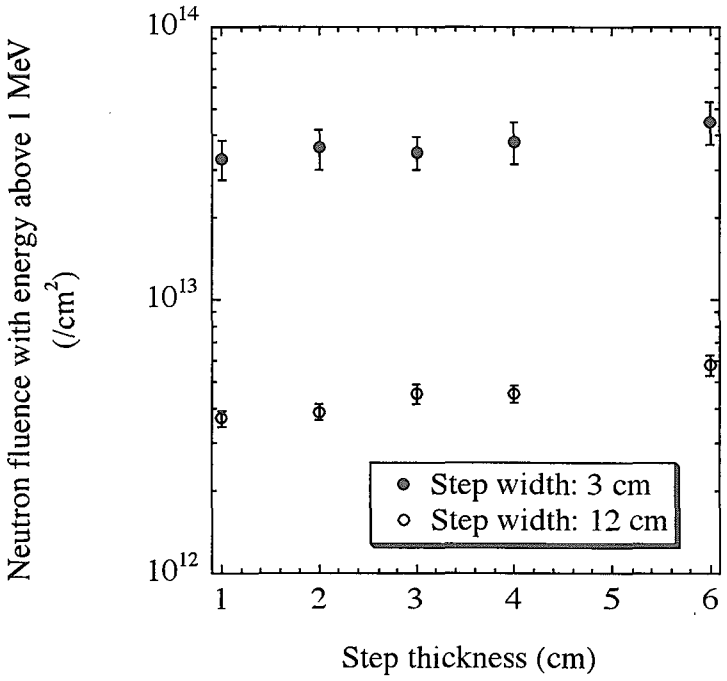

Fig. 5.30 Dependency of the peak neutron fluence in the TF coil winding pack with the energy above 1 MeV adjacent to the duct on the step thickness under the 3 cm wide slit, 100 cm thick shield plug, 20 cm thick duct wall and the integrated neutron wall loading of 1 MWa/m².

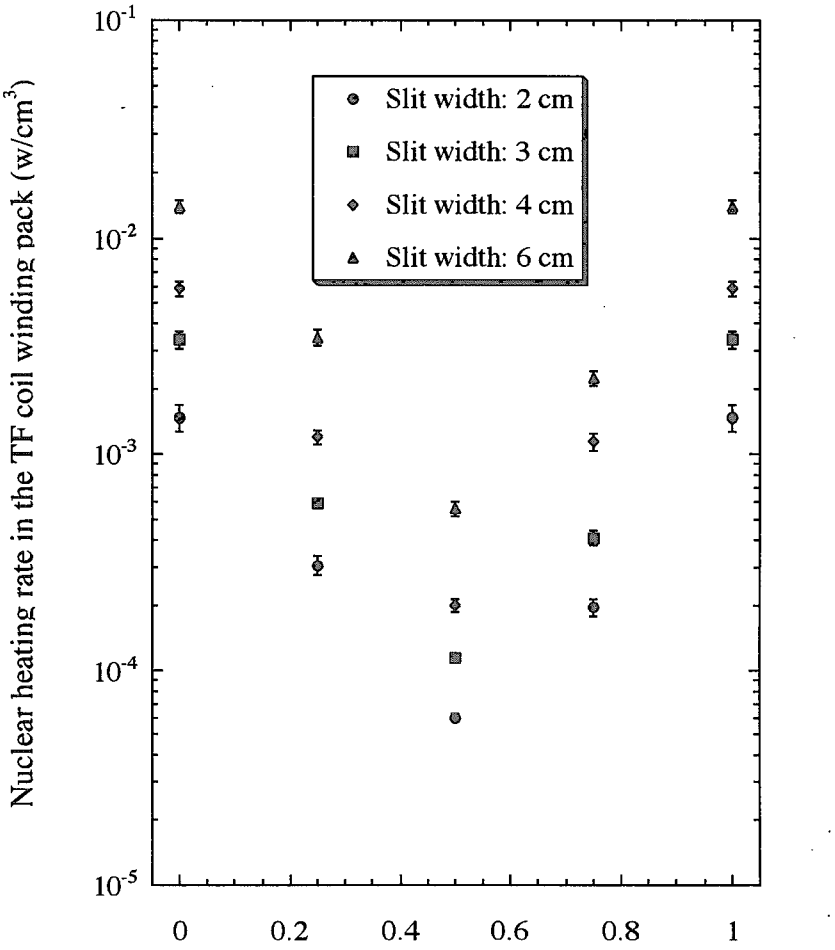

Fig. 5.31 Dependency of the peak nuclear heating rate in the TF coil winding pack adjacent to the duct on the step position.

6. Decay Gamma-ray Dose Rates around Large Opening Duct in Vacuum Vessel

6.1 Introduction

Many ducts are installed in the tokamak-type DT nuclear fusion reactor, and they penetrate the blanket and the vacuum vessel as mentioned above. In Chapter 5, the nuclear properties are discussed in the TF coil adjacent to the duct by the radiation streaming through the large opening duct in the vacuum vessel. In this Chapter, the decay gamma ray dose rates after shutdown are discussed in the region around the duct by the radiation streaming through the large opening duct in the vacuum vessel. Structures around the duct will be highly activated due to the neutron streaming through the duct. Personnel access outside the cryostat is required for hands-on maintenance at several days after shutdown, and inside the cryostat for rescue maintenance that can be conducted in a longer time (~ a month) after shutdown. Therefore, it is important to minimize the decay gamma ray dose rates around the duct to make these works possible. Dose rates at a few days to a few month are almost constant since ^{58}Co (half-life: 70.8 days) and ^{60}Co (half-life: 5.271 years) become major contributors after shorter half-life isotopes (^{56}Mn in stainless steel and ^{24}Na in concrete) decayed.

In the previous study [6.1], the decay gamma ray dose rates are evaluated by using the two dimensional SN method with the activation code. In the case of the two dimensional calculational geometry, the duct opening is assumed infinite in the Z direction, i. e. poloidal direction. Consequently, the results are overestimated by about one order of magnitude at the cryostat as shown in Chapter 2 [6.2]. Also in the previous studies [6.2 - 6.5], the fast neutron flux is estimated by the Monte Carlo neutron transport calculation, and the decay gamma ray dose rate was evaluated by multiplying the fast neutron flux with the constant flux-to-dose conversion factor based on the past experiences. In this case, the uncertainty due to the conversion factor is a critical issue [6.4 - 6.6].

In order to evaluate the decay gamma ray dose rate around the duct after shutdown with good accuracy, the Monte Carlo decay gamma-ray transport calculation is required. The spatial distribution of induced activity, which forms the decay gamma ray source, is needed for the decay gamma-ray transport calculation, and it can be obtained from the neutron flux distribution by using the activation code such as ACT-4 [6.7], FISPACT [6.8] or CINAC [6.9]. It requires a very fine (small) cell definition and huge calculation time to obtain the detailed neutron flux distribution in the overall region of the nuclear fusion reactor, and it is not realistic for the actual design calculation.

Valenza et al. have proposed the Monte Carlo calculation method replacing the prompt gamma ray spectrum with the decay gamma ray spectrum to conduct the Monte Carlo decay gamma-ray transport calculation and evaluate the decay gamma-ray dose rate after shutdown with good accuracy [6.6, 6.10]. In this method, decay gamma ray can be generated at the exact location where the radioisotopes are produced by the nuclear reaction induced by the neutron, and the neutron and decay gamma-ray transport calculation can be simultaneously conducted. This method dose not require a very fine (small) cell definition, though it may a little fine cell definition to reduce the statistical error by the weight window importance. However, it requires a very long calculation time to apply this method to the actual design

calculation of the nuclear fusion reactor, and to reduce the statistical error (calculation time) and obtain the calculated results with good accuracy is a critical concern for the application of this method to the actual design calculation.

In order to apply this method to the actual design calculation of the tokamak-type nuclear fusion reactor with drastically reducing the calculation time, the effective variance reduction method is proposed by the application of the weight window technique and the specification of the decay gamma ray generation region in this Chapter [6.11]. This method identifies the region producing the decay gamma ray which can contribute the decay gamma ray flux in the evaluation location, and the gamma ray transport calculation is forcibly terminated in the region except for the identified region. This method is applied to the ITER shielding calculation with the detailed calculational geometry simulating the overall region of the tokamak-type nuclear fusion reactor. Decay gamma ray dose rates after shutdown are evaluated around the maintenance and Neutral Beam Injection (NBI) ducts to demonstrate the effectiveness of this method [6.11, 6.12].

6.2 Calculation Method

6.2.1 Decay gamma-ray transport calculation [6.10]

The Monte Carlo calculation code MCNP-4B is applied with the fusion evaluated nuclear data library FENDL-1 in this Chapter. Figure 6.1 shows the Monte Carlo decay gamma-ray transport calculation procedure applied in this Chapter. It is possible to conduct the neutron and prompt gamma-ray transport calculation in the original MCNP code. By replacing a prompt gamma ray spectrum with a decay gamma ray spectrum in the nuclear data library and also a modest change in the original MCNP code, the neutron and the decay gamma-ray transport calculation is conducted simultaneously in MCNP. The decay gamma rays are generated from the radioisotopes of ^{51}Cr, ^{54}Mn, ^{59}Fe, ^{58}Co and ^{60}Co, which dominate dose rates. Inside the cryostat, the decay gamma ray dose rate at 10^6 seconds after shutdown (typical time point of interest concerning maintenance operation) can be determined by these five radio isotopes [6.4 – 6.6, 6.10], whose production rates can be obtained by MCNP.

The data table in MCNP consists of the NXS array (contains various conters and flag), the JXS array (contains pointers) and the XSS array (contains all of the nuclear data). The sixth entry is the total number of photon production reactions in the NXS array. This value is modified according to the number of radioactive isotopes for the isotope applied in this Chapter. The ^{58}Ni isotope produces only one isotope of ^{58}Co via (n, p) reaction. The ^{59}Co isotope produces three different radioactive isotopes of ^{59}Fe, ^{58}Co and ^{60}Co via (n, p), (n, 2n) and (n, γ) reactions, respectively. In the JXS array, each entry is a pointer to same specific location in the next array (XSS). Some of these entries are modified according to the modification which is introduced in the XSS array. The XSS array consists of several sub-arrays. Only those involving the gamma production data (reactions, spectrum, yield) implementing the decay schemes are modified. The decay gamma ray spectra of ^{60}Co used in the present MCNP calculation is shown in Table 6.1. The gamma ray spectra implemented in this Chapter are discrete spectra, which mean that only the gamma rays with the energy

shown in Table 6.1 are produced. For all the other isotopes, the prompt gamma production can be turned off, switching the NXS(16) value to –1. [6.10]

In order to differentiate the gamma rays from the five radioisotopes, the subroutine ACEGAM.F, which is assigned to calculate the photon production, is modified. For tallying purposes, a few tenth lines are added to control the birth time of the photon (the default value is 0) depending on the emitting radioisotope. By doing so, it is possible to score easily the single contribution to the total dose level using a time flag. Another modification is to evaluate the correct gamma production probability. In a normal situation, MCNP calculates the prompt gamma production probability as the ratio of $\sigma_{\gamma\ \text{production}}$ / σ_{total}. This part of the subroutine calculating the decay gamma ray production probability is modified as the following formula;

$$(\sigma_{(n,\ x)} / \sigma_{\text{total}})\ P_{\gamma},$$

where P_{γ} is decay gamma ray probability shown in Table 6.1 [6.10].

The decay gamma rays are emitted from the location where the radioisotopes are generated by the nuclear reactions induced by the neutrons in this method. Therefore, the location where the decay gamma ray is emitted can be exactly determined without error. The actual activity (decay rate) of each radioisotope after shutdown is usually smaller than the production rates, and it depends on the machine operation scenario and time after shutdown [6.10]. The ratio of the actual activation level to the production rate is shown in Table 6.2 for each radioisotope at 10^6 seconds after shutdown based on the ITER operation scenario. These ratios are different for each radioisotope as shown in Table 6.2, therefore the contribution to the total dose level from each other is separated using a time bins. The hypothetical birth time of the photon is given depending on the emitting radioisotope by modifying the subroutine ACEGAM.F in MCNP. The different time delays are given for different decay gamma ray productions [6.10]. The decay gamma ray flux due to each radioisotope can be obtained, and the total gamma ray flux can be obtained by multiplying each gamma ray flux with each ratio of the actual activation level to the production rate.

6.2.2 Variance reduction method [6.11]

The Monte Carlo decay gamma ray calculation method introduced in Section 6.2.1 requires a very long calculation time to apply the method to the actual design calculation of the tokamak-type DT nuclear fusion reactor as mentioned above. In order to apply the method to the actual design calculation with drastically reducing the calculation time, the effective variance reduction method is proposed in this Chapter. It is shown in Fig. 6.2. It consists of three processes; 1) preparation of the weight window table for the neutron transport calculation, 2) specification of the decay gamma ray generation region, 3) preparation of the weight window table for the neutron and decay gamma-ray transport calculation based on the information obtained by these two processes in the final process.

6.2.2.1 Weight window generation for neutron transport calculation

The conceptual view of the vertical cross section of the fusion reactor is shown in Fig. 6.3. The 14 MeV neutron source is sampled from an isotropic neutron distribution according to the fusion reaction distribution in the plasma region shown in Fig. 6.3. Only neutron transport calculation is conducted in this process. It is nearly impossible to obtain the overall spatial distribution of the neutron flux with good accuracy in realistic calculation time using the Monte Carlo method. In this process, the neutron flux in the region around the duct penetration, Location B shown in Fig. 6.3, is estimated using the weight window technique [1.19] which is a space-energy-dependent splitting and Russian roulette variance reduction procedure in order to reduce the computing time without loosing the accuracy. The generation method is proposed to prepare the effective weight window importance for the region around the duct penetration. This method is shown in Fig. 6.4. Reducing the value of the weight window importance along the track of the neutron streaming from the plasma to the target in the region around the duct, Location B shown in Fig. 6.3, results in a large number of neutrons with low weight that reach the target region. By assigning the target location, the reasonable weight window importance table is automatically generated in MCNP-4B [1.19]. To generate the table, a considerable number of neutrons must reach the target location. When the designated target location is in the region around the typical duct in the fusion rector, e.g. the NBI duct [6.13 - 6.15], an enormous number of histories and long calculation time are required to generate the weight window table in a single step. This occurs because only 10^{-7} to 10^{-9} of neutrons born in the plasma can reach the target region. In this process, the target locations are sequentially moved from the inlet of the duct opening, Location A shown in Fig. 6.3, to the region around the duct, Location B shown in Fig. 6.3, along the expected neutron streaming track, a broken line shown in Fig. 6.3, in steps and the weight window importance table for each target location is generated [6.4, 6.16]. When the neutron flux is obtained at the target location with good statistical error, e. g. less than 10 %, the target location is moved to the next target location. The Monte Carlo neutron transport calculation is conducted for the next target location, and the reasonable weight window importance table is generated for the next target location. The effective weight window importance table for the final target location in the region around the duct is then prepared in the final step of this process.

6.2.2.2 Specification of the decay gamma-ray generation region

Tracking each decay gamma ray that occurred from the overall region of the nuclear fusion reactor make the calculation unpractical and time-consuming. In this process, the region producing the decay gamma ray which can contribute the decay gamma ray flux in the final target location, Location B shown in Fig. 6.3, are identified. The method is proposed to identify the region producing the decay gamma ray. This method is shown in Fig. 6.5. Prior to the decay gamma-ray transport calculation by using the method shown in Chapter 6.2.1, the hypothetical gamma ray sources with the energy of 2 MeV, which cover the energy region for the decay gamma ray in this Chapter, are set at the final target location, and the gamma-ray transport calculation is conducted by MCNP with the same calculation model. The

information of the particle collision can be obtained in each cell from the output result by MCNP. The hypothetical gamma ray that occurred from the final target location can not reach the cell where the particle collision density is 0 or negligible small. Namely, the decay gamma ray occurred from the cell where the particle collision density is 0 or negligible small can not reach the final target location. From the information of the particle collision in the calculated results, the cells where the gamma ray occurring from the final target location are collided can be identified as the cells producing the decay gamma ray which can contribute the decay gamma ray flux in the final target location. The weight window table is set for the gamma ray to the positive value in the identified cells. The weight window table is set for the gamma ray to the negative value, e. g. –1, in the cells except for the idenified cells, e.g. most parts of inboard vacuum vessel and TF coil shown in Fig. 6.3, to remove the decay gamma ray occurring from the cells except for the identified cells. By applying the negative values to the weight window importance table, the gamma ray transport calculation can be forcibly terminated in the cells except for the identified cells. Only the decay gamma rays occurring from the identified cells can be contributed to the decay gamma ray flux in the final target location.

6.2.2.3 Final weight window generation for neutron and decay gamma-ray transport calculation

Based on the generated weight window table for neutron transport calculation in the process a) shown in Fig. 6.2 and the specification of the cells for the decay gamma ray generation region in the process b), the final weight window table is generated for neutron and decay gamma-ray transport calculation. The generation procedure is proposed, and it is shown in Fig. 6.6. In the specified cells for the decay gamma ray generation, the values of the weight window table are set for the decay gamma-ray transport calculation to the same values as those of the weight window importance table for the neutron transport calculation generated in the process a) as the tentative values in the initial guess of this process. In the cells except for the specified cells for the decay gamma ray generation, the values of the weight window table are set for the decay gamma-ray transport calculation to –1 as the negative values as mentioned above. The neutron and decay gamma-ray transport calculation is conducted by using the initial weight window table and the algorithm generating the reasonable weight window table, and the effective final weight window table is generated for neutron and decay gamma-ray transport calculation in the final step of this process.

6.3 Application to ITER Shielding Design [6.11, 6.12]

6.3.1 Calculational geometry

In order to demonstrate the effectiveness of the calculation method shown in Chapter 6.2, the actual shielding design calculation of the nuclear fusion reactor is conducted by this method. It is applied to the shielding design of ITER maintenance and NBI ducts. The calculational geometries used in this Chapter are shown in Figs. 6.7 – 6.9 for the maintenance

duct, and they are shown in Figs. 6.10 – 6.13 for the NBI duct. The features of the geometries are as follows.

(a) Maintenance duct

1) The 20° sector of the overall torus region is applied in toroidal (horizontal) direction.
2) The overall region including the upper and lower, i.e. divertor, ducts is applied in poloidal (vertical) direction.
3) One maintenance duct is installed, and three shield plugs and the limiter alignment support are installed inside the maintenance duct as shown in Figs. 6.7 – 6.9.
4) The 2 cm wide slits are installed between the shield plug and the blanket/vacuum vessel in toroidal and poloidal directions.
5) The 20 cm thick vacuum vessel duct wall, the 20 cm thick plug flame and the10 cm thick cryostat duct wall are installed.
6) The shield plug-1, 2 and 3 are 54 – 60, 50 and 50 cm thickness, respectively.
7) The 15 cm wide annular gap is installed between the limiter alignment support and the shield plug-2. The inner and outer diameters of the annular gap are 45 and 75 cm, respectively.
8) The limiter alignment support consists of two cylinder configurations. The front and rear parts are 45 and 30 cm diameters, respectively.
9) A distance from the end of the front part of the limiter alignment support to the shield plug-3 is 130 cm.
10) Compositions of the shield plug and the plug flame are 80 % SS/20 % water and 60 % SS/40 % water, respectively.
11) The vacuum vessel duct wall consists of SS inner wall, shield part and SS outer wall.
12) The PF coil support structure with L-shape configuartion is installed at the space behind the TF coil as shown in Fig. 6.9, and it is 15 cm width in toroidal direction.

(b) NBI duct

1) The 60° sector of the overall torus region is applied in toroidal direction, and the overall region is applied in poloidal direction.
2) Three NBI ducts, i.e. NBI-1, NBI-2 and Diagnostic NBI (D-NBI) ducts, are installed. The D-NBI duct is close to the NBI-1 duct.
3) Dimensions of the duct opening inlet of the NBI-1 and 2 ducts are about 58 cm width and 123 cm height, and those of the D-NBI duct are about 40 cm width and 40 cm height.
4) Each NBI duct consists of a multi-layered port wall, and the detailed dimensions are shown in Figs. 6.11 – 6.13.
5) Thinnest thicknesses of the upper and lower duct walls are about 40 and 48 cm, respectively.
6) Compositions of the duct wall, cryostat wall and cryostat additional shield are 84 % SS/16 % water, 100 % SS and 100 % SS, respectively.
7) The Poloidal Field (PF) coil support structures with L-shape structure are installed at the

space behind the Toroidal Field (TF) coils as shown in Fig. 6.11, and they are 15 cm width in toroidal direction.

6.3.2 Evaluation results

6.3.2.1 Maintenance duct

Neutron flux of the energy above 1 MeV in the space inside the maintenance duct and behind the shield plug-3 are shown in Fig. 6.14 for the fusion power with 500 MW. Neutron flux of the energy above 1 MeV in the space inside the maintenance duct and behind the shield plug-3 are 5 x 10^5 to 1 x 10^6 neutrons·cm^{-2}·s^{-1} as shown in Fig. 6.14, and they are reduced by about eight orders of magnitude compared with those at the plasma region. The decay gamma ray dose rates are shown in Fig. 6.15 at 10^6 seconds after shutdown based on the ITER operation scenario by the calculation method shown in Chapter 6.2. The decay gamma ray dose rates in the space inside the maintenance duct and behind the shield plug-3 are 6 x 10^0 to 2 x 10^1 μSv/hour at 10^6 seconds after reactor shutdown as shown in Fig. 6.15. The decay gamma ray dose rates in the space outside the maintenance duct and behind the TF coil are 6 x 10^0 to 2 x 10^1 μSv/hour, and those in the space at above or below the maintenance duct in the poloidal direction and behind the PF coils are 5 x 10^0 to 1 x 10^1 μSv/hour. The decay dose rates around the maintenance duct at 10^6 seconds after shutdown are less than the tentative design target of 100 μSv/hour by about one order of magnitude, therefore they can fully satisfy the design target.

6.3.2.2 NBI duct

Neutron flux of the energy above 1 MeV in the space at the equatorial plane between three NBI ducts, and those in the space above the NBI-1 duct in the poloidal direction are shown in Figs. 6.16 and 6.17, respectively. Neutron flux of the energy above 1 MeV in the space between three NBI ducts are 1 x 10^7 to 4 x 10^8 neutrons·cm^{-2}·s^{-1}, and they are reduced by 5 to 7 orders of magnitude compared with those at the plasma region. The PF coil support structure with L-shape structure works as good shield, and the neutron fluxes are reduced by a factor of about eight as shown in Fig. 6.16. The decay gamma ray dose rates in the space at the equatorial plane between three NBI ducts, and those in the space at above the NBI-1 duct in the poloidal direction are shown in Figs. 6.18 and 6.19, respectively. The dose rate just outside the wall of NBI-1 duct is very high giving the maximum around 3000 μSv/hour. The dose rate near the cryostat is reduced by more than one order of magnitude. It is still significantly higher than the tentative design target of 100 μSv/hour for hands-on maintenance. The equatorial plane is not the place to access for maintenance of components, such as break boxes of magnet system, and the space along the cryostat between these ducts and PF coil is a place to access for the maintenance works. Figure 6.19 shows the dose rates at the place. They are much lower than those at equatorial plane, and almost equal to the tentative design target of 100 μSv/hour.

In the Monte Carlo calculation, the history of a particle is tracked in a shielding system in accordance with the probability law, so that each course that a particle passes through can be recognized. By using the cell flagging card, the passage of particle can be recognized in MCNP. Only the particles passing through the flagging cell are flagged, and the other particles are not flagged. Moreover, the flagged particles and the nonflagged particles are distinguished at specified locations. Therefore, each tracked course to the specified locations can be recognized [6.17]. The flagging technique is applied for this Chapter to evaluate the main passage of particle for the neutron flux of the energy above 1 MeV in the space above the NBI-1 duct in the poloidal direction, and the result is shown in Fig. 6.20. In the cell A shown in Fig. 6.20, the total neutron flux of the energy above 1 MeV and the neutron flux streaming through the cell 1 are 9.4 and 8.1 x 10^7 neutrons·cm^{-2}·s^{-1}, respectively, and the fraction of the neutron flux streaming through the cell 1 to the total fast neutron flux in the cell A is about 86 %. The fraction of the fast neutron flux streaming through the cell 2 to the total fast neutron flux in the cell B is about 70 %. It is found that the neutron flux of the energy above 1 MeV passing the cell 1 and 2 shown in Fig. 6.20 mainly contribute to the neutron flux in the space above the NBI-1 duct in the poloidal direction. It can be concluded that the neutron flux of the energy above 1 MeV can be drastically reduced, which results the reduction of the decay gamma ray dose rates, by installing the thin additional shields such as about 10 cm thick SS in the limited area around the cells 1 and 2, and it is expected that the decay gamma ray dose rates can fully satisfy the tentative design target of 100 μSv/hour.

6.4 Discussions [6.11]

In addition to the calculated values, the values of Fractional Standard Deviation (FSD) representing the statistical error are also shown in Figs. 6.14 – 6.20. In the MCNP code, the values of FSD with less than 10 % are required to obtain the reliable calculated value [6.13]. The values are 3 to 10 % for the FSD at the evaluation location in the present results, and good values can be obtained. The values of FSD can satisfy the requirement as the reliable calculated value. It can be concluded that the calculation method proposed in this chapter can give the reliable value for the evaluation of the decay gamma ray dose rate around the duct penetration in the nuclear fusion reactor.

The values of FSD for the decay gamma ray dose rate in the cell S and the cell T are shown in Fig. 6.21 at the same history. The cell S is not target cell, but is very close to the plasma, i.e. neutron source region. On the other hand, the cell T corresponds to the target one, but is very far from the plasma. Although the cell T is much further from the neutron source than the cell S, the value of FSD for the decay gamma ray dose rate in the cell T is much better that that in the cell S. It can be concluded that the value of FSD for the decay gamma ray dose rate in the target cell located very further from the neutron source can be improved by the variance reduction method proposed in Chapter 6.2.2..

The comparisons between the value of FSD obtained by this method with the specification of the decay gamma ray generation region shown in Chapter 6.2.2 and that without the specification are shown in Fig. 6.22 for the decay gamma ray dose rates in the space above the NBI-1 duct in the poloidal direction at the same calculation time. In this

figure, the upper values correspond to the values of FSD by this method with the specification of the decay gamma ray generation region, and the lower ones to those without the specification. It is found that the values of FSD can be drastically improved by the specification of the decay gamma ray generation region. Therefore it can be concluded that the proposed method shown in Chapter 6.2.2 are much useful for improving the values of FSD.

Ratios of the decay gamma ray dose rates at 10^6 seconds after shutdown to the neutron flux of the energy above 1 MeV are obtained by dividing the values shown in Fig. 6.19 with those in Fig. 6.17. The ratios, which are used as the constant flux-to-dose conversion factor in the previous studies [6.2 - 6.5], are shown in Fig. 6.23, and it is found that they are 0.3 – 2.4 x 10^{-5} μSv/hour for one fast neutron flux. In the previous studies [6.2 - 6.5], the decay gamma ray dose rates are evaluated using the fast neutron flux obtained from the three dimensional Monte Carlo calculation and the constant conversion ratio obtained from the two dimensional Sn calculation with the activation calculation. The calculational sequence applied in the previous study is shown in the flowchart in Fig. 6.24. Neutron flux distribution is obtained using Sn calculation. Activation calculation is performed based on the operation scenario to estimate the residual gamma ray source at 10^6 seconds after shutdown. Decay gamma ray transport calculation is performed using the residual gamma ray source to determine the decay gamma ray dose rates by the two dimensional Sn calculation. The conversion ratios of the fast neutron flux to the decay gamma ray dose rates are obtained by dividing the the decay gamma ray dose rates by the two dimensional Sn calculation with the fast neutron flux by the two dimensional Sn calculation. The conversion ratios of fast neutron flux to the decay gamma ray dose rate at 10^6 seconds after shutdown are estimated for the neutron flux of the energies above 0.1 or 1 MeV in the previous study since ^{58}Co via (n, p) reaction of ^{58}Ni is expected to be main residual gamma-ray source. The ^{58}Ni(n, p) cross section has a flat maximum value (~0.63 barn) from 6 to 11 MeV and decreases to ~0.3 barn at 3 MeV. The examples of the conversion ratios around the ITER NBI duct estimated in the previous study are shown in Figs. 6.25 – 6.30 [6.4]. The two dimensional Sn calculational geometry is shown in Fig. 6.25, and it includes the blanket modules, vacuum vessel, cryostat, biological shield, five TF coils, one PF coil, three NBI and two standard equatorial ducts. A contour of the neutron flux of the energy above 0.1 and 1 MeV obtained from two dimensional Sn calculation are shown in Figs. 6.26 and 6.27, respectively. A contour of the decay gamma ray dose rate is shown in Fig. 6.28 at 10^6 seconds after shutdown. Dividing the values shown in Fig. 6.28 with those in Figs. 6.26 and 6.27 yield the conversion ratios. The contours of the conversion ratio are shown in Figs. 6.29 and 6.30 for the neutron flux of the energies above 0.1 and 1 MeV, respectively. From the results in Figs. 6.29 and 6.30, it is estimated that the conversion ratios are 1.5 to 2 and 3 to 4 x 10^{-5} μSv/hour/(cm^{-2}sec.$^{-1}$) for the neutron flux of energies above 0.1 and 1 MeV, respectively. In the previous studies [6.2 – 6.5], these conversion ratios are applied to estimate the decay gamma ray dose rate from the fast neutron flux obtained from the three dimensional Monte Carlo calculation. However, it is found that the conversion ratios are varied with the range of a factor of eight depending on the location at the space around the NBI duct from the results shown in Fig. 6.23. Therefore it can be concluded that the calculation method proposed

in this Chapter should be required to evaluate the decay gamma ray dose rate with good accuracy.

The calculation method shown in Chapter 6.2.1 is experimentally validated by Morimoto et al [6.18]. The experiment is conducted by FNS (Fusion Neutronics Source) at JAERI, and the decay gamma ray dose rates are measured from about two days to about two weeks after shutdown. The schematic view of the experimental set-up with the positions of the measurement is shown in Fig. 6.31 [6.18]. An example of the time dependence of measured and calculated tissue equivalent dose rate is shown in Fig. 6.32 [6.18]. The results by the present calculation method agree with the experimental results with the tissue equivalent dose meter within the experimental error (about 10 %). Therefore it can be demonstrated that this method can be used to evaluate the dose rate with high accuracy.

6.5 Conclusion

In order to apply the decay gamma ray Monte Carlo calculation, which is the method to conduct simultaneously the Monte Carlo neutron and decay gamma ray transport calculation by the modification of the nuclear data library replacing a prompt gamma ray spectrum with a decay gamma ray spectrum, to the actual design calculation of the tokamak-type nuclear fusion reactor with drastically reducing the calculation time, the effective variance reduction method is proposed by the application of the weight window technique and the specification of the decay gamma ray generation region in this Chapter. Using this method, the shielding analyses are performed for the ITER maintenance and NBI ducts. It was found that this method was much useful for improving the statistical error. The good statistical errors can be obtained, therefore the effectiveness of this calculation method is demonstrated for the actual design calculation. From the calculation results, it was found that the decay gamma ray dose rates around the maintenance duct could fully satisfy the tentative design target of 100 μSv/hour at the space required for the human access, and those around the NBI duct were almost equal to the tentative design target. Ratios of the decay gamma ray dose rates to the fast neutron flux are varied with the range of a factor of eight depending on the location at the space around the NBI duct, therefore it can be concluded that the calculation method proposed in this Chapter is required to evaluate the decay gamma ray dose rates with good accuracy.

REFERENCES

[6.1] K. Maki, et al., Biological shield around the neutral beam injector duct in the ITER conceptual design, Fusion Eng. Design, 24, 315-325 (1994).

[6.2] S. Sato, H. Iida, Monte Carlo Analyses for ITER NBI Duct by 1/4 Tokamak Model, J. Ncul. Sci. Technol., Supplement 1, 258-262 (2000).

[6.3] S. Sato, R. Plenteda, D. Valenza, et. al., SHIELDING ANALYSES OF THE ITER NBI PORTS, Fusion Technol., 34, 1002-1007 (1998).

[6.4] S. Sato, H. Iida, R. Plenteda, D. Valenza, R. T. Santoro, Evaluation of Biological Dose Rates around the ITER NBI Ports by 2-D SN/Activation and 3-D Monte Carlo Analyses, Fusion Eng. Design, 47, 425-435 (2000).

[6.5] S. Mori, A. Ito, S. Sato, et. al., Dose Rate Analyses around the Equatorial and Divertor Ports during ITER In-Vessel Components Maintenance, J. Nucl. Sci. Technol, Supplement 1, 248-252 (2000).

[6.6] H. Iida, D. Valenza, R. Plenteda, R. T. Santoro, et al., Radiation Shielding for ITER to Allow for Hands-on Maintenance inside the Cryostat (Methodology for Estimating Shutdown Dose Rate in a Complex Geometry), J. Ncul. Sci. Technol., Supplement 1, 235-242 (2000).

[6.7] Y. Seki, H. Iida, H. Kawasaki, et al., THIDA-2: An Advanced Code System for Transmutation, Activation, Decay Heat and Dose Rate, JAERI 1301, Japan Atomic Energy Research Institute, (1986).

[6.8] S. W. Cierjacks, et al., Development of a Novel Algorithm and Production of New Nuclear Data Libraries for the Treatment of Sequential (x, n) Reactions in Fusion Material Activation Calculations, Fusion Technology, 24, (1993) 277-287.

[6.9] H. Fukumoto, New Approach to Neutron-Induced Transmutation, Radioactivity and Afterheat Calculations and Its Application to Fusion Reactors," J. Ncul. Sci. Technol., 23, 97-109 (1986).

[6.10] D. Valenza, H. Iida, R. Plenteda, R. T. Santoro., Proposal of shutdown dose estimation method by Monte Carlo code, Fusion Eng. Design, 55, 411-418 (2001).

[6.11] S. Sato, H. Iida, T. Nishitani, Evaluation of Shutdown Gamma-ray Dose Rates around the Duct Penetration by 3-D Monte Carlo Decay Gamma-ray Transport Calculation with Variance Reduction Technique, J. Nucl. Sci. Technol., 39, 1237-1246 (2002).

[6.12] H. Iida, V. Khripunov, S. Sato, et. al., Nuclear Analysis of ITER, Proceedings of The 12th Biennial Topical Meeting of the Radiation Protection and Shielding Division of the American Nuclear Society (ANS) Santa Fe, New Mexico, on April 14-18, (2002).

[6.13] T. Inoue, et al., Design and R&D of high power negative ion source/accelerator for ITER NBI, Proc. 19th Symp. on Fusion Technol., Lisbon, Portugal, Sep. 16-20, 1996, p. 701, Portugal (1996).

[6.14] A. Krylov, et al., General design of the neutral beam injection system and integration with ITER, Proc. 19th Symp. on Fusion Technol., Lisbon, Portugal, Sep. 16-20, 697, (1996).

[6.15] K. Shibata, et al., Design analysis for reducing dose rate in the NBI to realize direct access by workers for a fusion experimental reactor, Proc. 19th Symp. on Fusion

Technol., Lisbon, Portugal, Sep. 16-20, 1799, (1996).

[6.16] (Eds.) K. Sakurai and T. Yamamoto, Use Experiences of MCNP in Nuclear Energy Study (II) - Review of Variance Reduction Techniques -, JAERI-Review 98-010 (1998) (in Japanese).

[6.17] K. Ueki, M. Kawai, Analyses and Development of Effective Compensation Shields in a Multilegged Duct Streaming System, Nucl. Technol., 132, 281 (2000).

[6.18] Y. Morimoto, K. Ochiai, S. Sato, J. Hori, M. Yamauchi and T. Nishitani, "Shutdown Dose Evaluation Experiment for ITER," to be presented at 22nd Symposium on Fusion Technology, 9 – 13 Sep., 2002, Helsinki, and to be published in Fusion Eng. Design.

Table 6.1 Decay gamma ray spectra of ^{60}Co used in the present decay gamma ray MCNP calculation

Energy (MeV)	Probability (%)
0.34693	0.0038
0.82628	0.0038
1.17320	49.9759
1.33250	50.0160
2.15880	0.0005
2.50500	1.00E-06

Table 6.2 Ratio of the actual activation level to the direct production rate for each radioisotope at 10^6 seconds after shutdown based on the ITER operation scenario.

Isotope	Ratio
^{58}Co	0.0431
^{60}Co	0.0303
^{59}Fe	0.0460
^{54}Mn	0.0377
^{51}Cr	0.0493

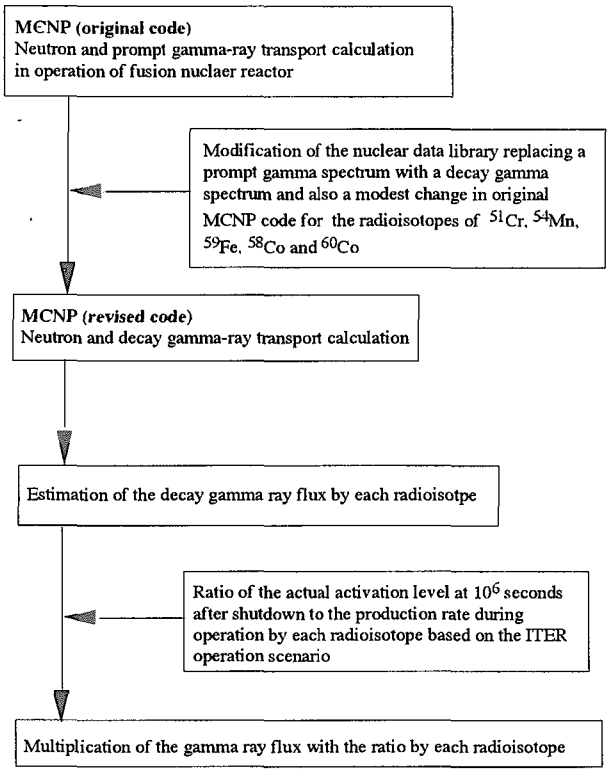

Fig. 6.1 Monte Carlo decay gamma-ray transport calculation procedure applied in this Chapter.

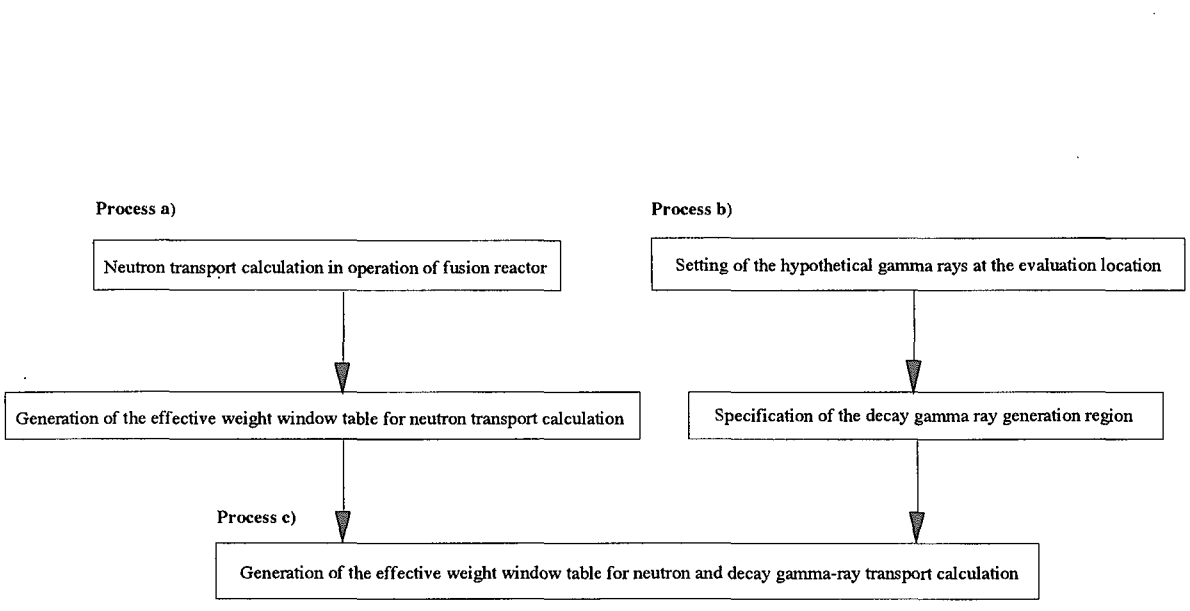

Fig. 6.2 Variance reduction method proposed in this Chapter

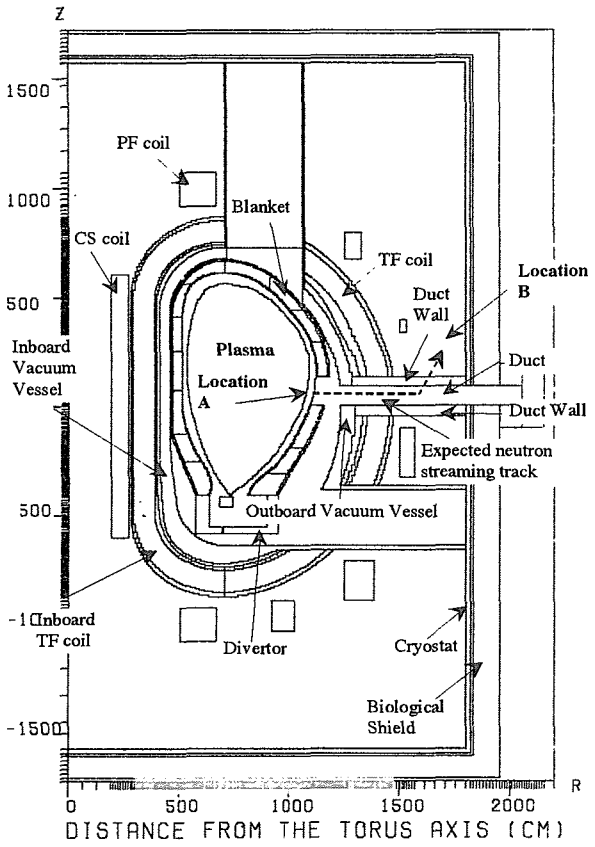

Fig. 6.3 Conceptual view of the vertical cross section of the fusion reactor

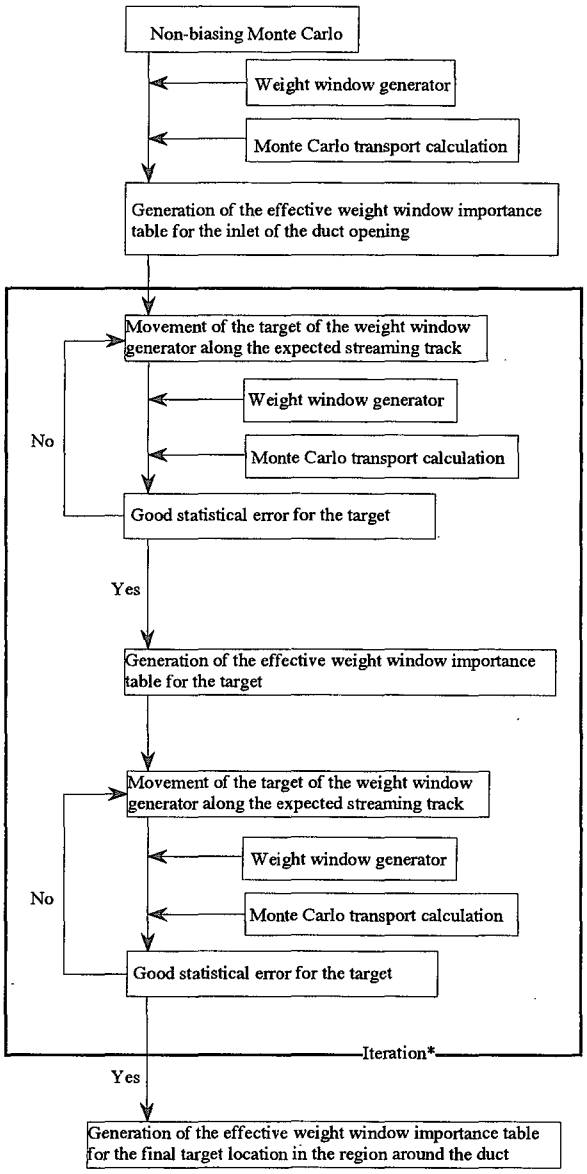

Iteration*: The target locations are sequentially moved from the inlet of the duct opening to the final target location in the region around the duct.

Fig. 6.4 Generation method to prepare the effective weight window importance for the region around the duct penetration.

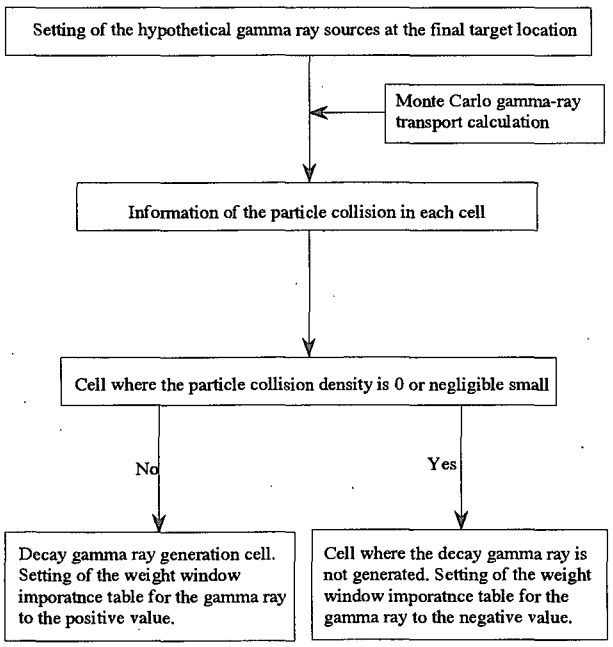

Fig. 6.5 Method to identify the region producing the decay gamma ray.

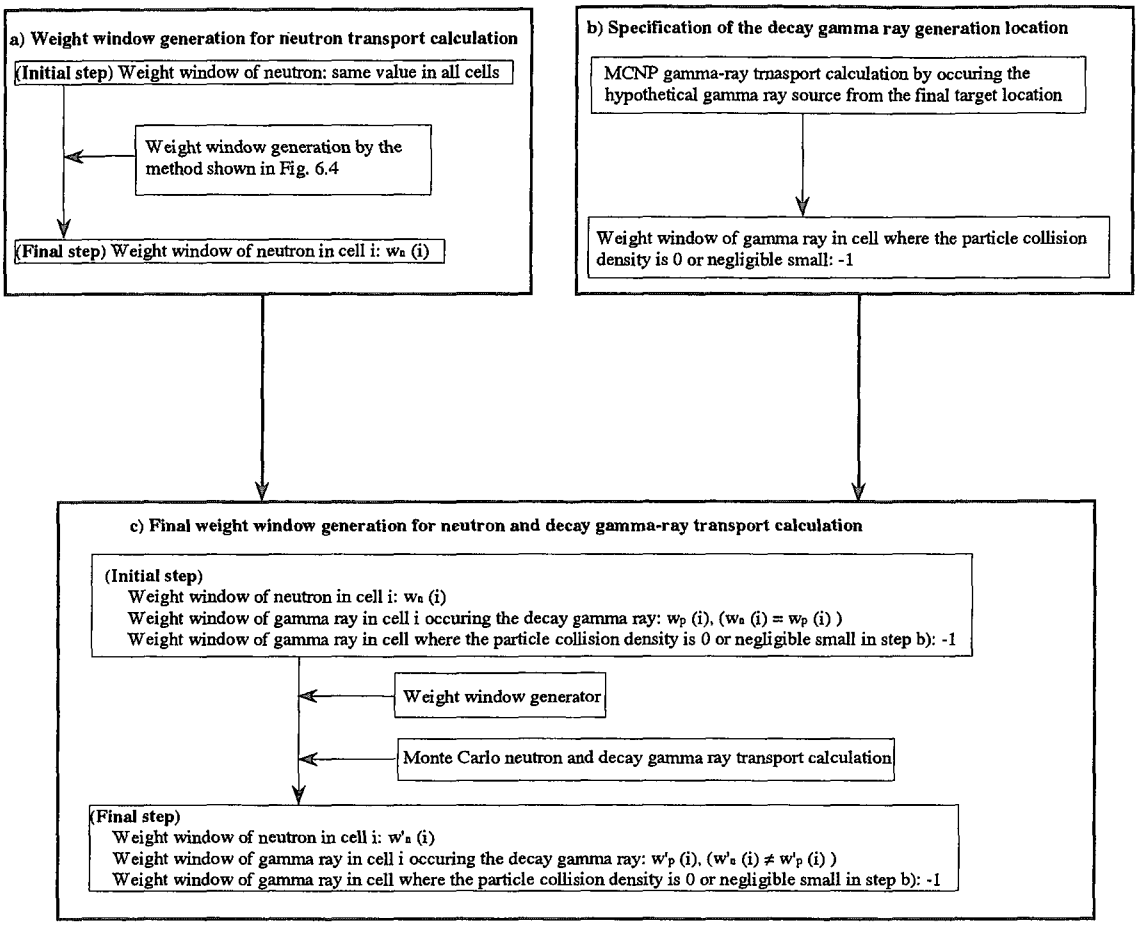

Fig. 6.6 Generation procedure of the final weight window table for neutron and decay gamma-ray transport calculation

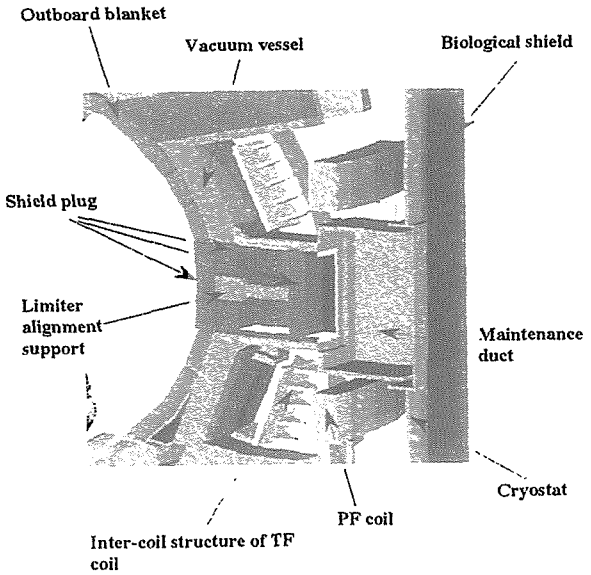

Fig. 6.7 Bird's-eye view of the Monte Carlo calculational geometry for the ITER maintenance duct

This is a blank page.

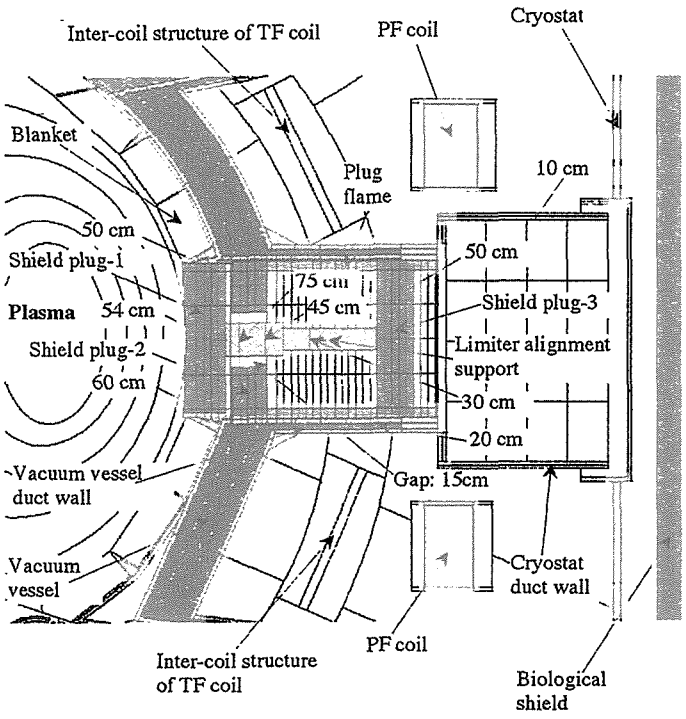

Fig. 6.8 Vertical cross-section view of the Monte Carlo calculational geometry for the ITER maintenance duct

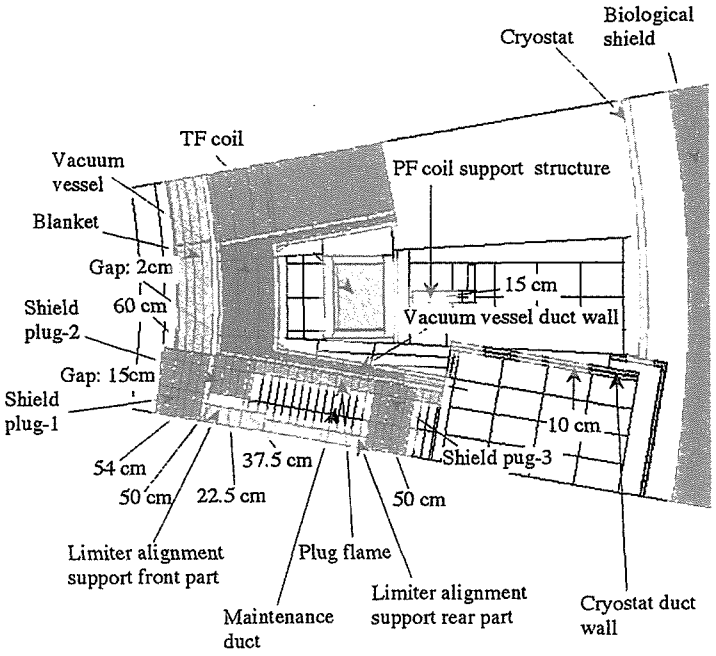

Fig. 6.9 Horizontal cross-section view of the Monte Carlo calculational geometry for the ITER maintenance duct

This is a blank page.

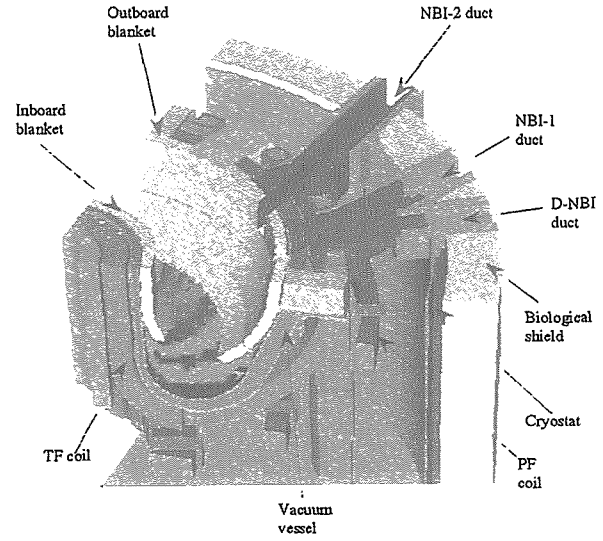

Fig. 6.10 Bird's-eye view of the Monte Carlo calculational geometry for the ITER NBI duct

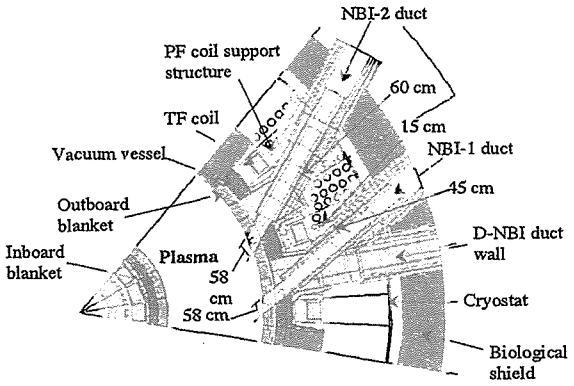

Fig. 6.11 Horizontal cross-section view of the Monte Carlo calculational geometry for the ITER NBI duct

This is a blank page.

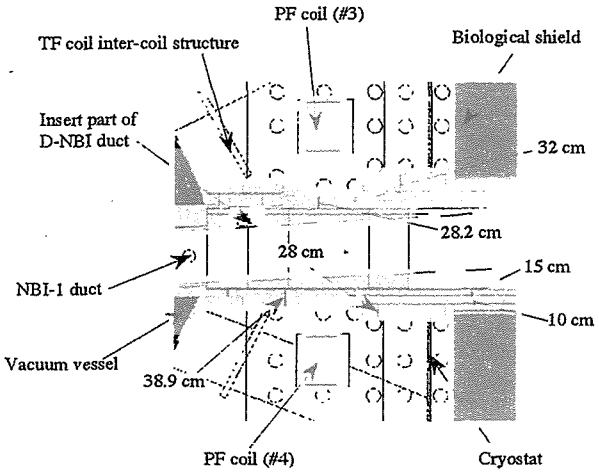

Fig. 6.12 Vertical cross-section view of the Monte Carlo calculational geometry for the ITER NBI duct

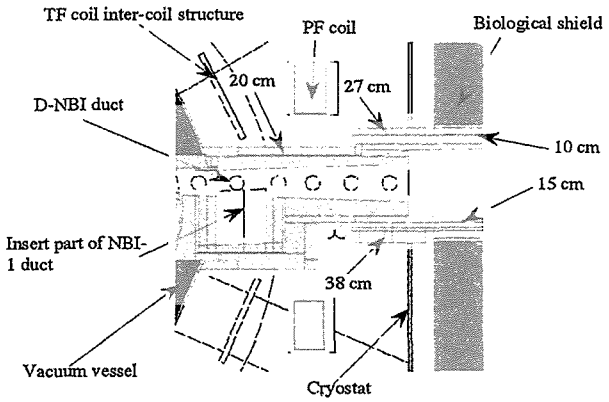

Fig. 6.13 Vertical cross-section view of the Monte Carlo calculational geometry for the ITER NBI duct.

This is a blank page.

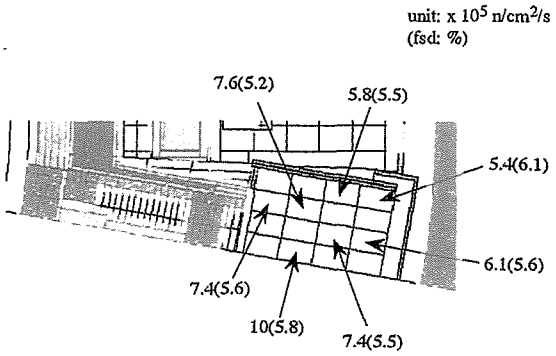

Fig. 6.14 Neutron flux of the energy above 1 MeV inside the maintenance duct (Fusion power: 500 MW).

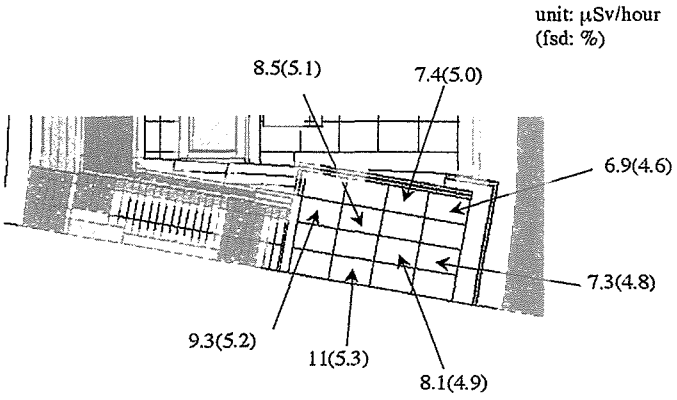

Fig. 6.15 Decay gamma-ray dose rates at 10^6 seconds after shutdown inside the maintenance duct

This is a blank page.

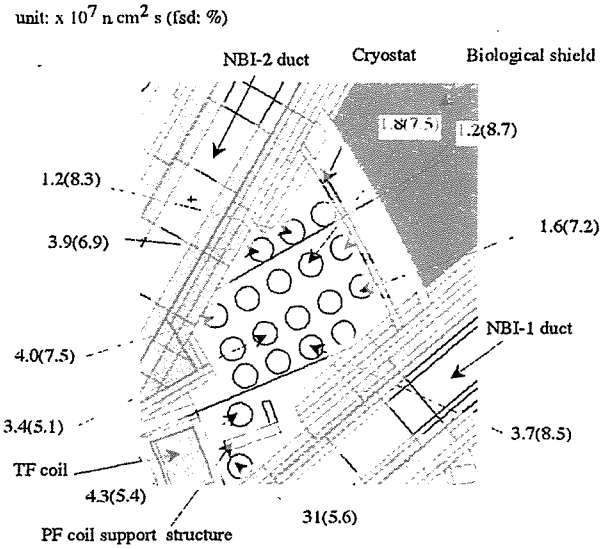

Fig. 6.16 Neutron flux of the energy above 1 MeV in the space at the equatorial plane between three NBI ducts (Fusion power: 500 MW).

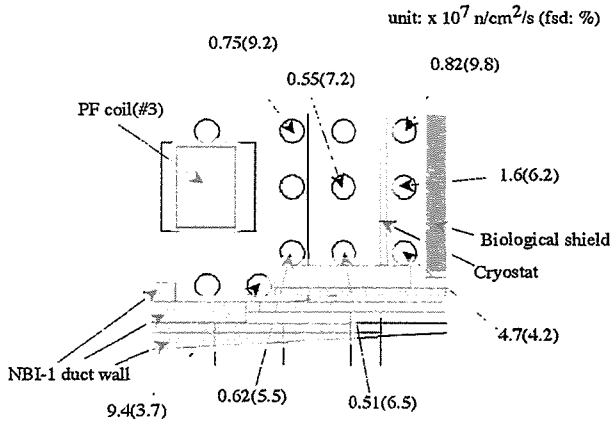

Fig. 6.17 Neutron flux of the energy above 1 MeV in the space at above the NBI-1 duct in the poloidal direction (Fusion power: 500 MW).

This is a blank page.

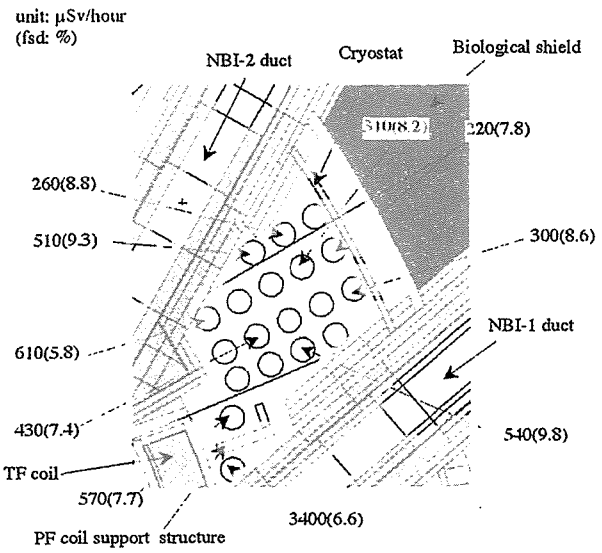

Fig. 6.18 Decay gamma-ray dose rates in the space at the equatorial plane between three NBI ducts at 10^6 seconds after shutdown.

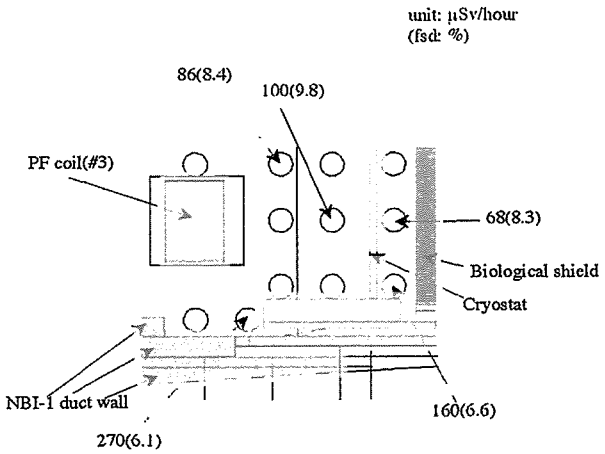

Fig. 6.19 Decay gamma ray dose rates in the space above the NBI-1 duct in the poloidal direction at 10^6 seconds after shutdown.

This is a blank page.

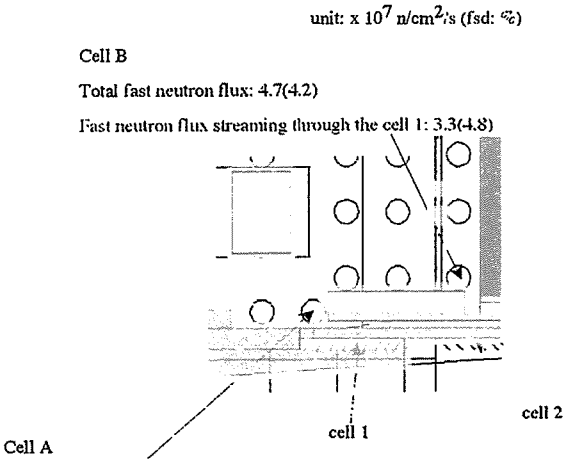

Fig. 6.20 Main passage of particle for the neutron flux of the energy above 1 MeV in the space above the NBI-1 duct in the poloidal direction.

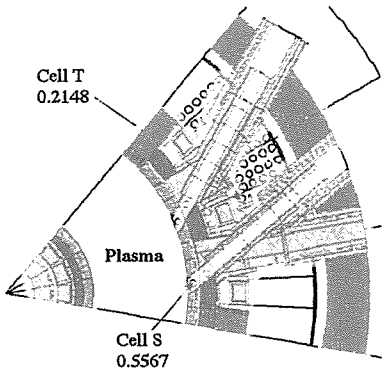

Fig. 6.21 Values of FSD for the decay gamma ray dose rate in the cell S and the cell T at the same history.

This is a blank page.

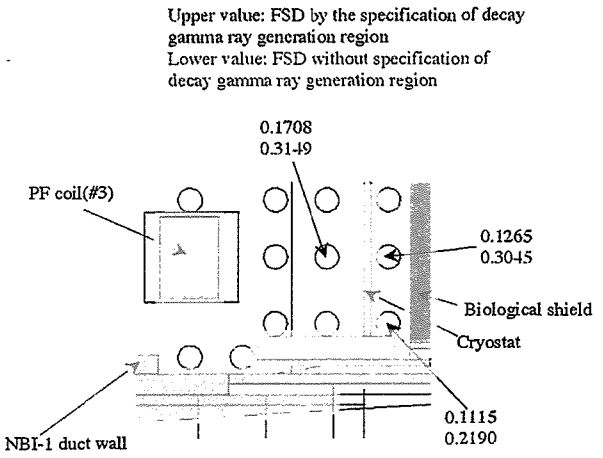

Fig. 6.22 Comparison between the value of FSD obtained by this method with the specification of the decay gamma ray generation region shown in Chapter 6.2.2 and that without the specification in the space above the NBI-1 duct in the poloidal direction at the same calculation time.

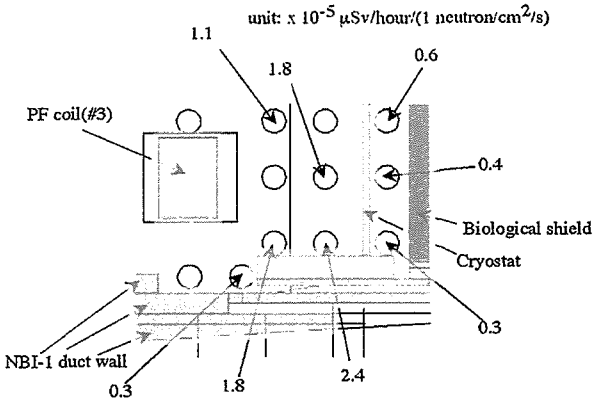

Fig. 6.23 Ratios of the decay gamma ray dose rates at 10^6 seconds after shutdown to the neutron flux of the energy above 1 MeV in the space above the NBI-1 duct in the poloidal direction.

This is a blank page.

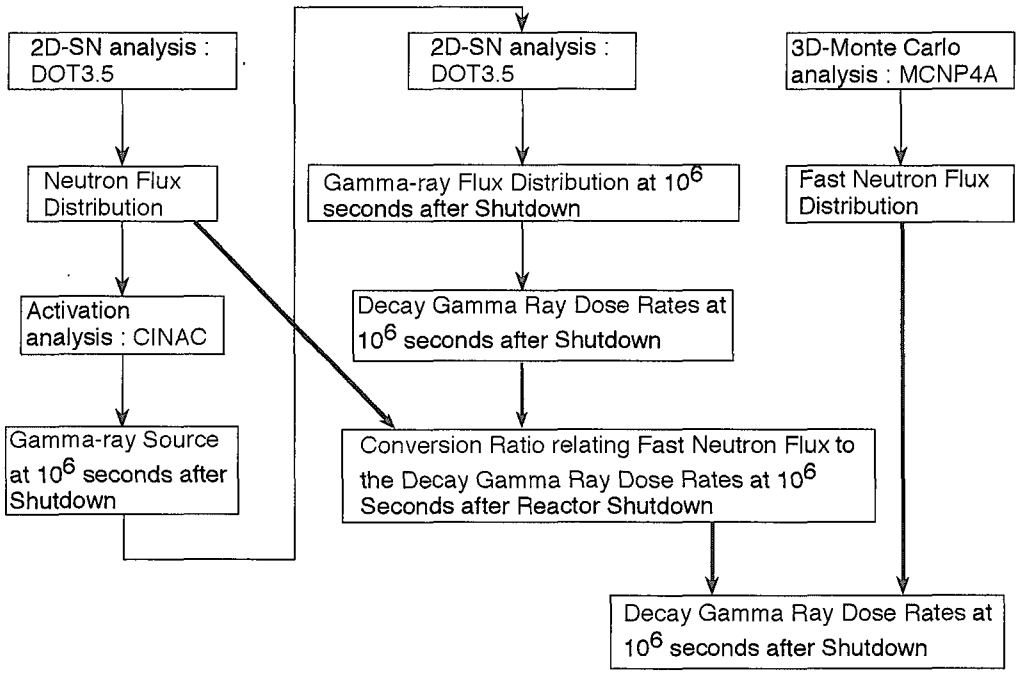

Fig. 6.24 Evaluation Method by conversion ratios relating fast neutron flux to the decay gamma ray dose rates

This is a blank page.

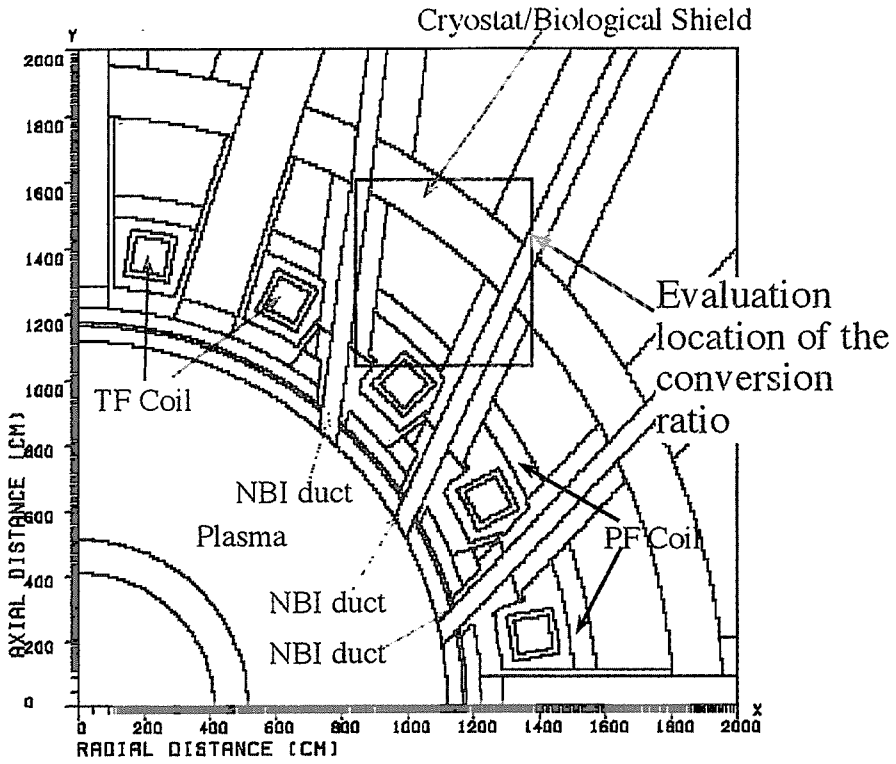

Fig. 6.25 Two dimensional DOT Calculational genmetry (rectangular model)

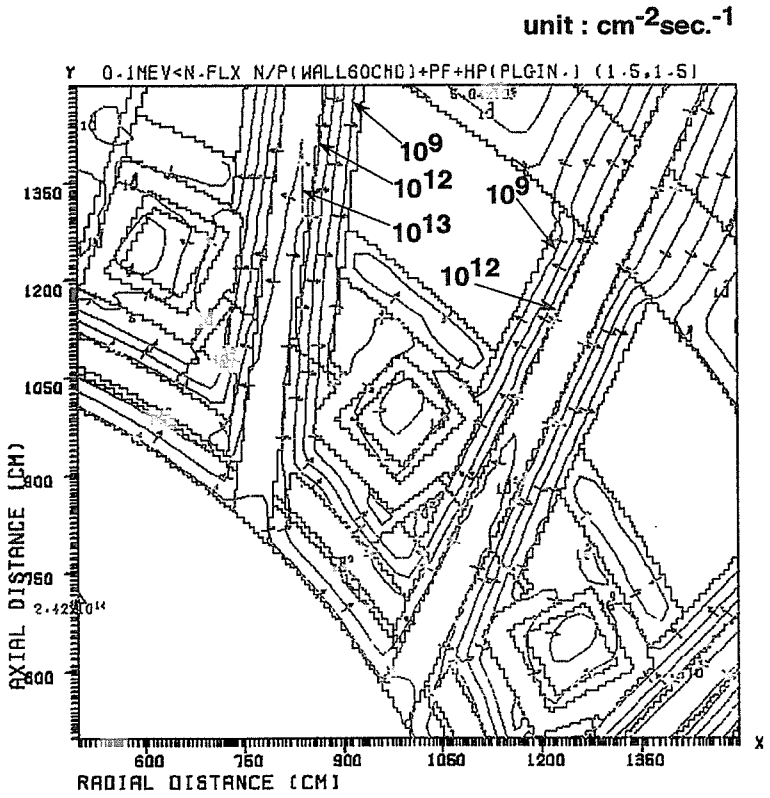

Fig. 6.26 Contour of the neutron flux of the energy above 0.1 MeV by 2D Sn calculation code (DOT3.5)

This is a blank page.

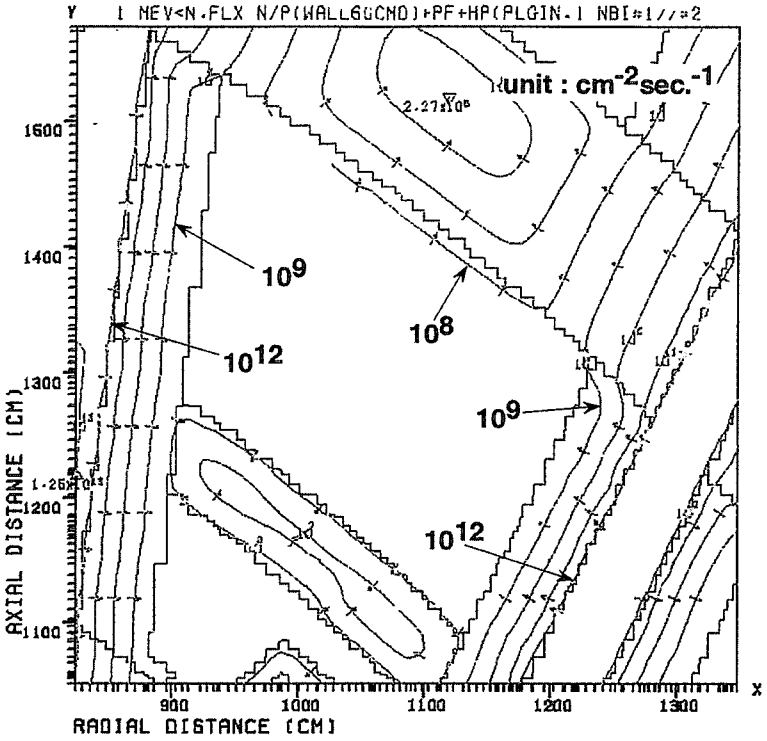

Fig. 6.27 Contour of the neutron flux of the energy above 1 MeV by 2D SN calculation code (DOT3.5)

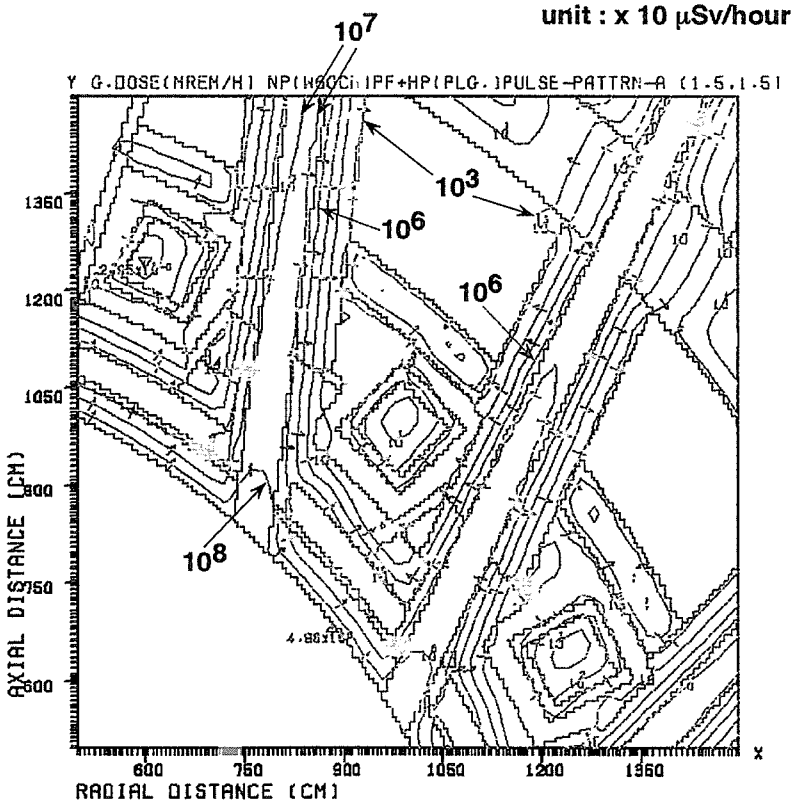

Fig. 6.28 Contour of the decay gamma ray dose rate at 10^6 sec. after shutdown

This is a blank page.

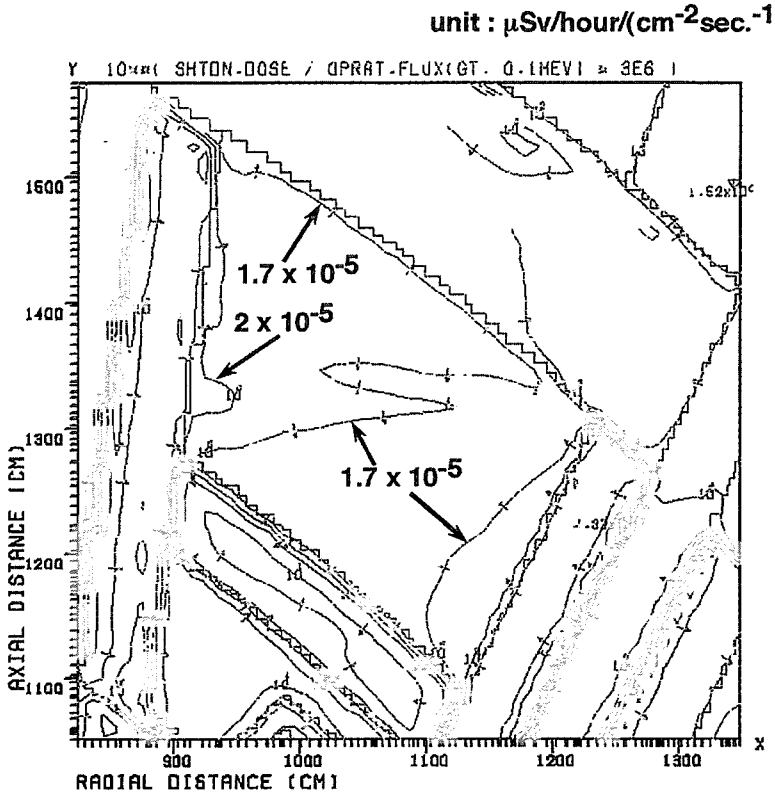

Fig. 6.29 Contour of the conversion ratio relating fast (> 0.1 MeV) neutron flux to the decay gamma ray dose rate in the space along the cryostat between adjacent NBI ducts and PF coil.

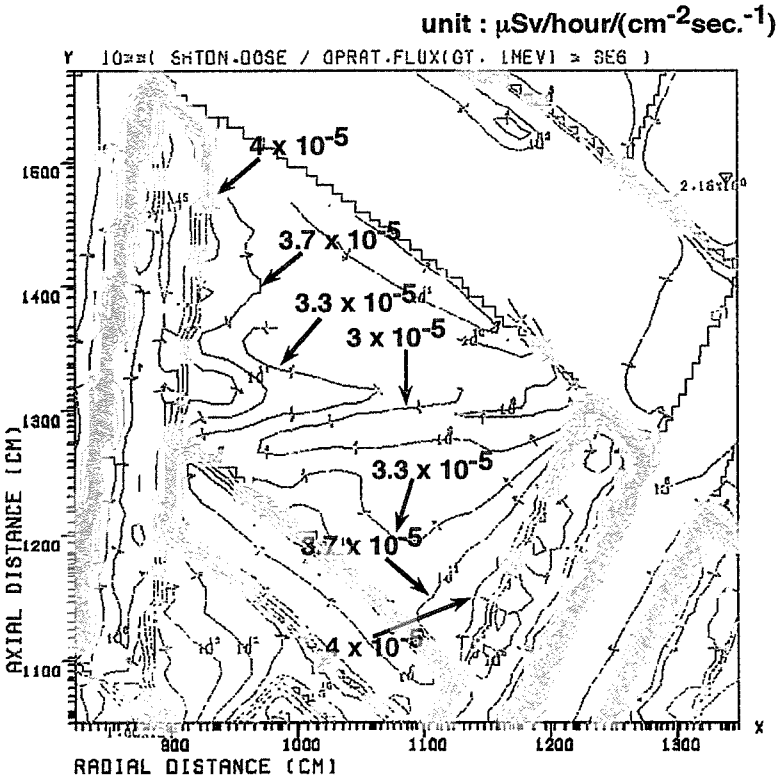

Fig. 6.30 Contour of the conversion ratio relating fast (> 1 MeV) neutron flux to the decay gamma ray dose rate in the space along the cryostat between adjacent NBI ducts and PF coil.

This is a blank page.

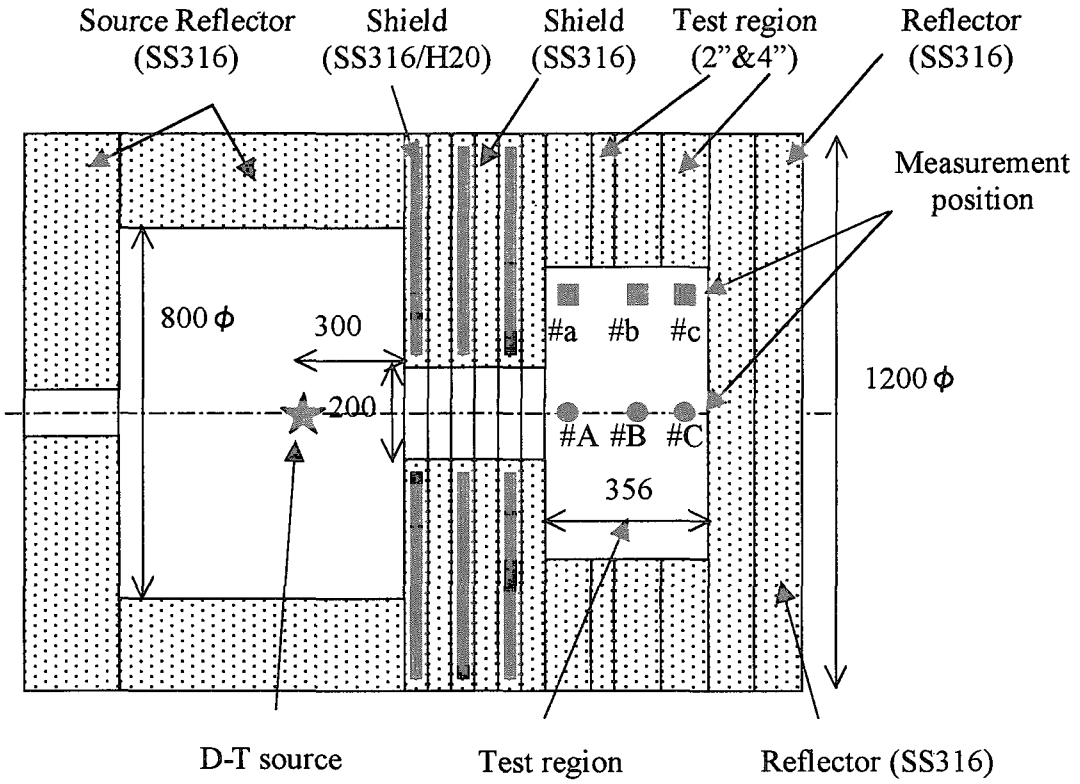

Fig. 6.31 Schematic view of experimental set-up with the positions of the measurement

This is a blank page.

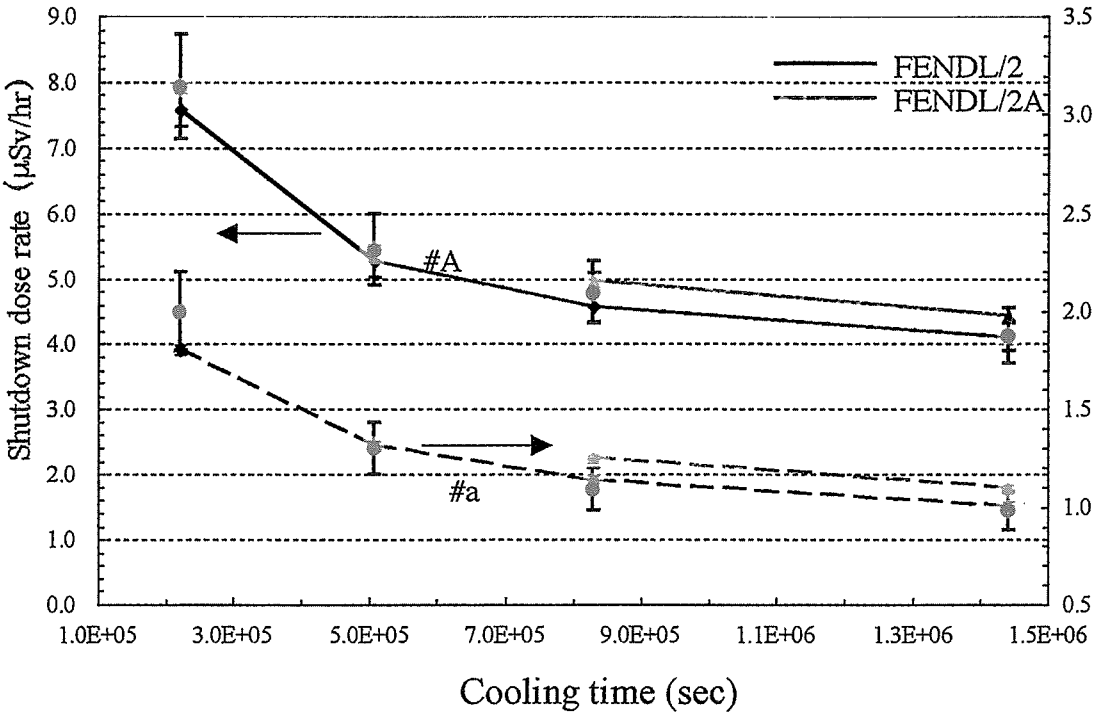

Fig. 6.32 Time dependence of measured and calculated tissue equivalent dose rate at #A and #a

This is a blank page.

7. Conclusion

There are various type slits and ducts in tokamak-type DT nuclear fusion reactor. The helium production in the rewelding location in the blanket and the vacuum vessel, the nuclear properties in the super-conductive TF coil, e.g. the nuclear heating rate in the coil winding pack, are enhanced by the radiation streaming through these slits and ducts, and they are critical concern in the shielding design of the tokamak-type DT nuclear fusion reactor. The decay gamma ray dose rate after shutdown around the duct penetrating the blanket and the vacuum vessel is also enhanced by the radiation streaming through the duct, and they are also critical concern. In order to evaluate these nuclear properties with good accuracy, three dimensional Monte Carlo calculation is necessary, which needs large computer resources. In the present study, these nuclear properties are systematically calculated for the various type slits and ducts by the three dimensional Monte Carlo calculation. The dependency of these nuclear properties on the configuration of these slits and ducts are clarified. Based on the systematically calculated results, the analytical representations on these nuclear properties are established as functions of the parameter of the configuration of these slits and ducts, e.g. slit width, duct opening height, shield thickness, and so on. The analytical formula thus-obtained is applied to clarify the shielding design conditions required to satisfy the shielding design criteria for the DT fusion reactor. In addition, the calculation method is developed for the evaluation of the decay gamma ray dose rate around the duct by the Monte Carlo calculation.

In Chapter 1, the outline of the nuclear fusion and the feature of the shielding design for the tokamak-type DT nuclear fusion reactor are introduced, and the background and the objective of the present study is described.

In order to evaluate the applicapability of the calculation method to the evaluation of the radiation streaming in the tokamak-type DT nuclear fusion reactor design, the comparison is performed for the radiation streaming by three dimensional Monte Carlo and two dimensional Sn calculations in Chapter 2. Numerical analyses are performed to evaluate the radiation streaming through the slit between the adjacent blanket modules, and to calculate the neutron flux, the nuclear heating rate and the helium production in the vacuum vessel surface along the slit. Due to ray-effect, these nuclear properties by the Sn calculation are under-estimated by a factor of two - four compared with those by the Monte Carlo calculation. The radiation streaming through the NBI duct, which penetrates the blanket and the vacuum vessel, is evaluated, and the neutron flux is calculated along the NBI duct. In the two dimensional Sn calculation, the XY slab calculation geometry is applied. The neutron fluxes by the two dimensional Sn calculation are over-estimated compared with those by the three dimensional Monte Carlo calculation due to approximation of calculational geometry, i.e. assumption of the infinite continuous opening of the duct in the calculation geometry. As the duct opening heights are lower, the over-estimations of the two dimensional Sn calculation are larger. In the ITER condition with the about 90 cm high duct opening, the neutron flux of the energy above 0.1 MeV by the two dimensional Sn calculation is over-estimated by a factor of about eight at

the cryostat. It can be concluded that the three dimensional Monte Carlo calculation is required to evaluate the nuclear properties with good accuracy taking into account the radiation streaming in the tokamak type DT nuclear fusion reactor.

In Chapter 3, the radiation streaming through the slit between the adjacent blanket modules is evaluated by the three dimensional Monte Carlo calculation, and the nuclear properties are systematically calculated in the vacuum vessel and the TF coil along the slit for the various configurations. From the results, the following findings are obtained.

(1) The helium production in the vacuum vessel surface along the slit increases linearly with the slit width, and it also increases linearly with the boron content of the trace element in SS.
(2) The helium production in the vacuum vessel surface along the slit decreases exponentially with the blanket thickness.
(3) As the slit width increases, the nuclear properties in the TF coil along the slit increase in proportion to the exponential and power functions of the slit width in the range of 30 – 45 and 45 – 60 cm thick blankets, respectively.
(4) The nuclear properties in the TF coil along the slit decrease exponentially with the blanket and the vacuum vessel thicknesses.

Based on the results, the analytical representations on the helium production in the vacuum vessel surface along the slit are established as functions of the slit width, the boron content and the blanket thickness. Also, the analytical representations on the nuclear properties in the TF coil along the slit are established as functions of the slit width, the blanket thickness and the vacuum vessel thickness. The established representations can be applied with good accuracy in the range of 1 – 8 cm wide slits, 0.1 – 100 wppm boron contents, 30 – 60 cm thick blankets and 20 – 40 cm thick vacuum vessels. The dependency of these nuclear properties on the blanket and the vacuum vessel compositions are also clarified. The analytical representation is applied to clarify the shielding design conditions required to satisfy the shielding design criteria.

In Chapter 4, the radiation streaming through the small circular duct in the blanket modules is evaluated, and the helium productions are systematically calculated in the blanket cooling water pipe along the duct for the various configurations. Also, the nuclear properties in the TF coil along the duct are calculated. From the results, the following findings are obtained.

(1) The helium production along the duct increases exponentially with the duct diameter.
(2) The helium production along the duct increases linearly with the boron content of the trace element in SS, and it decreases exponentially with the blanket thickness.
(3) Significant differences are not found among the 1 - 6 cm diametric ducts for the nuclear properties in the TF coil along the duct.

Based on the results, the analytical representations on the helium production in the blanket cooling water pipe along the duct are established as functions of the duct diameter, the boron

content and the blanket thickness. The established representations can be applied with good accuracy in the range of 1 – 6 cm diametric ducts, 0.1 – 100 wppm boron contents, 25 – 45 cm thick blankets. The dependency of the helium production along the duct on the blanket compositions is clarified. The analytical representation is applied to clarify the shielding design conditions required to satisfy the shielding design criteria.

In Chapter 5, the radiation streaming through the large opening duct in the vacuum vessel, which penetrates the blanket and the vacuum vessel, is evaluated, and the nuclear properties are systematically calculated in the TF coil adjacent to the duct for the various configurations. They are calculated for the cases with and without the shield plug in the duct. In case the shield plug is not installed in the duct, the following findings are obtained.

(1) The nuclear properties in the TF coil adjacent to the duct increases linearly with the duct opening height.
(2) As the duct opening width increases, the nuclear properties increase in proportion to the power function of the duct opening width.
(3) The nuclear properties decrease exponentially with the duct wall thickness.
(4) The nuclear properties decrease exponentially with the shield thickness adjacent to the duct, which corresponds to sum of the blanket and vacuum vessel thickness adjacent to the duct. The dependency of the nuclear properties on the shield thickness is much little compared with that on the duct wall thickness.

Based on the results, the analytical representations on the nuclear properties in the TF coil adjacent to the duct are established as functions of the duct opening height, the duct opening width, the duct wall thickness and the shield thickness adjacent to the duct. The established representations can be applied with good accuracy in the range of the 50 – 280 cm high and 50 – 160 cm wide duct openings, 20 – 40 cm thick duct walls, and the 100 – 200 cm thick shields. The dependency of the nuclear properties on the duct wall and shield compositions are also clarified. The nuclear properties are almost constant in the range of 10 % SS/90 % water to 90 % SS/10 % water in the shield composition. The analytical representation is applied to clarify the shielding design conditions required to satisfy the shielding design criteria.

When the shield plug is installed in the duct opening, there are a few centi-meter wide slits between the duct wall and the shield plug. In case the shield plug is installed in the duct, the following findings are obtained.

(1) As the slit width increases, the nuclear properties in the TF coil adjacent to the duct increase in proportion to the power function of the slit width between the duct wall and the shield plug.
(2) The nuclear properties in the TF coil decrease exponentially with the shield plug and the duct wall thicknesses.

Based on the results, the analytical representations on the nuclear properties in the TF coil adjacent to the duct with the shield plug in the duct are established as functions of the slit width, the duct wall thickness and the shield plug thickness. The established representations

can be applied with good accuracy in the range of the 2 – 10 cm wide slits, 10 – 30 cm thick duct walls, and the 70 – 200 cm thick shield plugs.

By installing the step configuration to the slit between the duct wall and the shield plug installed in the duct, the nuclear properties in the TF coil adjacent to the duct decrease. Therefore the nuclear properties are systematically calculated in the TF coil adjacent to the duct for the various step configurations, and the following findings are obtained.

(1) The nuclear properties in the TF coil adjacent to the duct are drastically reduced by installing the step configuration to the slit. They decrease with increasing the step width. They are almost constant value when the slit width is more than four times wider than the slit width. The nuclear properties with the step width with more than four times of the slit width are the values of about 1/30 compared with that without the step configuration in the 100 cm thick shield plug.
(2) Although the nuclear properties slightly increase with increasing the step thickness, the dependency of the nuclear properties on the step thickness is much little compared with that on the step width.
(3) When the step configuration is installed at the middle of the shield plug thickness with the slit, the nuclear properties show the minimum value. It can be concluded that the optimum position to install the step configuration is the middle of the shield plug from the view point of the shielding design.
(4) It can be concluded that applying the step configuration with the step width of four times of the slit width at the middle of the shield plug is most effective from the view point of the shielding design.

The evaluation method is developed for the decay gamma ray dose rate after shutdown around the large opening duct in the vacuum vessel by the decay gamma ray Monte Carlo calculation in Chapter 6. The neutron and decay gamma ray transport Monte Carlo calculation is simultaneously conducted by the modification of the nuclear data library replacing a prompt gamma ray spectrum with a decay gamma ray spectrum. In order to apply this method to the calculation of the tokamak-type DT nuclear fusion reactor with drastically reducing the calculation time, the effective variance reduction method is proposed by the application of the weight window technique and the specification of the decay gamma ray generation region. Using this method, the shielding analyses are performed for the ITER maintenance and NBI ducts. It was found that this method was much useful for improving the statistical error. The good statistical errors could be obtained, therefore the effectiveness of this method was demonstrated for the shielding design calculation. From the calculation results, it is found that the decay gamma ray dose rates around the maintenance duct can fully satisfy the tentative design target of 100 μSv/hour at the space required for the human access, and those around the NBI duct are almost equal to the tentative design target. Ratios of the decay gamma ray dose rate after shutdown to the fast neutron flux are varied with the range of a factor of eight depending on the location at the space around the duct, therefore it can be concluded that this method applied in this Chapter is required to evaluate the decay gamma ray dose rates with good accuracy.

ACKNOWLEDGEMENTS.

The author wishes to acknowledge Professors T. Nakamura, Y. Kitamura, M. Baba and H. Hashizume of Tohoku University for helpful advices concerning the present study, affectionate support and encouragement. Especially I would like to acknowledge helpful discussions concerning the results of the shielding calculations and the shielding design study with Professor T. Nakamura.

The author acknowledges Drs. S. Matsuda, M. Ohta, M. Seki, T. Tsunematsu, Y. Seki, S. Seki, H. Iida, H. Takatsu, T. Kuroda, E. Tada, K. Shibanuma, K. Koizumi, H. Tsuji, Y. Ohara, M. Akiba and T. Nishitani of Japan Atomic Energy Research Institute for their permanent support and encouragements. Especially I would like to acknowledge helpful discussions concerning the results of the shielding calculations and motivation of the present study with Drs. H. Takatsu, H. Iida and T. Nishitani.

The author would like to acknowledge helpful discussions concerning the Monte Carlo calculation method with Drs. H. Iida, R. T. Santoro, R. Plenteda, D. Valenza and L. Petritz during author's a few months working in ITER Joint Central Team at Munich.

The author acknowledges Drs. K. Maki and S. Mori for their helpful discussion concerning the shielding design of the nuclear fusion reactor.

The author would like to acknowledge helpful support concerning the Monte Carlo calculation method with Dr. H. Nakashima, H. Iida and S. Mori. The author would like to acknowledge helpful support concerning the SN calculation method with Dr. Y. Seki and K. Maki.

The author acknowledges Drs. H. Maekawa, Y. Ikeda, C. Konno, F. Maekawa, Y. Morimoto, M. Yamauchi, K. Ochiai J. Hori, M. Nakao, Y. Terada and R. Tanaka for their helpful discussion concerning the nuclear fusion shielding.

The author would like to acknowledge helpful support concerning the calculation work with Mr. T. Ustumi and S. Ishigaki.

The author acknowledges Dr. S. Kinase for his advise concerning helpful information, and Mr. M. Wada and K. Ohatani for their helpful supports.

Appendix List of Publications

Chapter 2

[1] S. Sato, H. Takatsu, Y. Seki, T. Utsumi, Streaming Analysis of Gap between Blanket Modules for Fusion Experimental Reactor, Fusion Technol., 30, 1129-1033 (1996).

[2] S. Sato, H. Iida, Monte Carlo Analyses for ITER NBI Duct by 1/4 Tokamak Model, J. Nucl. Sci. Technol., Supplement 1, 258-262 (2000).

Chapter 3

[1] S. Sato, Establishment of Shielding Design Conditions in Fusion Shielding Blanket by 3-D Monte Carlo Calculation, J. Nucl. Sci. Technol., Supplement 1, 253-257 (2000).

[2] S. Sato, K. Maki, Analytical Representation for Neutron Streaming through Slits in Fusion Reactor Blanket by Monte Carlo Calculation, Fusion Eng. Design, 65, 501-524 (2003).

Chapter 4

[1] S. Sato, H. Iida, R. Plenteda, R. T. Santoro, Monte Carlo Analysis of Helium Production in the ITER Shielding Blanket Module, Fusion Eng. Design, 46 1-9 (1999).

[2] S. Sato, T. Nakamura, T. Nishitani, Helium Production due to Neutron Streaming through Small Circular Ducts in Fusion Reactor Blanket by Analytical Fitting from Monte Carlo Calculation Results, Fusion Sci. Technol., 43, 559-568 (2003).

Chapter 5

[1] S. Sato, K. Maki, Y. Seki, H. Takatsu, S. Mori, EVALUATION OF RADIATION STREAMING THROUGH THE ANNULAR GAPS AROUND DIVERTOR COOLING PIPES IN FUSION EXPERIMENTAL REACTORS, Proc. 8th International Conference on Radiation Shielding, 1039-1046 (1994).

[2] S. Sato, H. Takatsu, T. Utsumi, et. al., STREAMING ANALYSIS FOR RADIATION THROUGH ITER MID-PLANE PORT, Fusion Eng. Design, 42 213-219 (1998).

Chapter 6

[1] S. Sato, R. Plenteda, D. Valenza, et. al., SHIELDING ANALYSES OF THE ITER NBI PORTS, Fusion Technol., 30, 1076-1080 (1996).

[2] S. Sato, R. Plenteda, D. Valenza, H. Iida, R. T. Santoro, Evaluation of Biological Dose Rates around the ITER NBI Ports by 2-D SN/Activation and 3-D Monte Carlo Analyses, Fusion Eng. Design, 47, 425-435 (2000).

[3] H. Iida, V. Khripunov, S. Sato, et. al., Nuclear Analysis of ITER, Proceedings of The 12th Biennial Topical Meeting of the Radiation Protection and Shielding Division of the American Nuclear Society (ANS) Santa Fe, New Mexico, on April 14-18, 2002.

[4] S. Sato, H. Iida, T. Nishitani, Evaluation of Shutdown Gamma-ray Dose Rates around the Duct Penetration by 3-D Monte Carlo Decay Gamma-ray Transport Calculation with Variance Reduction Technique, J. Nucl. Sci. Technol., 39, 1237-1246 (2002).

This is a blank page.

国際単位系（SI）と換算表

表1　SI基本単位および補助単位

量	名称	記号
長さ	メートル	m
質量	キログラム	kg
時間	秒	s
電流	アンペア	A
熱力学温度	ケルビン	K
物質量	モル	mol
光度	カンデラ	cd
平面角	ラジアン	rad
立体角	ステラジアン	sr

表2　SIと併用される単位

名称	記号
分，時，日	min，h，d
度，分，秒	°，′，″
リットル	l，L
トン	t
電子ボルト	eV
原子質量単位	u

1 eV=1.60218×10^{-19}J

1 u=1.66054×10^{-27}kg

表3　固有の名称をもつSI組立単位

量	名称	記号	他のSI単位による表現
周波数	ヘルツ	Hz	s^{-1}
力	ニュートン	N	$m\cdot kg/s^2$
圧力，応力	パスカル	Pa	N/m^2
エネルギー,仕事,熱量	ジュール	J	N·m
工率，放射束	ワット	W	J/s
電気量，電荷	クーロン	C	A·s
電位，電圧，起電力	ボルト	V	W/A
静電容量	ファラド	F	C/V
電気抵抗	オーム	Ω	V/A
コンダクタンス	ジーメンス	S	A/V
磁束	ウェーバ	Wb	V·s
磁束密度	テスラ	T	Wb/m^2
インダクタンス	ヘンリー	H	Wb/A
セルシウス温度	セルシウス度	℃	
光束	ルーメン	lm	cd·sr
照度	ルクス	lx	lm/m^2
放射能	ベクレル	Bq	s^{-1}
吸収線量	グレイ	Gy	J/kg
線量等量	シーベルト	Sv	J/kg

表4　SIと共に暫定的に維持される単位

名称	記号
オングストローム	Å
バーン	b
バール	bar
ガル	Gal
キュリー	Ci
レントゲン	R
ラド	rad
レム	rem

1 Å=0.1nm=10^{-10}m

1 b=100fm^2=10^{-28}m^2

1 bar=0.1MPa=10^5Pa

1 Gal=1cm/s^2=10^{-2}m/s^2

1 Ci=3.7×10^{10}Bq

1 R=2.58×10^{-4}C/kg

1 rad=1cGy=10^{-2}Gy

1 rem=1cSv=10^{-2}Sv

表5　SI接頭語

倍数	接頭語	記号
10^{18}	エクサ	E
10^{15}	ペタ	P
10^{12}	テラ	T
10^{9}	ギガ	G
10^{6}	メガ	M
10^{3}	キロ	k
10^{2}	ヘクト	h
10^{1}	デカ	da
10^{-1}	デシ	d
10^{-2}	センチ	c
10^{-3}	ミリ	m
10^{-6}	マイクロ	μ
10^{-9}	ナノ	n
10^{-12}	ピコ	p
10^{-15}	フェムト	f
10^{-18}	アト	a

（注）

1．表1－5は「国際単位系」第5版，国際度量衡局 1985年刊行による。ただし，1 eVおよび1 uの値はCODATAの1986年推奨値によった。

2．表4には海里，ノット，アール，ヘクタールも含まれているが日常の単位なのでここでは省略した。

3．barは，JISでは流体の圧力を表わす場合に限り表2のカテゴリーに分類されている。

4．EC閣僚理事会指令ではbar，barnおよび「血圧の単位」mmHgを表2のカテゴリーに入れている。

換算表

力	N(=10^5dyn)	kgf	lbf
	1	0.101972	0.224809
	9.80665	1	2.20462
	4.44822	0.453592	1

粘度　1 Pa·s(N·s/m^2)=10 P(ポアズ)(g/(cm·s))

動粘度　1m^2/s=10^4St(ストークス)(cm^2/s)

圧力	MPa(=10bar)	kgf/cm^2	atm	mmHg(Torr)	lbf/in^2(psi)
	1	10.1972	9.86923	7.50062×10^3	145.038
	0.0980665	1	0.967841	735.559	14.2233
	0.101325	1.03323	1	760	14.6959
	1.33322×10^{-4}	1.35951×10^{-3}	1.31579×10^{-3}	1	1.93368×10^{-2}
	6.89476×10^{-3}	7.03070×10^{-2}	6.80460×10^{-2}	51.7149	1

エネルギー・仕事・熱量	J(=10^7 erg)	kgf·m	kW·h	cal(計量法)	Btu	ft·lbf	eV
	1	0.101972	2.77778×10^{-7}	0.238889	9.47813×10^{-4}	0.737562	6.24150×10^{18}
	9.80665	1	2.72407×10^{-6}	2.34270	9.29487×10^{-3}	7.23301	6.12082×10^{19}
	3.6×10^6	3.67098×10^5	1	8.59999×10^5	3412.13	2.65522×10^6	2.24694×10^{25}
	4.18605	0.426858	1.16279×10^{-6}	1	3.96759×10^{-3}	3.08747	2.61272×10^{19}
	1055.06	107.586	2.93072×10^{-4}	252.042	1	778.172	6.58515×10^{21}
	1.35582	0.138255	3.76616×10^{-7}	0.323890	1.28506×10^{-3}	1	8.46233×10^{18}
	1.60218×10^{-19}	1.63377×10^{-20}	4.45050×10^{-26}	3.82743×10^{-20}	1.51857×10^{-22}	1.18171×10^{-19}	1

1 cal= 4.18605J（計量法）

= 4.184J（熱化学）

= 4.1855J（15℃）

= 4.1868J（国際蒸気表）

仕事率　1 PS(仏馬力)

= 75 kgf·m/s

= 735.499W

放射能	Bq	Ci
	1	2.70270×10^{-11}
	3.7×10^{10}	1

吸収線量	Gy	rad
	1	100
	0.01	1

照射線量	C/kg	R
	1	3876
	2.58×10^{-4}	1

線量当量	Sv	rem
	1	100
	0.01	1

（86年12月26日現在）

Study on Shielding Design Method of Radiation Streaming in a Tokamak-type DT Fusion Reactor Based on Monte Carlo Calculation